THE UNIVERSITY *of* EDINBURGH

Rapid screening of novel nanoporous materials for carbon capture separations

Enzo Mangano

For the degree of Doctor of Philosophy

School of Engineering

The University of Edinburgh

2012

Declaration

I certify that I composed this thesis, the work contained is my own and has not been submitted for any other degree or professional qualification.

Enzo Mangano

Edinburgh, 14/09/2012

ABSTRACT

In this work the experimental results from the rapid screening and ranking of a wide range of novel adsorbents for carbon capture are presented. The samples were tested using the Zero Length Column (ZLC) method which has proved to be an essential tool for the rapid investigation of the equilibrium and kinetic properties of prototype adsorbents.

The study was performed on different classes of nanoporous materials developed as part of the EPSRC-funded "Innovative Gas Separations for Carbon Capture" (IGSCC) project. More than 120 novel adsorbents with different key features for post-combustion carbon capture were tested. The classes of materials investigated were:

- PIMs (Polymers of Intrinsic Microporosity)
- MOFs (Metal - Organic Frameworks)
- Mesoporous Silica
- Zeolites
- Carbons

All the samples were tested at experimental conditions close to the ones of a typical flue gas of a fossil fuel power plant: 35 ºC and 0.1 bar of partial pressure of CO_2.

The results from the ranking of the CO_2 capacity of the materials, at the conditions of interest, indicate the Mg and Ni-based MOF samples as the adsorbents with the highest uptake among all the candidates. The best sample shows a CO_2 capacity almost double than the benchmark adsorbent, zeolite 13X (provided by UOP). The ranking also shows some of the zeolite adsorbents synthesised as promising materials for carbon capture: uptakes comparable or slightly higher than 13X were obtained for several samples of Rho and Chabazite zeolite.

Water stability tests were also performed on the best MOFs and showed a deactivation rate considerably faster for the Mg-based MOFs, proving an expected higher resistance to degradation for the Ni based materials.

A focused investigation was also carried out on the diffusion of CO_2 in different ion-exchanged zeolites Rho samples. The study of these samples, characterised by extremely slow kinetics, extended the use of the ZLC method to very slow diffusional time constants which are very difficult to extract from the traditional long time asymptotic analysis. The results show how the combination of the full saturation and partial loading experiment can provide un-ambiguous diffusional time constants. The diffusivity of CO_2 in zeolite Rho samples shows to be strongly influenced by the framework structure as well as the nature and the position of the different cations in the framework.

The kinetics of the Na-Cs Rho sample was also measured by the use of the Quantachrome Autosorb-iQ™ volumetric system. To correctly interpret the dynamic response of the instrument modifications were applied to the theoretical model developed by Brandani in 1998 for the analysis of the piezometric method. The analytical solution of the model introduces parameters which allow to account for the real experimental conditions. The results confirm the validity of the methodology in the analysis of slow diffusion processes.

In conclusion the advantages offered by the small size of the column and the small amount of sample required proved the ZLC method to be a very useful tool for the rapid ranking of the CO_2 capacity of prototype adsorbents. Equilibrium and kinetic measurements were performed on a very wide range of novel nanoporous materials. The most promising and interesting samples were further investigated through the use of the water stability test, the partial loading experiment and the volumetric system. The ZLC technique was also extended to the measurements of systems with very slow kinetics, for which is very difficult to extract reliable diffusional time constants. An improved model for the interpretation of dynamic response curves from a non-ideal piezometric system was developed.

AKNOWLEDGMENTS

I would like to express my deepest gratitude to my supervisor, Professor Stefano Brandani, for his irreplaceable help and support during the years of my PhD studies. The passion he has for his work, the attention to the details, and his constructive comments have been of great inspiration for me. I also appreciate the patience when helping in correcting my mistakes and his guidance towards my progress. It has been and honour and a pleasure to work with him.

A special thank goes to Dr. Maria-Chiara Ferrari, for her valuable advice and active collaboration during this project. Her encouragement and her sincere and rare friendship have been essential to overcome the different problems encountered during the studies and take the most from this experience.

I am also grateful to Dr. Daniel Friedrich for his help in the analytical solution of the piezometric model and all the issues encountered in the different implementations in Matlab.

I want to thank also all the other members of the Carbon Capture Group and in particular Davide Bocciardo and Zoe Kapetaki, for their support and encouragements during these years and for their special friendship. I really enjoyed working with them.

Most of the project was based on experimental work, and for this reason my gratitude goes to all the technicians of the workshop and in particular to Steve Gourlay, for the effort and the continuous help in the several developments of the ZLC system and all the other instruments. A special thought goes to the memory of David Archibald who sadly died a few days before the submission of this dissertation. His expertise was essential in the construction of all the electronic circuits of the ZLC system.

I want also to acknowledge all the partners of the IGSCC consortium for providing the materials, and for the useful discussions and feedback on the samples:

Magdalena Lozinska, Juegen Kahr and Prof. Paul A. Wright (University of St. Andrews); Hosna Shamsipour and Prof. Peter Budd (University of Manchester); Matthew Croad and Prof. Neil B. McKeown (Cardiff University); Bingjiun Zhu and Prof. Zheng X. Guo (University College London).

A special thought goes to my brother and my closest friends.

Finally my deepest gratitude goes to my parents for their unconditional love, their efforts and encouragement during all my studies. Nothing would have been possible without their help. Thank you

TABLE OF CONTENTS

LIST OF FIGURES

LIST OF TABLES

1. INTRODUCTION

The concentration of carbon dioxide in the atmosphere has registered an unprecedented increase in the last decades, rising from 280 ppm in the pre-industrial era to 379 ppm in 2005 [1] and 394 ppm in 2012, as reported from the most recent measurements at the Scripps Institution of Oceanography [2]. Of course a contribution from natural sources of CO_2 is included in these values, but there is strong evidence that most of the warming of the past 50 years is attributable to human activities [3]. CO_2 is the most important anthropogenic greenhouse gas (GHG), with a value of 77% of the total anthropogenic emissions. The combustion of fossil fuels, mainly used for the production of electrical energy, but also in the cement industry and transport, is responsible for the greatest part of the CO_2 emitted from anthropogenic sources. In order to achieve a worldwide reduction in CO_2 emitted by 50% by 2050 it has been estimated that a reduction of the direct emissions from industry of 21% compared to the actual levels [4] is needed.

Deep reductions in the emissions rate could be achieved by switching to renewable energy sources but even though the effort invested in the research has increased in recent years some constraints are limiting the spread of these technologies. Limitations are mainly due to geographical location, intermittency of supply, land use and finally relatively high costs.

A more mature technology, and ready to be used, is instead represented by carbon capture and storage (CCS). This approach involves a portfolio of methods which can be used to capture the CO_2 generated from large source points and store it in geological structures.

There are three main approaches which can be used for CO_2 capture [3a]:

- Post-combustion capture;
- Pre-combustion capture;
- Oxy-fuel combustion capture.

Post-combustion capture refers to the separation of CO_2 from flue gas generated from the combustion of fossil fuels. The post combustion unit is fed with the flue

gas just before being released into the atmosphere, so its implementation in existing plants requires only some process modification. It is therefore applicable to new builds as well as retrofits to existing plants.

In the pre-combustion capture method the fossil fuel reacts with oxygen or air to produce a stream composed by carbon monoxide and hydrogen. CO is then converted to CO_2 and hydrogen by reacting with steam in a catalytic shift reactor. Finally the CO_2 is separated from the stream and the H_2-rich stream is used as fuel to generate energy. Relative to the flue gas fed to the post-combustion process, in the pre-combustion case the separation operates at higher CO_2 concentration, making the capture process more efficient and typically the pressure is also higher leading to lower CO_2 compression costs. This approach is feasible only in Integrated Gasifier Combined Cycle plants and the introduction of the CO_2 separation unit implies major changes which are only applicable to new builds.

Oxy-fuel combustion capture involves the use of high purity oxygen instead of air in the combustion producing a flue gas composed mainly by CO_2 and H_2O which is then processed in the capture unit for the separation of CO_2. In this case the CO_2 separation is easier relative to the post combustion case but the need of high purity oxygen implies the introduction of air separation units and a redesign of the combustion units, and both have a high cost impact in the overall process.

Despite the less favourable separation conditions, post-combustion capture has the main advantage that it can be retrofitted to existing power plants with no further modifications, so it is very likely to be the capture method adopted for most of the existing plants, while oxy-fuel and pre-combustion technologies have more chances to be implemented in the next generation power plants. Considering that the lifetime of power plants is over 40 years and given the large number of units that have been put into operation in the last 10 years, for example China added over 90 GW of new coal-fired power plant capacity in 2006 alone [5], it is clearly important to consider both retrofit and new build applications of carbon capture.

Different separation methods can be used for the CO_2 capture process. The one considered to be the benchmark for first deployment is based on absorption with amine-based solvents[6]. Solvent based processes represent a very mature technology,

which has been used in large scale for long time, but the need of very large amounts of water and the relatively high temperature for the solvent regeneration make them an energy demanding process. In addition solvent degradation and loss during operation might have negative environmental consequences [6c, 7].

With this regard separation of CO_2 using either membranes or porous adsorbents might be one of the options which can satisfy the environmental and energetic constraints. In adsorption processes nanoporous materials such as molecular sieves or activated carbons can be used to capture CO_2 which is then released in the regeneration step. The regeneration of the adsorbent can be done by pressure (or vacuum) swing (PSA or VSA, respectively) or by thermal swing (TSA). Due to the need of heating up the bed of particles and the longer cycle time, less effort has been put on the investigation of TSA which is intrinsically less competitive than the PSA option [8].

The flue gas from a power plant is released generally at atmospheric pressure and the CO_2 contents vary depending on the fossil fuel used for the combustion: from 3-4 % for a natural gas combined cycle, to 11-13 % and 12-15 % for an oil or coal fired power plant, respectively [3a]. Several reviews [9] have appeared recently summarising the studies reported on different classes of adsorbents which may have the characteristics of possible candidates for a post combustion PSA process, but very often the data reported on the performance of the adsorbents refer to conditions that are far from the real point of interest for a flue gas stream.

The main aim of this study is to provide, for the first time, a direct and systematic comparison of the adsorption performance of several materials belonging to the most promising classes of adsorbents. This was possible by testing the samples using the same experimental technique and at the same conditions. With this regard the Zero Length Column (ZLC) revealed to be an essential tool for the rapid ranking of prototype adsorbents, allowing the characterisation of the equilibrium and kinetic properties of more than 120 different samples. The experimental conditions were chosen in order to be representative of the real conditions of a typical flue gas stream from a power plant: 0.1 bar of CO_2 and 35 °C.

The novel adsorbent materials were synthesised as part of the "Innovative Gas Separations for Carbon Capture" (IGSCC) project, a UK-wide research consortium aiming to develop novel separations based on absorption, adsorption and membrane processes which are needed to reduce the energy consumption and cost of carbon capture. The consortium is led by the University of Edinburgh (UoE) and involves the collaboration with the University of St. Andrews (StA), Cardiff University (CU), Imperial College London (ICL), the University of Manchester (UoM), and University College London (UCL). As a result of the different expertise contributed by the members of the consortium, several classes of materials were investigated: several types of zeolites, MOFs and mesoporous silicas (StA); carbons (UoM, CU, and UCL); and oxides with surface functional groups (UCL).

The present dissertation is organised as follows:

- Chapter 1 presents a literature review of the most relevant classes of adsorbents for post-combustion carbon capture. The chapter analyses separately the results reported for the different materials trying to identify the key factors which affect the adsorption performance.
- Chapter 2 introduces the theory on which the ZLC technique is based, showing how, by knowing the key characteristics and the limitations of the method, it is possible to change the experimental conditions in order to optimise the measurement.
- Chapter 3 provides a detailed description of the ZLC systems used for the experiment. The flexibility of the two apparatuses used allows different types of experiments and a description of the relative experimental procedures is also provided.
- Chapter 4 presents the results obtained for the ranking of the CO_2 capacity for all the samples investigated. The different classes of samples are analysed separately, and to facilitate the discussion, when possible, subcategories of samples were created. This allows to investigate the effects of the different modification on the adsorption performance.
- Chapter 5 presents the results obtained from the kinetic measurements on the ion-exchanged Rho zeolite samples using the ZLC method. The results

show how the combination of the full saturation and partial loading experiment can provide un-ambiguous diffusional time constants. The results for the diffusivity of CO_2 in zeolite Rho samples resulted to be strongly influenced by the framework structure as well as the nature and the position of the different cations in the framework.

- Chapter 6 reports the results on the kinetic experiments performed on zeolite Rho and 13X using a volumetric apparatus. To interpret the dynamic response of the system the theoretical model developed by Brandani in 1998[10] for the analysis of the piezometric method was used. Due to the particular configuration of the instrument, modifications to this simplified model were applied in order to take account of the real experimental conditions.

2. ADSORBENT MATERIALS FOR CO_2 CAPTURE

A large number of adsorbents have been proposed and investigated as possible candidates for carbon capture. The selection of the best samples can not be based only on their adsorption properties (i.e. capacity, heat of adsorption, kinetics) because when one goes beyond considering the sample-scale and looks at the overall capture process other factors may play a crucial role in the final choice. For this reason economic criteria have to be always taken into account. These are not only related to the costs of synthesis of the materials, but, in larger scale, for example:

- the size of the equipment is related to the volume of the adsorbent needed, i.e. the adsorption capacity;
- the regeneration energy demand depends on the heat of adsorption;
- the cycle time depends on the equilibrium and kinetic properties of the sample and the process selected, i.e. pressure swing adsorption (PSA) vs. temperature swing adsorption (TSA);
- the hydrothermal stability has a great impact on the plant costs;
- the loss of performances due to the presence of impurities in the feed stream is probably one of the most important issues regarding the selection of the best adsorbent. This may affect the capacity, the shut down schedule of the plant and in many cases the need of removal systems for water and other impurities.

Based on these observations and with regard to post-combustion applications the best adsorbent should have high CO_2 capacity at low pressure, high selectivity for CO_2, fast adsorption/desorption kinetics, good mechanical properties, high hydrothermal and chemical stability as well as low costs of synthesis.
No adsorbent has been found to meet all these requirements and researchers are investigating different solutions to overcome the weak points of each class of adsorbents: from the tuning of the samples to increase the performances to process

design modifications to increase the efficiency of separation and reduce the overall costs.

Zeolites, as well as carbon-based materials, are probably the class of adsorbents most widely investigated. In recent years a considerable research effort has been put in the development and the study of a new class of adsorbent, MOFs (metal-organic frameworks) as promising candidates for CO_2 separation. With regard to membrane separation processes different classes of polymers have been investigated and very recently a new class of polymers, PIMs (polymers of intrinsic microporosity), characterised by enhanced separation properties, has received increasing attention from researchers.

The present work is focused on the screening of several materials belonging to different classes of adsorbents. All the materials tested are novel prototypes synthesised by our collaborators as part of the "Innovative Gas Separations for Carbon Capture" (IGSCC) project, an EPSRC-funded UK research consortium. The classes of materials investigated are:

- Zeolites, synthesised at the University of St. Andrews;
- MOFs, synthesised at the University of St. Andrews;
- Carbon-based adsorbents, synthesised at the University of Manchester and University College of London;
- Mesoporous silicas, synthesised at the University of St. Andrews;
- PIMs, synthesised at the University of Manchester and Cardiff University.

In this chapter a description of the main features of each class of adsorbents is presented. For each class, a brief review of the studies published in the literature is included, with focused attention on the materials related to the ones investigated in the present work. The main class of materials not studied directly as part of the IGSCC project, due to delays in the synthesis at UCL, are carbon-based materials with surface modifications based on amine groups.

2.1 Zeolites

Zeolites are crystalline aluminosilicates characterised by a highly ordered open structure. Their framework is the result of the coordination of tetrahedral units of AlO_4 and SiO_4 inter-connected through shared oxygen atoms. Zeolites can differ greatly for the framework type, the size and shape of the channels and cages as well as the Si/Al ratio. The negative charge introduced by the presence of the aluminum atoms is counter balanced by the exchangeable cations. The nature of the cations as well as their position and distribution inside the framework is a key factor for the desired adsorption properties of zeolites.

Low Si/Al ratios and high cation contents are the key features needed for good CO_2 adsorption properties. Type X and A zeolites, in this sense have been widely investigated in the last decades [9b]. They are generally characterised by a relative high CO_2 capacity at low pressure which makes them very promising candidates for CO_2 separation from atmosphere and flue gas. Several studies have indicated zeolite 13X as one of the best adsorbents for post combustion applications, for this reason is very often used as a benchmark material for the comparison with other candidates for CO_2 separation processes [11].

Zeolite 13X belongs to the faujasite (FAU) structure type which consists of an array of β-cages connected by double six-ring (D6R) units, as shown in Figure 2.1. Each cage is connected to four other cages through 12-membered oxygen channels with a diameter of about 7.4 Å [12].

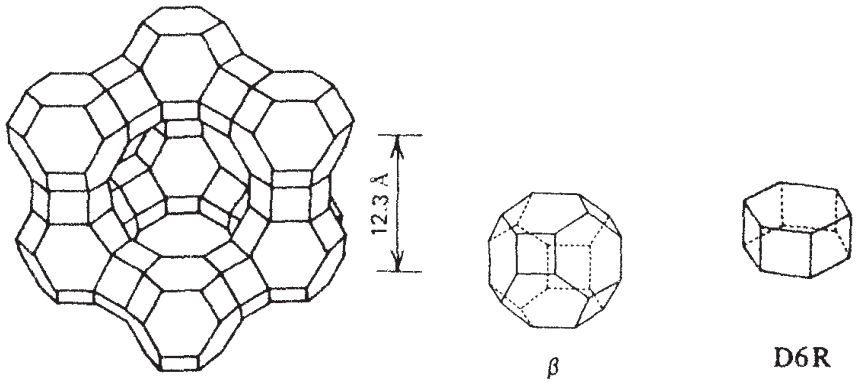

Figure 2.1: Framework structure of FAU type zeolite, with β cage and D6R unit [12].

In the present work all the novel nanoporous materials investigated were compared with a commercial sample of 13X beads, provided by UOP, a Honeywell company, and tested at the same experimental conditions.

Chue et al. [11a] were one of the first to indicate zeolite 13X as one of the best adsorbents for bulk separation of CO_2 from flue gas. They presented a comparison of zeolite 13X and activated carbon for the recovery of CO_2 from flue gas using a PSA cycle. The equilibrium properties of the samples were measured using a volumetric apparatus: 13X exhibited a CO_2 uptake more than three times higher than the activated carbon at 15 °C and 0.1 atm, with a value of about 3 mol/kg. From the isotherms at different temperatures the heats of adsorption were extracted: values of 36 and 30 kJ/mol were obtained for 13X and activated carbon, respectively. Despite the higher heat of adsorption, the higher working capacity and selectivity of zeolite 13X, resulted in a PSA cycle with higher product purity and recovery.

Harlick and Tezel [11b] carried out a screening study on 13 selected suitable zeolites for CO_2 separation from flue gas. From the adsorption isotherms obtained, 13X and NaY were identified as the most promising adsorbents for carbon capture applications, with a CO_2 capacity of about 2.6 and 2 mol/kg respectively at 22 °C and 0.1atm. A study on the expected working capacity was also performed. In this analysis the 13X and NaY adsorbents were directly compared: the results indicated 13X as equilibrium adsorbent more suitable for low regeneration pressure and NaY for high regeneration pressure. Based on this the authors suggest 13X as the adsorbent to be chosen for CO_2 separation from low concentration streams.

Siriwardane et al. [13] used a volumetric system to study the adsorption of the natural zeolites to be used in a PSA process for carbon separation. From the analysis of the competitive adsorption of the three gases emerged that the separation performances for CO_2 increase with the Na-content of the adsorbent, indicating the chabazite sample as the best one. TPD (temperature-programmed desorption) measurements showed also that most of the CO_2 is physically adsorbed, while just a small amount chemically reacts to form carbonate products. Subsequently the same authors[14]

conducted a similar study on five different types of zeolites (4A, 5A, 13X, APG-II, and WE-G 592) chosen as suitable candidates for CO_2 capture at high temperature from high CO_2 pressure streams. Tests were performed at 120 °C in a flow reactor, a volumetric and a gravimetric system: the results indicated the zeolites with the highest Na/Si ratio, 13X and WE-G 592, as the most promising among all the samples tested. The heats of adsorption measured with a calorimeter had values between 55 kJ/mol and 66 kJ/mol. From these values of the interaction between the CO_2 molecules and adsorption sites of the zeolites was recognised as something in between a weak physical interaction and a chemical interaction.

Cavenati et al. [15] used a Rubotherm balance to measure the equilibrium properties of nitrogen, methane, and carbon dioxide on a 13X sample at different temperatures. The results proved the higher affinity between CO_2 and 13X relative to the other sorbates, with an uptake slightly higher than 2 mol/kg at 308 K and 0.1 bar. Furthermore the high selectivity for CO_2 obtained makes the adsorbent a good potential adsorbent for methane purification from natural gas or for carbon capture from flue gas.

More recently, Dasgupta et al. [16] presented a comparative study of CO_2 separation from mixture with N_2 using a VSA cycle apparatus. The adsorbents compared were a zeolite X based sample and a commercial CuBTC-MOF. The results show that a higher selectivity for the zeolite X at low pressure, while a higher working capacity is registered for the MOF sample. With regards to the overall process the use of the zeolite X as adsorbent will result in higher purities process, while using CuBTC higher recoveries will be obtained. The authors conclude suggesting the zeolite X as the better choice for CO_2 recovery from flue gas.

Yi, Deng et al. [17] recently published a comparative study about the adsorption equilibrium of SO_2, NO and CO_2 on some samples of FAU and LTA zeolites (NaX, NaY, and CaA), 13X and 5A. The samples were tested on a static volumetric adsorption system at 323 K up to a pressure of 0.6 bar. For 13X and 5A isotherms at different temperatures (323, 348 and 363 K) were also produced. The results show that for all the samples the strongest adsorbed species is SO_2, then in order CO_2 and NO. The sample with the higher affinity is the NaX, which is also the one with the

highest polarity. In order to obtain information on the kinetics, breakthrough experiments were carried out on the FAU and LTA samples. The results indicated CaA as the sample with slowest kinetics, while due to the wide pore distribution NaY shows the minimum mass transfer resistance. Regarding the comparison between 13X and 5A, the analysis shows that under equilibrium conditions 5A is a better candidate for the co-adsorption of SO_2, NO and CO_2 than 13X.

Despite the good adsorption properties for CO_2, one difficulty with using zeolites in carbon capture applications is that they are generally hydrophilic materials: the strong interaction with water induces a displacement of the CO_2 from the adsorption sites, lowering the adsorption performance.

Brandani et al. [18] used the ZLC technique to measure the equilibrium isotherms of CO_2 some ion exchanged X type zeolites at different temperatures. From the study of the shape of the isotherms obtained it was possible to have an insight of the distribution of the cations in the framework of the zeolites. NaLSX has a higher uptake than NaX mainly due to the higher density of cations of the LSX zeotype, but both the samples showed evidence that the two different adsorption sites for these sample have small energetic differences. On the other hand for LiLSX, CaX and CaA, the distribution of the cations in the zeolite framework generated two energetically different types of adsorption sites. The values of the heat of adsorption obtained are between 40 and 50 kJ/mol and were found to be lower than the ones obtained from other calorimetric measurements reported in the literature. In fact due to the nature of the ZLC experiment only the physically adsorbed CO_2 is desorbed so the heats of adsorption extracted are associated only to the reversible adsorption of CO_2. From the study also emerged that for high hydrophilic adsorbents, such as LiLSX, the presence of even very small amount of water can significantly affect the resulting CO_2 uptake.

With this regard Brandani and Ruthven [19] further investigated the effect of small amounts of water on the adsorption of CO_2 and C_3H_8 on several X type zeolites: Li- and Na-LSX, and Na and Ca-X. The ZLC experiments showed for all the samples a decrease of the adsorption capacity with the increase of the water loading. The comparison between the systems with the two different sorbates showed that this

effect is less pronounced for propane than for CO_2. The adsorption energy of CO_2 is mainly due to interaction between the quadrupole and the electric field induced by the presence of the cations. Inversely for propane (non-polar species) the energy of adsorption is based on van der Waals forces, and the alteration of the electric field induced by the presence of water has a minor effect on the strength of adsorption. These results [18-19] indicate that the relatively low heats of adsorption reported in the literature may be due to the presence of even small amounts of water in the samples used.

Li et al. [20] investigated the impact of the presence of water on a VSA process to capture CO_2 from a synthetic flue gas using a 13X adsorbent. As expected, the presence of water highly affected the adsorption capacity of CO_2 of the zeolite, and as a result a consistent reduction of the CO_2 recovery, purity and productivity of the process was registered. The analysis concluded that despite the negative impact of the presence of water, under adequate conditions, the process could run with no need of pre-drying the flue gas stream.

Only limited results have been published regarding diffusion measurements of CO_2 in zeolites. Table 2.1 lists some of the data found for selected zeolites.

Table 2.1: Literature values of CO_2 diffusivity for various types of zeolites

Adsorbent	Technique	T [K]	D [m^2/s]	E_a [kJ/mol]	D/R^2 [s^{-1}]	R [μm]	Ref.
4A	Grav.	308.15	$1.17x\ 10^{-13}$	23	-	1.75	[21]
4A	Grav.	308.15	1.02×10^{-15}	20	-	1.75	[21]
4A	Chromat.	308.15	1.5×10^{-12}	20.5	-	-	[21b, 22]
5A	Grav.	308.15	1.37×10^{-12}	12.5	-	17	[21]
Na-A	Volum.	323	4.8×10^{-14}		-	1.085	[23]
5A	Grav.	-	-	20.7	-	1.5	[24]
5A	ZLC	308.15	2.55×10^{-10}	9.4	-	25	[25]
Ca-A	Freq. resp.	-	-	14.3	-	1.5	[24]
4A	Grav.	308.15	5.06×10^{-16}	24.57	1.33×10^{-4}	1.95	[26]
Ca-X	Grav.	308.15	3.06×10^{-14}	15.97	8.04×10^{-3}	1.95	[26]
13X	Volum.	303.2	6.49×10^{-15}			1.25	[27]
Na-Y	Chromat.	313.15		41.9	0.00067	-	[28]
Na-Y	Breaktrh.	323			0.0321	-	[17a]
Na-X	Breaktrh.	323			0.0023	-	[17a]
Ca-A	Breaktrh.	323			0.0017	-	[17a]

2.1.1 Ion-exchanged zeolites

Recent studies on zeolites have been also directed towards the investigation of the effects of the exchanging cations on the adsorption properties. The nature and the distribution of the cations inside the framework not only induces modifications of the electrical field inside the pores, but also morphological changes in the structure of the zeolites. This means that high charge density cations should in theory increase the adsorption capacity of the zeolite but the position assumed in the framework plays a crucial role in the kinetics of the process.

Ridha and Webley [29] investigated the adsorption of CO_2 on Li-, Na- and K-Chabazite, reporting a CO_2 uptake which follows the sequence $Li^+ > Na^+ > K^+$. The

highest value obtained for Li-Chabazite is in agreement with the high electrostatic interactions on the small Li^+ cation. From the study also emerged that the Na and K samples also presented a low pressure hysteresis between the adsorption and desorption isotherms. This behaviour was associated to the larger size of the Na and K cations which should be responsible for a phenomenon of hindering diffusion inside the windows of the structure. The larger hysteresis in the case of the K cation may be explained by a more intense blockage of the windows generated compared to the Na cation.

Pirngruber et al. [30] presented a study on the adsorption CO_2 on faujasite Y with different extra-framework cations. The effect of 4 different cations was investigated: Cs^+, K^+, Na^+ and Li^+. The trend of the CO_2 capacity obtained at low pressure does not follow the expected trend of the strength of the quadrupole-monopole interaction of the CO_2 molecule with the cation. In fact based on this one would expect that at low pressure a higher uptake would be obtained by the Li form which has the smallest cationic radius. Inversely the sequence obtained by Pirngruber et al. is CsY > KY > NaY > LiY. Further measurements proved that in addition to the interaction between the CO_2 molecule and the cations there is also an interaction between CO_2 and the oxygen atoms in the framework. This is mainly due to the basicity of the oxygen atoms in the framework which tends to stabilise the CO_2. Walton et al. [31] showed that this effect increases with the cation size and it is particularly strong in zeolite Y but is negligible in the X type of zeolites. The sequence of the CO_2 capacity at low pressure obtained by Pirngruber et al. is then mainly due to the predominant effect of the basicity of the framework relative to the strength of the quadrupole interaction. At high pressure the CO_2 uptake followed the sequence NaY > KY > LiY > CsY. The reason for such a trend was associated to the fact that close to saturation the effect of the volume occupied by the cations in the pores becomes prevalent relative to the charge density of the cations.

In a more recent work Lee et al. [32] investigated the role of the exchanged cations in the adsorption properties of zeolites. The tested samples were prepared impregnating a commercial sample of 13X with different cations: Li, K, Ca and Mg. Due to the nature of the cations the samples impregnated with Li and K (small

radius and monovalent) showed a smaller average pore size and a higher surface area than the Ca and Mg ones. From the dry tests performed, the CO_2 uptake was higher for the Ca and Mg, indicating that a key role is played by the electronic interactions between the adsorbing sites and the sorbate molecules, rather than the morphological pore properties. Wet tests were also performed simulating a typical indoor mixture (3000 ppm of CO_2 and 20% relative humidity). A decrease of the adsorption capacities was registered in all the samples in presence of water, and particularly in the one with highest polar nature, Ca–sample. TPD analysis also showed a small contribution of chemisorption in the Ca–sample.

Yang at al. [33] conducted a screening of CO_2 capacity of different ion-exchanged zeolites beta. The influence of the exchanged ion on the adsorption properties was investigated: measurements on a volumetric system showed an increase of the CO_2 capacity following the sequence of $K^+ > Na^+ > Li^+ > Ba^{2+} > Ca^{2+} \approx Cs^+ > Mg^{2+}$. From the results it is clear that in this case the capacity is dependent on the size and charge of the balancing cations, and also on the density and the distribution of the cations in the framework, which play a key role in the resulting interaction between the sorbate and the sorbent. Breakthrough experiments were also performed to extract the CO_2/N_2 selectivities and the heats of adsorption: the trend obtained for the selectivities is in general opposite to the one of the CO_2 capacity, while the heat of adsorption at zero loading showed an increase with the basicity of the exchanged cations.

2.1.2 Ion - exchanged Rho zeolites

An interesting case among the zeolites is represented by the Rho topology. This type of zeolites is characterised by an unusual framework flexibility and as a result the variation of the extra-framework cations has been proved to induce considerable distortions in the structure [34]. The zeolite Rho has a structure characterised by a body-centred-cubic arrangement of α-cages connected by double eight rings [34d], with an effective channel diameter of about 3.6 Å [35]. In this sort of configuration three sites can accommodate the extra-framework cations: the single eight-ring

(S8R), double eight-ring (D8R), and single six-ring (S6R) sites [36] (Figure 2.2, left). The degree of occupancy of each site depends on the nature of the cation and the charge distribution which arises from the allocation of the extra-framework cations has been demonstrated to induce the distortion in the original structure of the zeolite Rho [37]. In the case of the Cs-exchanged Rho, for example, the presence of the caesium cations, preferably allocated in the D8R sites, causes the structure to lose its original symmetry ($Im\bar{3}m$) for an acentric configuration ($I\bar{4}3m$) characterised by an elliptical arrangement of double-eight rings [34e] (Figure 2.2, right).

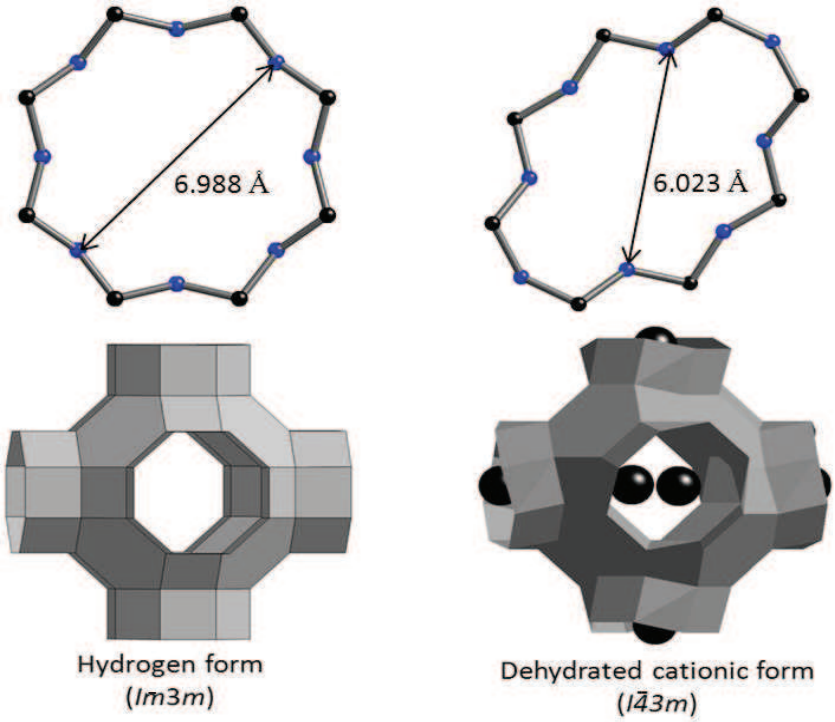

Figure 2.2: Structure of Rho zeolite in symmetric ($Im\bar{3}m$) and acentric ($I\bar{4}3m$) configuration (schemes prepared by Magdalena Lozinska, EaStCHEM School of Chemistry, University of St Andrews)

The implications of such modifications on the kinetics of adsorption of CO_2 will be discussed in detail in the next chapters of this dissertation.

A very recent work on the adsorption properties of a ion exchanged Rho zeolite has been published by Palomino at al. [38]. The sample showed a capacity of 2.2 mol/kg at 6 bar and 303 K and a very high CO_2/CH_4 selectivity. The explanation for such high selectivity arises from the structural modifications during the adsorption of

CO_2. X-ray measurement during adsorption indicated that before the adsorption of CO_2 a I43m structure can be recognised, characterised by elliptical pores with an effective aperture of 2.9 Å. At 2 bar a transition from $I\bar{4}3m$ to $Im\bar{3}m$ occurs. The transition is fully reversible by fluxing N_2 and it does not occur if CH_4 or N_2 are used as a sorbate, proving that the structural modifications are not associated to the pressure, but to the presence of CO_2.

2.2 MOFs

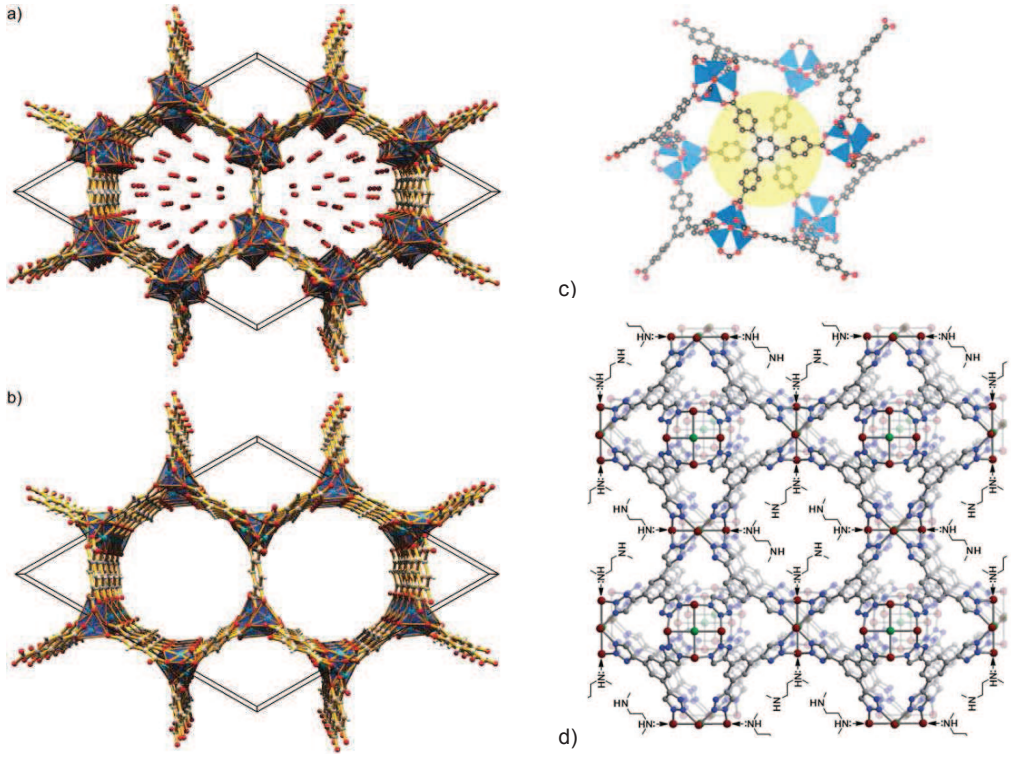

Figure 2.3: Crystal structures of MOF-74 a) hydrated and b)dehydrated [39]; c) MOF-177 [40], and d) mmen-CuBTTri [41].

MOFs are a relatively new class of adsorbents which have been widely investigated in the past few years; Figure 2.3 shows the structures of some of the most common MOFs for carbon capture applications. Their structure consists of organic-inorganic hybrid networks formed by metal ligand bonds [9c]. One of their main attractive features is the possibility to modify their structures and functional properties by changing the building blocks used in their construction: this gives the incredible advantage to finely control pore dimension, shape of the channels, and chemical potential of the surface, giving in the end the possibility to built the adsorbent with the desired adsorption properties [42]. Thanks to their high surface area and large pore volume MOFs show generally higher CO_2 capacity at high pressure compared to zeolites [43]. Despite their relatively low capacity at low partial pressure, their high

thermal stability and the fully reversible CO_2 adsorption make them very promising materials for pressure-swing processes [40, 43].

Gravimetric measurements on different MOF samples were performed by Millward et al. [40]. The experiments indicated the sample MOF-177 as the best one with an uptake of 33.5 mol/kg, at 42 bar and room temperature. The sample was then compared with two benchmark materials, zeolite 13X and Maxsorb (high surface area carbon), in a volumetric system: the results confirmed the considerably higher uptake of the MOF sample at high pressure, while revealing a pretty low adsorption capacity at low pressure. Zeolite 13X showed the higher uptake at pressures below 15 bar.

As mentioned previously a good adsorbent for post-combustion CO_2 capture should have a high CO_2 uptake at low pressure. In this regard MOF-74 (also called DOBDC, or CPO-27) and its politypes have shown attractive features for carbon capture. Caskey et al. [44] investigated the effect of different metal cations substituted on the MOF-74 structure. The metals used were Ni, Mg, Zn and Co. Low pressure isotherms at 296 K showed a CO_2 uptake trend increasing in the order Zn < Ni ~ Co < Mg, with a capacity of 23.6 wt % at 0.1 atm for the latter. The heats of adsorption were also measured and a value of 47 kJ/mol was registered for the Mg sample. The authors attributed the improved adsorption performances of the Mg sample to the higher ionic character of the Mg-O bond, which improves the affinity with CO_2 maintaining the reversibility of the adsorption process. VTIR measurements, performed by Valenzano et al. [45] confirmed the same value of the heat of adsorption for Mg-MOF-74. A more recent work of Valenzano et al. [46] on the Ni-MOF-74, confirmed the value of heats adsorption obtained by Caskey [44] and Dietzel [42].

The effect of water in the adsorption of CO_2 on Ni-MOF-74 was investigated by LeVan et al. [43]. The study wanted to compare the performances of Ni-MOF-74 with HKUST-1 at the conditions of interest for CO_2 capture from flue gas, 0.1 atm and 25 ºC. Pure component isotherms indicated Ni-MOF-74 as the sample with the highest CO_2 capacity, with an uptake value of 3.28 mol/kg at 0.1 atm. Regarding the water uptake the higher H_2O capacity was obtained for the HKUST-1 pellets (due to the higher surface area and pore volume). To study the effect of water in the

CO_2 adsorption, experiments at different H_2O loadings were carried out and the results were compared with literature data of 5A and NaX zeolites at the same conditions. As expected the CO_2 capacity decreased with the increase of the H_2O loading but this effect was less pronounced for the MOFs relative to the zeolites samples. The slope at low loading of the isotherms was also a measure of the strength of the interaction between the sorbent and the water molecules: for both the MOF samples the slopes were lower than NaX and 5A indicating an easier regeneration process of the adsorbents. Moreover hydrothermal stability tests showed a higher resistance to degradation due to vapour adsorption for Ni-MOF-74 than HKUST-1. Kinetic measurements were also performed, proving a very low transport resistance for both samples, while the dependence of the adsorption rate from the pellet size suggested the presence of a macropore diffusion control process.

An updated analysis on the adsorption properties of Ni-MOF-74, was recently presented by the same research group [47]. Adsorption experiments on a volumetric system and dynamic CO_2/N_2 breakthrough measurements were used to extract the adsorption properties of the sample. The CO_2 capacity at 25 ºC and 0.15 bar obtained from the volumetric experiment was 3.86 mol/kg, in good agreement with value obtained from the breakthrough method (3.74 mol/kg). The adsorption process was also proved to be fully reversible by simply purging with pure He. The study also investigated the effect of small amount of water on the dynamics of CO_2 adsorption. As expected, a significant loss of the CO_2 capacity was registered: from 3.74 to 2.69 mol/kg, in good agreement with the previous work. In particular from the water experiment it was noticed that the N_2 capacity was not very affected by the presence of water indicating that H_2O molecules interact specifically with the strong CO_2 adsorption sites rather than the weak sites. Furthermore, by repeating cyclically the experiment it was also noticed that the original CO_2 capacity could not be recovered, indicating that the adsorption of water permanently affects the performance of the material.

A comparative study was recently presented [48] to investigate the CO_2 capture performances of several zeolites (MFI, JBW, AFX, NaX) and MOFs (MgMOF-74,

MOF-177, mmen-CuBTTri). Selectivity and working capacity, obtained from molecular simulations, were used as performance indicators. As expected the highest value of the selectivity was obtained for the sample with lower N_2 uptake (lower values of surface area and pore volume), JBW, then in the order: JBW > mmen-CuBTTri > AFX ~ MgMOF-74 > NaX >> MFI > FAU-Si > MOF-177. The higher value of the working capacity was registered for Mg-MOF-74 at 300 K and 10 kPa. Breakthrough experiments using a CO_2/N_2 mixture were also carried out in order to identify the sample with the optimal combination of selectivity and working capacity for PSA applications. The dimensionless breakthrough times, which is a combination of selectivity and working capacity, was used as a measure of comparison among the samples: with regard to this the following sequence was obtained Mg-MOF-74 >> NaX > AFX > JBW ~ mmen-CuBTTri >> MFI >> MOF-177. From the screening emerged that the two best samples for post-combustion CO_2 capture are Mg-MOF-74 and NaX, highlighting that the MOF sample can adsorb twice as much CO_2 than NaX.

Herm et al. [49] also published a work focused on the separation of binary and ternary mixtures of CO_2, CH_4, and H_2 from high pressure streams using Mg-MOF-74. High pressure adsorption measurements showed that the sample had the highest affinity for CO_2 with an uptake of about 15 mol/kg at 313 K and 35 bar. From the analysis of the selectivities it was noted that a key role is played by the quadrupole moment of the CO_2 molecule and the relative polarizabilities of the components: CH_4 has a similar polarizability to CO_2 and higher than the one of H_2. This explains why the selectivity for CO_2/H_2 is higher than the one relative to the mixture CO_2/CH_4. Furthermore the CO_2/CH_4 selectivity strongly decreases with the increasing of the pressure and becomes almost constant at pressures higher than 5 bar: this can be associated to the strong CO_2 interaction in low pressures range indicated by the steep adsorption isotherm. CO_2 and CH_4 are then competing for the same adsorption sites. Based on these experimental results breakthrough calculations were made and compared with a 13X scenario. In all cases the MOF samples showed considerably higher performances relative to 13X.

Mg-MOF-74, has been also modified by the insertion of ethylene di-amine (ED) functionalised groups [50] in the open metal sites. The thermo-gravimetric experiments showed an increase of the CO_2 capacity for the modified sample relative to pristine one (1.51 mol/kg compared to 1.35 mol/kg for the pristine at 400 ppm of CO_2 at room temperature). Furthermore, cyclic adsorption and desorption runs have proved an improved regenerability for the amine modified sample, which maintained the same capacity in all the cycles, while the pristine sample lost about 20% of the original capacity after the first cycle.

Very recently, an extensive work on MOF-74 with different metal sites was carried out from Hu [51]. The Zero Length Column method was used for the ranking of the CO_2 capacity at 38 ˚C and 0.1 bar for samples of Zn-, Co-, Ni- and Mg-MOF-74; zeolite 13X (from UOP) was used as benchmark material. The trend obtained for the CO_2 uptake was Zn < Co < Ni < Mg, in good agreement with what reported in literature [44]. The isotherms extracted resulted to be fairly linear in the range of pressure of interest, only the Mg- form showed a slight deviation from linearity. Kinetic tests on Ni-MOF-74 and 13X pellets showed evidence of a mass transfer process controlled by macropore diffusion. Moreover the samples were also tested with regard to the effect of impurities (water, SO_x and NO_x) on the CO_2 capacity. The results showed that in presence of impurities and water all the MOF samples undergo significant deactivation, with the Ni-MOF-74 resulting to be the more resistant to degradation. The author concluded that drying units should be used prior to the carbon capture adsorption process.

2.3 Carbon-based adsorbent

Carbon-based adsorbent are synthesised by the thermal decomposition of carbonaceous materials. Their structure is characterised by randomly oriented microcrystallites of graphite which originate a wide pore size distribution. They have been investigated and used for a wide range of gas separation, this reason, as well as the relatively low cost of the synthesis (due to the raw materials needed), increased the interest in possible applications of this class of adsorbents for CO_2 separation processes. Looking at the CO_2 adsorption capacity they are generally characterized by lower values than zeolites at low CO_2 partial pressure but higher in high pressure region [52]. Despite their lower capacities compared to zeolites what makes carbon-based materials promising for carbon capture is the excellent reversibility of adsorption, which is a key feature for any application at low energy requirement. This is essentially due to the lower values of the heat of adsorption which is directly related to the surface affinity for CO_2 [53]. In this sense one of the most interesting research issue in carbon materials is the attempt to increase their adsorption properties by the introduction of different surface functional groups. Adding basic chemical groups has the advantage of an increase of the affinity for CO_2, but, at the same time, also for water, making the material more hydrophilic. Moreover, due to the presence of the chemical groups, a decrease of the available surface area for adsorption [53] is generally observed.

Siriwardane et al. [52], compared the adsorption properties of a commercial activated carbon (G-32 H) with two molecular sieves: 13X and 4A. The equilibrium isotherms, obtained from a volumetric measurements, showed higher CO_2 uptakes for both the molecular sieves at pressures lower than 2 bar, while at higher pressures the activated carbon registered the highest CO_2 capacity (8.5 mol/kg at 20 bar and 25 ˚C, compared with values of 4.2 and 5.8 mol/kg for 4A and 13X, respectively). This may be associated to the higher surface area of the activated carbon. The stability of the sample was also investigated by repeating cyclically the experiment: the activated carbon maintained the same capacity over 10 cycles,

while the molecular sieves showed a slight decrease of the capacity over the cycles. CO_2/N_2 selectivities were also calculated for all the samples: the highest values were obtained for both the molecular sieves. A decreasing trend of the selectivity with the pressure was common to all the adsorbents, but less pronounced for the activated carbon. From the isotherms at different temperatures isosteric heats of adsorption were extracted. A coverage dependence of the heats was noticed: as expected 13X had the highest value (from 50 to 10 kJ/mol at high loading), while values from 28 to 11 kJ/mol were found for the activated carbon. The dependence of the heat of adsorption on the adsorbed amount indicated the presence of strong adsorption sites with different adsorption energies.

Himeno et al. [54] compared four commercial carbon based adsorbents with regard to the CH_4/CO_2 separation performances: activated carbons A, A10 fiber, Maxsorb, Norit R1 Extra and BPL. A volumetric apparatus was used to extract the pure component isotherms up to 60 bar. For all the samples the adsorbed amount of CO_2 was almost twice the one for CH_4 and the highest capacity obtained was for Maxsorb, then in order activated carbon A, Norit R1 Extra, A10 and BPL. The trend of the capacity, the same as the one of the surface area and pore volume, confirmed the strict relationship between these physical properties and the CO_2 uptake. The presence of heterogeneous adsorption sites was confirmed by the fact that the isosteric enthalpies were not independent from the coverage. In order to evaluate the strength of the interaction between of the adsorbents the CO_2 molecules, zero loading enthalpies were extracted from the Henry's law constants. The values obtained were in order: 25.7 kJ/mol for BPL , 22.0 kJ/mol for Norit R1 Extra, 21.6 kJ/mol A10, 17.8 kJ/mol for activated carbon A and 16.2 kJ/mol for Maxsorb.

Shen et al. [55] studied the equilibrium and kinetic properties of CO_2 adsorption of pitch-based activated carbon beads at different temperatures. A Rubotherm magnetic suspension microbalance was used to measure the equilibrium isotherms on the adsorbent: the CO_2 uptake obtained was 1.92 mol/kg at 303 K and 1 bar. The isotherms were than fitted using the virial model and a multi-site Langmuir model developed by Nitta et al. [56] which assumes that each adsorbate molecule can occupy

more than one site on a homogeneous surface, with the same energies. The fitting of the experimental data showed a good agreement at low pressure while discrepancies were observed at high pressure. The authors associated such inconsistency to the fact that the multi-site Langmuir model used is based on the assumption of independence of the isosteric heat of adsorption from the coverage: the energy associated to the adsorption was assumed the same for all the sites and equal to the isosteric heat of adsorption at zero loading. The calculated isosteric heats showed a strong dependency with the coverage indicating the presence of a heterogeneous surface. A value of 23.16 kJ/mol for the heat of adsorption at zero coverage was obtained from the Henry's law constants at different temperatures, which is consistent with typical values for carbon based materials. Dilute breakthrough experiments at different temperatures were used to investigate the kinetics of the adsorbent. The results were interpreted as micropore diffusion control process for both CO_2 and N_2, with higher value of the diffusivity of N_2 compared with CO_2. The CO_2 molecule has a smaller kinetic diameter relative to N_2 (0.33 nm for CO_2 and 0.364 nm for N_2 [57]), therefore a faster micropore diffusion is expected for CO_2 compared to N_2. It is very likely that what it was measured was a macropore and not a micropore diffusion control process.

Having obtained the fundamental properties of the sample, Shen et al. [58] wanted to investigate the use of the activated carbon in a four-steps Skarstrom-type VPSA process to capture CO_2 from flue gas. Fixed bed breakthrough experiments were carried out with a range of CO_2 compositions from 15 to 50%. The performances of the overall capture process were evaluated by changing the key parameters of the process (feed flowrate, composition, temperature and pressure). With a feed concentration of 15% of CO_2 in N_2 at 303 K and 131.25 kPa, purity of 48.56% and recovery of 55.35% were obtained, while doubling the feed pressure values of 93.70% and 78.23% were obtained for purity and recovery respectively.

Recently the same research group used the results from the previous works to study the application of activated carbon for CO_2 capture from flue gas, presenting a combination of experimental and simulated results on a two stage VPSA process [59]. Using a feed composition of 15% of CO_2 in N_2, feed pressure of 10 kPa and

temperature of 303 K, values of 95.36 and 73.62% were obtained for CO_2 purity and recovery respectively.

A sub-class of carbon based materials is represented by the carbon molecular sieves (CMS) microporous materials with a narrow pore size distribution which allows the kinetic separation gas mixtures. With regards to this, Carruthers et al. [60] recently investigated the possibility of application of these new class of carbons for CO_2 separation from flue gas. CO_2 isotherms for three commercial samples (ACS-1, ACS-2 and ACS-3) at different temperatures were obtained using a gravimetric magnetic suspension balance. The results indicated ACS-3 as the best sample, with a CO_2 uptake of 4.2 mol/kg at 1 bar and 294 K. An average value of 26.5 kJ/mol for the isosteric heat was reported for all the samples. In order to test the performances in a PSA application, the samples were tested first in a single bed apparatus, then in PSA lab-scale system and finally ACS-3 was tested in a pilot scale vertical reactor. The conditions used were the ones of interest for CO_2 capture from flue gas: 15% of CO_2 in N_2 atmospheric pressure and ambient temperature. ACS-3 showed relatively fast kinetics, very low attrition resistance and high hydrothermal stability: the CO_2 capacity was almost not affected by the presence of water in the flue gas. The study concluded that despite the lower capacity relative to other adsorbents (MOFs and zeolites) the low heats of adsorption and the stability of carbon-based adsorbents make them competitive for CO_2 capture from flue gas.

The adsorption properties of activated carbon can be significantly improved by the incorporation of amine functional groups into their porous structure. The CO_2 chemically reacts with the amine groups forming bicarbonate and/or carbamate, resulting in high equilibrium capacity but generally slow kinetics [9a].

Maroto-Valer et al. [61] compared the CO_2 capacity at different temperatures of fly ash carbons impregnated with different amine compounds: MEA, DEA, MDEA, and MDEA + MEA. The samples were first activated in presence of steam at high temperature to increase the surface area and then chemically impregnated with amines. As a result of the increased surface area the activated carbons exhibited a higher capacity than the pristine samples, and the clear physical adsorption process was observed. At 30 ˚C the impregnated samples exhibited a CO_2 capacity lower

then the only-activated ones. This is mainly due to the loss of porosity due to introduction of the amine groups in the structure. At higher temperature an increase of the CO_2 capacity was observed, resulting from the chemisorption of CO_2 with formation of carbamate (promoted by the higher temperature). For the impregnated samples the adsorption process resulted in a combination of physi- and chemisorption: as the temperature increases, the contribution from physical adsorption decrease quickly and probably levels off any gain in the chemical adsorption due to the increase in temperature.

2.4 Mesoporous Silicas

Mesoporous silicas are generally characterized by low CO_2 uptake due to the weak surface interaction with CO_2 molecules. What makes them attractive for carbon capture is the possibility to introduce functional groups (usually amine-based groups) to increase the affinity with CO_2. The advantage of having large and uniform pores is that it is possible to introduce surface modification avoiding any steric hindrance of the adsorption sites. As a result of the introduction of functional groups a significant increase of CO_2 uptake at low pressure has been shown compared to the pure silica; this is due to the fact that in this case the CO_2 adsorption process is driven by chemisorption [62]. The adsorption properties are mostly influenced by density of amine active sites and by the accessibility to the sites (pore size) [63].

Among all mesoporous silicas the materials which have attracted more the interest of the research with regard to carbon capture applications are MCM-41 and SBA-15. Their structure is characterised by well-ordered mesoporous arrays of hexagonal symmetry (P6mm), with alternating channels and siliceous framework, as shown in Figure 2.4.

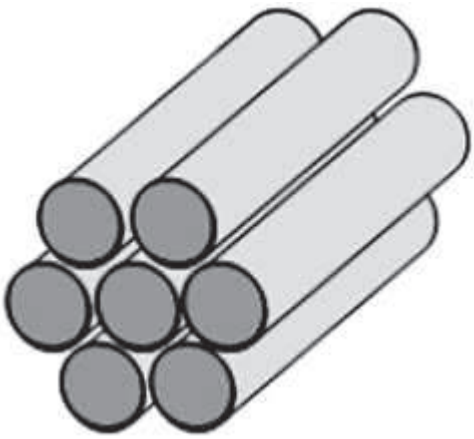

Figure 2.4: Typical structure of SBA-15 and MCM-41 mesoporous silicas [62].

Belmabkhout et al.[64] synthesised four different samples of MCM-41 at different synthesis temperatures: this resulted in samples with different surface areas and pore size distributions. CO_2 adsorption measurements on a Rubotherm balance showed that the uptake increased with the surface area and pore ordering of the particles. Compared with the CO_2 uptakes of typical benchmark adsorbents for carbon capture (MOF-177, Maxsorb-AC, IRMOF-1, Norit-AC, 13X) MCM-41 showed a capacity of 14.7 mol/kg at 45 bar and 298 K, higher than the capacities reported for 13X and Norit-AC at the same conditions. On the other hand the sample had the lowest capacity in the low pressure region. The evolution of the isosteric heat of adsorption with the CO_2 loading proved to be relatively constant indicating the absence of energetically heterogeneous sites on the surface of the sample. Compared with other classes of adsorbents, a relatively low heat of adsorption at zero loading was obtained with a value of 21.6 kJ/mol. The authors concluded that the good working capacity at high pressure make the sample competitive for PSA at high/moderate pressure applications. Further investigations were done on MCM-41 to check the adsorption performances in presence of mixtures in order to evaluate the possible use of the adsorbent for CO_2 separation from flue gas, biogas and syngas [65]. Pure component isotherms up to 25 bar at ambient temperature were measured for CO_2, N_2, CH_4, H_2 and O_2 and the ideal adsorption solution theory (IAST) was used to calculate the selectivity of the material for CO_2/ N_2, CO_2/ CH_4 and CO_2/ H_2 mixtures. The selectivity obtained for a CO_2/N_2 mixture with a CO_2/N_2 ratio equal to 20/80 was around 11 for pressures below 10 bar, but this value increased to about 15 as the pressure increased to 45 bar. The calculations of the performances in a proposed PSA at high (45 bar)/moderate (10 bar) pressures showed a working capacities of 11.1%wt with a feed concentration of 20% of CO_2 in N_2, proving how the sample could be a promising material for CO_2 separation from high pressure streams.

Successively the same research group presented a detailed study [66] comparing the adsorption performances of three forms of MCM-41: conventional MCM-41, a pore-expanded form of MCM-41 named PE-MCM-41, and a triamine surface-modified PE-MCM-41 named TRI-PE-MCM-41. From their work emerged that the

PE-MCM-41 exhibited a higher CO_2 uptake at high pressure (the CO_2 uptakes at 20 bar and 298 K resulted about 8 mol/kg and 6 mol/kg for PE-MCM-41 and MCM-41, respectively) while there was not a significant improvement in the low concentration region. On the other hand the TRI-PE-MCM-41 sample, which combined the advantages of a large pore structure to the presence of amine groups, showed a dramatic improvement of the adsorption capacity especially in the low pressure region. The CO_2 uptake at 0.1 bar and 298 K was about 2.2 mol/kg, a value which is comparable with the one of a typical zeolite 13X [66b]. Even though the capacity is comparable with 13X, differently from the zeolites the sample exhibited a significant increase of the CO_2 uptake in presence of water. This represents a very important advantage compared to other conventional adsorbents which makes this sample one of the promising candidate for CO_2 capture applications.

Xu et al. [67] impregnated MCM-41 with polyethylenimine (PEI) and investigated the effect of the preparation conditions on the adsorption performances of the sample. As expected with the increase of the PEI content, a reduction of surface area, pore size and pore volume was observed. On the other hand the CO_2 capacity resulted to be increased with the PEI loading and the temperature, reaching the highest value (3.02 mol/kg at 1 bar) at 75 ˚C for the sample with 75 wt. % of PEI. Moreover an improvement of the adsorption performances was observed with the increase of the Si/Al ratio of MCM-41 and the solvent/MCM-41 ratio. Finally the adsorption process at low temperature resulted to be strongly kinetically controlled.

Xu et al. [68] continued the investigation on PEI-MCM-41 by testing the sample with a simulated flue gas (14.9 % of CO_2, 4.25 % O_2 and 80.85 % N_2) from 25 to 100 ˚C. The sample showed very high selectivity with a value higher than 1000 for CO_2/N_2 and about 180 for CO_2/O_2, but, due to the simultaneous adsorption of NO_x, it was suggested to use a NO_x separation unit prior the CO_2 adsorption process.

More recently, Zhao et al. [69] investigated the role of the introduction of MgO in SBA-15 and MCM-41 in the CO_2 adsorption, focusing on the effect of the MgO loading and the dispersion methods. Using a volumetric apparatus the CO_2 capacities at different MgO loadings were evaluated: the introduction of the basic MgO groups clearly enhanced the interaction of the adsorbents with the acidic

molecules of CO_2 increasing the uptake relative to the pristine samples. For SBA-15 the amount adsorbed increased with the MgO loading with a maximum (0.86 mol/kg at 1 atm and 25 ºC) corresponding to a Si/Mg ratio of 1.5; increasing the MgO content the capacity decreased to 0.67 mol/kg at Si/Mg = 3 and 0.64 mol/kg at Si/Mg = 6. This trend was associated to the dispersion state of the MgO groups in SBA-15: crystal state was recognised in MgO-SBA-15-(3) while further loading resulted in an amorphous state in MgO-SBA-15-(6). For MCM-41 the same trend was reported with a maximum in the CO_2 capacity (0.97 mol/kg) corresponding to Si/Mg = 40: further increasing in the MgO loading resulted in the blockage of the pores. The influence of the dispersion method was also evaluated. The crucial point was to ensure the dispersion of the MgO groups inside the narrow channels of the samples: among all the techniques tested the use of basic agents to improve the transport efficiency inside the pores proved to be the best method. The CO_2 uptakes increased to 1.35 mol/kg for SBA-15 and 1.32 mol/kg for MCM-41.

Samples of mesoporous silicas were synthesised at the University of St. Andrews in the last months of the project and for this reason they could not be tested on time to be included in the present dissertation. Future tests will be carried out on the samples received in order to obtain the CO_2 capacity.

2.5 PIMs

PIMs (Polymers of Intrinsic Microporosity) are a new class of polymers recently invented by Prof. Budd (University of Manchester), Prof. McKeown (Cardiff University) and collaborators.

In 2004 Budd et al. [70] presented for the first time this new class of non-network polymers which acted like microporous materials with no need of a network of covalent bonds. The key factor of their microporosity is the presence of a "site of contortion", a spiro-centre, which hinders the rotation of the chains around it and, hence, prohibits any efficient space packing in the solid state, Figure 2.5. Their microporosity is intrinsic because it comes exclusively from the molecular structure and it is totally independent from any thermal or processing history of the material. Nitrogen adsorption confirmed the microporous nature and the high surface area of the materials, with micropores dimensions in the range of 0.4 – 0.8 nm.

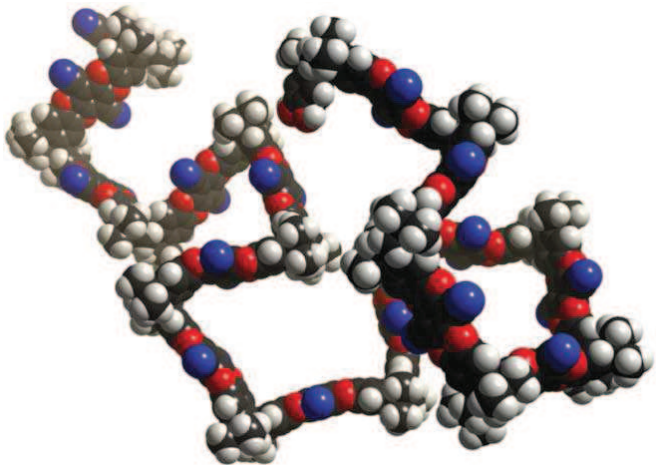

Figure 2.5: Molecular model showing the rigid and contorted structure of PIM-1 [71].

The potential of these polymers to make membranes was first demonstrated by using PIM-1 to make a solvent-cast film for the removal of phenol from aqueous solutions through pervaporation [72].

Lately, the permeation properties for different gases were obtained from the tests on two membranes prepared using PIM-1 and PIM-2 [73]. The permeability obtained for both the PIMs followed the sequence $CO_2 > H_2 > He > O_2 > Ar > CH_4 > N_2 > Xe$.

Typically high permeable polymers have low selectivity or vice versa: in 1991 Robeson [74]demonstrated the limits of such performances and fixed the empirical upper bounds in plots of selectivity vs. permeability for various gas pairs. PIMs showed relatively high values of permeability and selectivities significantly higher than other polymers. This combination allowed PIMs to cross Robeson's upper limit for O_2/N_2 and CO_2/CH_4 separation, proving their potential for oxygen enriched air separation and CO_2 capture from methane. Due the recent developments in the synthesis of new materials Robeson's upper bounds were updated in 2008 increasing the trade-off values [75].

In subsequent studies [71] Budd and McKeown proved the possible application of PIM membranes as reactive membranes inserting in the structure metal-ions with catalytic properties. Moreover H_2 adsorption experiments showed that some PIMs have an uptake comparable to that of the best examples of zeolites, MOFs and carbons with similar values of surface area.

PIMs were also successfully used to increase the permeation properties of polyimides [76]. Polyimides-based membrane are characterised by good properties with regard to chemical and thermal stability and mechanical robustness, but they are generally lacking in permeability. Combining PIMs with polyimides a new class of polymers was obtained, PIM-PI, which, maintaining the main features of polyimides, exhibited a considerable increase in permeability and selectivity relative to conventional polyimides.

More recently, membranes made by modifying PIM-1 with the incorporation of thioamide functionality [77] exhibited good CO_2 permeability and high CO_2/N_2 selectivity, with a values of 1120 Barrer and 30.3, respectively (Figure 2.6).

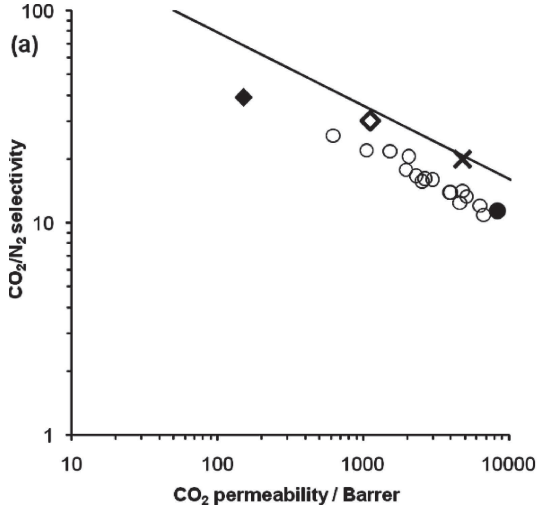

Figure 2.6: Logarithmic plot of CO_2/N_2 selectivity vs. permeability for Thioamide-PIM-1 (◊),compared with other literature data. Solid line = Robeson's 2008 upper bounds [77].

Recent publications of different research groups on PIMs are mostly focused on the improvement of the performances that can be reached by blending PIMs with commercial polymers [78] and in the effect of the synthesis procedure on the final properties of the samples [79]. This proves the increase of interest in this novel class of polymers as promising candidates for membrane separation processes.

Part of this dissertation will be focused on the screening of the CO_2 capacity of new PIMs synthesised by the research groups of Prof. Budd the University of Manchester and Prof. McKeown at Cardiff University, inventors and first developers of PIMs. No previous work on the screening of the CO_2 uptake of PIMs has been found in the existing literature.

3. THEORY OF THE ZERO LENGTH COLUMN (ZLC) TECHNIQUE

The Zero Length Column (ZLC) technique was first introduced in 1988 by Eic and Ruthven [80] as a new experimental method which could maintain the advantages of a classic chromatographic technique, while trying to overcome the difficulties encountered in measuring diffusivities of strongly adsorbed components.

The chromatographic method has, relative to other batch methods, the typical advantages of a flow system: low heat and mass transfer resistances. This has directed the interest of researchers towards the use of this technique for the measurements of intracrystalline diffusion. One of the limitations of the technique is the difficulty of decoupling axial dispersion and mass transfer resistance: this can be solved by acting on some experimental conditions. The contribution of the axial dispersion on the total dispersion of the response curve can be evaluated by running series of experiments changing the velocity of the gas, the carrier gas and the particles size [81].

In order to have accurate measurements of the intra-crystalline diffusion, experiments with unaggregated crystals or very small particles should be carried out. The crystal size could be an inevitable issue, especially if working with zeolites, and working with very small particles could lead to additional problems linked to high pressure drops, reducing the range of available gas velocities.

Furthermore if the diffusivity is too high the contribution of the axial dispersion is no longer negligible and no accurate measurements can be obtained. With strongly adsorbed species the retention times become too long and the intra-crystalline diffusion strongly influences the axial mixing, complicating in practice the distinction between the two transport mechanisms.

The ZLC method was developed aiming to increase the accuracy in the determination of the intra-crystalline diffusivities by minimising such uncertainties.

The traditional Zero Length Column consists of a very small adsorption column (infinitesimal) in which a small amount of adsorbent material is arranged as monolayers between two sinter discs.

The technique consists in first equilibrating a sample of adsorbent with a constant flowrate of a known sorbate concentration. When equilibrium is reached the desorption starts by purging with a constant flowrate of an inert gas.

By arranging the adsorbent as monolayers a good contact between the gas and the solid phase is ensured, allowing the assumption of negligible external diffusional resistance. This can be proved by running experiments with different purge gases: the difference in molecular weight (i.e. molecular diffusivity) should give different desorption rates if there is any intrusion of external resistance.

The improved gas – solid contact, characterised by relatively high flowrates, also ensures rapid heat transfer between the two phases: isothermal conditions can then be assumed.

For porous materials external film resistance is generally assumed to be smaller relative to the internal diffusion inside the pores. In the development of the theory of the ZLC this assumption has been considered valid even though further investigations have given the directions to distinguish between the internal diffusion and the surface resistance control [82].

In practice the operating conditions are usually adjusted in order to operate in the Henry's law region, so a further basic assumption of the ZLC theory is the linearity of the adsorption isotherm. This condition is quite often fulfilled, but it may not be valid for strongly adsorbed species, for this reason the original model of the ZLC was later modified including a non-linearity coefficient [83], to take into account such deviations from the linear region. The linearity of the system can be verified by running tests at different sorbate concentrations.

Assuming the adsorbent sample as spherical particles, the transport inside the pores of the adsorbents can be described as a Fickian diffusion process, governed by the following equation:

$$\frac{\partial q}{\partial t} = D\left(\frac{\partial^2 q}{\partial r^2} + \frac{2}{r}\frac{\partial q}{\partial r}\right) \qquad (3.1)$$

In which q is the adsorbed phase concentration, r is the radius of the particle and D is the diffusivity. The diffusivity is generally assumed to be independent from the concentration in dilute systems [84]: for the experimental conditions in which the ZLC is operated this assumption can be considered valid and can be proved by the use of the partial loading variant of the ZLC technique [85].

Finally, the column is assumed to be short enough (infinitesimal) that the axial dispersed plug flow model, generally used to describe the flow through packed beds, can be simplified to a CSTR model. The column is then considered as a well-mixed cell: to check the validity of this assumption tests with different amount of sample can be carried out.

Based on all the previous assumptions the mass balance on the system is then given by the following equation:

$$V_S \frac{d\overline{q}}{dt} + V_g \frac{dc}{dt} + Fc = 0 \qquad (3.2)$$

In which V_s and V_g are the volume occupied by the solid and the gas phase inside the column, respectively; q and c are the adsorbate concentration in the solid and in the gas phase; and F is the carrier gas flowrate.

Initial and boundary conditions are defined as follows:

$$c(0) = c_0;$$
$$q(r,0) = q_0 = Kc_0;$$
$$\left.\frac{\partial q}{\partial r}\right|_{r=0} = 0;$$
$$q(R,t) = Kc(t)$$

In which K is the Henry's law constant.

From the analytical solution of the model the following governing equation for the response curve is obtained [86]:

$$\frac{c(t)}{c_0} = \sum_{n=1}^{\infty} \frac{2L}{\beta_n^2 + \left(L - 1 - \gamma\beta_n^2\right)^2 + L - 1 + \gamma\beta_n^2} \exp\left(-\frac{\beta_n^2 Dt}{R^2}\right) \tag{3.3}$$

where β_n is given by the roots of:

$$\beta_n \cot\beta_n + L - 1 - \gamma\beta_n^2 = 0 \tag{3.4}$$

with:

$$L = \frac{FR^2}{3KV_s D}$$

and

$$\gamma = \frac{V_g}{3KV_s}$$

The dimensionless parameter L is defined as the ratio between the diffusional time constant (D/R^2) and the washout time constant (F/KV_s): it is a measure of how far is the system from equilibrium control [87]. The parameter γ is the ratio between the hold-up in the fluid phase and accumulation in the solid; for gaseous system it is generally very small and can be neglected, but it can become significant if the adsorption is relatively weak or in case of liquid systems [86, 88].

One of the main advantages of the technique is that is possible to operate the system in equilibrium or kinetic conditions by just adjusting the purge flowrate: at high flowrate the desorption rate is controlled by the diffusion inside the particle, while at low flowrate the controlling process is the convection under equilibrium conditions. Experiments at different flowrates are needed to prove which regime is controlling the system [18, 89]. In eq. 3.3 this means to operate on the L parameter in order to run the experiment at the desired conditions: for $L >> 1$ the system is under kinetic control, while for $L < 1$ the system is under equilibrium control.

3.1 Kinetic control

In the diffusion controlled regime, in the long-time region the higher order term of the summation can be neglected, reducing eq. 3.3 to:

$$\frac{c}{c_0} = \frac{2L}{\beta_1^2 + \left(L - 1 - \gamma\beta_1^2\right)^2 + L - 1 + \gamma\beta_1^2} \exp\left(-\frac{\beta_1^2 Dt}{R^2}\right) \tag{3.5}$$

In a log-linear plot of c/c_0 vs. t the long time asymptote approaches a straight line, hence from the slope and the intercept L and D/R^2 can be extracted. To validate the diffusional time constant extracted using this approach (Long Time analysis), experiments at different flowrates are needed. The resulting response curves will be characterised by the same slope of the long time asymptote, but different intercepts due to the different value of the L parameter (flowrate dependent), since when L is greater than 20 β_1 is approximately constant and equal to π.

3.2 Equilibrium control

As mentioned previously, at low flowrate, when the contact time is large compared to the diffusional time constant, the system approaches equilibrium. In this condition (i.e. at $L \rightarrow 0$) and assuming linear equilibrium relationship, the response curve reduces to a simple exponential decay, given by the following equation [18]:

$$\ln\frac{c}{c_0} = -\frac{Ft}{KV_S + V_g} \tag{3.6}$$

Eq. 3.6 in a semi-log plot c/c_0 vs. Ft is a straight line through the origin with slope -1/(KV_s + V_g). For strongly adsorbed species, since $KV_s >> V_g$, from the slope of the

curve it is possible to extract directly the Henry's law constant. For weakly adsorbed component the KV_s and V_g are comparable, so in order to calculate the correct value of K, the value of V_g needs first to be determined. This can be obtained by running a "blank" experiment which consists in repeating the experiment in the same condition using an empty column.

If the system is operating beyond the linear region, the model can be modified using a Langmuir equilibrium isotherm:

$$\frac{q^*}{q_s} = \frac{b\,c}{1+b\,c} \tag{3.7}$$

In which q^* and q_s are the adsorbed phase concentration at equilibrium and saturation, respectively. The resulting governing equation will be then [83]:

$$\ln\frac{c}{c_0} = -\frac{F\,t}{KV_S + V_g} - \frac{KV_S}{KV_S + V_g}\left[\frac{1}{1+b\,c} - \frac{1}{1+b\,c_0} + \ln\left(\frac{1+b\,c_0}{1+b\,c}\right)\right] \tag{3.8}$$

In this case the Henry's law constant can be extracted from the slope of the long time asymptote: this could be a problem for highly non-linear systems since the asymptote will correspond to experimental signals too close to the baseline.

Eq. 3.6 and 3.8 show also that the equilibrium controlled desorption rate is invariant with the flowrate, but it depends only on the volume of purge gas passing through the column. Running experiments at different flowrates provides an easy way to check if the conditions of equilibrium control are fulfilled.

3.3 Isotherm calculation

Under equilibrium conditions each point of the desorption curve is an equilibrium point, the desorption curve can be then integrated and the equilibrium isotherm can

be easily extracted. The resulting expression for the adsorbed phase concentration is given by [18]:

$$q^* = \frac{C_T}{V_s}\int_0^{\infty}(F\,y)_{out}\,dt - \frac{C_T}{V_s}\int_0^{t}(F\,y)_{out}\,dt - \frac{V_g\,C_T}{V_s}\,y \qquad (3.9)$$

in which C_T is the total concentration in the gas phase and y is the molar fraction of sorbate in the gas phase, defined as $\frac{c}{c_0} = \frac{y}{y_0}$. The first term of eq. 3.9 represents q_0, the adsorbed phase concentration at equilibrium with c_0; the second term is the adsorbed phase concentration at equilibrium with c at time t of the desorption; while the last term represents the dead volume of the system.

To solve eq. 3.9, constant flowrate can be assumed only for trace systems, for which the sorbate concentration is very low. For systems with higher sorbate concentrations, such an assumption will lead to a calculated value of the amount adsorbed erroneously underestimated.

For this reason the variation of the total outlet flowrate during desorption must to be taken into account [90], this can be expressed as:

$$(F\,y)_{out} = \frac{F_{in}}{1-y}\,y_{out} \qquad (3.10)$$

In which F_{in} refers to the inlet purge flowrate. Substituting eq 3.10 into eq. 3.2 the following equation for the mass balance is obtained:

$$V_S\,\frac{dq^*}{dt} + V_g\,\frac{C_T\,dy}{dt} + F_{in}\,C_T\,\frac{y}{1-y} = 0 \qquad (3.11)$$

The expression for the isotherm is then obtained by integration of eq. 3.11:

$$q^* = \frac{F_{in} C_T}{V_s} \int_0^{\infty} \frac{y}{1-y} dt - \frac{F_{in} C_T}{V_s} \int_0^{t} \frac{y}{1-y} dt - \frac{V_g C_T}{V_s} y \qquad (3.12)$$

Sometimes, when comparing different samples, it might be more convenient to normalise the desorption curves plotting as c/c_0 vs. Ft/V_s (Ft/M, where M is the mass of the sample). The area under the curve is proportional to the amount adsorbed and eq. 3.12 can be re-written as:

$$q^* = C_T \int_0^{\infty} \frac{y}{1-y} d\left(\frac{F_{in} t}{V_s}\right) - C_T \int_0^{t} \frac{y}{1-y} d\left(\frac{F_{in} t}{V_s}\right) - \frac{V_g C_T}{V_s} y \qquad (3.13)$$

3.4 Moment analysis

Regardless whether the system is kinetically or equilibrium controlled, integrating the mass balance equation 3.2 with respect to the adsorbed phase concentration the total amount adsorbed can be obtained. In practice this means to integrate numerically the experimental desorption curve. The main problem encountered in the numerical integration of the experimental curves is the decrease of accuracy as the curve approaches the baseline. At these values of the signal the noise of the instrument becomes of the same order of magnitude as the baseline. To avoid that the error induced in the integration of this part of the curve could affect the calculated value of the integral it becomes very useful to apply the solution of the theoretical model of the ZLC in the calculation of the time integral. In fact a typical ZLC response curve is characterised by an exponential decay in the long time region which could be seen as $a\ exp(-bt)$. Then the integral of the curve can be obtained by the following equation [91]:

$$\int_{t=0}^{t=\infty} \frac{c}{c_0} dt = \int_{t=0}^{t=t_0} \frac{c}{c_0} dt + \frac{a}{b} \exp(-b\, t_0) \tag{3.14}$$

in which t_0 is the time at which the curve starts to show a pure exponential decay. Therefore from both kinetic or equilibrium controlled curves one can obtain the values for c_0, q_0 at equilibrium, i.e. a single point on the adsorption isotherm. This can be repeated at different initial gas phase concentration to obtain the full isotherm, but it is clearly more time consuming than the procedure outlined in section 3.3, unless the system is characterised by a very slow diffusion process and it is not possible to achieve equilibrium controlled conditions.

3.5 Partial loading experiment

The partial loading experiment is a variant of the traditional ZLC experiment which was first introduced by Brandani and Ruthven in 1995 [85] with the aim of investigating the effect of partial saturation on the parameters extracted from long time analysis. The key difference to the traditional ZLC experiments is that in this case the sample is purposely exposed to the sorbate for a time considerably less than the time needed to reach full saturation. At time 0 the flow is switched to the purge and the desorption is monitored. The predicted desorption curve is given by [85, 92]:

$$\frac{c}{c_0} = \frac{\sum_{n=1}^{\infty} \frac{2L}{\beta_1^2 + \left(L-1-\gamma\beta_1^2\right)^2 + L - 1 + \gamma\beta_1^2} \left[1 - \exp\left(-\frac{\beta_n^2 D\tau}{R^2}\right)\right] \exp\left(-\frac{\beta_n^2 Dt}{R^2}\right)}{1 - \sum_{n=1}^{\infty} \frac{2L}{\beta_1^2 + \left(L-1-\gamma\beta_1^2\right)^2 + L - 1 + \gamma\beta_1^2} \left[\exp\left(-\frac{\beta_n^2 D\tau}{R^2}\right)\right]} \tag{3.15}$$

In which τ is the time the sample has been exposed to the sorbate and β_n is given by the roots of eq. 3.4.

Eq.3.15 clearly shows that the shape of the response curve for the partially loaded sample is the same as the fully saturated one, but, the introduction of the parameter τ implies a lower intercept for the long time asymptote of the partially loaded desorption curve. The validity of the parameters L and D/R^2, derived from the long time analysis of the fully equilibrated experiment, can be proved if, at the same conditions, the response of a sample loaded for a known time τ can be predicted.

The partial loading experiment coupled with experiments at multiple flowrates provides an essential tool for the measurement of the internal diffusion.

In order to have a better understanding of the effects of partial loading it becomes very useful to look at the adsorbed phase concentration profile inside the crystal. To solve the model with respect to the adsorbed phase concentration the following initial condition needs to be used [85]:

$$\frac{q(r,0)}{q_1} = 1 - \frac{R}{r}\sum_{n=1}^{\infty} \frac{2L}{\beta_n^2 + \left(L - 1 - \gamma\beta_n^2\right)^2 + L - 1 + \gamma\beta_n^2} \frac{\sin\left(\beta_n \frac{r}{R}\right)}{\sin\beta_n} \exp\left(-\frac{\beta_n^2 D\tau}{R^2}\right) \quad (3.16)$$

in which q_1 is the amount adsorbed at the time τ of loading.

The corresponding concentration in the gas phase is given by:

$$\frac{c_0}{c_1} = 1 - \sum_{n=1}^{\infty} \frac{2L}{\beta_n^2 + \left(L - 1 - \gamma\beta_n^2\right)^2 + L - 1 + \gamma\beta_n^2} \exp\left(-\frac{\beta_n^2 D\tau}{R^2}\right) \quad (3.17)$$

Assuming linear equilibrium relationship:

$$\frac{q(r,t)}{q_0} = \frac{q(r,t)}{q_1}\frac{q_1}{q_0} = \frac{q(r,t)}{q_1}\frac{c_1}{c_0} \quad (3.18)$$

The general solution can be therefore obtained [85]:

$$\frac{q(r,t)}{q_0} = \frac{\frac{R}{r}\sum_{n=1}^{\infty}\frac{2L}{\beta_n^2+\left(L-1-\gamma\beta_n^2\right)^2+L-1+\gamma\beta_n^2}\frac{\sin\left(\beta_n\frac{r}{R}\right)}{\sin\beta_n}\left[1-\exp\left(-\frac{\beta_n^2 D\tau}{R^2}\right)\right]\exp\left(-\frac{\beta_n^2 Dt}{R^2}\right)}{1-\sum_{n=1}^{\infty}\frac{2L}{\beta_n^2+\left(L-1-\gamma\beta_n^2\right)^2+L-1+\gamma\beta_n^2}\exp\left(-\frac{\beta_n^2 D\tau}{R^2}\right)} \quad (3.19)$$

Knowing the profile inside the particle provides an easy method to distinguish between two different mass transfer mechanisms: intracrystalline diffusion and surface barrier. Loading a sample for a limited amount of time will create two different internal concentration profiles depending on the controlling mechanism. If the adsorption process is controlled by the internal diffusion, the adsorbate concentration profile inside a partially saturated sample will be characterised by the gradient of concentration towards the external surface rather than the central part of the crystals [87, 93]. As a consequence of the greater concentration close to the external surface, the desorption rate will be faster in the short time region compared to a fully equilibrated sample. Inversely, in the case of surface barrier the adsorbate profile will be uniform inside the crystals, then the desorption rate will be same for both a fully and a partially saturated sample. The comparison between the adsorbed phase concentration trends of the fully and partially saturated experiments is then an easy way to identify the controlling process: in case of surface barrier the two curves should overlap, in contrast a higher desorption rate for the partial loading experiment is a clear indication of an internal diffusion control [92].

4. EXPERIMENTAL APPARATUS: THE ZLC SYSTEM

The screening of novel materials for carbon capture requires a technique which allows for the rapid ranking of the CO_2 capacity using a small amount of sample. Conventional methods such as volumetric and gravimetric techniques and breakthrough experiments are generally used to measure the adsorption properties of adsorbents, but these techniques are very time demanding and require relatively large amounts of sample (hundreds of milligrams or even grams). Prototype materials are usually synthesised in small amounts (<50 mg) and the accuracy of the conventional methods drastically drops when such small amounts are used.

With regard to this the small size of the column (infinitesimal) of the ZLC method represents the crucial feature on which are based the advantages offered by this method compared to the conventional ones. First of all the small column greatly reduces the amount of sample required: 10-15 mg of material are generally used for CO_2 applications. This is an order of magnitude larger than the original ZLC measurements which used 1-2 mg [80] and is due to the reduced value of the Henry law constant. This in turn requires a larger sample volume if the value of the L parameter discussed in the theory section is to have a value corresponding to ZLC response curves in the optimal region. This may require also the selection of different mass flow controllers, including smaller ranges if equilibrium control is to be achieved.

As a result of the small amount of solid used, the complexity of the analysis methods is also reduced because axial dispersion as well as heat and mass transfer resistances are typically negligible. Finally the system also allows for testing the stability of the samples in the presence of H_2O, SO_x and NO_x in the feed mixture. All these features combined in a single experimental apparatus allow for the rapid ranking of the CO_2 capacity of novel prototype materials.

As mentioned previously more than 120 samples were investigated in the present work, as part of the Innovative Gas Separations for Carbon Capture project. Two ZLC systems were used for the experiments: a traditional ZLC system and an

upgraded, built-in-house, semi-automated ZLC system. In order to understand fully and discuss the experimental results a detailed description of the two systems will be presented in this chapter.

4.1 Traditional ZLC system

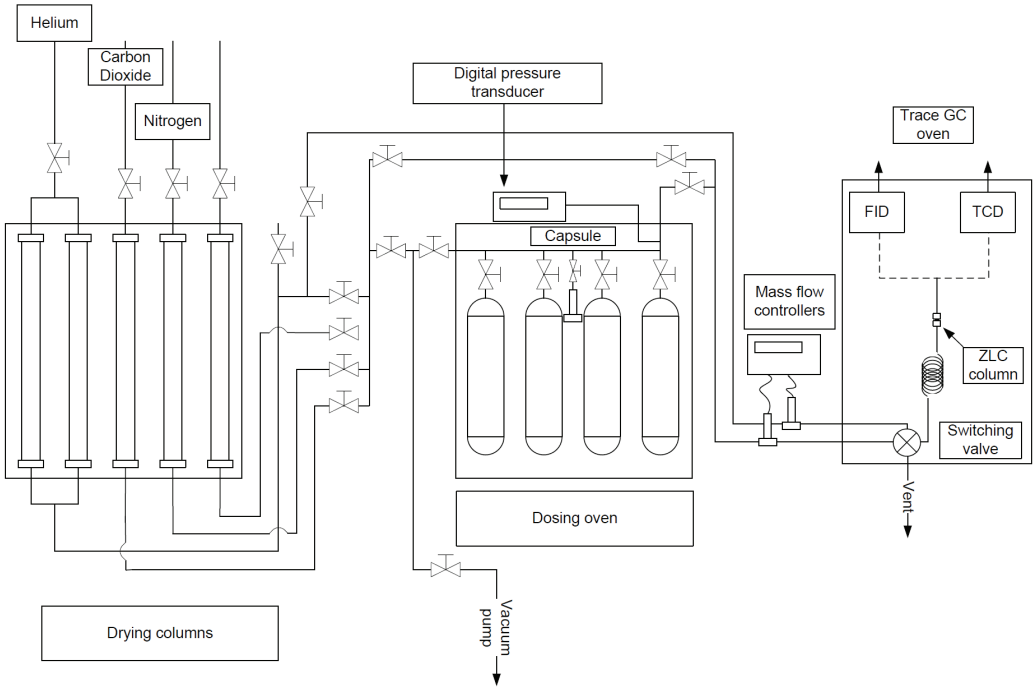

Figure 4.1: Schematic view of the ZLC system.

Figure 4.1 shows a schematic diagram of the traditional ZLC apparatus. The system is composed by:

- Four drying columns;
- A dosing oven, with a capacity of 4L;
- Two massflow controllers;

- Gas-chromatograph (TRACE GC), in which the ZLC is placed.

Figure 4.2 shows the traditional ZLC system used for this study.

Figure 4.2: Traditional ZLC system.

Three gas lines are connected to the system: He, CO_2 and N_2. Even though the gases are coming from high purity gas cylinders, traces of water may enter the system either from the cylinders or leaks in the lines. Water can heavily affect the adsorption performance of the adsorbent. For this reason it is essential to ensure a water-free environment during the experiments. As shown in Figure 4.1, drying columns are located on each gas line to pre-dry the gases entering the system. The drying columns are filled with a top layer of silica gel (inlet) followed by one of zeolite 13X. A duplicate drying system is also used in the semi-automated ZLC system which allows monitoring the water content coming from the dryers. This has been used to define the time interval between thermal regenerations of the drying columns. Periodically the drying columns are detached from the lines and regenerated at 300 ºC under flow of N_2 (counter-current to the normal gas flow) in purposely designed regeneration ovens.

The feed gas mixture, typically 10% v/v of CO_2 in He, is prepared in a dosing oven composed of 4 cylinders of 1L each, provided with a digital pressure transducer.

The dosing oven is connected to a vacuum pump. The system can be purged by repeated flushing with a gas and connection to the vacuum pump. This is carried out each time the system is used to prepare a new mixture.

Liquids, such as water, methanol or other solvents, can be added to the gas mixture. A properly designed capsule filled with the liquid of interest can be connected to the lines inside the dosing oven. By increasing the temperature of the dosing oven (up to 200 ºC) evaporation of the liquid is induced, Figure 4.3. The difference in weight of the capsule before and after the evaporation gives the exact amount of liquid evaporated in the mixture. To avoid the presence of any cold spot in which condensation of the vapours present in the mixture could occur, the line from the dosing oven to the ZLC is heated with electrically regulated heating tape.

Figure 4.3: Capsule for the preparation of mixtures with liquids connected to the cylinders of the dosing oven.

The flowrate of the feed and the purge are regulated by a high flowrate massflow controller on each line. The operative range of the massflow controllers is from 0 to 50 ml/min. The massflow controllers are operated manually by the operator.

To ensure isothermal conditions during the experiments the ZLC is placed inside a TRACE GC gas-chromatography oven (T_{max} = 300 ºC), Figure 4.4. Internally to the TRACE GC a rotary switching valve allows to switch the inlet flow to the ZLC from the feed to the purge. The rotary switching valve has two inlets, the feed and the purge, and two outlets, the line connecting to the inlet of the column and the vent.

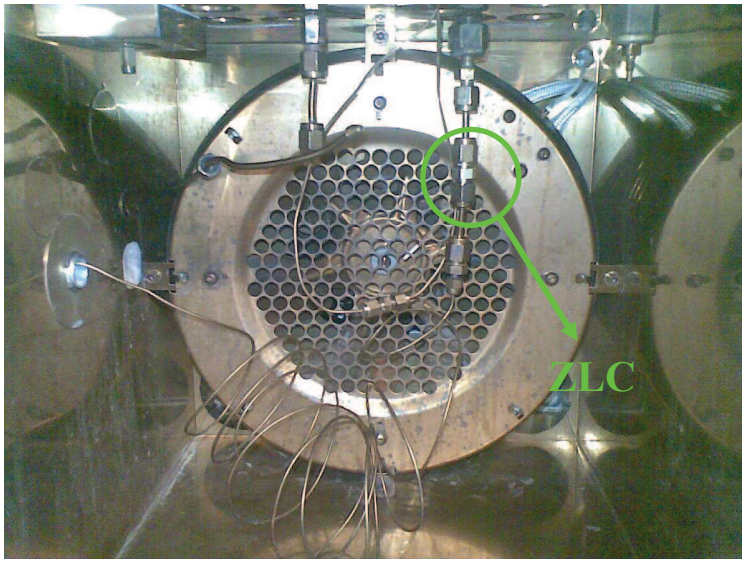

Figure 4.4: TRACE GC oven and zero length column

By switching the valve the mechanism rotates connecting each inlet line, alternatively, to the vent or the inlet of the ZLC and vice versa. In the rotation from a position to the other, for some fraction of a second the inlet lines are not connected to the outlets because the ports are not aligned properly. This generates a slight overpressure in the inlet lines, which results in peak visible in the signal acquired (Figure 4.5). Once can see that the valve switching time is approximately 0.1 s.

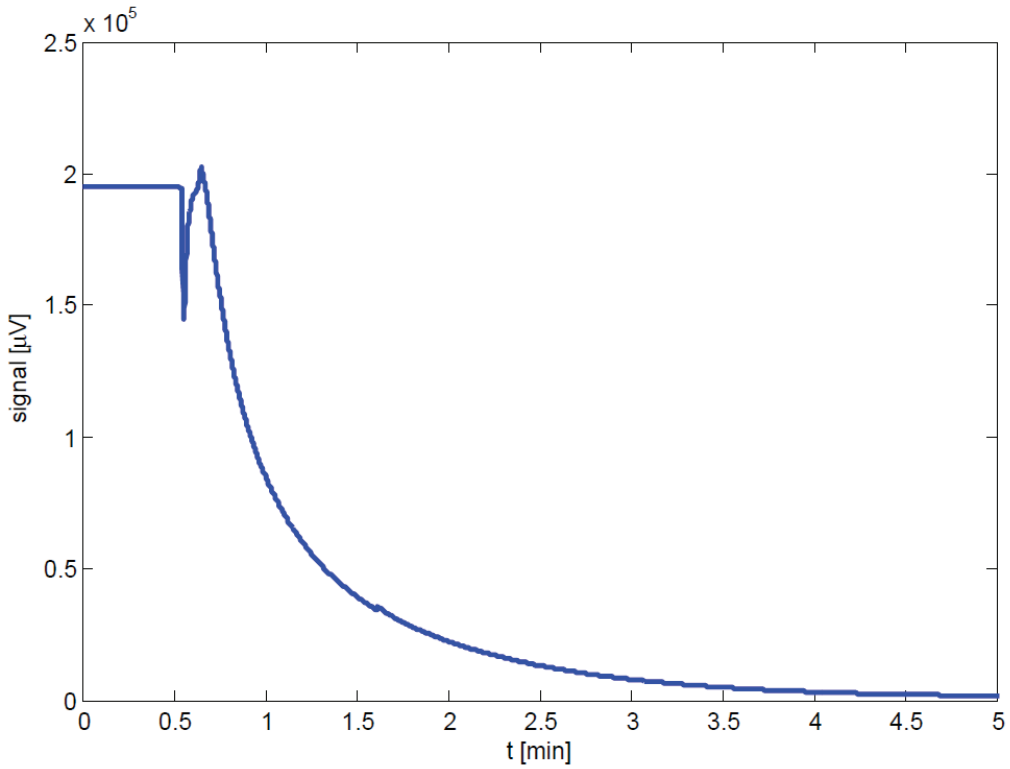

Figure 4.5: Signal as acquired from TRACE GC, showing the peak related to the switch of the valve.

A 1/16" coil, about 2 m long, ensures that the inlet gas to the column can equilibrate with the temperature of the oven. The small ID of this line ensures that the conditions are close to plug-flow and this is an important issue given that the heating line is after the switching valve.

The TRACE GC is provided with two internal detectors: a Thermal Conductivity Detector (TCD) and a Flame Ionisation Detector (FID), which are used depending if the monitored species is non-organic (TCD) or organic (FID).

The TRACE GC is connected to the PC for data acquisition, and can be operated both manually (using the front panel) or through its software.

4.2 *Semi-automated ZLC system*

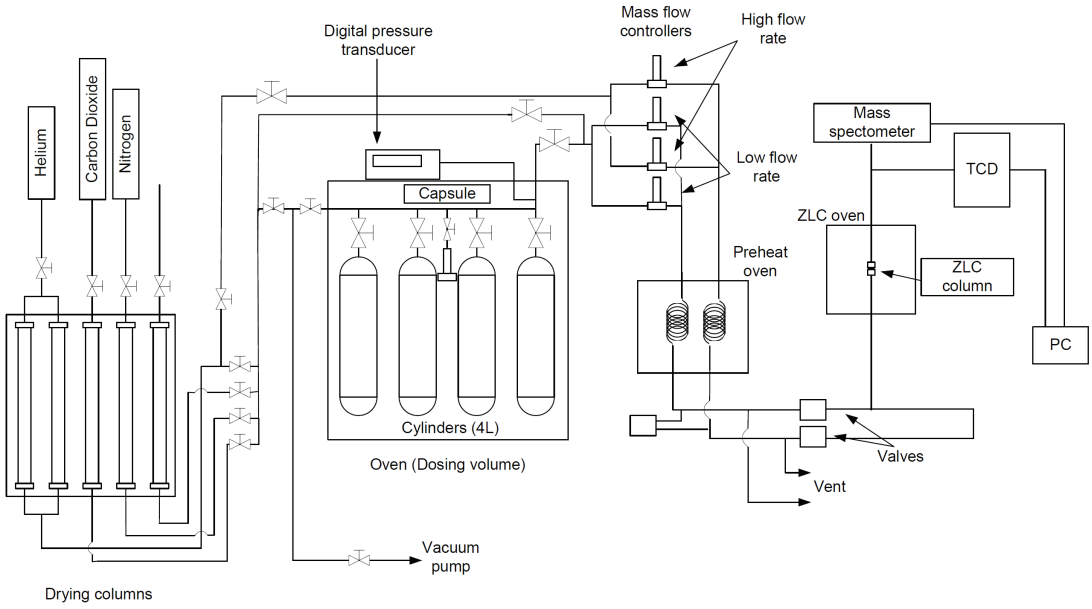

Figure 4.6: Schematic view of the semi-automated ZLC system.

Figure 4.7: Semi-automated ZLC system.

The semi-automated ZLC system (Figure 4.6 and Figure 4.7) is an upgraded version of the traditional ZLC system, which presents several improvements relative to the traditional one and was designed for ranking novel MOF materials for carbon capture applications.

The system is exactly the same in the part relative to the configuration of the inlet gas lines to the drying columns and the dosing oven.

Differently to the traditional system, the feed and the purge line are provided with a high flowrate massflow controller (0-50 ml/min) and a low flowrate one (0-3 ml/min) for each line. A differential pressure read-out measures the pressure difference between the feed and the purge gas line, allowing to balance the pressure drops for a smoother transition when the valves are switched. During normal operation the massflow controllers need to be continuously in flow, for this reason, in order to save mixture while experiments are not running, a by-pass line is provided which feeds the massflow controllers in the feed line with pure He from the cylinders.

The TRACE GC is replaced by a preheat and a ZLC oven (T_{max} = 400 ºC). The ovens consist of electrical panels placed in an isolated box controlled by two independent units (Figure 4.8). A thermocouple inserted inside each oven monitors the temperature inside the ovens.

Figure 4.8: ZLC oven of the semi-automated ZLC system

The switching valve is substituted by four ON/OFF valves which are connected in pairs and ensure a smoother response signal.

The valves are placed between the preheat and the ZLC oven: this means that there is a small section of the lines which is exposed to the ambient temperature. To take account of the heat loss in this section the temperature of the preheater is set 10-20 ºC higher than the ZLC oven.

The outlet of the ZLC is connected to a quadrupole mass spectrometer (Ametek Benchtop) which monitors the outlet gas composition, using a capillary that samples approximately 0.1 ml/min. The use of the mass spectrometer allows to run this system with multicomponent mixtures. A TCD is also connected to the outlet of the column and can be used for pure CO_2 capacity testing. The two detectors were used to confirm that consistent blanks were obtained.

Massflow controllers, valves, preheat and ZLC ovens, and the TCD are all controlled from the PC through LabView (National Instrument, USA) software. The mass spectrometer is operated through its own software. Once the series of experiments has been set by the operator, if the TCD is used as detector, the system can then run and acquire data automatically. Using the mass spectrometer the data acquisition needs to be started independently using the software of the instrument.

4.3 The Zero Length Column

The zero length column consists of a 1/8" Swagelock union in which the sample is housed, as mono-layers, between two sinter discs. In Figure 4.9 a schematic view of the packed column is shown.

The preparation of the column is fairly straightforward. A sinter disc (mesh 1 μm, 1/8" OD) is first inserted and locked into position at the bottom of the column. Rockwool is placed on top of the sinter disc: this will avoid any blockage of the

grid due to smaller particles. The column is then weighted in a Mettler-Toledo(XS205 DualRange) balance which has an accuracy of +/– 0.01 mg. The balance is housed inside a glove box and antistatic guards ensure the absence of static interactions which could affect the measured weight. For highly hydrophilic samples the packing of the column can be carried out under an inert atmosphere. Once the weight of the column has been determined, the balance is zeroed and the sample can be added. Generally a layer of 5 mg of sample is placed on top the rock wool. Two or three layers separated by rock wool are usually inserted inside the column. Once the column is filled a sinter disc on top is tightened to close the column.

Immediately after the preparation the column is placed inside the ZLC oven (or the TRACE GC) for the regeneration procedure.

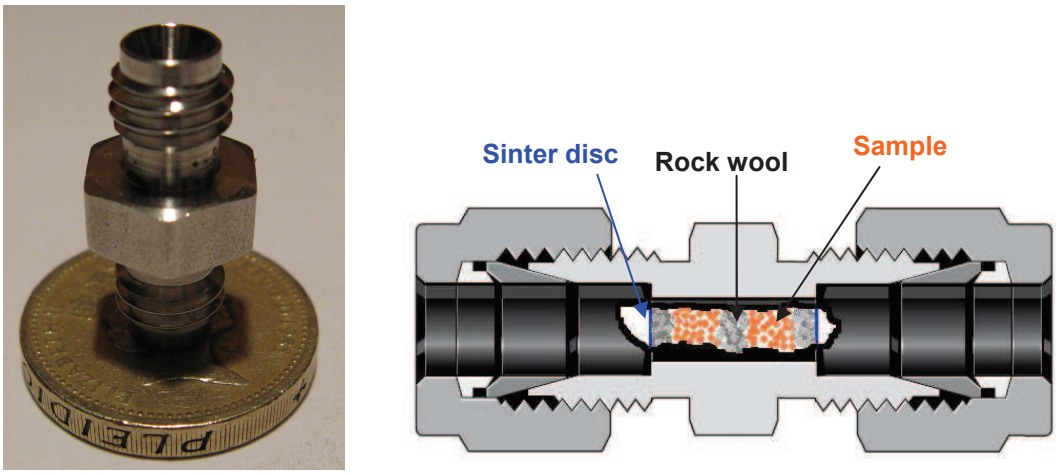

Figure 4.9: On the left the zero length column; on the right schematic view.

4.4 Regeneration procedure

Before each experiment the sample needs to be regenerated to ensure that any water present inside the pores will evaporate from the sample. The apparatus allows to regenerate and test the sample in the same oven, avoiding in this way any contact

with air between the regeneration and the test. The regeneration is carried out under constant flow of He (about 10 ml/min) and it consists in a slow ramping of temperature (1 °C/min) from room temperature to 110 °C (holding for 1h) and then to the regeneration temperature of the sample. This is provided with the sample and represents the temperature which ensures the complete de-hydration of the sample without compromising the adsorption properties. The sample is held at the regeneration temperature for at least 8 hr and then cooled down to the experimental temperature. The experiment can start when the sample is equilibrated with the temperature of the oven.

4.5 Ranking of the CO_2 capacity – procedure

All the samples were first tested for the CO_2 capacity. This consists in running a ZLC experiment and calculate the amount of CO_2 adsorbed by integrating the desorption curve using eq. 3.14. The experiment is repeated at least at two different flowrates in order to confirm the CO_2 capacity. The uncertainty is largest for the samples that show low CO_2 capacity. In the experiments carried out the uncertainty was found to be < 6%. The experiments at different flowrates also allow to verify the controlling transport mechanism, by comparing the *Ft* plots, according to sections 3.1 and 3.2.

The samples were tested in the traditional or the semi-automated ZLC system depending on the known and expected characteristics of the material and the adsorption properties. The semi-automated system was usually preferred for samples with low uptakes, when the presence of water needed to be monitored, for samples with very slow kinetics, and for ZLC tests with low concentration of CO_2.

The gas mixture to be used for the saturation of the sample is prepared the day before the experiment, allowing, in this way, the time for gases to reach complete mixing. For the ranking of the CO_2 capacity the mixture is composed by 10% v/v CO_2 in He. The capacity of the dosing oven allows to run several experiments with the same mixture.

When the sample, after regeneration, is equilibrated with the experimental temperature the saturation can be started. The mass flow controllers are set to the desired flowrate so that the baseline of the signal can be recorded. When the experiment is carried out in the traditional system, a function of the TRACE-GC system is used to auto-zero the baseline of the signal. Once the baseline is set the inlet flow is switched to the mixture of He and CO_2 from the dosing oven.

It has to be noted that the monitored variable is the gas phase concentration, so even if the signal of the detector indicates that equilibrium has been reached, this may be not true for the adsorbed phase. For this reason, for a new sample, experiments are repeated doubling the saturation time to confirm equilibration. Desorption is then started by switching the inlet flow to pure He. The experiment ends when the signal reaches the baseline. If the CO_2 capacity is found to be independent of the saturation time, experiments are then carried out to characterise the material. If full equilibration is not achieved, the saturation time is again doubled and the experiment repeated.

As mentioned previously the experiments are carried out at least at two different flowrates, so it may require more than one day to complete the series of experiments needed to characterise a sample. Usually an intermediate regeneration of the material is performed if the sample has been exposed to adsorption and desorption cycles for longer than 10-12 hours.

The data of the entire experiment are acquired and the signal is converted in concentration using the following equation:

$$\frac{c}{c_0} = \frac{\sigma - \sigma_{\min}}{\sigma_0 - \sigma_{\min}}$$

in which σ_0 is the value of the signal at time 0 (value at saturation) and σ_{min} is the value of the baseline.

According to eq. 3.2 to evaluate the CO_2 capacity of the sample the dead volume of the system needs to be subtracted from the total ZLC response curve. For this reason, before all the ZLC experiments, blank tests have been carried out at all the

flowrates of interest. Differently from a normal ZLC experiment, a blank test is run using an empty column: the resulting area under the blank curve is the dead volume of the system. From this it is clear that a new blank curve is needed if any modification is introduced to the apparatus which might change the response of the system.

4.6 Partial loading experiment – procedure

As explained in the theory section, in the partial loading experiment the sample is purposely exposed to the feed mixture for a time considerably less than the one needed to reach complete saturation. Hence the experimental procedure is exactly the same as the one just described for the ranking of the CO_2 capacity with the difference that the desorption starts before the signal approaches a constant value. The exposure time is decided according to the desired shift between the fully and partially saturated curves. Generally to facilitate the analysis of the data the partial loading curve should be not too close to the fully saturated one but also not too close to the blank to avoid any influence of the kinetics of the system. Prior the experiment the partial loading curve is then predicted by changing the exposure time in eq. 3.15.

In the case of the partial loading experiment the σ_0 corresponding to the initial gas phase concentration is the maximum of the signal just before the time at which the valve is switched: the resulting curve is then normalised and can be directly compared to the fully saturated experiment.

4.7 Water stability test – procedure

Some of the samples with highest CO_2 capacity were investigated with regard to their stability in presence of water. The test consists in exposing the sample for

several hours to a mixture of 1 % of H_2O, 16 % of CO_2 and He. The water and CO_2 content of the mixture were chosen to be close to the one of a typical flue gas stream. After the exposure to the mixture the sample is regenerated and a ZLC experiment is performed to estimate the CO_2 capacity (the gas mixture used in this case is the one with 10 % of CO_2 and He). This cycle of exposure to the mixture and ZLC experiment is then repeated until the sample is either stable or significantly de-activated.

The critical point in the water stability experiment is the preparation of the mixture, and in particular the addition of water. As mentioned in the previous sections the dosing oven is provided with a connection for a proper designed capsule for liquids. The temperature of the dosing oven is increased to let the water contained inside the capsule evaporate into the cylinders; the pressure transducer allows to monitor the increase of the pressure due to the evaporation.

The exact amount of water introduced inside the system is calculated by the difference between the weight of the capsule before and after the evaporation: this allows high accuracy in the preparation of mixture with vapours.

As already mentioned the lines between the dosing oven and the ZLC are heated to prevent the presence of cold spot in which condensation of water may occur.

The semi-automated ZLC system is also equipped with a cylinder that contains traces of SO_2 and NO. Test on the stability of the samples to these impurities in the presence of water can also be performed and follow the same procedure as for the water stability tests, but the gas from the mixture cylinder is used as provided by BOC, since the drying-columns would adsorb the trace amount of impurities.

5. CO_2 ADSORPTION CAPACITY RANKING OF NOVEL MICROPOROUS MATERIALS

In this chapter the results of the ZLC experiments on all the samples investigated are presented. The samples were synthesised as part of the UK-wide academic research consortium collaborating as part of the IGSCC project. The different expertise of the members of the consortium allowed to investigate a wide range of samples:

- PIMs (Polymers of Intrinsic Microporosity), synthesised by the University of Manchester and Cardiff University
- MOFs (Metal - Organic Frameworks), synthesised by the University of St. Andrews
- Mesoporous silicas, synthesised by the University of St. Andrews
- Zeolites, synthesised by the University of St. Andrews
- Carbons, synthesised by the University of Manchester and University College London

The ranking of the CO_2 capacity, using the ZLC method, was performed in the same conditions for all the samples: temperature of 35 ºC and partial pressure of CO_2 of 0.1 bar. This is representative of post-combustion capture conditions.
With regard to the utilisation of the adsorbents in a PSA process, it has been discussed in the previous sections that, in addition to the CO_2 capacity also the shape of the equilibrium isotherm greatly affects the overall efficiency of the process. In fact since a PSA process involves adsorption and desorption a linear isotherm is desirable: deviation from linearity (either towards the type I or type II isotherm) will result in slowing down one of the two processes [94]. Small deviations are acceptable but it is necessary that the isotherm is perfectly reversible in the region of interest for the PSA process. It has been explained in the section about to the theory of the ZLC method that the shape of the semilog plot of c/c_0 vs. Ft, under

equilibrium control, reflects the shape of the isotherm. In the case of linear isotherm the plot should yield a straight line through the origin with slope inversely proportional to the Henry's law constant, while in case of non-linearity of the isotherm the ZLC response will approach a straight line in the long time asymptote [18].

Zeolite 13X beads and silicalite HiSiv3000 pellets (provided by UOP, a Honeywell company) were used as benchmark materials. The samples were tested in the ZLC system at the same conditions and the CO_2 uptake obtained were 3.03 and 0.38 mol/kg respectively. It has to be noted that differently from the prototype materials, the commercial adsorbents 13X and HiSiv3000 are provided as pellets (crystals + binder). This means that the measured weight of the samples includes the binder and the crystals. Generally the concentration of the binder is around 20% in weight which means that the CO_2 capacity of the same weight of crystals would 20% higher than the one obtained. HiSiv3000, due to the lower uptake, was used as the benchmark for the adsorbents for which a relatively low uptake was expected: PIMs, carbons and mesoporous silicas.

Three activated carbons (provided by Calgon) were also added as low capacity benchmarks. The samples are called SRD 09 006 SRD 09 009 and SRD 10 061 and the capacities obtained are 0.286, 0.253 and 0.246 mol/kg respectively.

In order to simplify the discussion, the chapter is divided in sections in which the results of each class of materials will be discussed separately.

At the beginning of each section a table is presented with the code associated to the sample, the type of sample, the amount used for the ZLC experiment and any additional information provided with the sample (BET surface area, regeneration temperature, etc…). The samples are usually provided with a thermo-gravimetric plot which shows the weight loss with the temperature increase. The weight loss at the regeneration temperature was used to estimate the weight of the sample on a dry basis. The resulting amount was used as the "true" weight of the sample for all the calculations of the CO_2 capacity; a note is added for the samples for which no TG plot was available.

5.1 Zeolites

In this section the results of the ZLC experiments carried out on the zeolite adsorbents are presented and discussed. The samples were all synthesised by the research group of Prof. P.A. Wright at the University of St. Andrews.

The work at the University of St. Andrews was mainly focused on the optimisation of the adsorption properties of different types of zeolites with specific characteristics for CO_2 adsorption. The adsorption performance of zeolites can be greatly enhanced by creating internal space to host the CO_2 and improving the electrostatic interactions between the adsorbent and CO_2 by the insertion of extra-framework cations. At the University of St. Andrews a series of frameworks have been identified to have these characteristics and include Chabazite and Rho zeolites, which were developed through a fine control of the arrangement of the cations in the framework to improve the CO_2 uptake. Chabazite and Rho zeolites are characterised by a structure which is easy and inexpensive to make and also very resilient. By changing the cations composition in the framework more free space can be made available, but on the other hand cations are needed to adsorb the CO_2 and give stability to the structure.

Cations with different sizes and different charge density have been exchanged in the structure and by knowing the nature and the amount of cations used it is also possible to predict the position of the exchanged cations in the framework. The aim is to find a good compromise between good affinity for CO_2 (i.e. more cations) and high free volume (i.e. fewer cations). This process is not always successful: sometimes large cations can block the entrance to the cages and as a result there is no accessibility for the CO_2 molecules.

In addition to the cation exchanging process, other methods were also tried to improve the materials. Nitridation, for example, involves the replacement of oxygen with nitrogen in order to create new adsorption sites: this process generally improves the separation of CO_2 from N_2 or CH_4.

Another method used is to change the Si/Al ratio: Al can be removed from the framework by heating up in presence of water. Reducing the Al content generally

makes the material less hydrophilic which represents one of the weak points of the use of zeolites as adsorbents for CO_2. This also increases the stability of the material. In table 5.1 all the zeolite samples synthesised by the University of St. Andrews and tested on the ZLC system are listed. Due to the different nature of the samples the discussion of the results will be organised in separate sub-sections depending on the framework type.

Table 5.1: List of the zeolite samples investigated. (*) TGA not available. (**) Pellet form.

Name	Sample	Amount tested [mg]
MML37	ITQ-13	10.7
MML77	K-Chabazite (less crystalline)	6.79
MML146	K,H-Chabazite (0 K/Unit cell)	10.2
MML142	K,H-Chabazite (1.5 K/Unit cell)	9.18
MML140	K,H-Chabazite (3 K/Unit cell)	9.45
MML148	K,H-Chabazite (3.5 K/Unit cell)	8.26
MML284	K-Chabazite (4 K/unit cell)	5.18
MML162	K,H-Chabazite (4.5 K/Unit cell)	12.3*
MML241	K,H-Chabazite (6 K/Unit cell)	5.2
MML138	K-Chabazite (9 K/Unit cell)	10.7
MML247	K-Chabazite (9 K/Unit cell)	6.4
MML270	Na,H -Chabazite (8.8 Na/unit cell)	9.42
MML276	Na,H -Chabazite (6.5 Na/unit cell)	9.7
MML267	Na,H -Chabazite (6 Na/unit cell)	9.1
MML268	Na,H -Chabazite (5 Na/unit cell)	9.01
MML251	Na,H -Chabazite (3 Na/unit cell)	14.7
MML308	Na,H-Chabazite (2.5 Na/unit cell)	10
MML256	Na,H -Chabazite (2 Na/unit cell)	7.34
MML309	Na,H-Chabazite (1 Na/unit cell)	8.34
MML266	Na,H -Chabazite (0 Na/unit cell)	13.7
MML313	Na,Cs-Rho	11.6

MML283	Li-Chabazite	7.71
MML239	K-ZK-5	6.04
MML274	H-ZK-5	8.4
MML269	Na-Rho (10 Na/unit cell)	7.14
MML275	Na,H-Rho (8.5 Na/unit cell)	7.58
MML280	Na,H-Rho (7 Na/unit cell)	8.23
MML299	Na,H-Rho (6 Na/unit cell)	5.96
MML286	Na,H-Rho (4.5 Na/unit cell)	8.48
MML287	Na,H-Rho (3.5 Na/unit cell)	13.9
MML288	Na,H-Rho (2.5 Na/unit cell)	7.63
MML312	Na,H-Rho	5.74
MML200	Steamed Rho	6.45
MML404	Ca,H-Rho (5 Ca/unit cell)	10.6
MML417	Ca,H -Rho (4 Ca/unit cell)	10.4
MML416	Ca,H -Rho (3 Ca/unit cell)	9.2
MML415	Ca,H -Rho (2 Ca/unit cell)	10.4
MML297	Ca,H-Chabazite (4.5 Ca/unit cell)	6.32
MML322	Ca,H-Chabazite (3.5 Ca/unit cell)	5.87
MML324	Ca,H-Chabazite (3 Ca/unit cell)	6.12
MML353	Ca,H-Chabazite (2.5 Ca/unit cell)	6.69
MML361	Ca,H-Chabazite (2 Ca/unit cell)	5.12
MML363	Ca,H-Chabazite (1.5 Ca/unit cell)	5.85
MML365	Ca,H-Chabazite (1 Ca/unit cell)	6.35
MML362	Ca,H-Chabazite (0 Ca/unit cell)	5.86
MML462	K-Rho	6.89
13X	13X (UOP)	13.6**

5.1.1 Chabazite

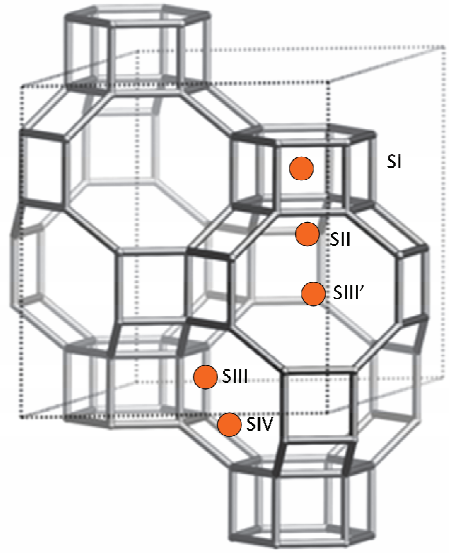

Figure 5.1: Structure of Chabazite showing the possible positions of the cations [35].

Figure 5.1 shows the structure of a typical Chabazite zeolite. The unit cell consists of one ellipsoidal cavity which is accessible through six 8-ring windows and through two double 6-ring (D6R) units. The nominal aperture of the 8-ring windows in a cation-free structure is 0.38 nm [35]. In this configuration, by introducing AlO_4 units in the structure a negative charge is created which needs to be counter-balanced by exchangeable cations. As shown in Figure 5.1, five coordination positions were identified as possible cation sites in the framework of Chabazites: one at the centre of the D6R unit (SI), one at the window of the D6R hexagonal prism (SII), the SIII site located at the 8-ring window, SIII' also locate at the 8-ring window but closer to the 8-ring window than SIII [95], and finally SIV in proximity to the centre of the ellipsoidal cavity[96]. Some studies have proved that, due to the different size and charge density of each cation, there is a degree of preference in the occupancy of the available sites by the different cations [95, 97].

Table 5.2 shows the values of the cationic radii for the alkali metals used in the preparation of the ion-exchanged zeolites.

Table 5.2: Ionic radii of alkali metals [31]

Cation	Radius [Å]
Li^+	0.68
Na^+	0.97
K^+	1.33
Cs^+	1.67

The SII site is generally available for the smaller cations, for this reason Li shows a marked preference in the occupancy of this site, but at higher Li loading also the SIII positions are filled.

Na cations are generally located in the SIII and SIII' sites but at higher Na loadings there is also evidence of a low coverage of the SII sites. For Ca cations a preferential occupancy for the SI and SII sites is observed.

K cations have a larger size relative to Li and Na and they unequally distribute in the framework. The preferential occupancy is for the SIII and SIII' site, but also a low coverage for the SIV position has been observed [98]. Ridha at al. [99], have reported that the position of the K cation in the SIII' sites associated with the big size of the cation produce a severe blockage of the entrance to the pores, greatly reducing the accessibility to N_2 molecules: this results in an apparent low micropore volume. The reported trend of the micropore volume follows the trend of the cation radius: K < Na < Li.

The general synthesis is similar to the one reported in the literature [95] and involves the preparation of NH_4-Y zeolite by exchanging NH_4^+ cations in a Na-Y zeolite. NH_3 is then removed from the sample leaving the protonic form of H-Y. Finally KOH is added and the final product is recovered by filtration.

The fully exchanged K Chabazite is then exchanged to synthesise the different cation series of the zeolite. For convenience the results relative to the different series produced will be discussed separately.

5.1.1.1 K, H-Chabazite

The K, H series of Chabazites were prepared by removing the K cations from the fully exchanged sample MML138; samples at different content of potassium were produced using different concentrations of NH_4Cl. Figure 5.2 shows the N_2 uptake for the series measured at the University of St. Andrews. As reported by Webley et al. [99] the high content of K greatly reduces the accessibility to the pores for the N_2 molecules. The blockage action of the K cations seems to start when more than four K cations are loaded per unit cell. In Figure 5.3 the ranking of the CO_2 capacity measured from the ZLC system is presented. The graph also includes for comparison two other as-prepared K Chabazites which were synthesised before the K,H ion exchanged samples: MML77 and MML247. The difference in the CO_2 uptake of the three as-prepared K Chabazites arises from a different grade of crystallinity reached in the process of optimising the synthesis procedure.

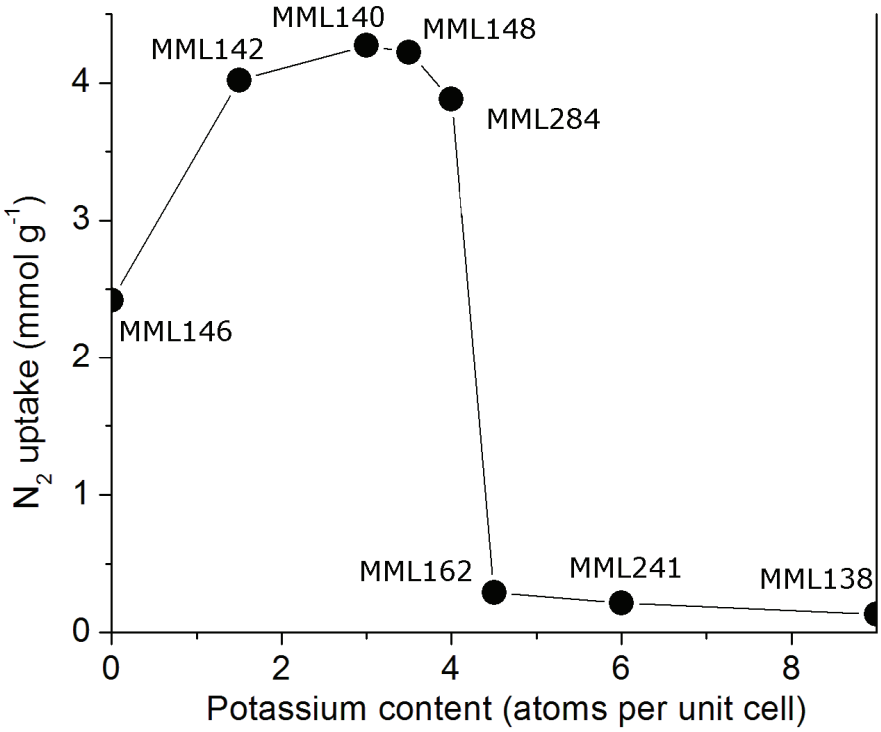

Figure 5.2: N_2 uptake for K, H-Chabazite at different K content (measurement performed at the University of St. Andrews).

Despite the hindering effect due to the presence of the K cations at the entrance of the pores, the results show that the CO2 molecules can still have access to the free volume.

Moreover the trend of the uptake observed shows a clear increase of the capacity with the K content. This confirms that, although the access to the pores may be more difficult in the as-prepared K-Chabazite, the higher electrostatic field definitely favours the CO_2 adsorption.

Figure 5.4 shows the *Ft/M* plot for the K,H Chabazite series. For the two best samples, MML 138 and MML247, a clear exponential decay can be seen indicating a fairly linear isotherm in the range of interest.

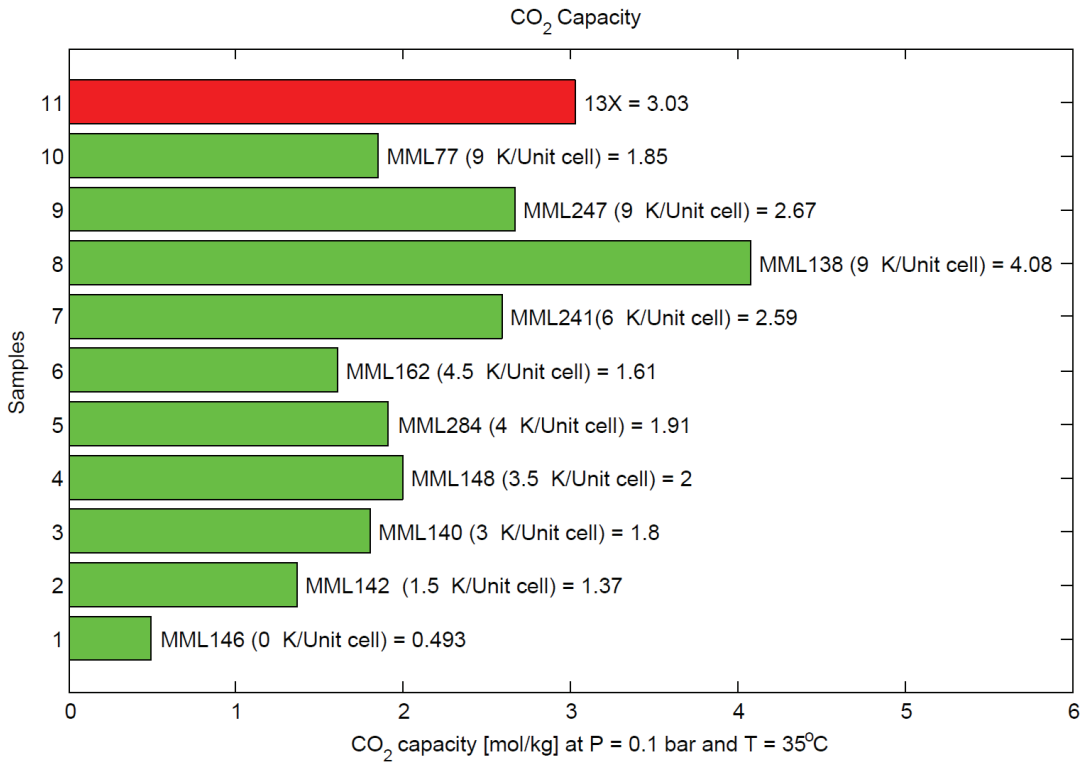

Figure 5.3: Ranking of the CO_2 capacity for K,H exchanged Chabazites at different K content.

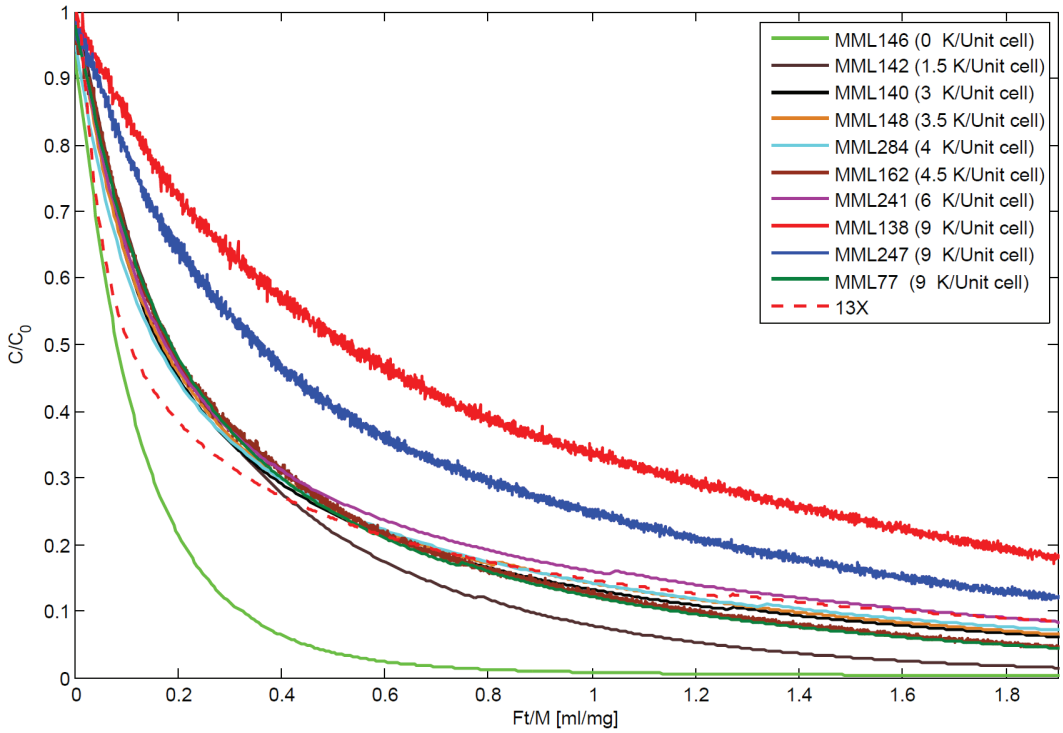

Figure 5.4: Ft/M plot for H,K-Chabazites

In Figure 5.5 the semi-log plot of c/c_0 vs. Ft is presented. As explained in the previous sections, the overlapping of the desorption curves at different flowrates in the Ft plot is proof of an equilibrium-controlled desorption process. In the case of the MML138 sample, the Ft plot shows clearly that the process is equilibrium-controlled: the curves overlap in the range of concentrations. Moreover in case of equilibrium controlled desorption process the shape of the ZLC curves give unambiguous information on the shape of the CO_2 isotherm in the relative range of pressure. For the MML138 sample the ZLC curves in the semi-log Ft plot have a clearly linear trend indicating a linear equilibrium relationship in the pressure range of interest.

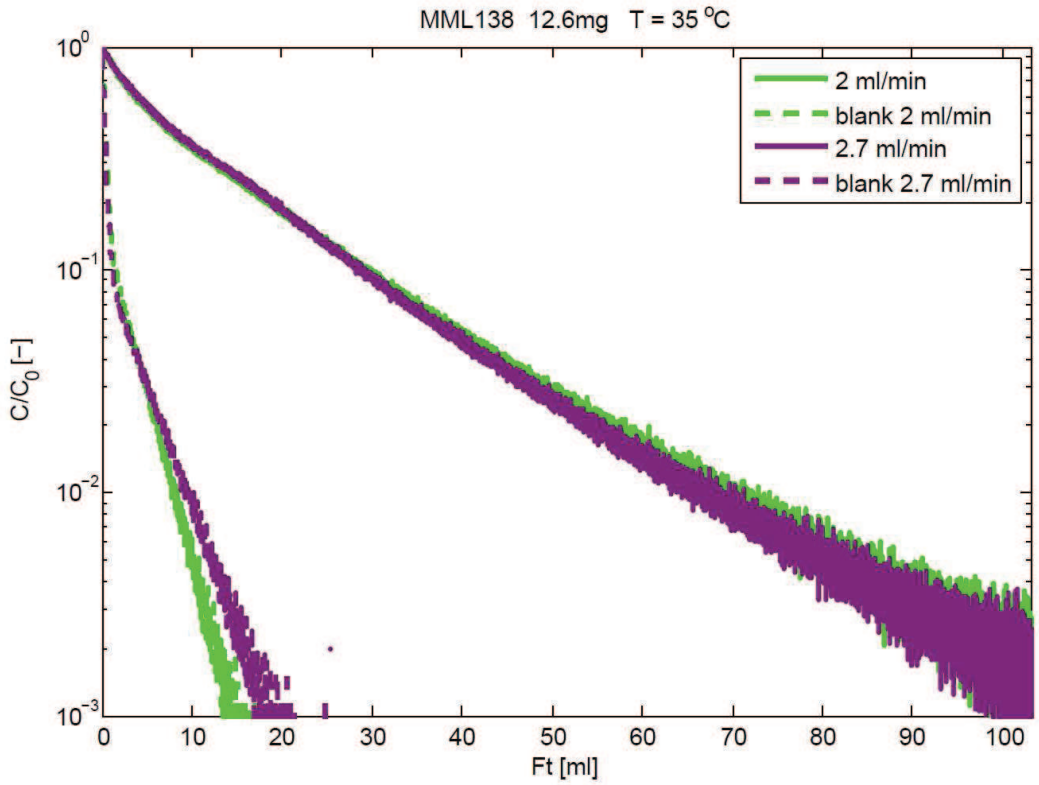

Figure 5.5: Ft plot for the ZLC experiment on the as-prepared K-Chabazite sample at two different flowrates.

When the desorption process is under equilibrium conditions, each point of the ZLC curve is an equilibrium point. This means that integrating the ZLC response, using eq. 3.12, the CO_2 isotherm can be extracted.

The isotherm for the fully exchanged K-Chabazite was also extracted by integration of the ZLC response curve at the lowest flowrate. Figure 5.18 , at the end of the Chabazites section, shows the comparison of the CO_2 isotherms for the best Chabazites tested.

5.1.1.2 Na,H Chabazite

The Na, H series of Chabazites was prepared by removing Na atoms from the fully exchanged Na Chabazite sample MML270. The Na Chabazite sample was synthesised by exchanging of Na cations in K-Chabazite; the resulting sample was then treated with NH_4Cl at different concentrations to obtain samples with different Na/H ratios. Figure 5.6 shows the N_2 uptake in the samples at different Na content, measured at the University of St. Andrews.

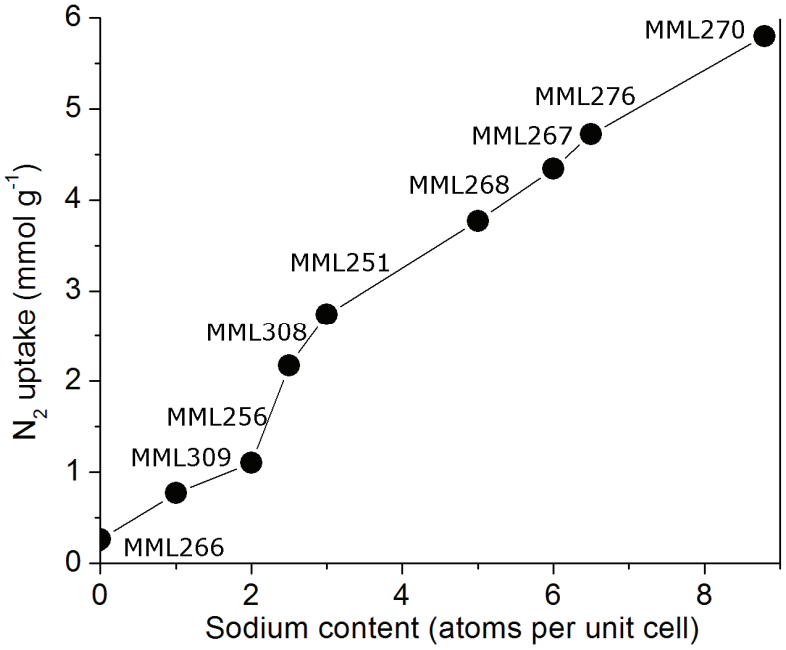

Figure 5.6: N_2 uptake for Na,H Chabazites at different Na content (measurements carried out at the University of St. Andrews).

Clearly, by removing the Na atoms from the framework of the fully exchanged sample, a decrease of the micropore volume is observed. This is mainly due to the fact that in the Chabazite series the structure is not stable in the fully acid form and increasing the amount of acid sites tends to induce deformations in the framework which may reduce the porosity of the material [100].

As expected the trend of the CO_2 capacity reflects the increase of the micropore volume of the samples, Figure 5.7 and Figure 5.8. The samples with the highest content of Na, 6.5 and 8.8, show an uptake of 3.26 and 3.5 mol/kg respectively,

slightly higher than the one obtained by the benchmark 13X. The value of the capacity obtained for the fully exchanged Na Chabazite is in good agreement with what is reported by Ridha et al.[101], who measured the CO_2 isotherm of Na Chabazite at 303 K: the CO_2 capacity reported is about 3.7 mol/kg at 0.1 bar. Recently Watson et al. [102] measured the CO_2 uptakes of a natural Chabazite at 305 K. Their value of the capacity, about 3.1 mol/kg at 0.1 bar, is lower than the one obtained in the present work. This is probably due to the fact that the natural Chabazite was tested as extracted with no purification procedure to remove impurities.

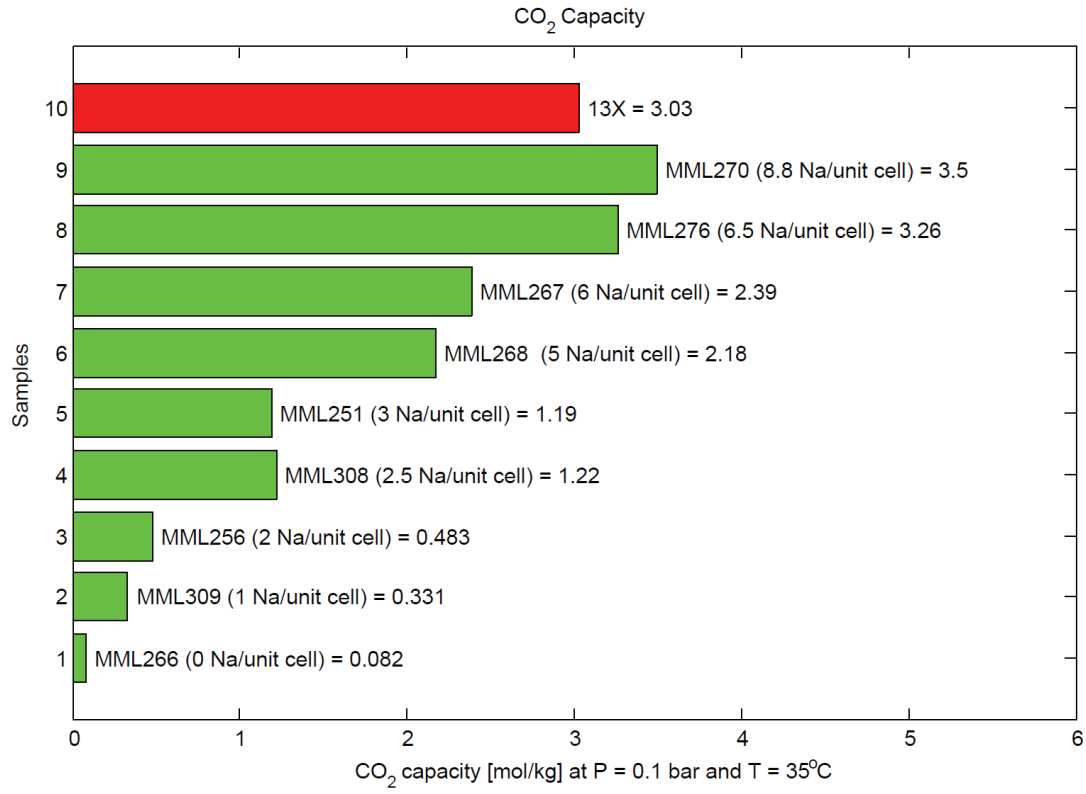

Figure 5.7: Ranking of the Na,H Chabazite series.

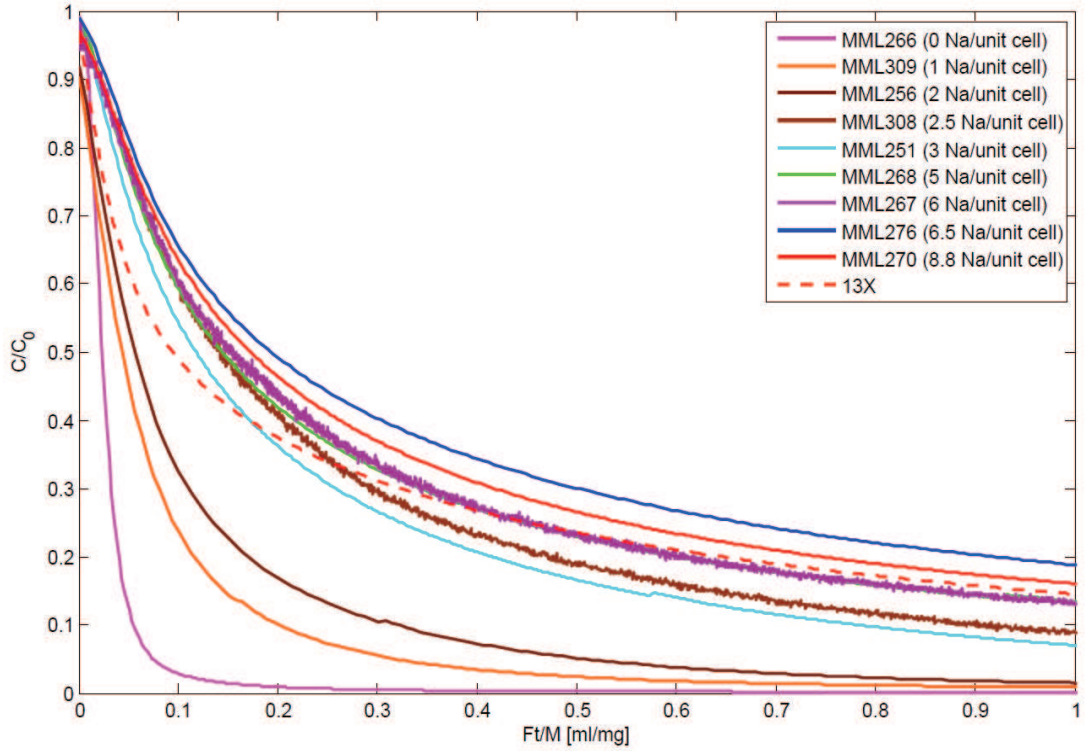

Figure 5.8: Ft/M plot for the Na,H Chabazite series.

All the samples tested show a clear equilibrium controlled desorption rate. This can be easily seen from the overlapping of the curves in the semi-log *Ft* plots which are presented in Appendix A. As an example, Figure 5.9 shows the *Ft* plot of the fully exchanged Na Chabazite. The sample was tested at relatively high flowrates (20, 30 and 40 ml/min) and the graph clearly shows the overlapping of ZLC curves.

The sample showed a good CO_2 capacity and for this reason it was further tested to extract the heat of adsorption. Under equilibrium conditions, in the long-time region the ZLC response curve in the *Ft* plot approaches a linear asymptote of slope -1/(KV_s + V_g). V_g is the dead volume of the system which is known from the blank experiment, K is the dimensionless Henry's law constant and V_s is the volume occupied by the solid. From this it is clear that by running ZLC experiments at different temperatures, under equilibrium conditions, the relative equilibrium constants can be extracted from the long-time asymptote of the *Ft* plots. In Figure 5.10 all the ZLC curves at different temperatures are displayed with the relative long-time asymptotes. The heat of adsorption is then calculated by using the Van't Hoff equation:

$$\ln(K V_s) = \ln(K_0 V_s) - \frac{\Delta U}{R}\left(\frac{1}{T} - \frac{1}{T_0}\right) \qquad (5.1)$$

The value obtained for the heat of adsorption at zero loading ($\Delta H_0 = \Delta U_0 - RT$) obtained from the temperature dependence of the Henry's law constants extracted from the ZLC experiments is equal to 51 kJ/mol which is higher compared to the value of 42.24 kJ/mol measured by Ridha et al. [101] at 3.65 molecules/unit cage. A value close to 50 kJ/mol was reported by Khvoshchev et al. [103] who measured the isosteric heat of adsorption for different ion-exchanged Chabazites.

Finally, from the integration of the ZLC curves, also the complete CO_2 isotherms in the range of interest were obtained. The isotherms at the three temperatures investigated are shown in Figure 5.10.

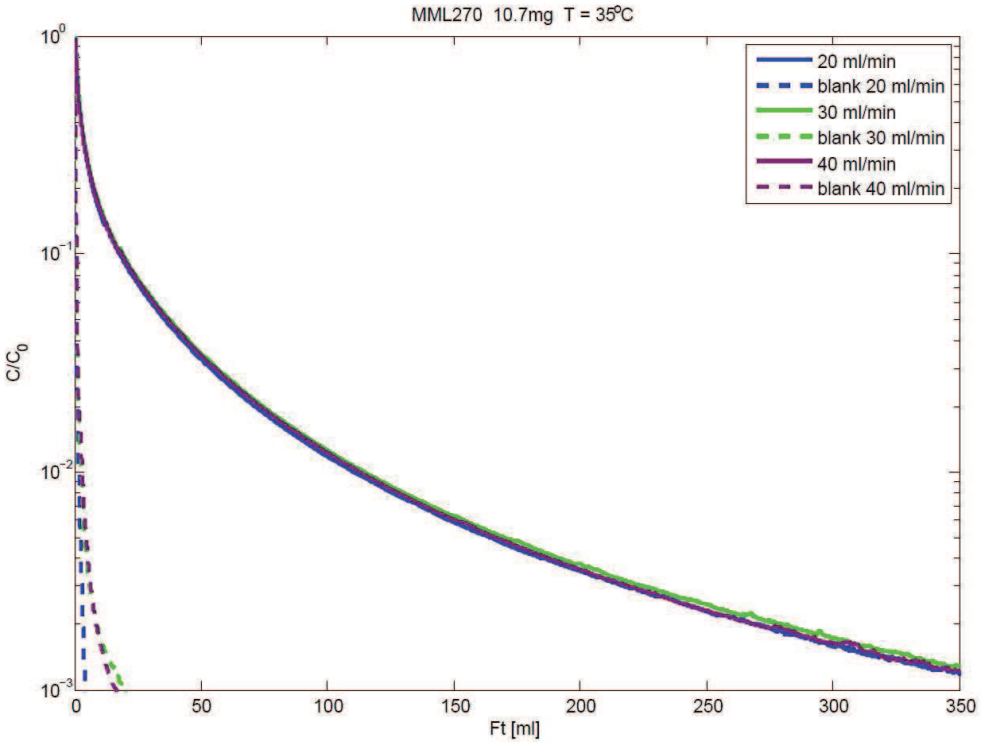

Figure 5.9: Ft plot for the fully exchanged Na Chabazite sample

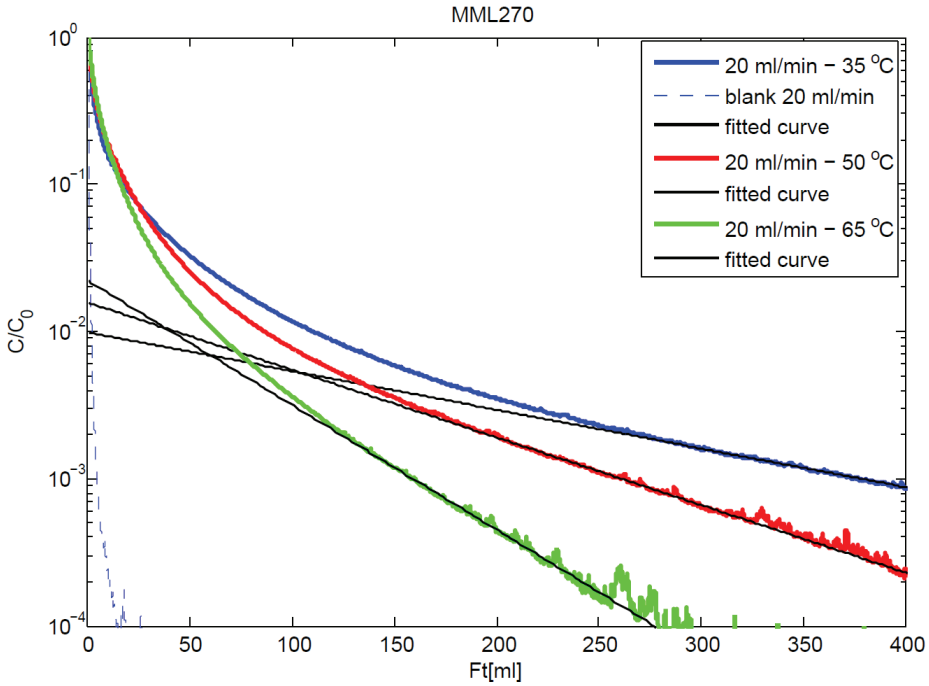

Figure 5.10: ZLC desorption curves at different temperatures for the fully exchanged Na Chabazite. The fitted curves show the long-time asymptotes which were used to calculate the Henry constants and the resulting heat of adsorption.

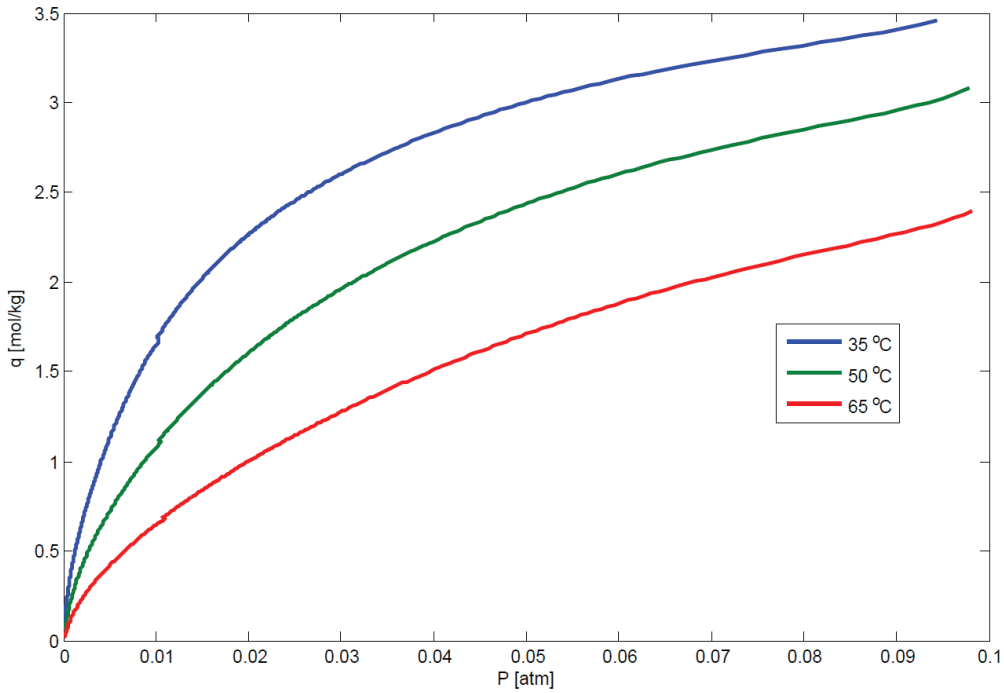

Figure 5.11: CO_2 isotherms at different temperatures for the fully exchanged Na-Chabazite sample.

5.1.1.3 H,Ca-Chabazite

The H,Ca-Chabazite series was prepared by removing Ca atoms from the fully exchanged Ca-Chabazite sample MML297. As for the other Chabazite series, the Ca-Chabazite sample was synthesised by fully exchanging Ca cations in K-Chabazite. The resulting sample was then treated with NH_4Cl at different concentrations to obtain samples with different Ca/H ratios. Figure 5.12 shows the N_2 uptake in the samples at different Ca content, measured at the University of St. Andrews.

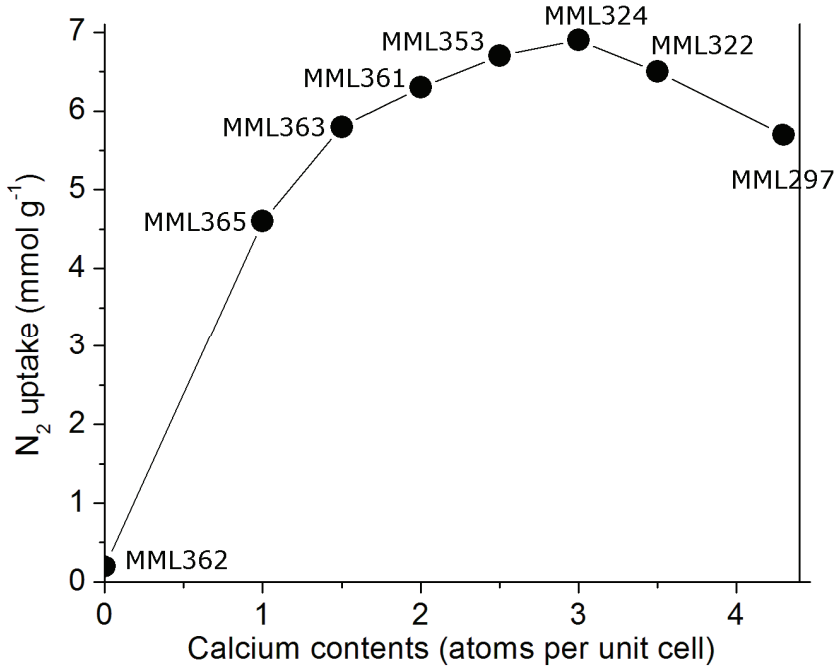

Figure 5.12: N_2 uptake for Ca, H-Chabazite at different K content (measurement performed at the University of St. Andrews).

As mentioned previously Ca atoms tend to occupy SI and SII sites, so there is no evidence of hindering effect for N_2 adsorption.

The trend of the micropore volume seems to have a maximum probably due to the increasing influence of the acid sites while the content of Ca decreases.

Figure 5.13 shows that the CO_2 capacity for the Ca,H-Chabazite series exhibits a general increase with the Ca content on the structure reaching a value of 3.1 mol/kg for the fully exchanged Ca-Chabazite, slightly higher that the one obtained for 13X.

The value of the capacity is consistent with the one of about 4 mol/kg measured at 273 K from Zhang et al in 2008 [104].

The same trend is shown in Figure 5.14 in which the ZLC curves of all the samples of the series are plotted as c/c_0 vs. Ft/M.

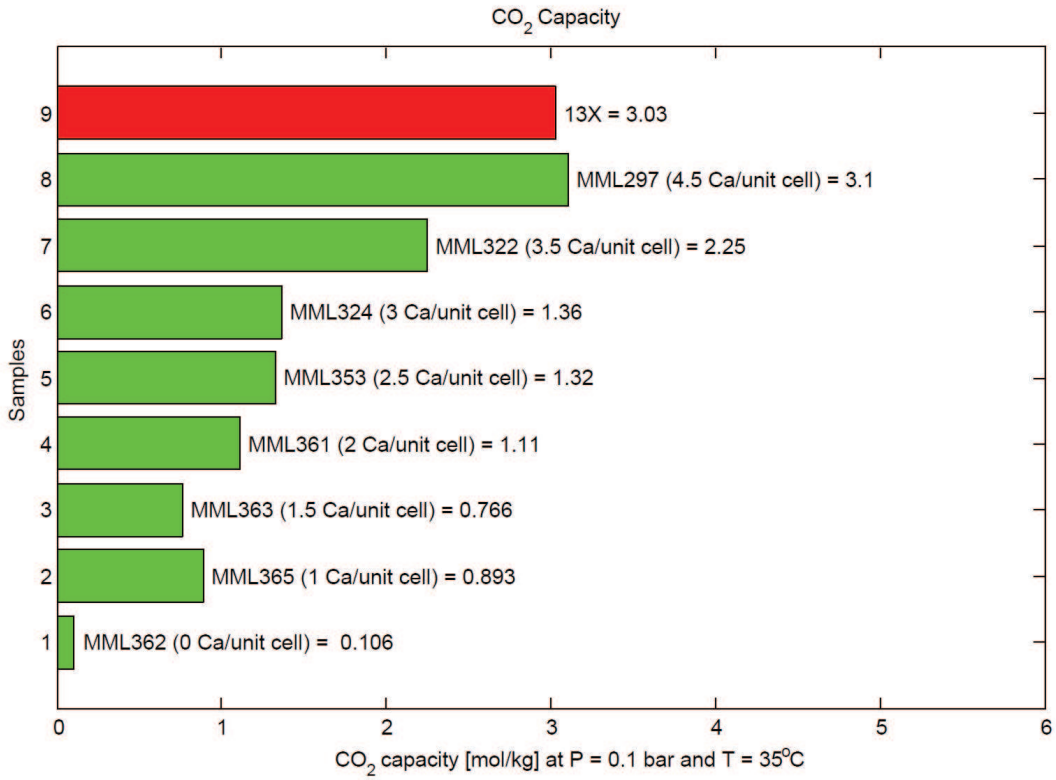

Figure 5.13: Ranking of the CO_2 capacity for the Ca,H-Chabazite series.

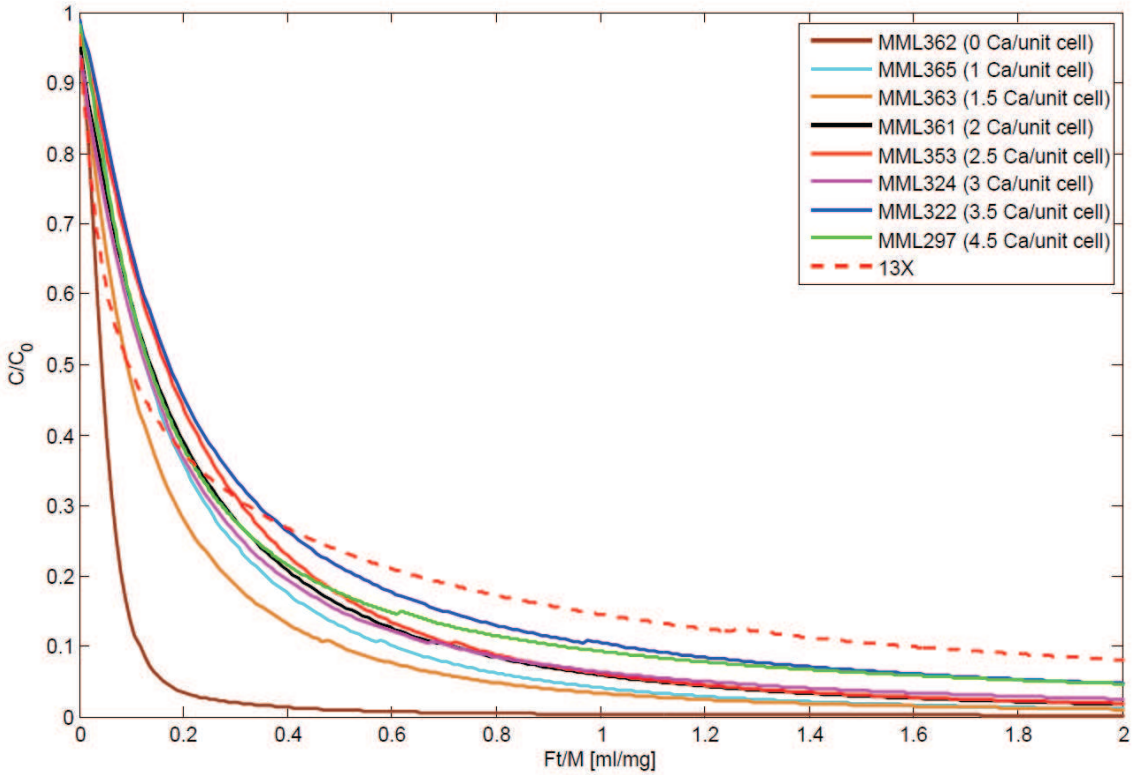

Figure 5.14: Ft/M plot for the Ca,H-Chabazite series.

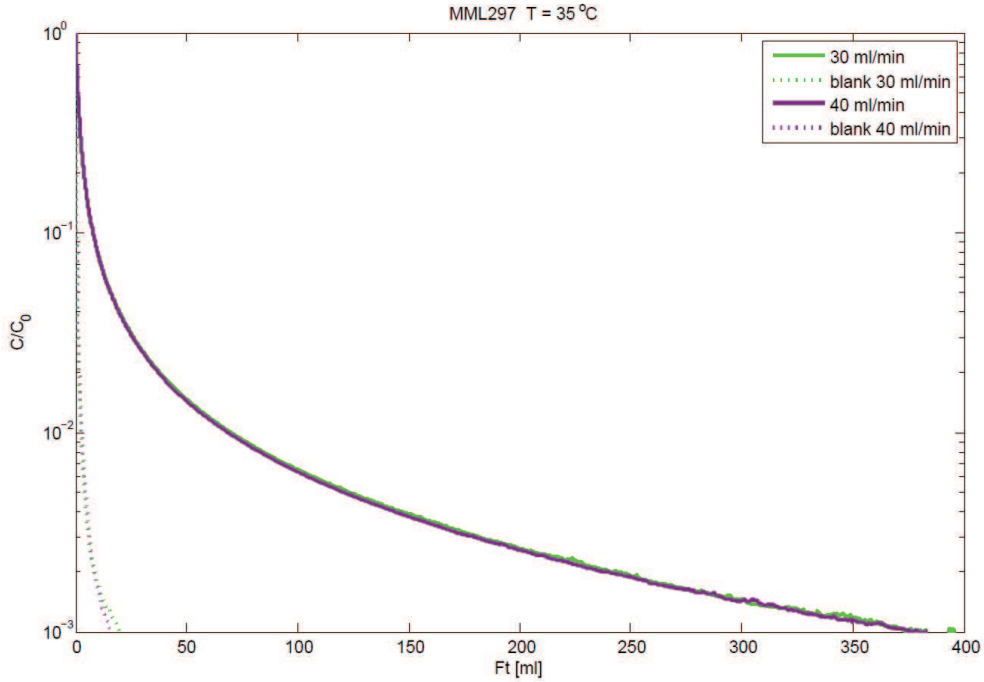

Figure 5.15: ZLC desorption curves for the fully exchanged Ca-Chabazite sample MML297 at different flowrates

All the samples showed a clear equilibrium-controlled desorption which can be observed from the *Ft* plots reported in the Appendix A. The fast kinetics for the Ca,H-Chabazite samples was expected due to the fact that the Ca cation in SI and SII do not block the entrance to the cages. In Figure 5.15 the ZLC response curves for the fully exchanged sample are presented. The evidence that the process is under equilibrium control conditions is given by the fact that the ZLC curves overlap in the plot of $ln(c/c_0)$ vs. *Ft*.

5.1.1.4 Li-Chabazite

Among the ion-exchanged Chabazites, a sample of fully exchanged Li-Chabazite was also synthesised. The sample was prepared by exchanging of Na-Chabazite with LiCl. The small size of the Li cations combined with the preferential occupancy in SII and SIII sites create the conditions for high free volume available for the adsorption of CO_2. This is confirmed by the value of the N_2 uptake measured, about 7 mol/kg, which is the highest among the Chabazite samples (N_2 uptake was measured at the University of St. Andrews). The high free volume of the sample resulted also in a high CO_2 capacity, reaching the same value of the K-Chabazite. Figure 5.16 shows the Ft/M plot of the ZLC curves compared to the one for 13X.

CO_2 isotherms on Li-Chabazite at different temperatures are reported in literature. At 273 K and 10 kPa the values of the CO_2 capacity reported are in the range from about 4.5 to 5.6 mol/kg [99, 101, 104], while at 303 K and 10 kPa value of about 5 mol/kg was measured by the same authors [101]; in the present work a value of 4.14 mol/kg was obtained. The difference in the results reported might be ascribed to a different grade of cristallinity of the different samples, which might also explain the lower value of the CO_2 uptake obtained in the present work. Also it has to be noted that Li is a strong adsorbent for water so even the small amount of water inside the system can affect the final uptake measured.

Not different from the other Chabazites, the desorption process of the Li sample is clearly equilibrium controlled, as confirmed by the overlapping of the curves at

different flowrates in the *Ft* plot of Figure 5.17. Also in this case the ZLC curves were integrated and the CO_2 isotherm was extracted as shown in Figure 5.18.

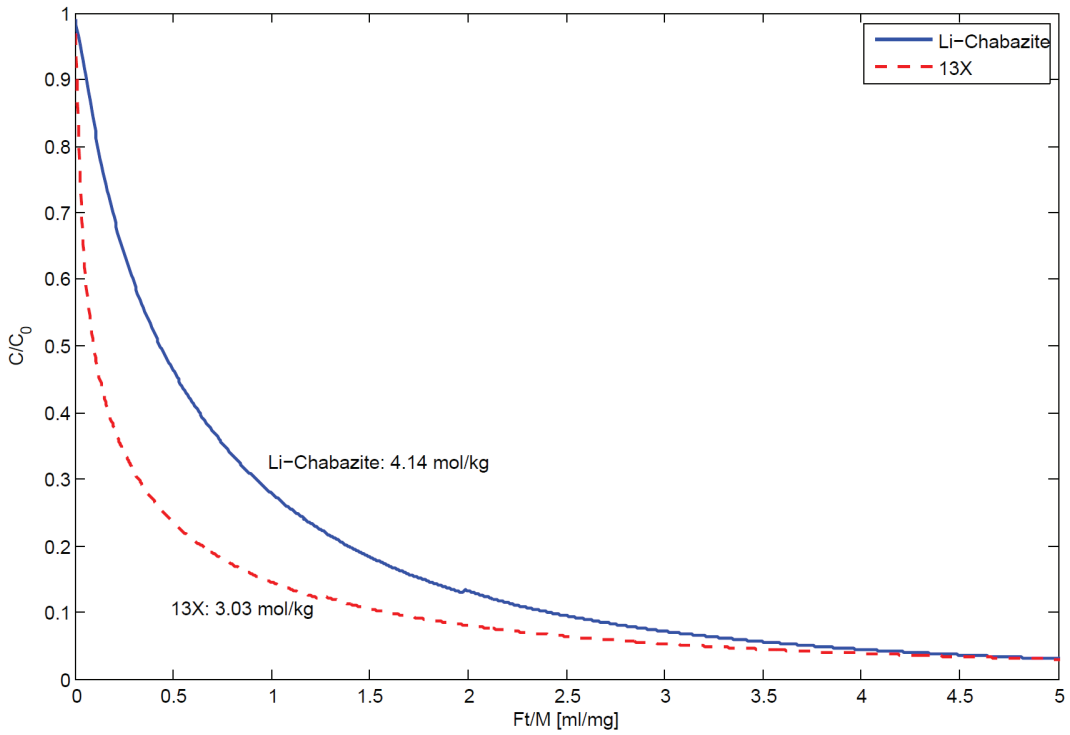

Figure 5.16: Ft/M plot of the fully exchanged Li-Chabazite compared with zeolite 13X

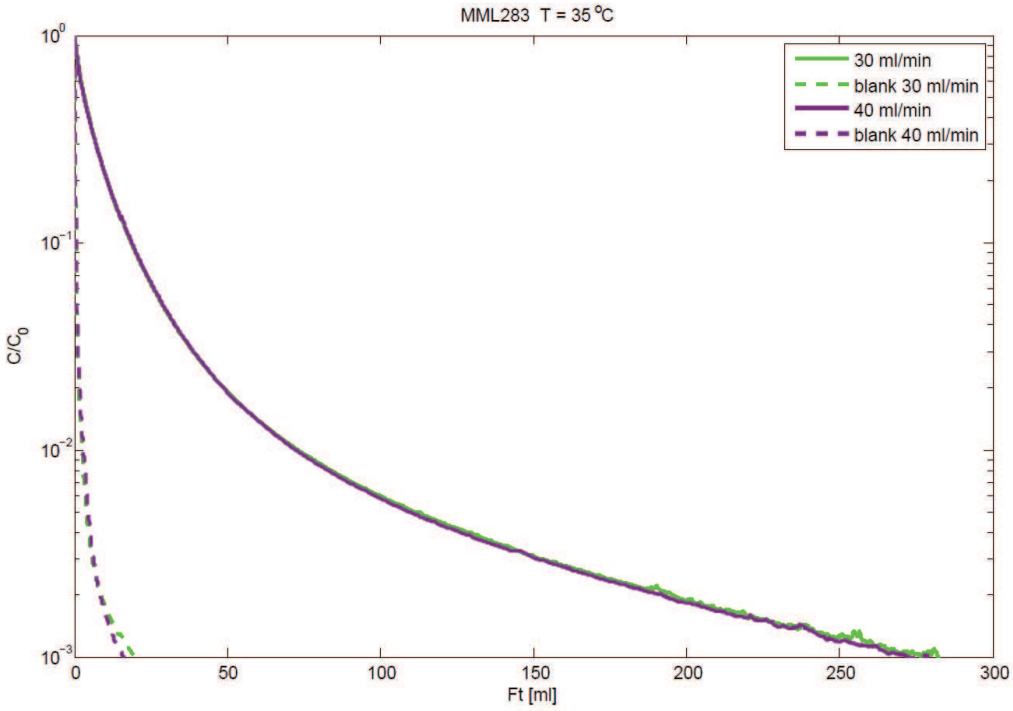

Figure 5.17: Ft plot for Li-Chabazite showing equilibrium controlled desorption

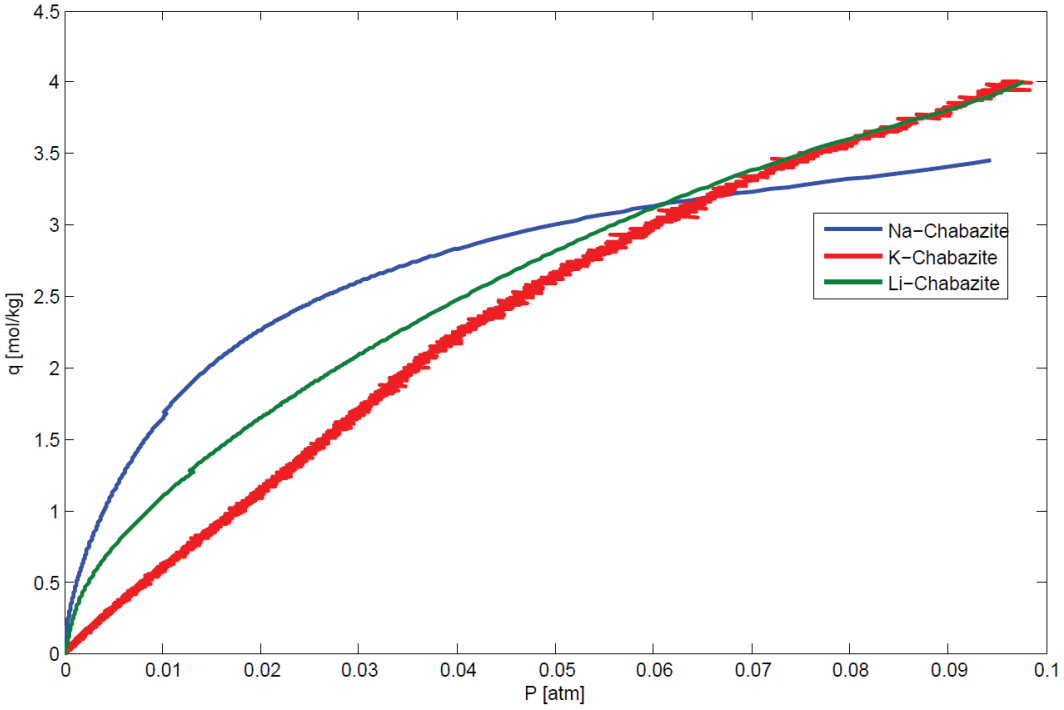

Figure 5.18: CO_2 isotherms at 35 ˚C for Li-, K- and Na-Chabazite.

5.1.2 Rho Zeolites

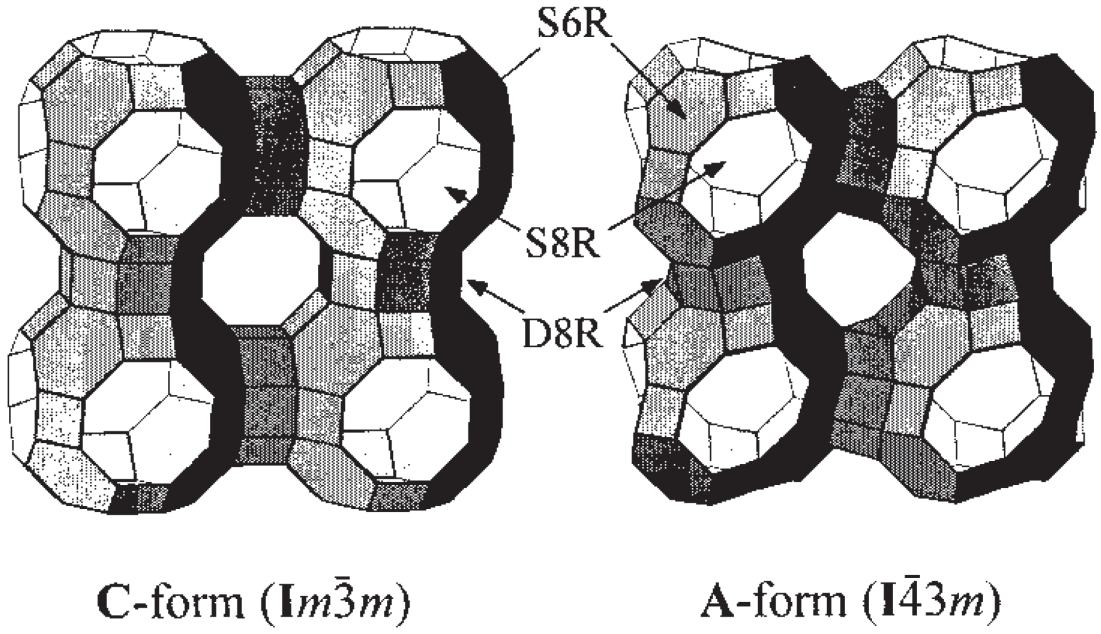

Figure 5.19: Structure of Rho zeolite in symmetric ($Im\bar{3}m$) and acentric ($I\bar{4}3m$) configuration [36].

Rho zeolites, similarly to Chabazites, are characterised by a large fraction of pore volume available for adsorption and relatively small cages which facilitate the interaction with the adsorbed molecules. As mentioned in the previous chapters, zeolite Rho has a structure characterised by a body-centred-cubic arrangement of α-cages connected by double eight rings [34d], with an effective channel diameter of about 3.6 Å [35]. The available sites which can accommodate the extra-framework cations are the single eight-ring (S8R), the double eight-ring (D8R), and the single six-ring (S6R) sites [36] (Figure 5.19).

It has been proved that, passing from the hydrated form to the ion-exchanged one, the structure of Rho zeolites passes from the centrosymmetric ($Im\bar{3}m$) structure to the non-centrosymmetric ($I\bar{4}3m$) [34a, b, 34d-f, 36-38, 105], Figure 5.19. From this follows that once extra framework cations are introduced in the structure, the deformation induced, together with size and the position occupied by the cations, may create a severe blocking action to the cages.

The different Rho samples presented were prepared at the University of St. Andrews according to procedures already published in literature [106]: the resulting Na,Cs-Rho was then converted to the ammonium form and, successively, to the different ion exchanged forms. In the next sections the different cationic types of Rho zeolites will be discussed separately.

5.1.2.1 Na,H-Rho

The Na, H Rho series was prepared by removing Na atoms from the fully exchanged Na-Rho sample MML269. Na-Rho was synthesised by fully exchanging Na cations in Na,Cs-Rho. Different Na/H ration were obtained by treating the fully exchanged Na-Rho with NH_4Cl at different concentrations. Figure 5.20 shows the N_2 uptake in the samples at different Na content, measured at the University of St. Andrews

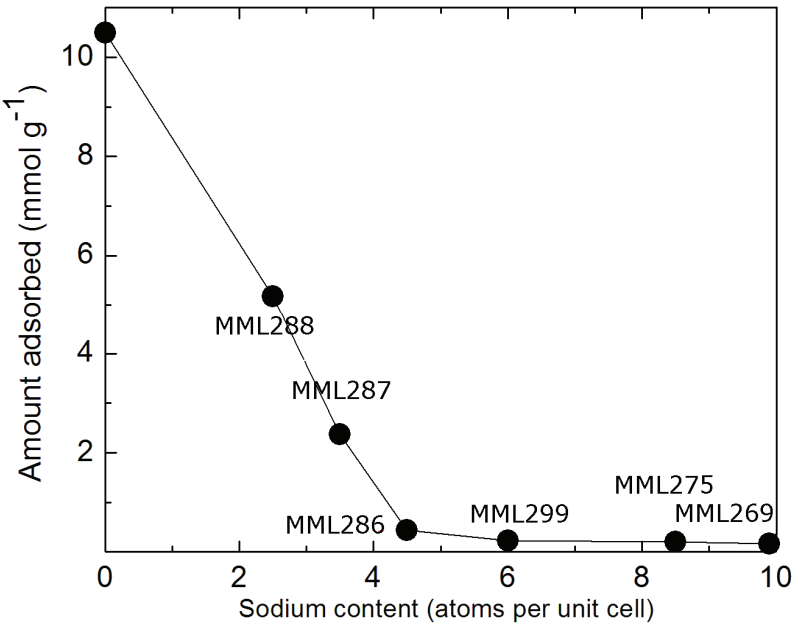

Figure 5.20: N_2 uptake at 0.1 bar and 77 K for Na,H-rho at different Na content (measurements performed at the University of St. Andrews).

Rietveld refinement from laboratory powder X-ray diffraction at 293 K, performed at the University of St. Andrews, revealed the preferential occupancy of Na cations in the S6R and S8R sites [107], in good agreement with what reported in the literature[34a,

[38]. By removing Na cation from the framework the hindering action of the Na cations is reduced and N_2 uptake is observed when the Na content is less than 4 cations per unit cell.

Figure 5.21 shows the CO_2 uptake obtained from the ZLC experiments for the samples of the Na, H series. Despite the higher accessible volume observed for the samples at low Na content, the CO_2 capacity follows the opposite trend, with higher capacity at higher Na content.

The cations have stronger electrostatic effects compared to the proton, and as a result a higher affinity with CO_2. The fact that there is CO_2 uptake indicates that the Na atoms are somehow able to move to allow the diffusion of CO_2, while the reduced mobility at low temperature does not allow the access of N_2 [107].

The H form of the Rho zeolites showed a relatively low uptake of CO_2 due to the lower interaction with CO_2. The value obtained is consistent with what obtained from the measurements performed at the University of St. Andrews [107] but higher than the one reported by Araki et al. for the H-Rho zeolite of their work [108]. The difference might be ascribed to the different conditions at which the ion exchanging process is induced.

By increasing the Na content, the sites S8R and S6R start to be fully occupied resulting in the creation of more energetic sites for CO_2 adsorption. As a result the highest CO_2 uptake is registered for the fully exchanged Na-Rho sample with a value of 3.22 mol/kg.

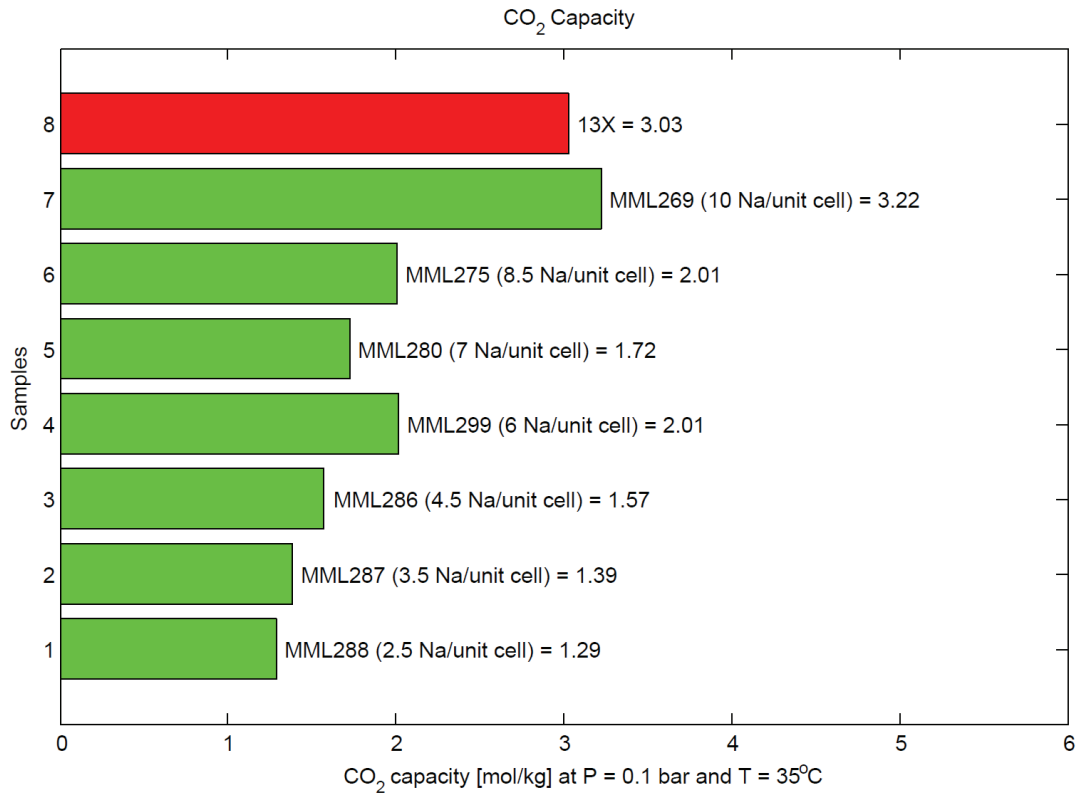

Figure 5.21: Ranking of the CO_2 capacity for the Na,H-Rho zeolite series.

In Figure 5.22 the *Ft/M* plot of all the samples of the series offers an alternative way of comparing the difference in the CO_2 capacity among the samples. Notably the presence of more energetic sites in the fully exchanged Na-Rho (MML269) can be observed by the shape of the curves.

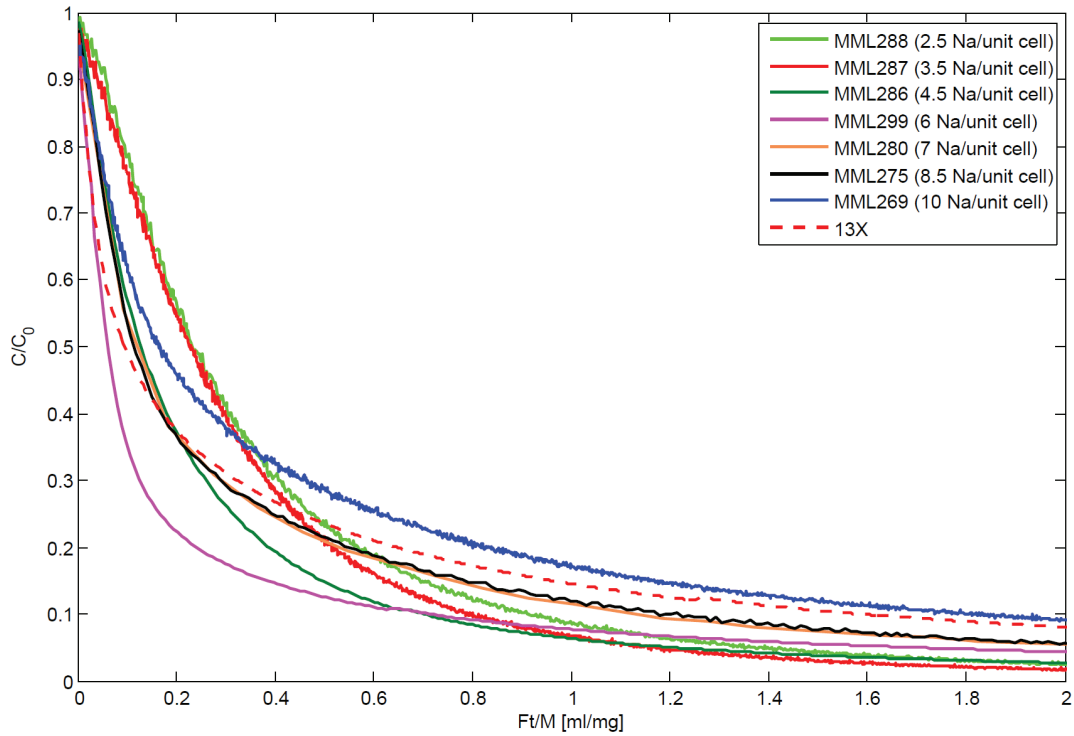

Figure 5.22: Ft/M plot for the Na,H-Rho series compared with zeolite 13X.

As an example, in Figure 5.23 and Figure 5.24, the ZLC desorption curves for the fully exchanged Na-Rho sample are shown. The plot of $ln(c/c_0)$ vs. time clearly shows that the desorption rate is slow, as a consequence of the hindering effect exerted by the Na atoms in the windows of the S8R ad S6R sites. The time needed to reach full saturation was about 3 hr and at least double of this time was need to complete the desorption. Because of the extremely slow kinetics of the sample the curves seem almost overlapping in the *Ft* plot. The presence of a kinetically controlled adsorption/desorption process was also detected from the small hysteresis observed in the type I isotherm measured at the University of St. Andrews [107]. A similar behaviour was also observed for the samples of the Na,H-Rho series at higher Na content, as it is possible to see from the plots in the Appendix A.

Detailed examinations of the desorption kinetics relative to the samples of the Na,H-Rho series were performed using the partial loading technique. The results of the investigation will be presented in the next chapter.

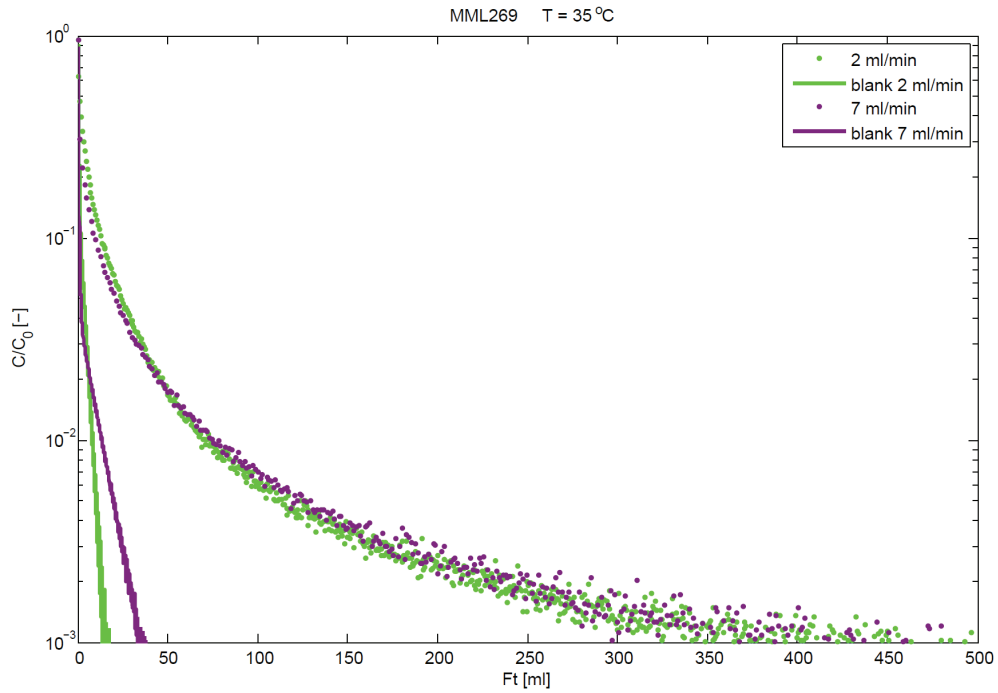

Figure 5.23: ZLC curves for the fully exchanged Na-Rho zeolite plotted as ln(c/c$_0$) vs.Ft.

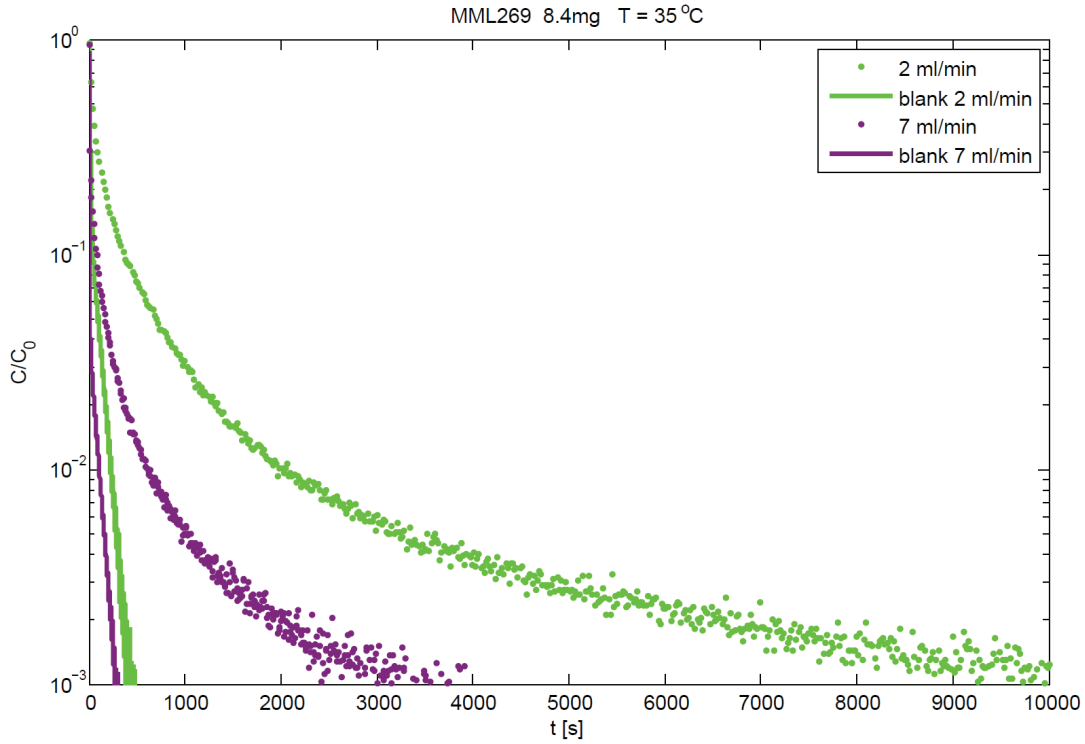

Figure 5.24: ZLC curves for the fully exchanged Na-Rho zeolite plotted as ln(c/c$_0$) vs. t.

5.1.2.2 Na,Cs- and K-Rho

Using the same synthesis routine applied to prepare the Na,H-Rho series also a sample of Na,Cs-Rho and one of K-Rho were prepared, namely MML313 and MML462. The Na,Cs-Rho is the as-prepared Rho precursor which was then fully exchanged to Na-Rho, while the K-Rho was prepared by exchanging K cation in NH_4-Rho.

Similarly to Na-Rho also the structure of Na,Cs-Rho shows a grade of distortion of the framework due to the presence of the Cs cations in the D8R sites and Na in the S8R sites [38, 107]. Also a recent work of Palomino et al. [38] reported the evidence of a change of the symmetry of the framework during the adsorption of CO_2 (above 1 bar) and, at higher pressures, also the displacement of the Cs from the D8R site to the S8R ones. As expected from the distribution of the cations in the structure no N_2 uptake was observed form the measurements carried out at the University of St. Andrews, while experiments on the volumetric system showed an appreciable CO_2 capacity [107], confirming that, at this temperature, the Cs and Na atoms can move from their original position to permit the diffusion of CO_2. The CO_2 isotherm reported by Araki et al. at 298 K [109] and the one measured at the University of St. Andrews are consistent with a value of about 2 mol/kg at 0.1 bar, and both are characterised by a noticeable hysteresis, like all the samples in which the cations occupy the sites in the windows of the α-cages. In Figure 5.25 and Figure 5.26, the desorption curves obtained from the ZLC experiments carried out on the sample are shown. Similarly to the Na-Rho zeolite, extremely slow kinetics is observed: the sample needed about 5 hr to reach the complete saturation before starting the desorption. The CO_2 capacity at 35 °C and 0.1 bar obtained for the samples is 2.13 mol/kg, which is consistent with the value measured at 298 K at the University of St. Andrews [107] and the one reported from Palomino et al. at [38] (about 1.8 mol/kg) and Araki et al. [109] at 303 K and 298 K, respectively.

The kinetics of adsorption was investigated in detail through the use of the partial loading technique and the results will be presented in the next chapter.

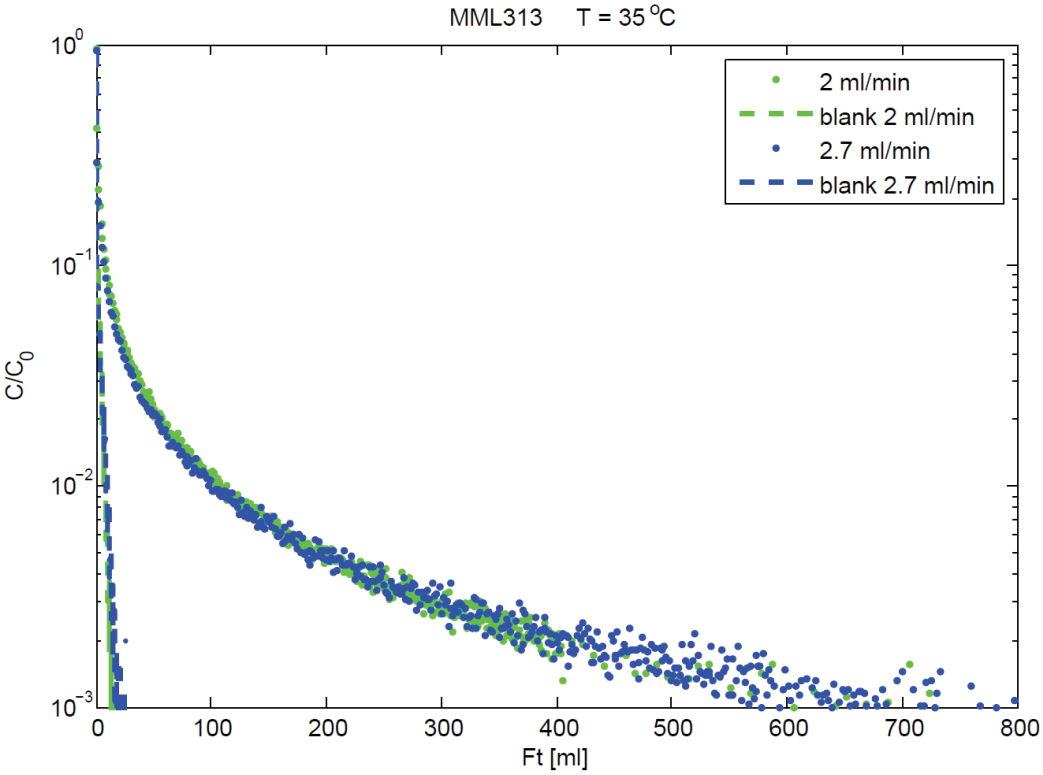

Figure 5.25: Plot of ln(c/c_0) vs. Ft of the ZLC desorption curves for the Na,Cs-Rho sample.

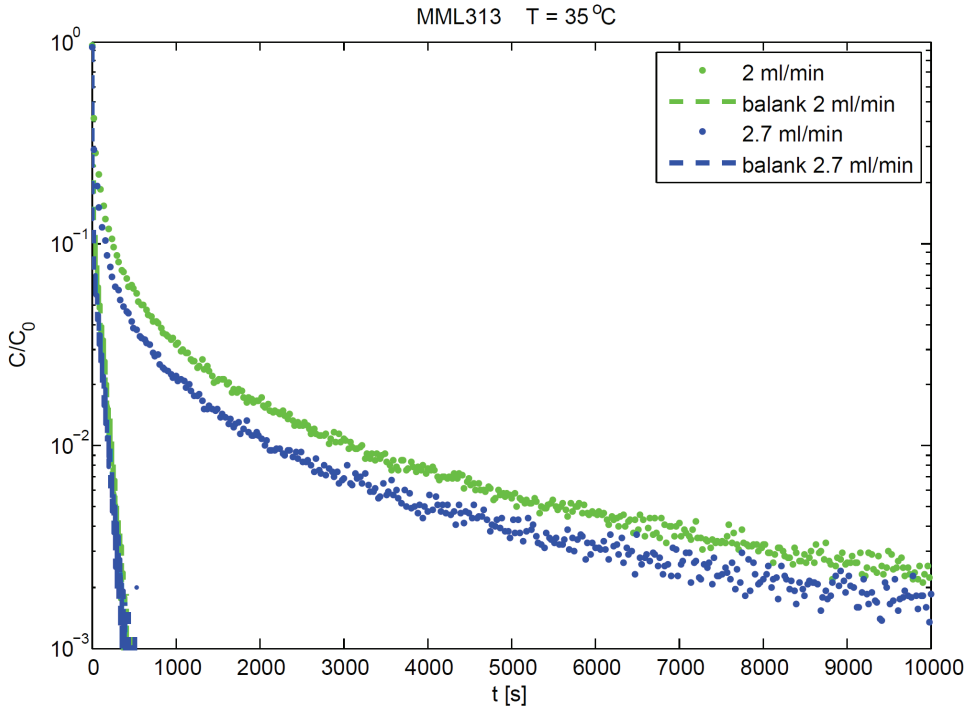

Figure 5.26: Plot of ln(c/c_0) vs. t of the ZLC desorption curves for the Na,Cs-Rho sample.

In the case of the K-Rho zeolite both the S8R and D8R sites are occupied so that at least one (but sometimes also two) cation per window can be found [107]. This greatly restricts the access to the cages and as a result a lower CO_2 uptake is observed compared to Na- and Na,Cs-Rho. The value obtained for the CO_2 capacity at 35 ˚C and 0.1 bar is 0.88 mol/kg which is in good agreement with the isotherm at 298 K measured at the University of St. Andrews [107]. Similarly to the other Rho samples investigated, the isotherm shows a noticeable hysteresis between the adsorption and the desorption branch which derives from the slow diffusion of CO_2 through the windows occupied by the K cations.

The presence of a kinetically controlled process is confirmed by the ZLC experiment shown in Figure 5.27 and Figure 5.28. The diffusion of CO_2 on this sample was investigated in detail and the results will be presented in the next chapter together with the kinetic measurements carried out on the other ion exchanged Rho zeolites.

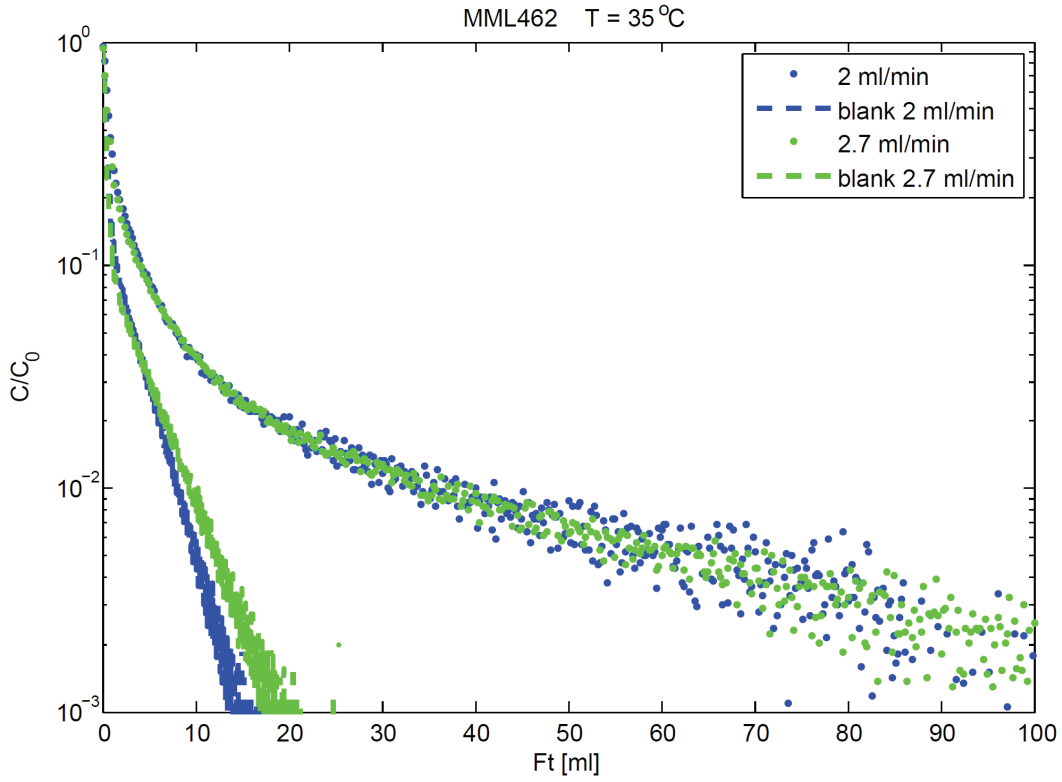

Figure 5.27: Plot of ln(c/c$_0$) vs. Ft of the ZLC desorption curves for the K-Rho sample.

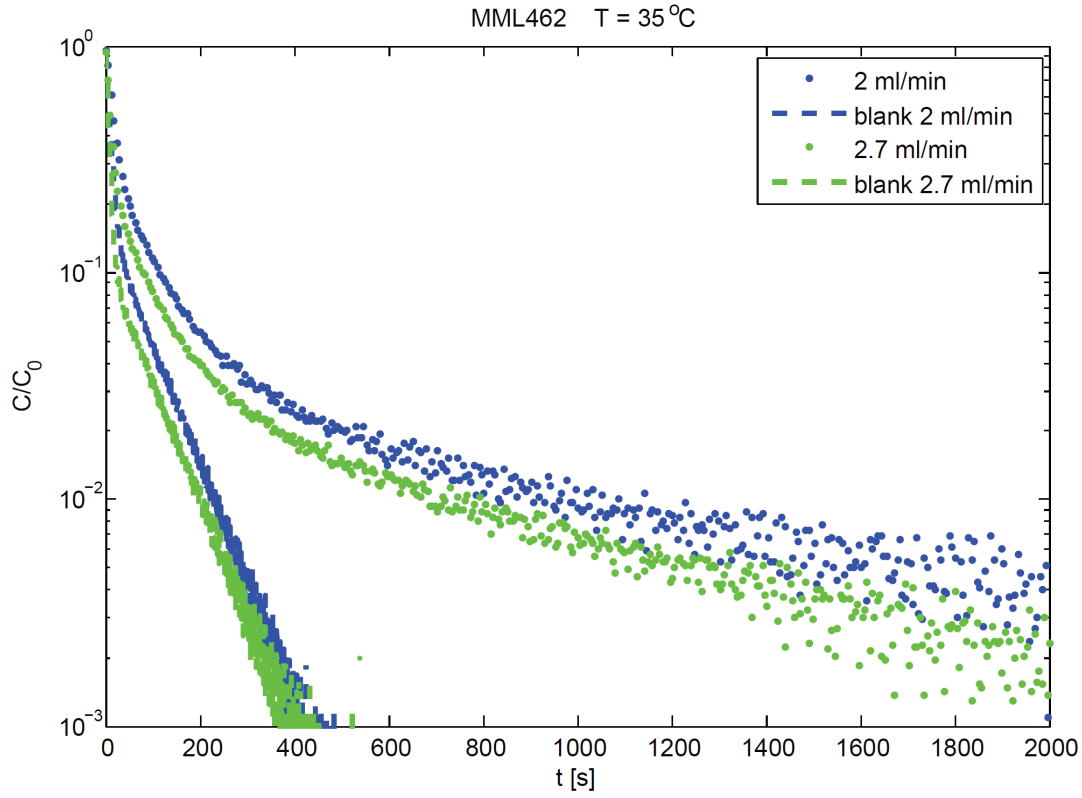

Figure 5.28: Plot of ln(c/c$_0$) vs. t of the ZLC desorption curves for the K-Rho sample.

5.1.2.3 Ca, H Rho

The samples of the Ca,H-Rho series were prepared by removing Ca from the fully exchanged Ca-Rho sample. The fully exchanged zeolites were synthesised by exchanging Ca in NH_4-Rho, the sample was then treated with NH_4Cl at different concentration to create sample with different Ca/H ratios. Similarly to the Na,H series, no uptake of N_2 is observed in the samples at higher Ca content (Figure 5.29). Langmi et al. suggested that the Ca cations are large enough to occupy the D8R sites, producing the complete blockage of the access to the cages [110]. This explains both the trend of the N_2 and CO_2 uptake (Figure 5.30). By increasing the Ca content of the samples, the blocking action of the Ca atoms in the D8R windows results in a low N_2 uptake, but the adsorption of CO_2 increases up to the point in which, for the fully

exchanged Ca sample, all the entrances to the cages are blocked and then a very small uptake of CO_2 is observed.

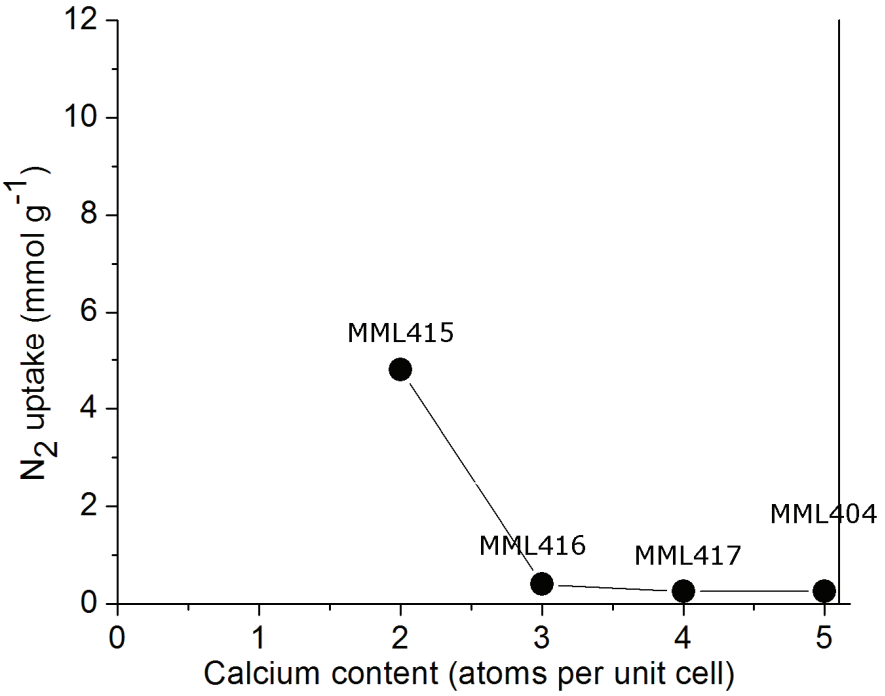

Figure 5.29:N_2 uptake at 77 K and 0.1 bar for the Ca,H-Rho series, measured at the University of St.Andrews.

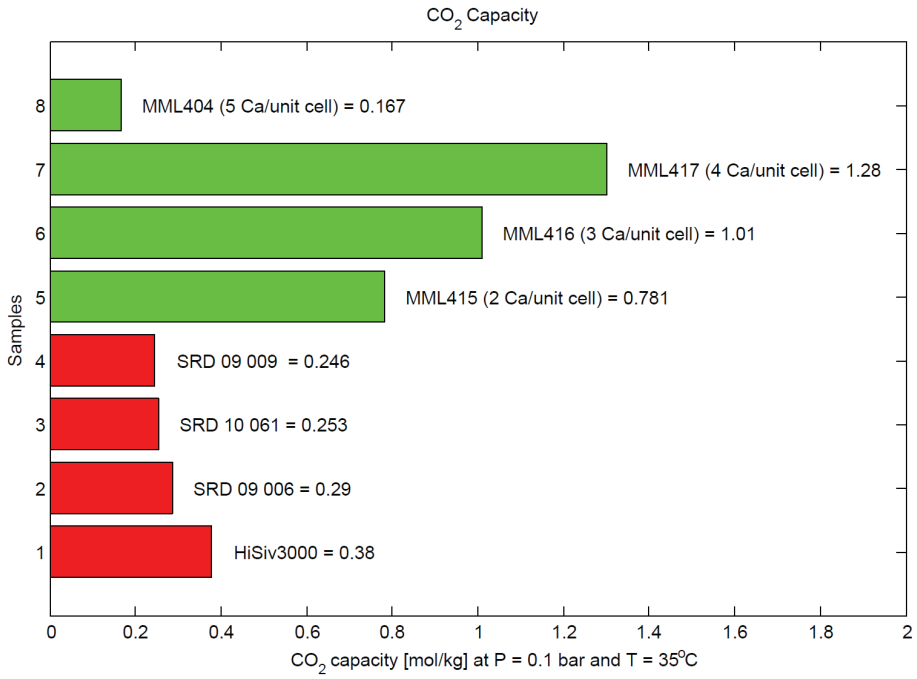

Figure 5.30: Ranking of the CO_2 capacity for the Ca,H-Rho zeolite series.

The maximum value of the CO_2 capacity obtained is higher than the one reported by Araki et al. [109] (about 0.4 mol/kg). The difference derives from the different Ca content: the samples tested by Araki et al. have a higher Ca content which makes the structure more close causing a lower uptake.

In Figure 5.31 the *Ft/M* curves area shown for all the samples of the series; due to the relatively low value of the capacity the desorption curves are compared with the ones of the HiSiv3000 and the activated carbons. The ZLC curves for the single samples are shown in Appendix A.

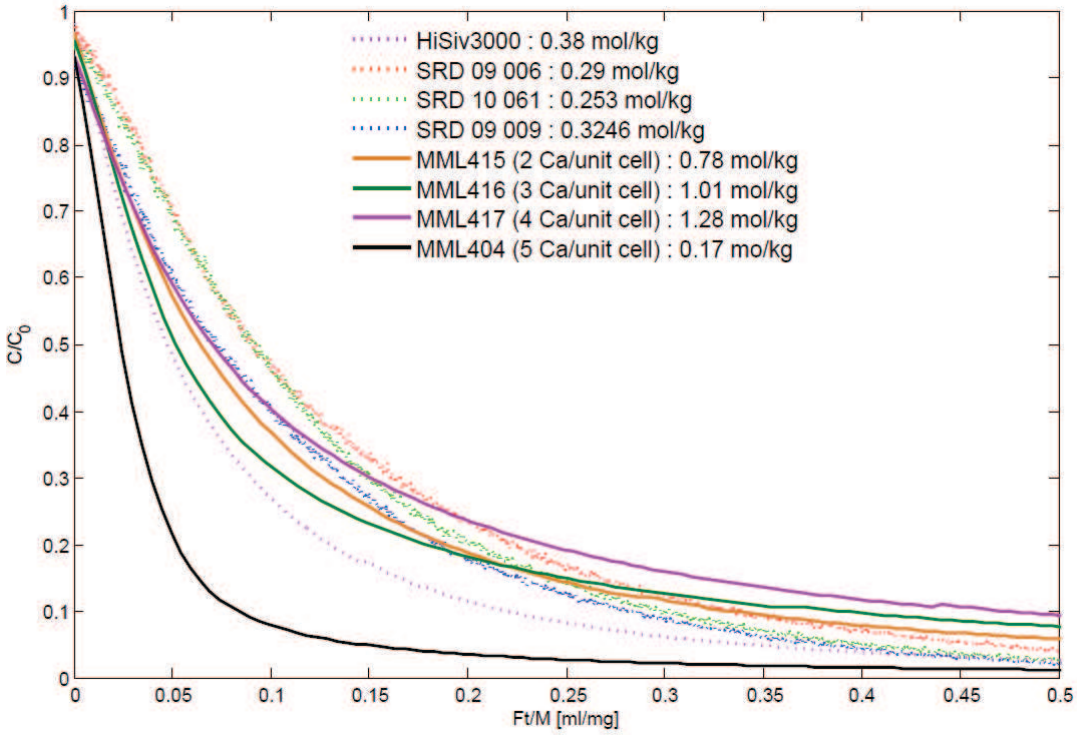

Figure 5.31: Ft/M plot for the Ca,H-Rho series with relative uptakes.

5.1.2.4 Steamed H-Rho zeolites

In this section the results of the ZLC experiment on some H-Rho zeolites are presented; the samples were subjected to hydrothermal treatment to increase the thermal stability and the hydrophobicity by reducing the Al/Si ratio. The samples

were prepared by fully exchanging Cs-Rho with NH_4Cl; the resulting NH_4-Rho is treated at high temperature to obtain H-Rho. The as-prepared sample is then subjected to post-synthesis hydrothermal treatment consisting of heating the sample to high temperature in the presence of N_2 and water. The process allows to remove Al atoms from the framework which may be substituted by Si units. This increases the thermal stability and the hydrophobicity of the material, but, on the other hand, it can also increase the acidity of the framework and some adsorption sites can be lost [111].

Figure 5.32 shows the ranking as *Ft/M* plot with the CO_2 capacities for the different samples steamed at different temperatures. The CO_2 capacity is relatively low and in the range of values reported for similar H-Rho zeolites [107, 109].

The increase of the steaming temperature seems to decrease slightly the CO_2 capacity, probably due to the loss of adsorption sites, while the two samples steamed at 470 °C seem to be not affected by the use of a fast flow of water.

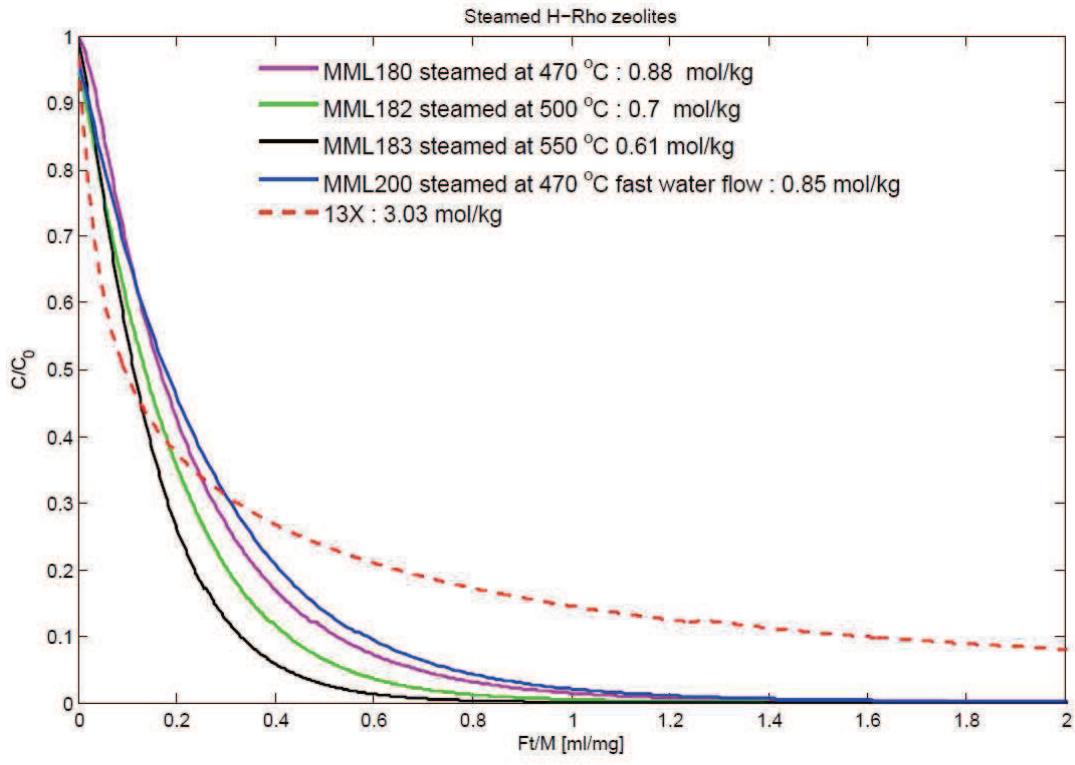

Figure 5.32: ZLC desorption curves plotted as Ft/M, for -Rho zeolites steamed at different temperatures with relative adsorption capacity.

As an example, in Figure 5.33 the ZLC curves for one of the H-Rho samples are shown. The curves overlap in the *Ft* plot and approach a straight line in the logarithmic scale indicating a fairly linear CO_2 isotherm for this sample.

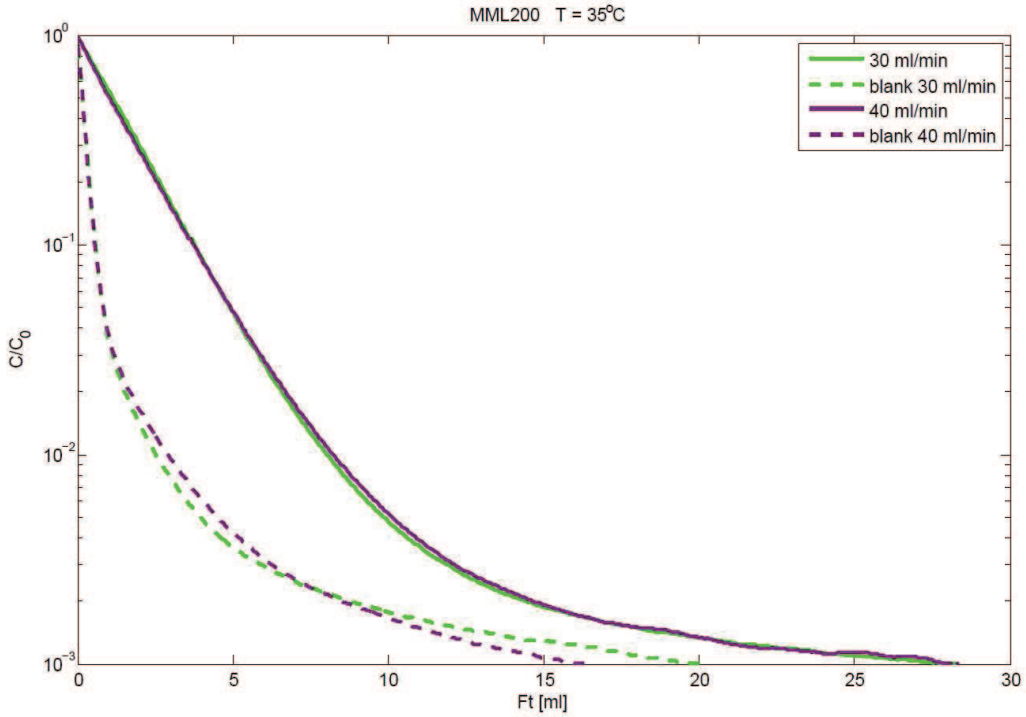

Figure 5.33: ZLC curves for one of the steamed H-Rho zeolites.

5.1.3 H- and K- ZK-5

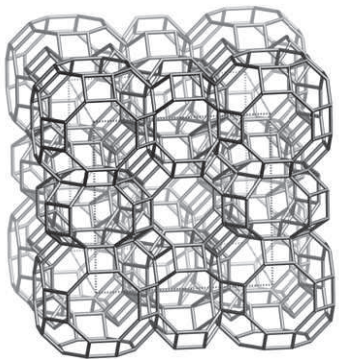

Figure 5.34: Framework structure of zeolite ZK-5[35].

Beside the different Chabazite and Rho zeo-types, another promising class of zeolites is represented by the ZK-5 (KFI structure code). Figure 5.34 shows the framework structure of ZK-5 zeolite which consists of two types of cages (large "α-cages" and small "γ-cages") interconnected by eight-membered oxygen rings with a diameter of 3.9 Å [35]. This results in a material characterised by a high grade of crystallinity and high pore volume. Moreover the framework is rich in K cations which can be exchanged. The K cations generally occupy the sites in the eight-membered rings and in the hexagonal prisms which interconnects the α-cages [112].

At the University of St. Andrews K-ZK-5 (MML239) was synthesised as reported in the literature [112a]. The fully exchanged H-ZK-5 sample was made by first treating MML239 with NH_4Cl and finally heating to remove the NH_4^+ cations.

Figure 5.35 and Figure 5.36 show the desorption curves obtained from the ZLC experiments for K-ZK-5 and H-ZK-5. Due to the larger size of the K cations a higher free volume is associated to the H form of the ZK-5 zeolite, but as a result of the stronger electrostatic field, a higher CO_2 capacity is observed for the K-ZK-5 sample. Furthermore the *Ft* plot of the ZLC curves for K-ZK-5 shows that the process is equilibrium controlled, indicating that the K cations are blocking the entrances to the cages. On the other hand the H-ZK-5 sample shows a kinetically-controlled desorption, as it is possible to notice from the ZLC curves displayed in Figure 5.36. This can be due to the possible deformations in the framework induced during the

ion exchanging process from the K- form to the H- form which may restrict the passage of the CO_2 molecules through the pores, as reported by van Well et al. [112b].

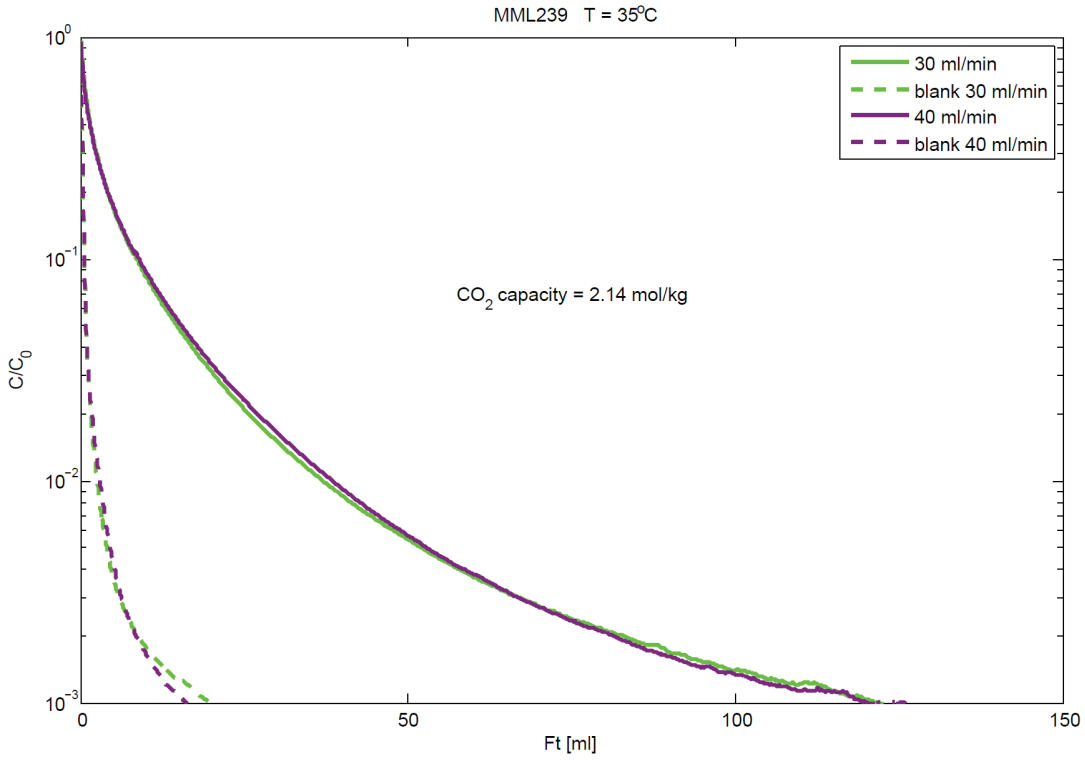

Figure 5.35: ZLC desorption curves for K-ZK-5 zeolite

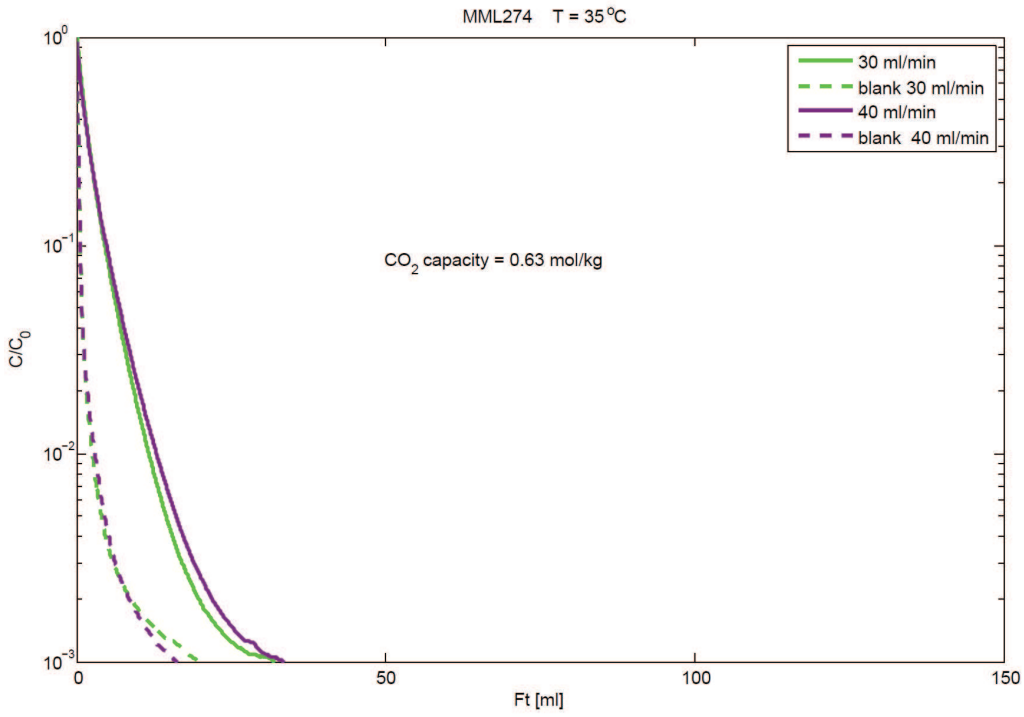

Figure 5.36: ZLC desorption curves for H-ZK-5 zeolite

5.1.4 ITQ-13 and Na-Y

ITQ-13 is a relatively new zeolite structure (ITH structure code) introduced by Corma at al. in 2003 [113]. The structure is characterised by the presence of three sets of intercrossed medium-pore channels with different sizes: a 9-ring channel (4.0 x 4.9 Å), and two sets of 10-ring channel (4.8 x 5.7 Å) and (4.7 x 5.1 Å), respectively [35, 113]. The sample was synthesised according to the procedure reported by the authors and from the ZLC experiment a relatively low uptake was observed with a value of 0.26 mol/kg, Figure 5.37. No literature data were found to compare the result obtained.

In Figure 5.37 the ZLC curve of a sample of commercial Na-Y is also displayed. The sample was used in the synthesis of all the Chabazite samples. The value obtained for the CO_2 adsorption is 2.25 mol/kg which is coherent with what reported in literature [11b, 31, 114].

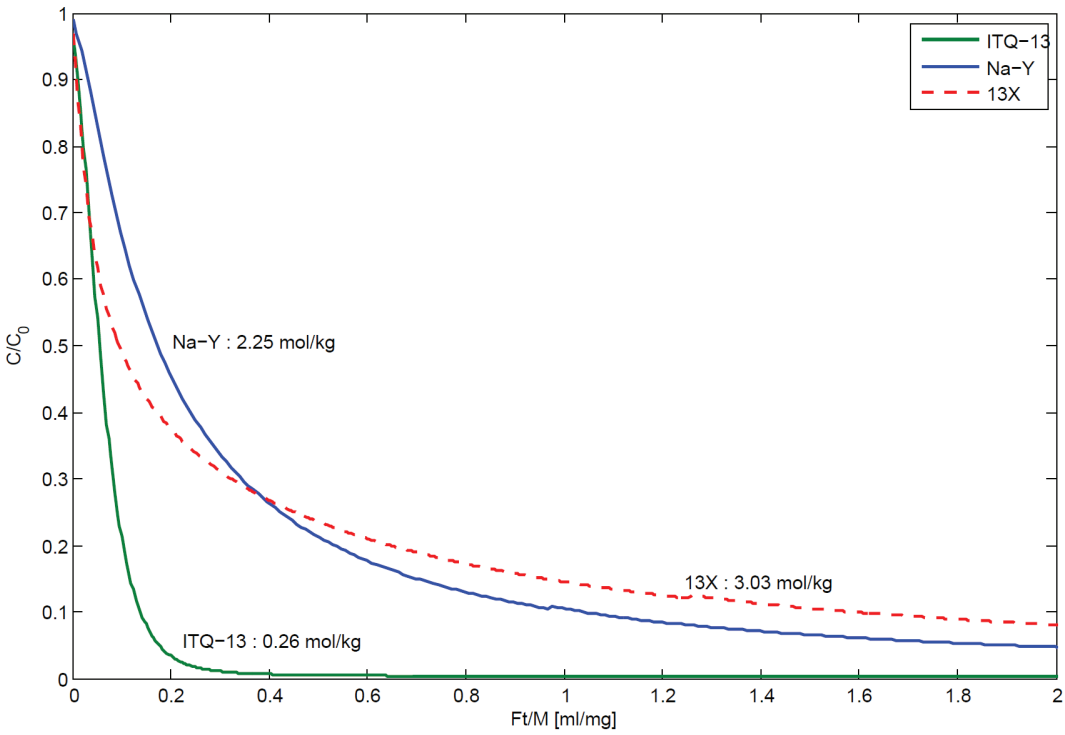

Figure 5.37: ZLC curves of ITQ-13 and Na-Y plotted as Ft/M, compared with 13X.

5.1.5 Conclusions

A wide range of ion exchanged zeolites were tested using the ZLC technique. Most of the investigation was focused on the different samples of Chabazite and Rho zeolites exchanged zeolites. The effect on the CO_2 adsorption resulted to be a complex function of the charge density, the distribution in the framework and the pore volume.

With regard to the Chabazite samples, series at different K-, Na- and Ca- content were investigated. Regardless of the nature of the cations, the CO_2 uptake increased with the cationic content for all the series, mainly due to the increased electrostatic interactions. The sequence of the CO_2 capacity observed was as follows: $Li^+ \sim K^+ > Na^+ > Ca^{2+}$, which is different from what reported by Webley et al. that observed a CO_2 decrease with the increase of the cationic radii: $Li^+ > Na^+ > K^+$. One possible explanation might be that the samples tested in the present work were not completely dry, the regeneration temperature suggested from the University of St. Andrews for these samples was 200 ˚C, but from later measurements at the University of St. Andrews it was found that for the Chabazite and Rho samples a regeneration temperature of 350 ˚C should be used to ensure complete dehydration.

The Rho samples were all re-tested because they needed to be included in a joint paper [107] and for some of the a slight increase of the adsorption capacity was observed. The Chabazite samples were not re-tested but it would be worth to repeat the experiment especially for the samples at higher capacity. Moreover the Li-Rho sample was not included in the ranking because from the partial loading test it was observed that the capacity was higher than for the full saturated sample (see Chapter 5). This indicated the presence of very small amount of water in the system which affected the capacity of Li-Rho which is very sensitive to water. This may explain why the Li Chabazite did not show a higher capacity relative to the K form.

With respect to the CO_2 capacity of the Rho samples the trend observed was as follows: $Na^+ > Na,Cs > Ca > K \sim H$, which is consistent with what reported by Araki et al. [109]. Due to the flexibility of the framework and the small size of the windows the presence of the cations greatly restricted the access to the cages, and, as a result, a very slow adsorption kinetics was observed for Na, Na,Cs and K-Rho. The detailed

analysis of the diffusion process of CO_2 in the ion exchanged Rho zeolites will be discussed in chapter 6.

5.2 MOFs

In this section the results of the ZLC experiments carried out on the MOF samples are presented and discussed. The adsorbents were all synthesised at the University of St. Andrews by the research groups of Prof. R. Morris and Prof. P. A. Wright.

The work at the University of St. Andrews was mainly focused on the investigation of methods to increase the CO_2 uptake of MOF74 [CPO-27 (Ni, Mg)] by modifying the porosity and the composition of the materials.

In the synthesis of CPO-27, an organic ligand is de-protonated by a base (usually THF) to allow the coordination with an unsaturated metal, dissociated from a salt added to the solution; precipitation is finally induced to separate the resulting material from the solution. From the basic description of the synthesis procedure it is easy to see how the framework type, the porosity and the density of metal sites in the framework greatly depend on the ligand used, the ratio of the base and the salt in the reactive solution.

At the University of St. Andrews several CPO-27 samples were developed starting from the general procedure described in literature[39, 115], and this was followed by introducing modifications of some of the crucial parameters of the synthesis. As a result several Mg-CPO-27 and Ni-Mg-CPO-27 samples were produced using different organic and inorganic ligands, different ligand/base ratios, and Mg/Ni content.

Furthermore, in order to enhance the adsorption performance, some of the resulting samples were also subjected to post-synthesis treatments to increase the final porosity of the materials. These consisted in the use of inorganic acids on the surface of the samples to open up the pores, facilitating in this way the access of CO_2 and enhancing the overall porosity. The activation procedure was also repeated more than once to investigate the resulting changes in the structure.

Beside the synthesis of CPO-27, other novel types of MOFs were synthesised for the first time and developed at the University of St. Andrews: ScBDC samples with amine functionalised groups, Sc-ABTC, STA-12 (Ni, Mg, Co) and STA-16-Co.

In table 5.3 all the MOF samples tested on the ZLC system are listed. Due to the number and the different types of samples, this section will be organised in an overview of all the samples followed by a separate discussion for the CPO-27 sample and the novel MOFs, in which the effects of the different modifications will be analysed.

Table 5.3: List of the samples tested. (*) TGA not available. (**) Pellet form.

Name	SAMPLE	Amount tested [mg]
JK43A	ScBDC pure Sc_2	9.2
JK44B	ScBDC 100% Amine functionalized	11.8
JK45A	ScBDC 50% Amine functionalized	10.1
JMEX301	STA-12(Ni)	8.33
JMEX342	Sc-ABTC (calcined at 200 ˚C)	6.93
JMEX 433	MIL-100(Sc)	7.1
JK33A	Ni-CPO-27	13.3*
JK34D	Mg-CPO-27	9.5
JK34A not activ.	Mg-CPO-27 (as prep. / not activated)	6.3*
JK34A	Mg-CPO-27 (activated in water)	8.9*
JK34M	Mg-CPO-27 (modified)	5.6*
JK-34N	Mg-CPO-27 (heated in vacuo at 250 ˚C for ~16h)	7.5*
JK53R	Mg-CPO-27 (modified)	5.9*
JK53Y	Mg-CPO-27 (modified)	4.9*
JK53Z	Mg-CPO-27 (modified)	7.4*
JK53G	Mg-CPO-27 (modified)	14.6*
JK61J	Mg-CPO-27 (modified)	6.2*
JK61K	Mg-CPO-27 (modified)	7.3*
JK61B	Mg-CPO-27 (modified)	6.4*
JK61V	Mg-CPO-27 (modified)	7.1*
ACM1	Mg-CPO-27	5.97
ACM2	Mg-CPO-27	10.9*
ACM3	Mg-CPO-27	10.3*

ACM4	Mg-CPO-27	10*
MTW622	STA-12(Mg)	7.5*
MTW559d	STA-16(Co)	4.1*
LM303	STA-12(Co)	14.1*
13X**	Zeolite 13X (UOP)	13.6

Figure 5.38 shows the overall ranking of all the MOFs tested with the relative CO_2 capacities compared with zeolite 13X as benchmark material. From the plot it can be easily seen that most of the modifications performed on the Mg-CPO-27 samples were successful producing samples with a capacity higher than the benchmark. The best samples are JK-61B and JK-61V with a CO_2 capacity of 6.23 and 5.34 mol/kg, respectively. The discrepancy between samples with the same composition and framework type indicates how the final performance of the samples can be influenced significantly by changing crucial parameters in the synthesis routine.

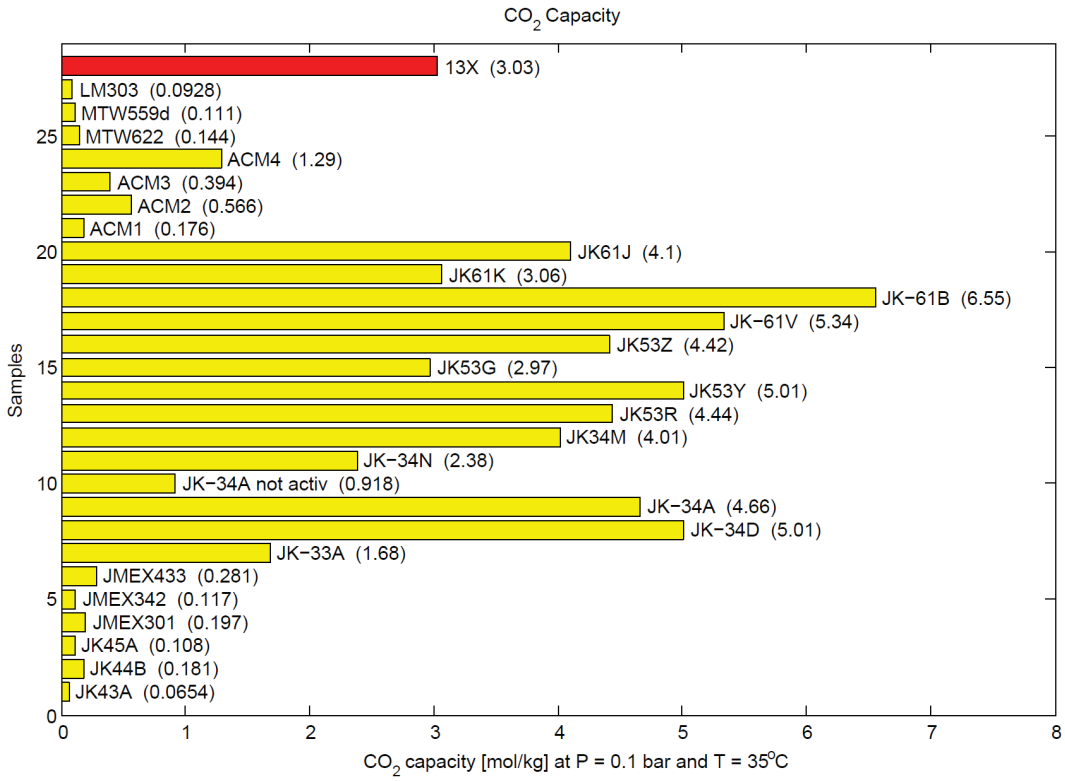

Figure 5.38: Ranking of MOF samples for carbon capture.

Figure 5.39 is an alternative way to appreciate the difference in CO_2 capacity among the samples. The plot is basically a *Ft* plot normalised by the mass of the sample used in the experiment: in this way the desorption curves can be directly compared. This plot does not rely on any manipulation of the ZLC data and shows how the experiment can be used as an effective tool to compare similar adsorbents. The plot shows clearly the difference in capacity, i.e. area under the curves, while the shape of the desorption curves gives very useful information on the performance of the sample from a process point of view.

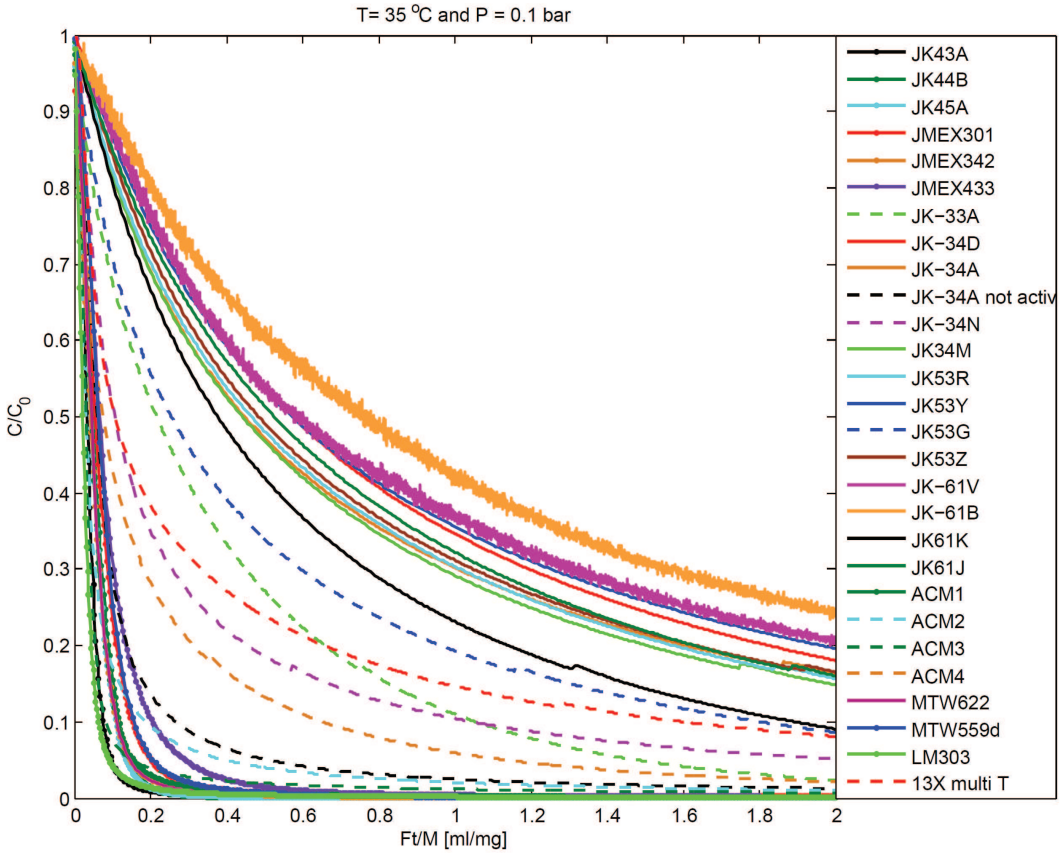

Figure 5.39: Ft/M plot for al the MOF sample tested.

5.2.1 Novel MOF samples from the University of St. Andrews

Figure 5.40 and Figure 5.41 show the ranking plot and the Ft/M plot of the materials that will be discussed in this section.

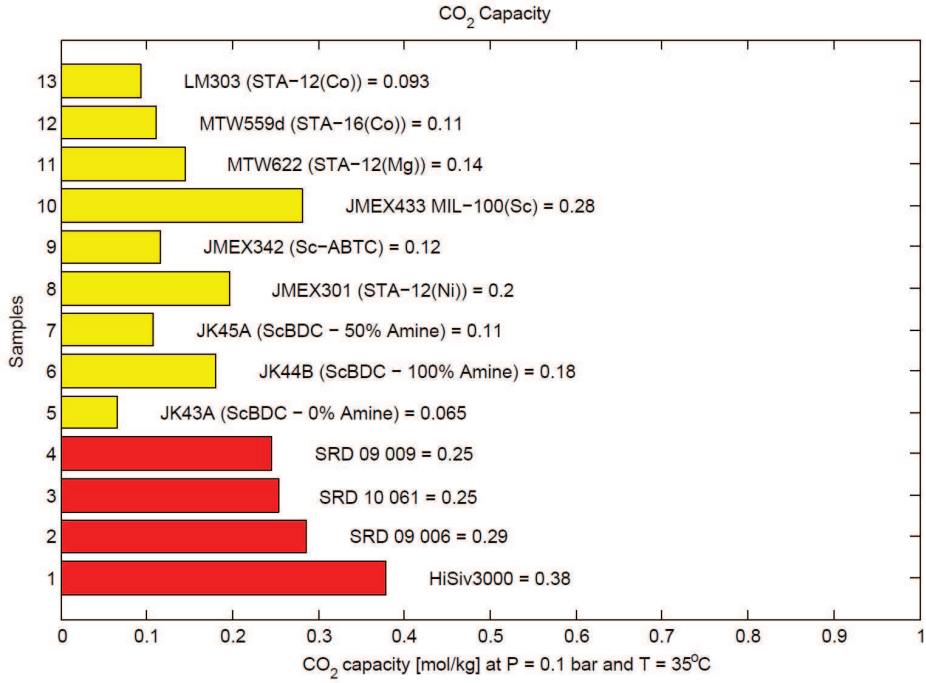

Figure 5.40: Ranking of novel MOFs invented at the University of St. Andrew. The samples of interest are ScBDC, ScABTC, STA and MIL-100.

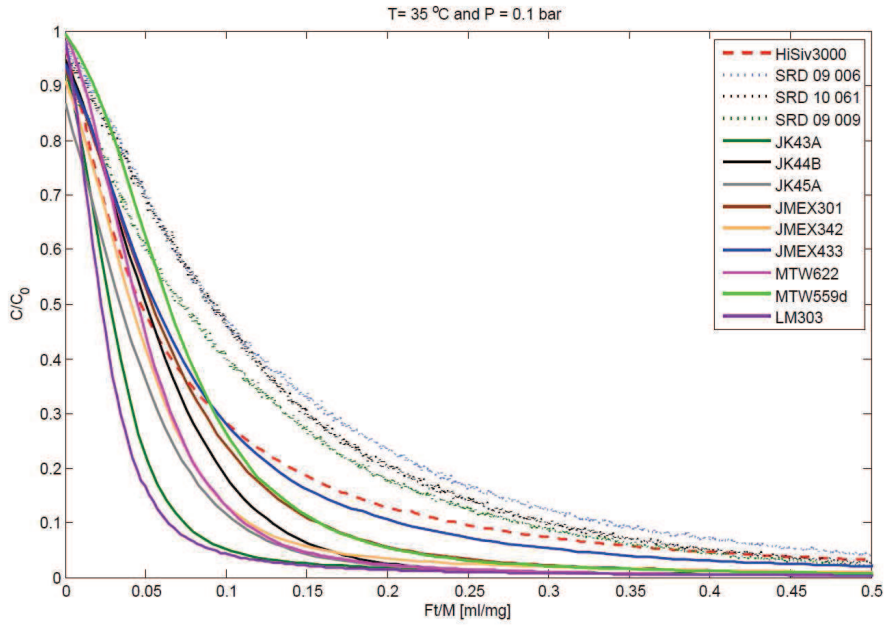

Figure 5.41: Ft plot normalised for the weight of the samples. The samples of interest are ScBDC , ScABTC, STA and MIL-100.

Among all the MOF samples tested there were two novel classes of materials, synthesised for the first time at the University of St. Andrews, namely ScBDC (BDC=1,4-benzenedicarboxylate) and STA (St. Andrews porous material).

ScBDC is a scandium terephthalate framework, constituted by interconnected chains of isolated ScO_6 octahedra, which create a system of channels with triangular cross sections of around 3 Å (Figure 5.42).

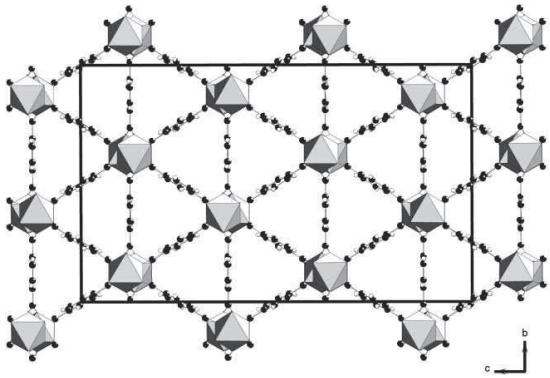

Figure 5.42: The framework compound ScBDC: ScO_6 units are represented as grey octahedral [116].

The framework does not present uncoordinated metal sites or hydroxyl groups and for this reason no thermal treatments for water removal are required. Furthermore the small size of the channels does not allow the access of water which makes the sample highly hydrophobic [116-117].

The ScBDC samples synthesised for this project were functionalised with different content of amine groups, namely 0, 50 and 100% as shown in table 5.3. The value of the CO_2 capacity obtained for the non-functionalised sample is coherent with the CO_2 isotherm at 304 K reported by Miller et al. [117].

As expected the capacity increases with the amine content reaching a value about three times higher the one of the non-functionalised sample: 0.11 and 0.065 mol/kg, respectively.

In addition to the ScBDC samples, two other types of microporous carboxylates, MIL-100 (Materials of Institut Lavoisier) and ABTC (azo-benzene-tetracarboxylate), were synthesised for the first time using SC^{3+} as metal site [118]. The trend of the CO_2

uptake for the three carboxylates follows the same sequence of the porosity, MIL-100(Sc) > Sc-ABTC > ScBDC, as reported by Mowat et al. [118] who measured the N_2 uptake and the CO_2 isotherms for the same samples at 196 K.

The Ni-STA-12 is a highly porous solid with channels of about 1nm in diameter. Dehydrating the sample results in freeing the channels from the molecules of water increasing greatly the CO_2 uptake [119]. The framework is characterised by a honeycomb arrangement built by helical chains of edge-sharing NiO_5N octahedral, Figure 5.43.

The STA-12 MOF type was synthesised with differently exchanged metal sites, Ni, Mg and Co. The CO_2 capacity obtained for the STA-12 samples decreases according to the sequence: Ni-STA-12 > Mg-STA-12 > Co-STA-12, while from the data reported by Wharmby et al. [120] the Mg form exhibited a CO_2 capacity at 195 K slightly higher than the Ni sample.

The synthesis of Co-STA-16 follows the consideration that the structure of STA-12 exhibit the possibility to be extended by using a linker with a longer chain [121]. The N,N'-piperazinebis can be then substituted with a 4,4'-bipiperidine. As a result the pore diameter is doubled relative to the STA-12 (Figure 5.43) and the pore volume is higher relative to a crystalline metal phosphonate [121]. The higher pore volume of the Co-STA-16 explains the higher CO_2 uptake observed if compared to the analogue Co-STA-12.

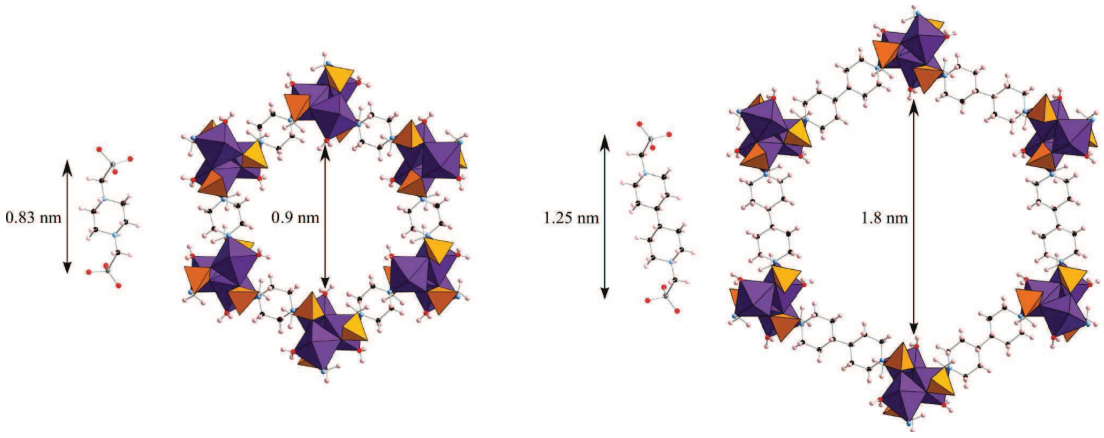

Figure 5.43: Comparison between the frameworks of STA-12 (left) and STA-16 (right)[121].

Due to the low uptake of the samples the ZLC desorption curves resulted too close to the blank to be further investigated with regard to the equilibrium and kinetics of adsorption.

5.2.2 CPO-27 samples

Table 5.4 shows the different series of CPO-27 samples prepared. The samples consist in different Mg and Ni-CPO-27 samples prepared by following the general procedure as described in literature[115b, 122]. In the case of Mg-CPO-27 the solvothermal synthesis was performed at 110 ˚C for 3 days and involved the use of Mg-nitrate (metal source) and 2,5-dihydroxyterephtalic acid. Once synthesised, the samples were then modified by adding nickel and different ligands (carboxylates, imidazolates, phosphonates or phosphorous acid) in different amounts, as shown in the scheme of Figure 5.44. The activation procedure normally consists in immersing the sample in water over a few days and heating in vacuum at 250 °C for 18 hr. Based on the details of table 5.4 each series of samples is the result of attempts of improving the adsorption performance by changing one of the key parameters of the synthesis. The discussion of the results obtained will be then organised following the same criteria.

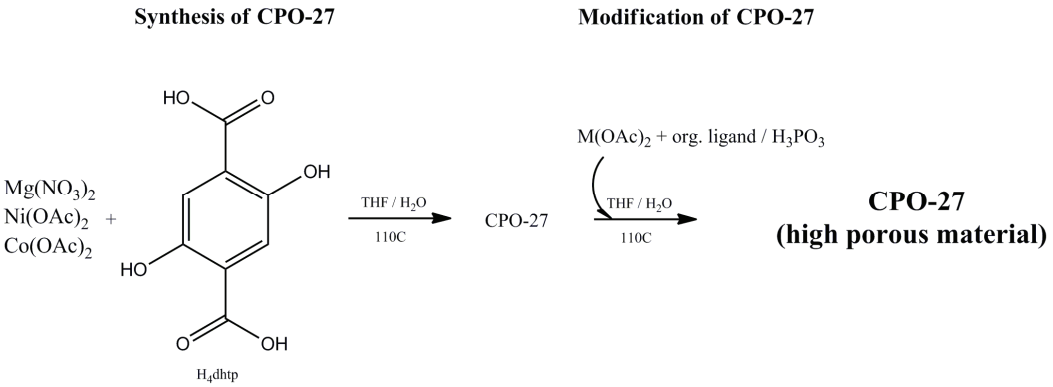

Figure 5.44: Reaction scheme for the synthesis of Mg-CPO-27.

Table 5.4: List of the CPO-27 MOF samples with details on the modifications applied

CPO-27		Material	Additives		
Label		M-CPO-27	Ligand additive	% nickel additive	% Ligand additive
JK34	A (not activ.)	Mg^{115b}	**no additive (not activated)**		
	A	Mg	**no additive (activated in water)**		
	D	Mg	**Carboxyphosphonate**	10	10
	M	Mg	**Carboxyphosphonate**	10	10
	N	Mg	**no additive (activated in vacuo at 250 ˚C -16 h)**		
JK53	G	Mg	**Carboxyphosphonate**	10	10
	R	Mg	**Piperazine**	10	10
	Y	Mg	**Bipiperadine**	10	10
	Z	Mg	**Piperazine**	10	10
JK61	B	Mg	**Carboxyphosphonate**	5	5
	J	Mg	**Carboxyphosphonate**	30	10
	K	Mg	**Carboxyphosphonate**	50	10
	V	Mg	**Carboxyphosphonate**	10	10
JK33	A	Ni^{122}	**No additive**		
ACM	1	Mg	**No additive**		
	2	Mg	**No additive**		
	3	Mg	**No additive**		
	4	Mg	**No additive**		

5.2.3 Effect of the activation method (JK-34 series)

The samples of the JK-34 series are all Mg-CPO-27: the as-prepared sample was activated in water and in vacuum at 250 ˚C, and two more samples were subjected to post-synthesis treatments using carboxyphosphonate acid as ligand and Ni as shown in Figure 5.44.

From the CO_2 capacity obtained for the different sample it can be seen that the activation procedure notably improves the adsorption performances opening up the pores and allowing the adsorption of higher amount of CO_2. Between the two activation methods it seems that the activation in presence of water has more benefits

than the normal activation in vacuum at high temperature with a capacity doubled relative to the one activated in vacuum. Probably a longer activation time was needed to activate all the adsorption sites.

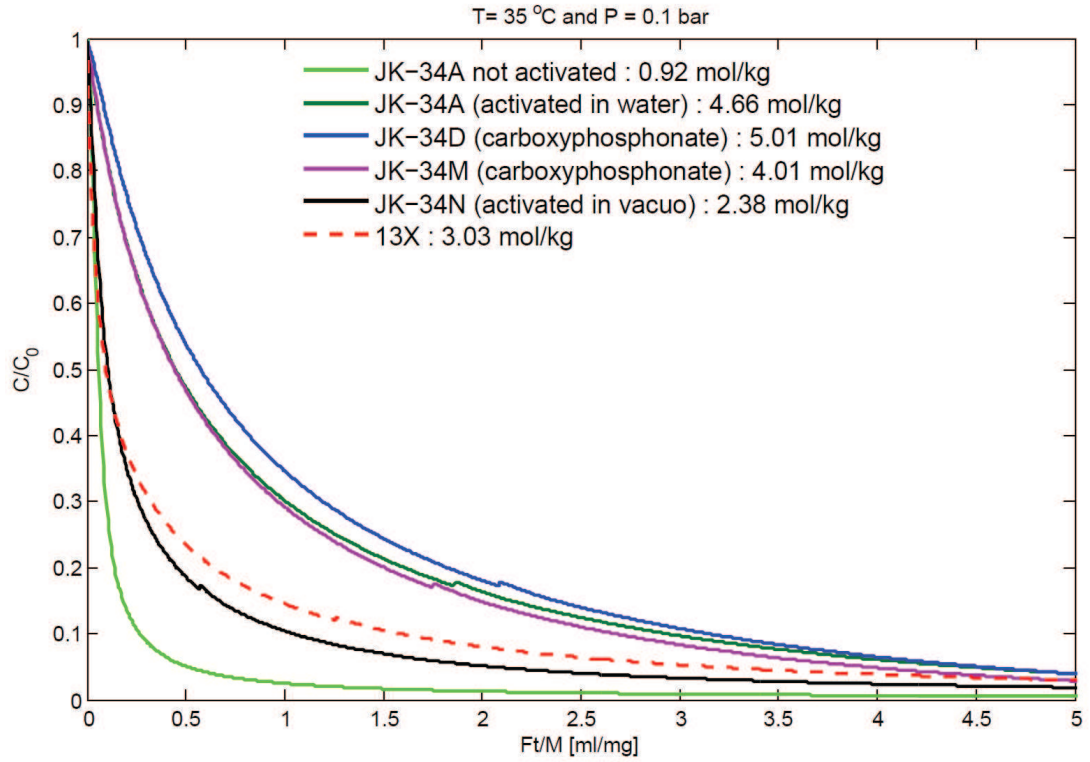

Figure 5.45: Plot of the ZLC curves for the JK-34 series of Mg-CPO-27 as c/c_0 vs. Ft/M with relative CO_2 capacity.

The treatment with carboxyphosphonate-based additive clearly improved the performance of the samples: one of the two modified samples resulted to be the best of the series with a capacity of 5 mol/kg. The treatment was tried twice to check the reproducibility of the results. Measurements performed at the University of St. Andrews showed evidence that most of the additive does not go into the pores but it is present just onto the surface creating extra porosity. Furthermore the presence of Ni should increase the affinity with CO_2. In the case of the samples D and M the N_2 uptake was lower for the sample D (6 mmol/g) than for M (9.5 mmol/g), but the sample D exhibited a higher Ni content which resulted in a higher CO_2 uptake. All this reflects the difficulty in predicting and reproducing modifications on Mg-CPO-27 with this type of ligand.

All the ZLC experiments, as expected from the relatively large pore size of CPO-27 (11-12 Å [39, 42]), resulted to be clearly equilibrium controlled. As an example, in

Figure 5.46, the ZLC desorption curve for the best sample is shown. The trend of the ZLC response in semilog scale is linear almost in all the range of concentrations, indicating a fairly linear CO_2 isotherm in the range of interest.

A high CO_2 capacity is desirable for a good adsorbent for CO_2 capture from flue gas streams, but what is more important is the working capacity, which depends on the ability to desorb CO_2, and for this one needs the shape of the isotherm. Fast adsorption/desorption kinetics are required to reduce the cycle time of the PSA process and a linear equilibrium isotherm helps to reduce the energy requirements. Under equilibrium conditions, as shown in the previous sections, the *Ft* plot of the desorption curve approaches a clear exponential decay.

The CO_2 isotherm for the best sample of the series was extracted from the integration of the ZLC response and it is shown in Figure 5.56 (at the end of the section) which displays the CO_2 isotherms for the best MOF samples.

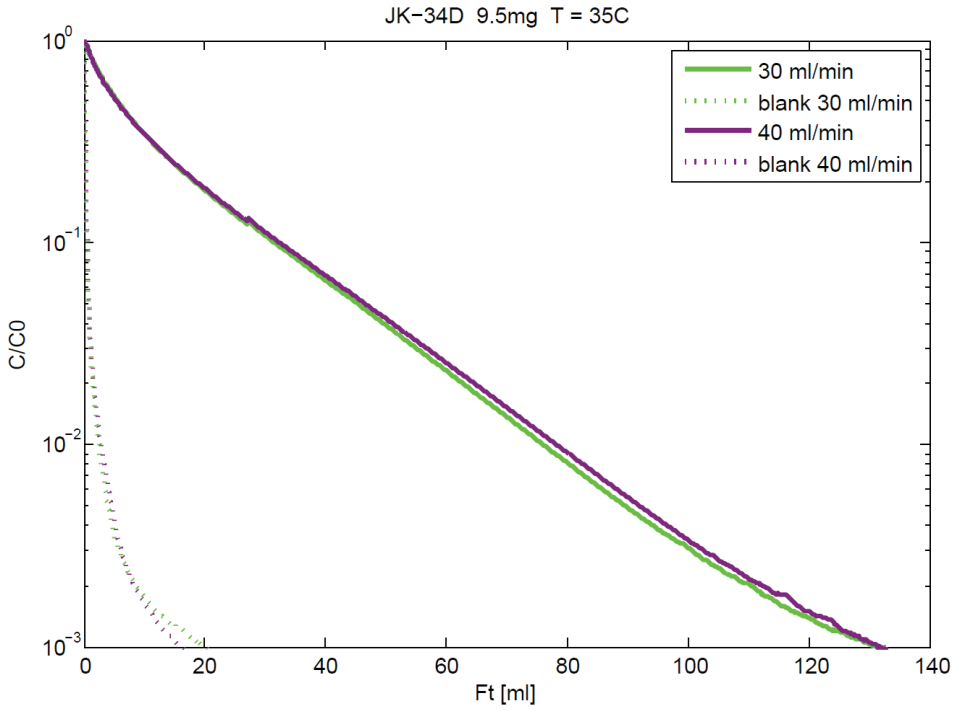

Figure 5.46: ZLC desorption curves at different flowrates for the best Mg-CPO-27 (JK-34D) of the series.

5.2.4 Effect of the ligand additive (JK-53 series)

In making the samples of the JK-53 series the main purpose was to investigate the effect of using different additives in the synthesis of Mg-CPO-27. The ligands used were carboxyphosphonate, piperazine, and bipiperadine. In Figure 5.47 the ZLC curves for the samples investigated are shown. For the sample JK-53G for which carboxyphosphonate was used as ligand, the synthesis was modified trying to scale up the process: this could have produced a less crystalline sample which can explain the loss of adsorption capacity if compared with the similar samples from the JK34 series. The sample prepared using the Piperadine-based ligand showed a very good reproducibility with a capacity of 4.4 mol/kg for both the samples prepared. The sample which exhibited the highest capacity is the one made using the Bipiperadine-based ligand, with a capacity of 5 mol/kg.

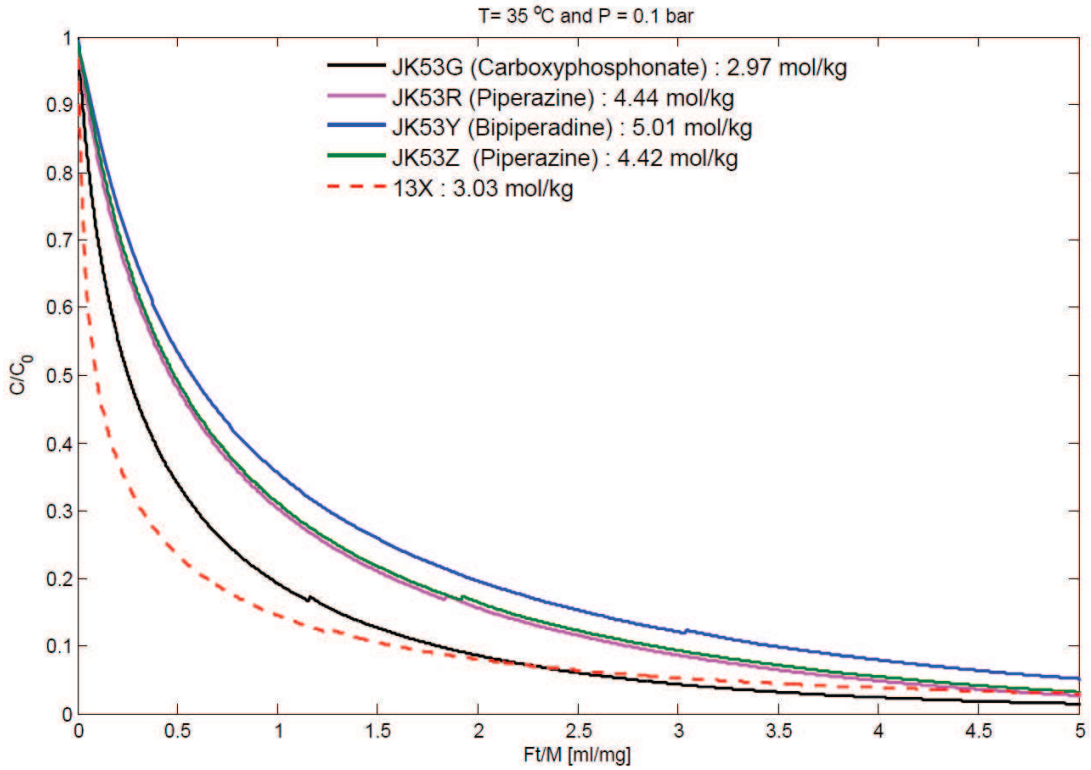

Figure 5.47: Plot of the ZLC curves for the Mg-CPO-27 sample of the JK-53 series of as c/c_0 vs. Ft/M with relative CO_2 capacity.

Table 5.5 shows the results from the EDX measurements performed at the University of St. Andrews on the samples prepared with different ligands. From this it can be seen the presence of Ni on the surface of the sample contributes to increase the adsorption capacity.

Table 5.5: EDX measurements performed at the University of St. Andrews for Mg-CPO-27 with different ligand used in the synthesis. (*) Relative to Mg.

Ligand	Mg /Ni ratio	Ni/P ratio	Ni found (%)*	P found (%)*
Carboxyphosphonate	10.4/1	10.3/1	8.8	0.9
Piperazine	9.8/1	1.5/1	9.3	13.0
Bipiperadine	9.5/1	1.2/1	9.5	8.0

Similarly to the other the Mg-CPO-27 samples, the adsorption was equilibrium controlled as it is possible to see from the ZLC curves (Figure 5.48) for the sample JK-53Y modified using bipiperadine-based ligand. Also in this case the curves in semilog plot approach a straight line in almost all the range of concentrations.

The ZLC curves relative to the other samples of the series are collected in the Appendix A.

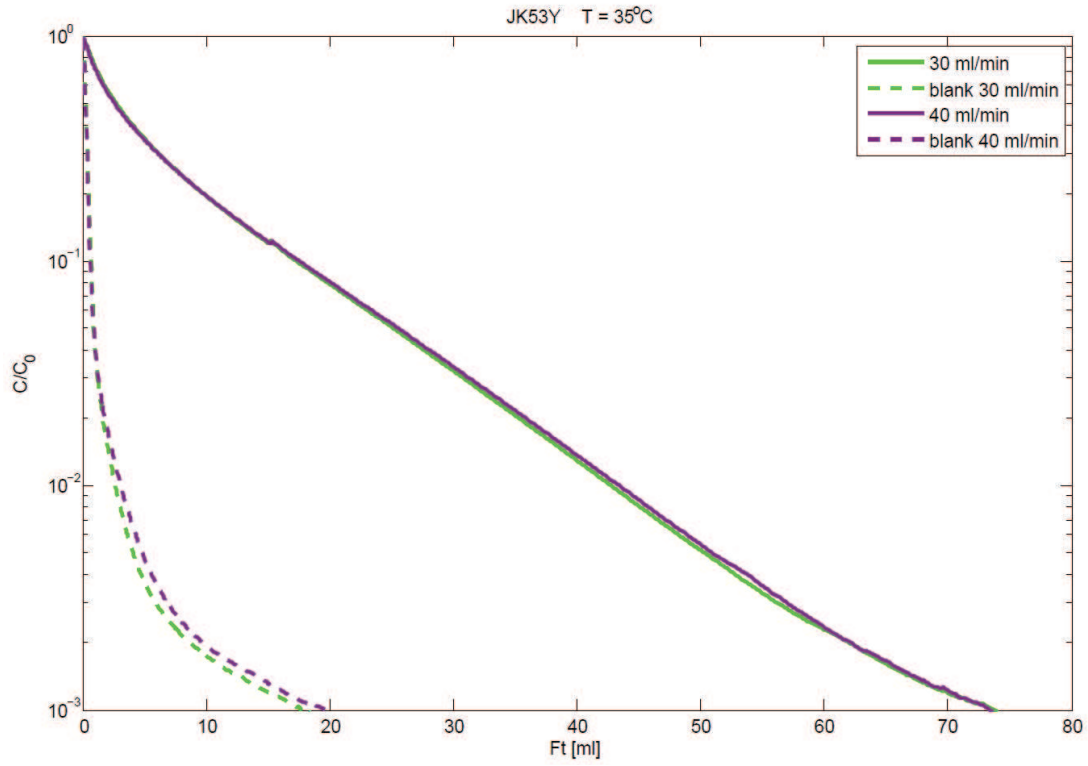

Figure 5.48: ZLC desorption curves at different flowrates for the Mg-CPO-27 sample modified using Bipiperadine-bases ligand.

5.2.5 Effect of the Ni content (JK-61 series)

The sample belonging to the JK-61 series were synthesised to investigate how the Ni content in the additive affects the final uptake of the modified Mg-CPO-27. The samples were prepared using the carboxyphosphate-based additive with different concentration of Ni added to the additive.

Figure 5.49 shows the ZLC desorption curves for all the samples of the series as c/c_0 vs. Ft/M with the relative adsorption capacity. Differently than what was expected, the CO_2 capacity obtained clearly increases when the Ni content in the additive decreases. Measurements at the University of St. Andrews show evidence that with lower amounts of additive it is possible to open up the pores and a layer of added metal and ligand is formed on the surface, which keeps the pores open. With higher amounts of additive the superficial layer gets thicker and a loss of porosity is observed. In this case evidently the increase of the amount of Ni may be responsible of the partial blockage of the pores.

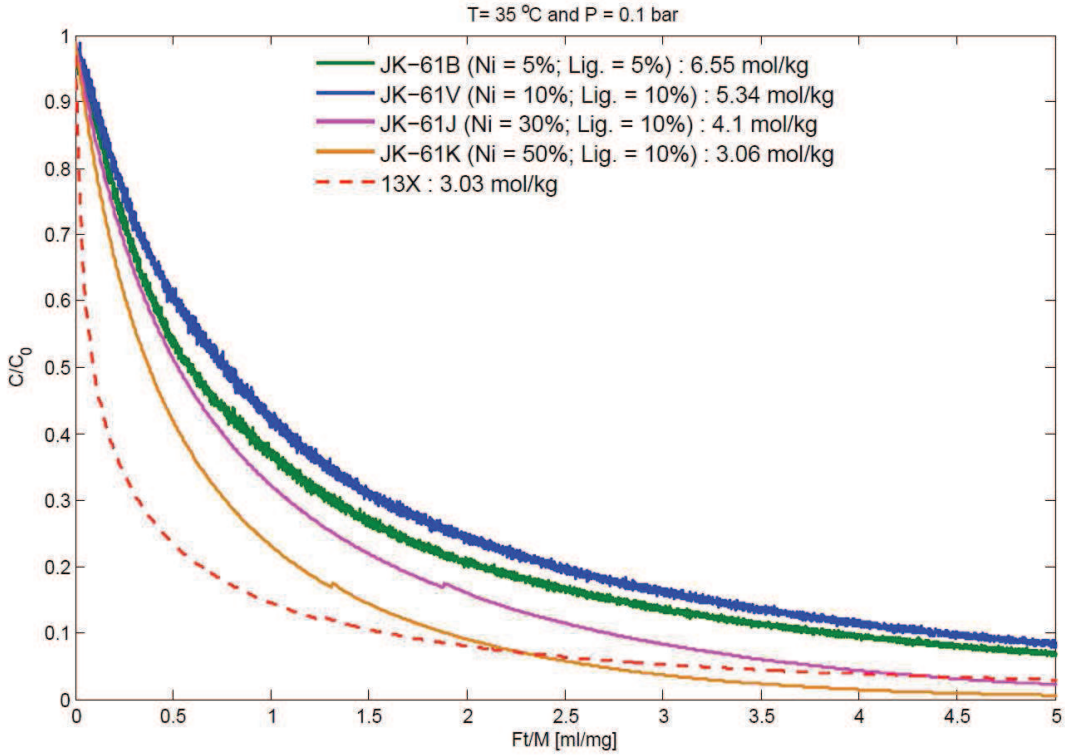

Figure 5.49: Plot of the ZLC curves for Mg-CPO-27 samples modified with additive at different Ni content.

Similarly to the other Mg-CPO-27 samples, also for the samples of this series adsorption was found to be equilibrium-controlled. In Figure 5.50 and Figure 5.51 the ZLC curves of the two best modified Mg-CPO-27 samples are shown. The samples exhibited the highest CO_2 capacities among all the samples tested and for this reason further tests were performed at different temperatures to extract the heat of adsorption. The ZLC experiments were run at 35, 50 and 65 °C, and, knowing that the slope of the long-time asymptote is equal to $1/(V_g+KV_s)$, then the heat of adsorption can be obtained using the Vant' Hoff equation.

Figure 5.52 and Figure 5.53 show the ZLC curves at different temperatures for the two samples investigated, with the relative long time asymptotes and the heat of adsorption obtained. The values obtained are very similar for the two samples: 46 and 45.6 kJ/mol for JK-61B and JK-61V, respectively.

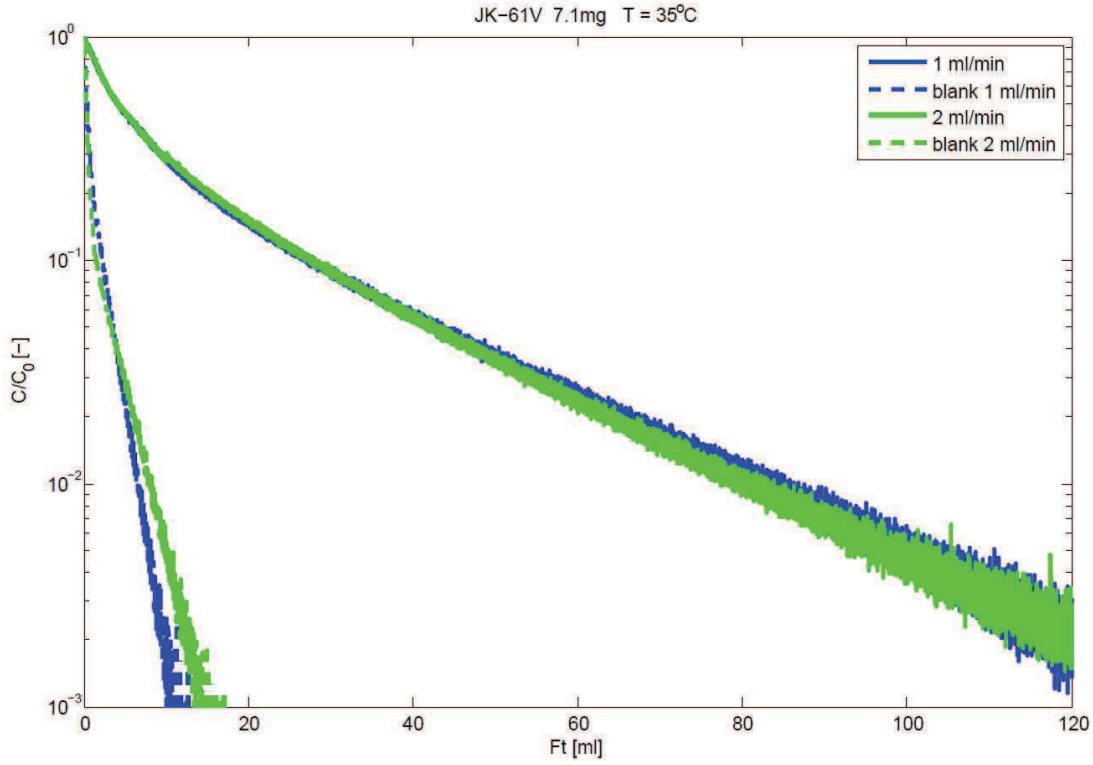

Figure 5.50: ZLC curves at different flowrates for the modified Mg-CPO-27 sample JK-61V.

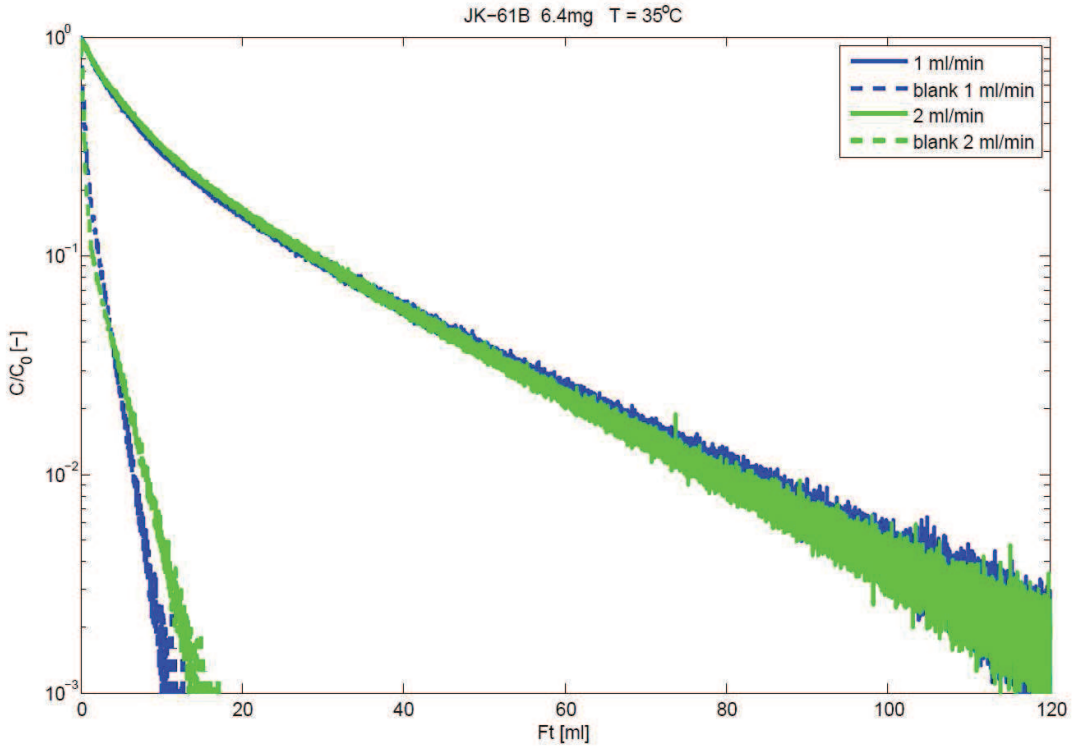

Figure 5.51: ZLC curves at different flowrates for the modified Mg-CPO-27 sample JK-61B.

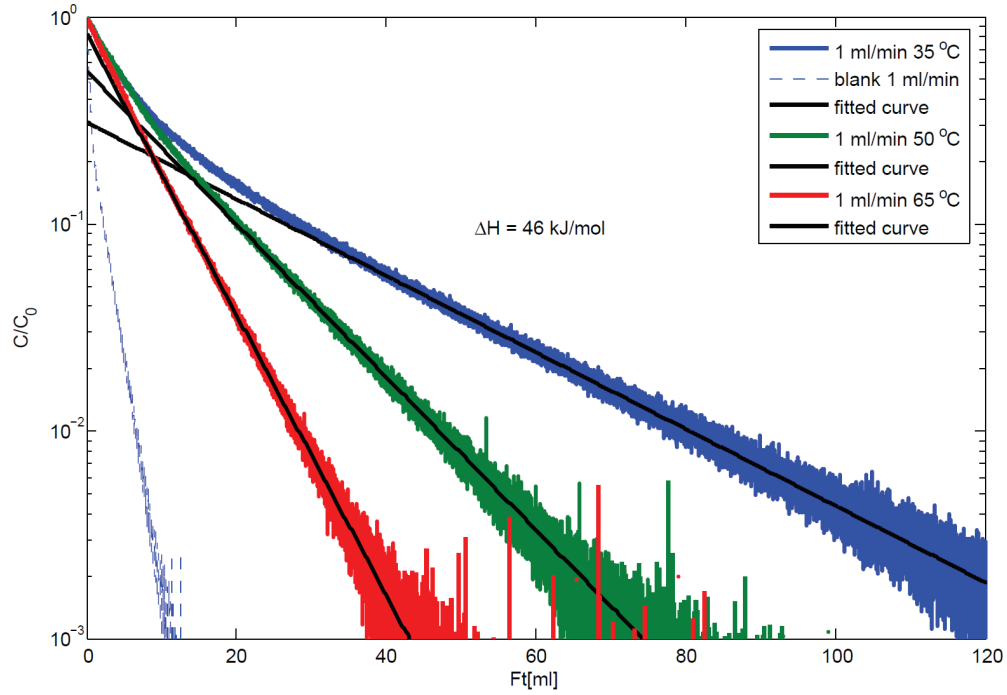

Figure 5.52: ZLC curves at different temperatures for the sample JK-61B. In black the long-time asymptote used to calculate the heat of adsorption.

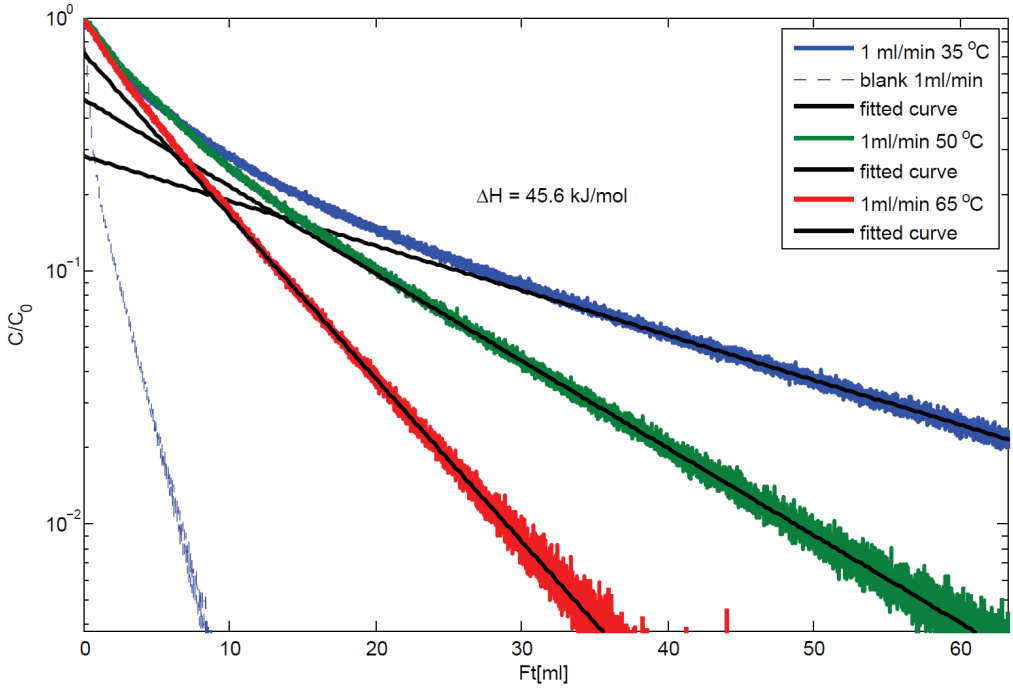

Figure 5.53: ZLC curves at different temperatures for the sample JK-61B. In black the long-time asymptote used to calculate the heat of adsorption.

The values obtained for the heat of adsorption are basically the same for the two samples and in good agreement with the literature data, as shown in table 5.6. The table shows also the CO_2 capacity reported in literatures for Ni and Mg CPO-27. The values obtained for the best Mg-CPO-27 samples in the present work vary from 20 to 28.8 %wt, which on average is higher than what reported in the literature. The difference may be due to the fact the results reported in literature are relative to samples which were not subjected to any post-synthesis modification.

Table 5.6: Selected literature data for the CO_2 capacity and heat of adsorption for Mg- and Ni-CPO-27. The data refer to P = 0.1 bar and different temperatures.

Sample	Temperature	CO_2 capacity		Heat of adsorption	Ref.
	K	mol/kg	%wt	kJ/mol	
Mg-CPO-27	298	-	~25	40	[42]
	298	-	~20	41	[123]
	-	-	-	47	[45]
	296	-	23.6	47	[44]
	-	-	-	39	[49]
	313	~5	-	-	[49]
Ni-CPO-27	303	-	~10	40	[115a]
	298	-	~18	38	[42]
	-	-	-	41	[45]
	298	3.28	-	-	[124]
	296	-	11.6	41	[44]
	298	3.4	-	-	[47]

5.2.6 As-prepared/not activated samples

The samples belonging to the ACM series were synthesised by the research group of Prof. R. Morris at the University of St. Andrews and are Mg-CPO-27 samples as-prepared which were not subjected to any post-synthesis treatment to open up the pores. The samples were prepared to check the reproducibility of the synthesis

method. Figure 5.54 shows the *Ft/M* for the samples tested and the relative CO_2 adsorption capacity. From the values of the CO_2 capacity it can be seen clearly that the method does not ensure a good reproducibility of the samples. The best sample has a capacity of 1.29 mol/kg, which is considerably lower than the value obtained for the activated samples, but is close to the value obtained for the not activated sample of the JK34 series. The difference in the capacity may be ascribed to the on-going attempts of optimising the method of synthesis.

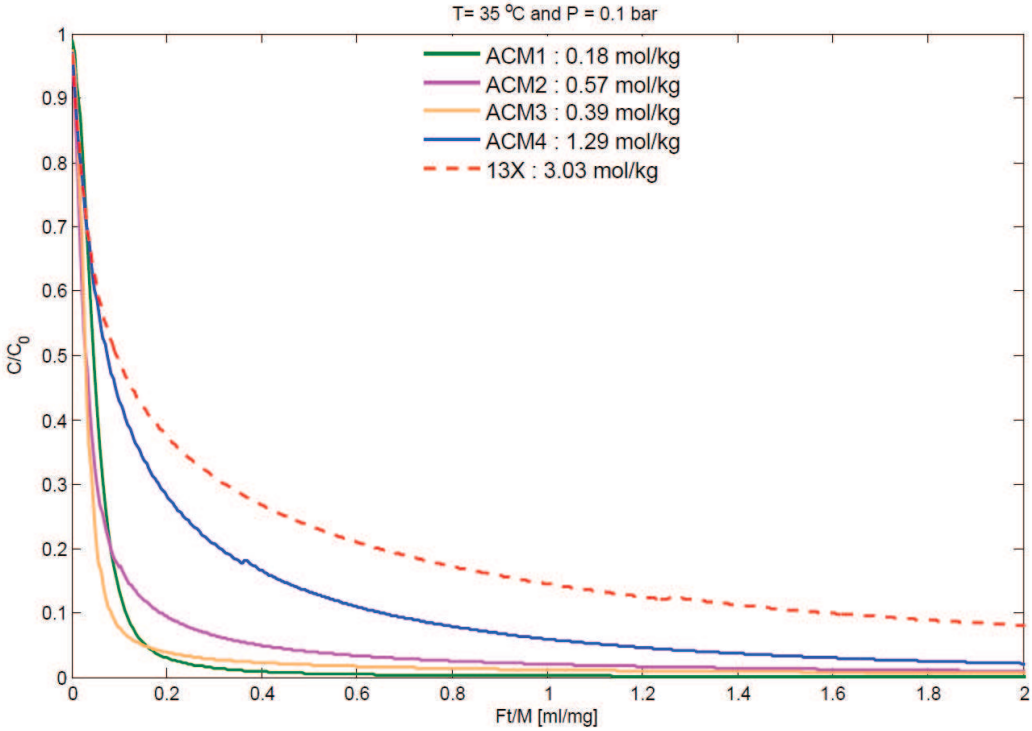

Figure 5.54: Plot of the ZLC curves for not-modified Mg-CPO-27 samples.

5.2.7 Ni-CPO-27

The synthesis procedure used for the preparation of the Ni-CPO-27 sample is very similar to the one used for the Mg-CPO-27 as reported in the literature [122]. As for the other CPO-27 samples after the synthesis the sample was activated in vacuum at 250 °C for 18 hr to open up the pores. Similarly to the Mg-CPO-27 sample also for the Ni form the adsorption process was found to be equilibrium controlled, as it can be seen from the overlapping of the ZLC experimental curves in the plot of Figure 5.55. The

CO_2 capacity exhibited from this sample is considerably lower than the one of the Mg form. This has been reported literature [42, 44] and is mainly due to the higher affinity of Mg with CO_2 (table 5.6). The high affinity of Mg-CPO-27 has been attributed to the ionic character of the Mg-O bond. This bond normally would chemically react with the molecules of CO_2 but when inserted in rigid framework of Mg-CPO-27 the rigidity of the framework does not allow such a reaction. As a result the ionic character of the bond is increased improving the adsorption performance of the sample[44].

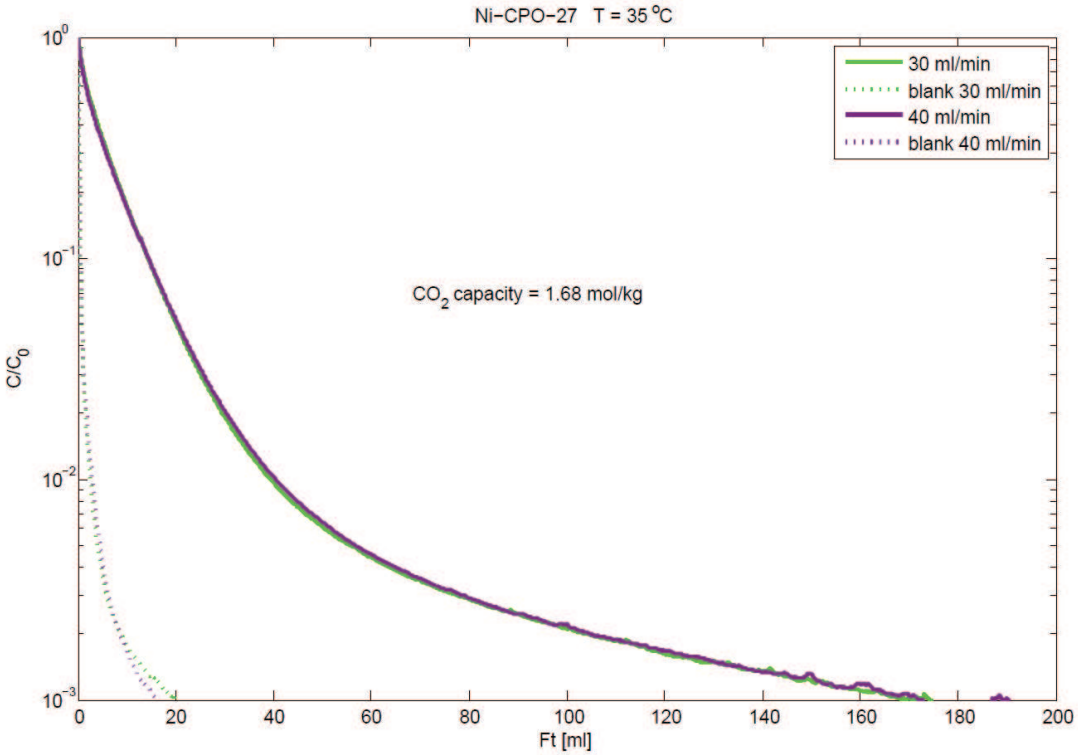

Figure 5.55: ZLC desorption curves at different flowrates for Ni-CPO-27.

In Figure 5.56 the isotherms for the best CPO-27 samples are displayed. These are obtained from integration of the ZLC response according to eq. 3.12.

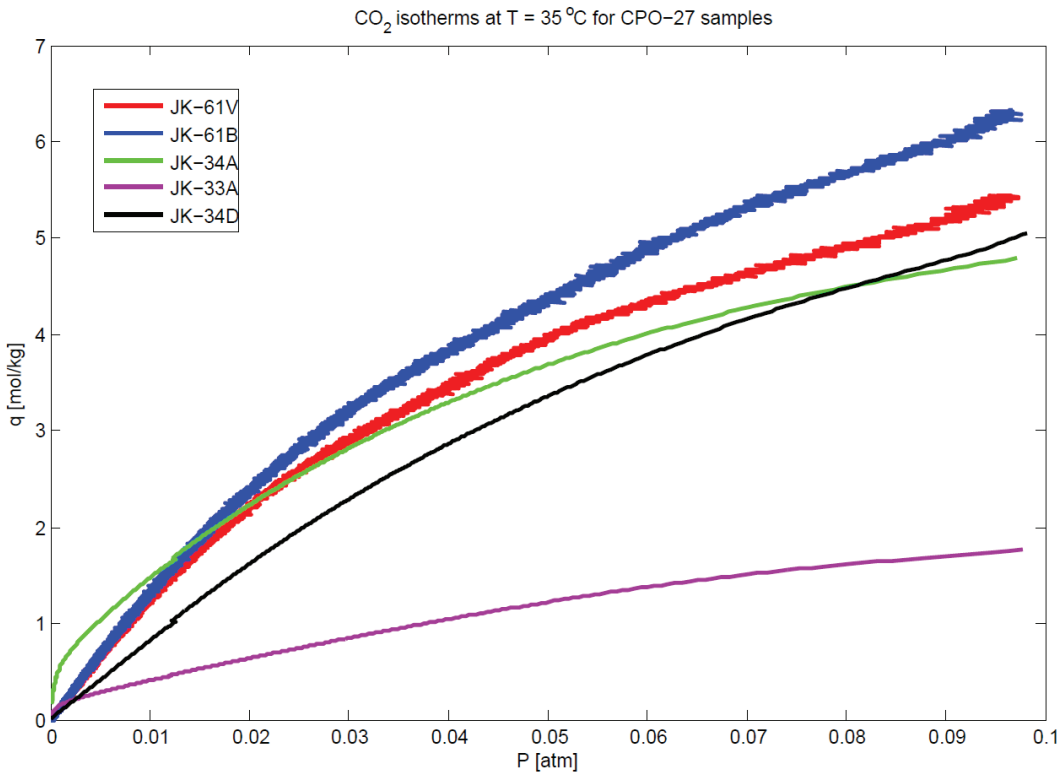

Figure 5.56: CO_2 isotherms for the best CPO-27 samples, calculated from the integration of the ZLC desorption curves.

5.2.8 Water stability test

A good candidate as adsorbent for a CO_2 capture process should ensure not only good separation properties, but it should be also resistant to impurities present in the real flue gas stream. In a real flue gas not only CO_2 is present but also other impurities such as SO_x NO_x and water which greatly affect the adsorption performance of the adsorbents. The ZLC system offers the advantage to test the stability of the samples by performing the so called water stability test.

As explained in section 4.7 the test consists in measuring the capacity of the sample after cyclic exposure to a mixture of He, CO_2 and H_2O. In order to be as close as possible to the real operating conditions the composition of the gas mixtures chosen was the one of a typical flue gas from a coal fired power plant, with 16% v/v of CO_2 dry basis. The dosing system can be used to introduce accurate amounts of water, which in a real application would be approximately 4% v/v. For the purposes of

stability to water in the ZLC system a reduced amount of water was used to avoid condensation in the low flowrate mass flow controllers. Considering that all the adsorbents with high capacity are hydrophilic, above 1000 ppm water the equilibrium is fairly close to saturation, so to test for water stability 1% v/v of water is used. After being exposed to the mixture for a fixed amount of time, the sample is regenerated and a standard ZLC experiment is performed. The sequence of exposure-regeneration-ZLC tests is repeated until the sample is either stable or significantly deactivated.

Three samples were chosen to be tested: Ni-CPO-27 (JK-33A), Mg-CPO-27 activated in water (JK-34A), and Mg-CPO-27 modified with carboxyphosponate (JK-34D). The test wanted to investigate the difference in the stability between the Ni and the Mg form; moreover it seemed interesting to check if the activation in water could help to improve the stability of the resulting Mg-CPO-27. For this reason the two Mg-CPO-27 samples were chosen from the same group of samples.

Figure 5.57 shows the results of the water stability test performed on the three CPO-27 samples as percentage of CO_2 capacity vs. the grams of water eluted per gram of sample. From the plot it can be easily seen that the Ni-CPO-27 is considerably more stable than the two samples of Mg-CPO-27. The good performance of the Ni-CPO-27 in presence of water were already reported by Liu et al. [124] who showed that the presence of water had a minor affect on the CO_2 capacity of the sample compared with zeolites 5A and NaX.

In the case under investigation the sample looses adsorption capacity in the first two cycles. After the second exposure it recovers the original CO_2 capacity and registers a capacity even higher than the original one at the fifth cycle. A possible explanation for such a trend could be that the repeated regenerations at high temperature may have opened up more pores resulting in a slight increase of the capacity. The highest value of the capacity obtained in the cycles was taken as the maximum capacity of the samples. After the fifth exposure the sample started to deactivate slowly but maintained more than 90% of the maximum capacity

The two Mg samples showed a relatively fast deactivation rate and similarly to the Ni sample activated in water reached the maximum capacity after the first regeneration cycle. Probably the first activation procedure did not open all the pores

and some of them were activated during the regeneration at high temperature after the first cycle.

Figure 5.58 shows the experimental ZLC desorption curves after each exposure cycle. Clearly, after the first exposure-regeneration cycle, the sample gains capacity, but once fully activated, it is rapidly deactivated by the presence of water.

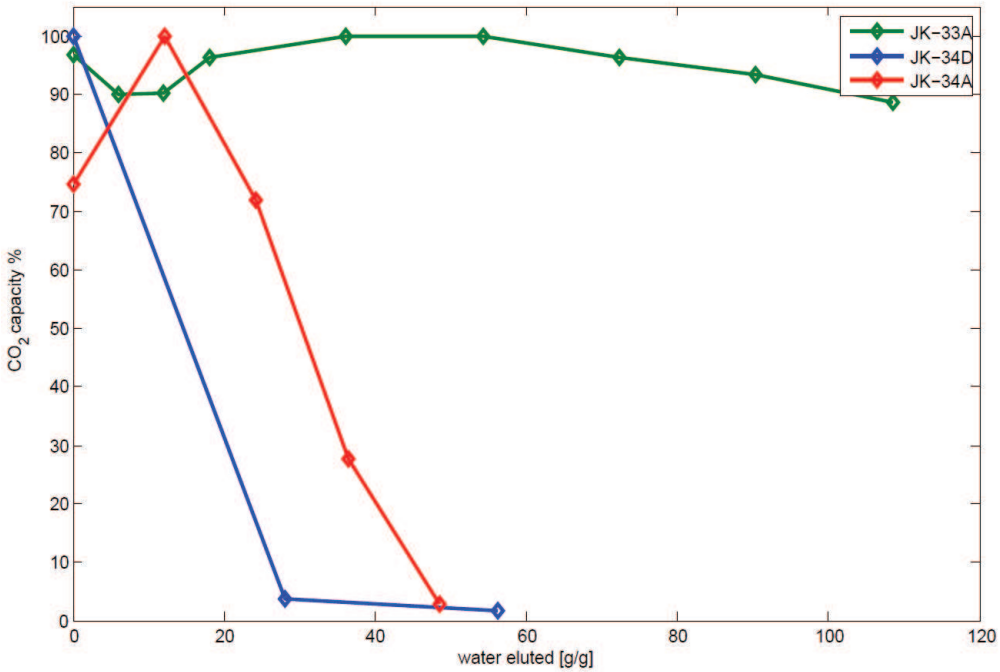

Figure 5.57: Deactivation trend in the water stability test for the Mg- and Ni-CPO-27.

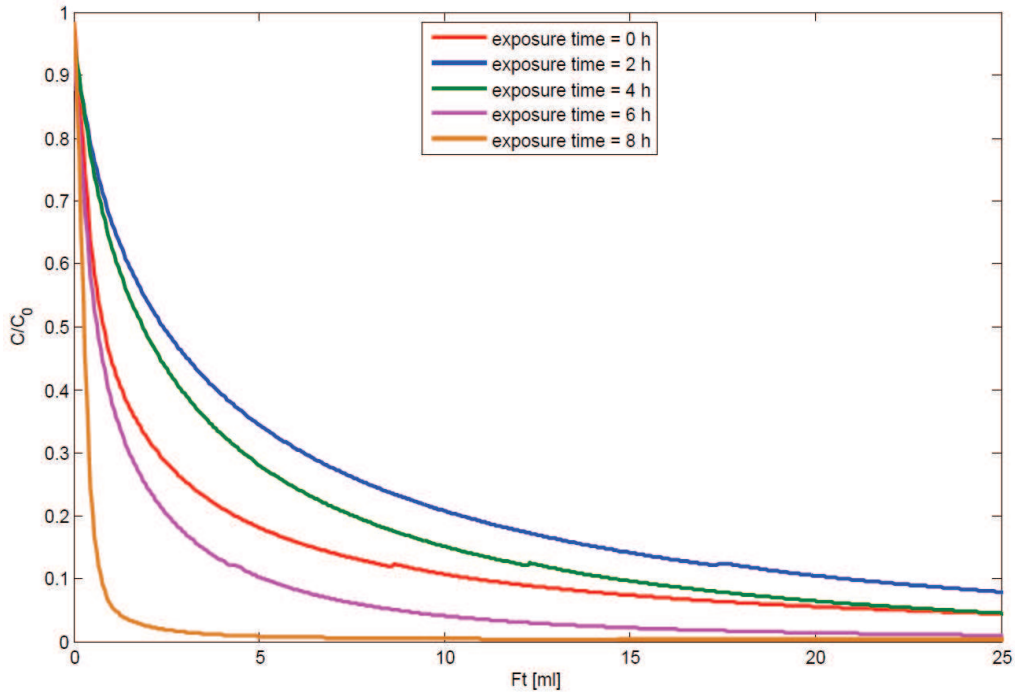

Figure 5.58: ZLC desorption curves obtained after different exposure cycles.

5.2.9 Conclusions

Several MOF samples synthesised the University of St. Andrews were tested using the ZLC technique. The samples consisted mostly in Mg-CPO-27 samples with different modifications applied: different activation methods, different ligands and Ni content in the additive used to increase the porosity of the samples.

The activation greatly increases the performance of the sample relative to the non activated one. The activated samples were also subjected to post-synthesis modification using additives and as a result extra porosity was gained. The amount of additive is a crucial parameter: an excessive amount may result in blocking the pores leading to a loss of porosity.

All the samples exhibited equilibrium controlled adsorption rates, as expected from the large pores characteristic of the framework. The best material was the one prepared using carboxyphosphonate-based additive: the resulting capacity was 6.55 mol/kg. The CO_2 uptakes are generally higher than the ones reported in literature which may be ascribed to the benefits of the post-synthesis modifications applied to

the samples. Moreover most of the samples exhibited a fairly linear isotherm which is a desirable feature for adsorbents to be used in fast PSA cycles.

The heats of adsorption extracted for the two best samples are in good agreement with what is reported in literature.

Stability tests performed on selected samples showed a rapid deactivation rate for Mg-CPO-27 in presence of water while the Ni form preserved more than 90% of the original capacity over a long period of time and repeated exposure cycles.

Moreover for Ni-CPO-27 was found that the regeneration temperature needed to dry the sample is relatively low, if compared with zeolite 13X, and the isotherm much more linear. All this together makes Ni-CPO-27 a promising material which should be considered further for post-combustion capture using rapid VSA cycles.

5.3 Carbon based materials

In the present section the results of the carbon-based adsorbents are presented. The samples were synthesised by the research groups of Prof. S. Yeates Crouch at the University of Manchester and Prof. Z. X. Guo at University College London.

The work at the University of Manchester is based in the functionalization of BPL carbon by the introduction of amine groups with the aim to increase the affinity with CO_2.

At UCL porous carbons are synthesised by using a chemical technique. The technique allows to create highly porous carbon by impregnating a polymer template, which is then removed. By changing the preformed polymer template, materials with different porosities can be obtained which can be successively functionalized with various functional groups.

All the samples are compared with HiSiv3000 and Calgon commercial activated carbons as benchmarks.

Due to the different nature of the adsorbents the results will be discussed in separate sections.

5.3.1 Functionalized BPL Carbons

BPL Carbon is a commercial activated carbon produced by Calgon. The material is characterised by high surface area, about 1000 m^2/g, and pore size of 10.2 Å [125]. Activated carbons have generally a low CO_2 uptake at low pressure and functionalization is one of the most common methods to try to enhance their adsorption properties. In the case of BPL Carbon the relative high surface area and the large pore size offer the advantage of an easy access for the molecules of CO_2 to the functional groups. On the other hand the introduction of functional groups inevitably reduces the accessible space, for this reason it is important that the pristine material is provided with a high surface area in order to minimise this effect on the resulting capacity.

In the attempt of improving the affinity to CO_2, different functional groups (mostly amine-based groups) were introduced in the structure of BPL Carbon. As a result of the functionalisation, the amine groups are directly attached to the structure of the BPL carbon as shown in Figure 5.59.

In table 5.7 the materials synthesised are listed, with relative surface area; the different molecular structures are reported in Figure 5.59.

Table 5.7: Details of the activated carbons tested. BET measurements were performed at the University of Manchester. (*) TGA not available.

Name	SAMPLE	BET [m^2/g]	Amount tested [mg]
BPL Carbon	BPL Carbon	1000 [125]	9.21
MOD163D	BPL-Piperazine	255.91	10.2
MOD198	BPL-Crown ether	394.21	11.5*
MOD183B	BPL- Benzeneacetamide, N-[2-(dimethylamino)ethyl]-	162	12.8*
MOD183A	Information not available	30	10.1
MOD229	Information not available	135	10.8*

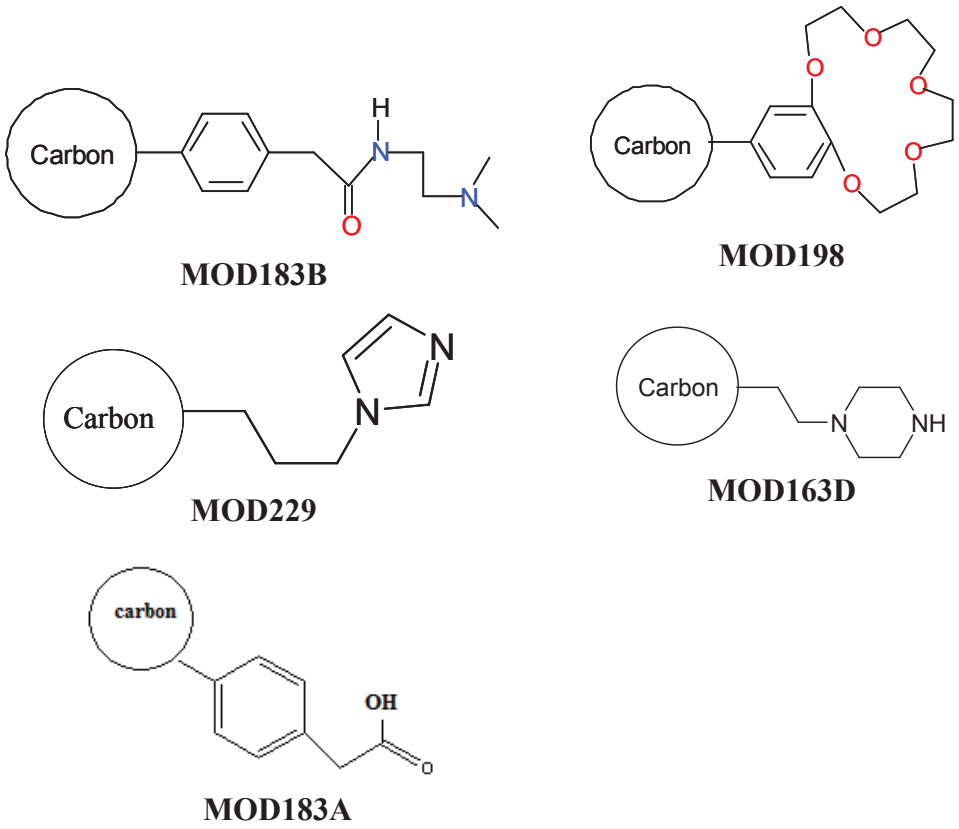

Figure 5.59: Molecular structures of the functionalised BPL Carbon.

Figure 5.60 shows the ranking of the CO_2 uptake resulting from the ZLC experiments.

As a result of the functionalisation a considerable reduction of the surface area is observed. The lack of free volume for the adsorption of CO_2 is the main reason of the loss of performance of the functionalised samples, which show a CO_2 uptake less than 1/3 of the non-functionalised BPL Carbon.

Surprisingly, among the amine-BPL samples, a slightly higher uptake is observed for the samples with the lowest surface area, MOD183A and MOD229. For these samples the higher affinity of CO_2 induced by the functional groups somehow compensates for the poor surface area. The structures of MOD229, MOD163D and MOD183 show the same nitrogen content, but the higher basicity of MOD229, due to the presence of two ternary nitrogens, makes the difference in the CO_2 capacity for this sample. Not differently the presence of high content of oxygen in the structure of

MOD183A and MOD198 seems to favour the adsorption process of CO_2 despite the poor surface area.

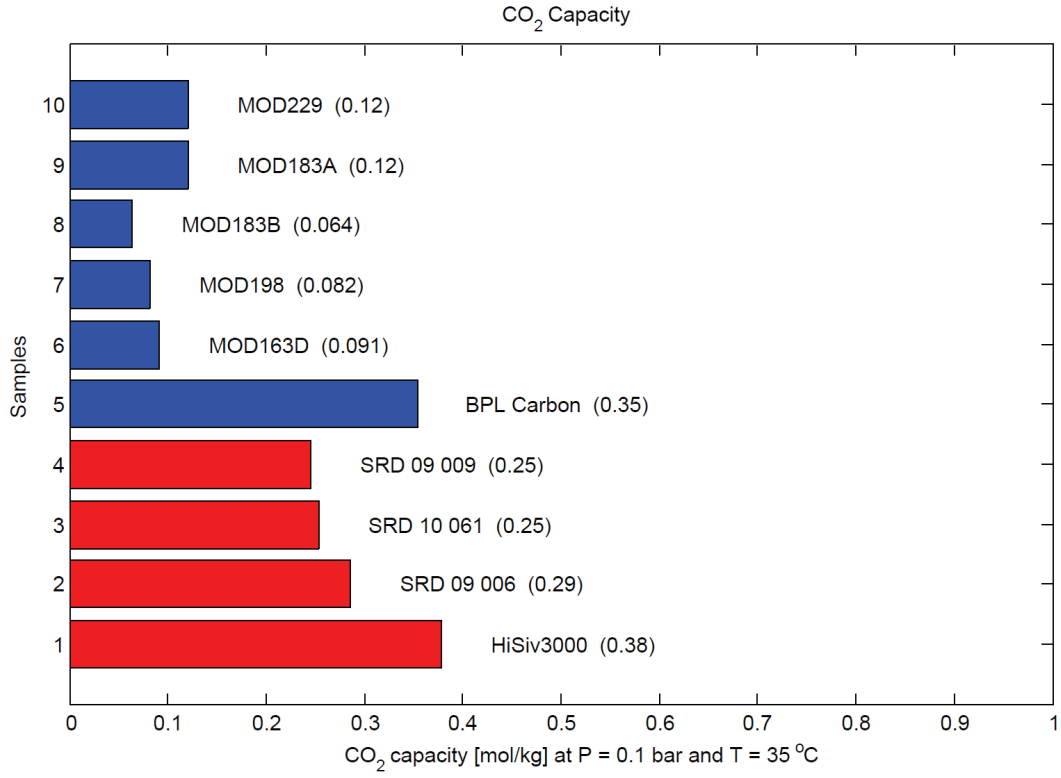

Figure 5.60: Ranking of the CO_2 capacity for amine-functionalised BPL carbons. In red the commercial materials used as benchmark.

The plot in Figure 5.61 shows the ZLC desorption curves for all BPL Carbons normalised for the weight of the sample used. From this representation it is easy to see how the area under the curves, which is proportional to the CO_2 uptake, is not very different among the modified samples, while it is considerably less if compared to the original BPL Carbon.

Figure 5.62 shows the *Ft* plot for BPL Carbon. The desorption curves do not overlap in the *Ft* plot indicating that the desorption rate is kinetically controlled for this sample, but the high influence of the blank, due to the low uptake of the sample did not allow for further investigations.

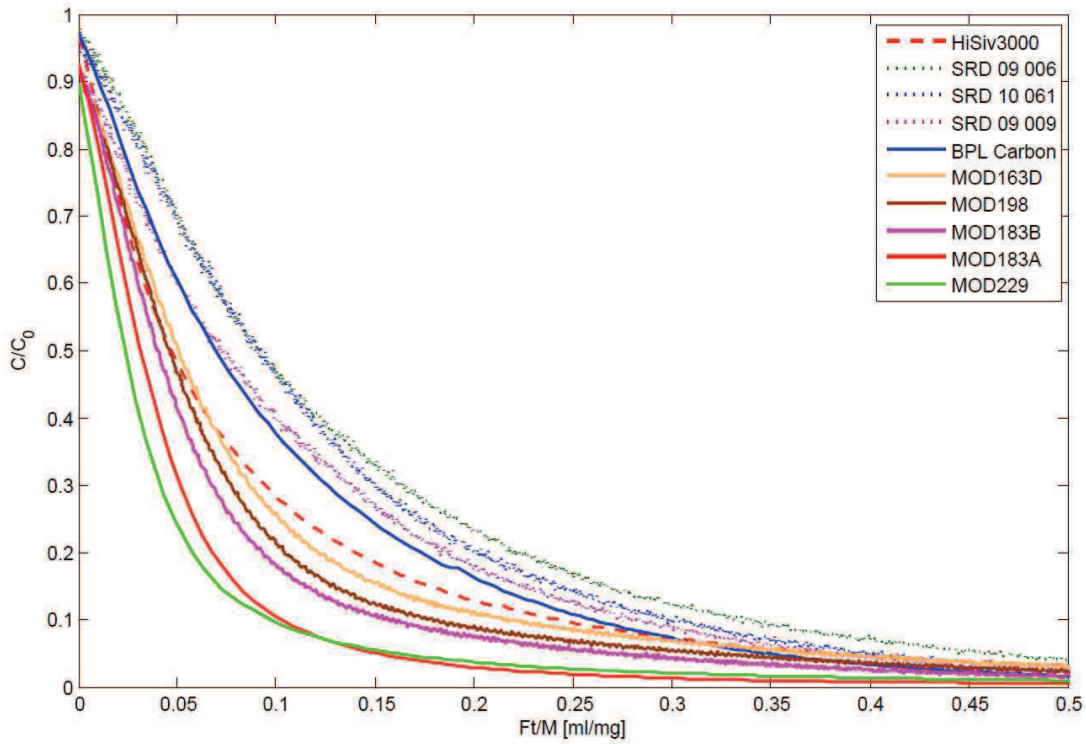

Figure 5.61: Ft/M plot for all the BPL carbons

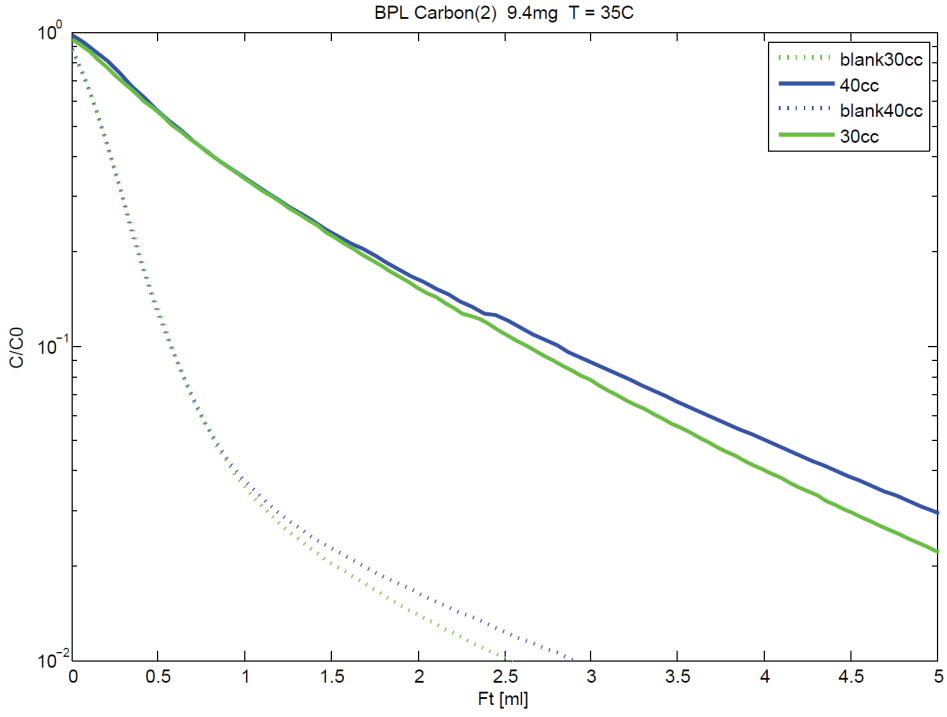

Figure 5.62: Ft plot for BPL Carbon at T = 35 ˚C and P = 0.1 bar.

5.3.2 Carbon foam adsorbents

In this section the results of the ZLC experiments on the carbon foams synthesised at University College London by the research group of Prof. Z. X. Guo are presented.
The synthesis of carbon foams consists in using a polymeric template in which a carbon precursor is infiltrated, the material is finally carbonised at high temperature and the template is removed. The template provides the initial porous structure but by varying the quantity of precursors used and the activation method the final materials can be tuned to enhance the final adsorption performances. The resulting micro and mesopores of the carbon foam not only provide adsorption sites for CO_2, but they can also be host-sites for the metal cations when the material is subjected to metal doping.
In table 5.8 the carbon foams prepared at the University College London are listed. The samples were all synthesised using phenol formaldehyde resin as carbon precursor at different concentrations, carbonised and activated at 600 °C. Before the ZLC experiments all the adsorbents were regenerated at 150 °C.

Table 5.8: List of the carbon based adsorbents synthesised at University College London. (*) TGA not available.

Name	SAMPLE	Precursor concentration [kg/L]	Amount tested [mg]
UCL-BZ-S1	Templated Carbon	0.4	8*
UCL-BZ-S2	Templated Carbon	0.4	7.4*
UCL-BZ-S3	Templated Carbon	0.2	11.3*
UCL-BZ-S4	Templated Carbon	0.6	15.7*
UCL-BZ-S5	Templated Carbon activated (KOH/precursor = 2)	0.2	2.1*
UCL-BZ-S6	Templated Carbon activated (KOH/precursor = 3)	0.2	7.7*

The samples UCL-BZ-S1 and UCL-BZ-S2 were prepared using the same initial precursor concentration, but the solvent of UCL-BZ-S1 was evaporated to form a viscous solution at high concentration of precursor.

The samples UCL-BZ-S5 and UCL-BZ-S6 were also further treated by using KOH for chemical activation at different KOH/Precursor weight ratio.

In Figure 5.63 the values of the CO_2 capacity obtained from the ZLC experiments are presented, compared with the benchmark adsorbents.

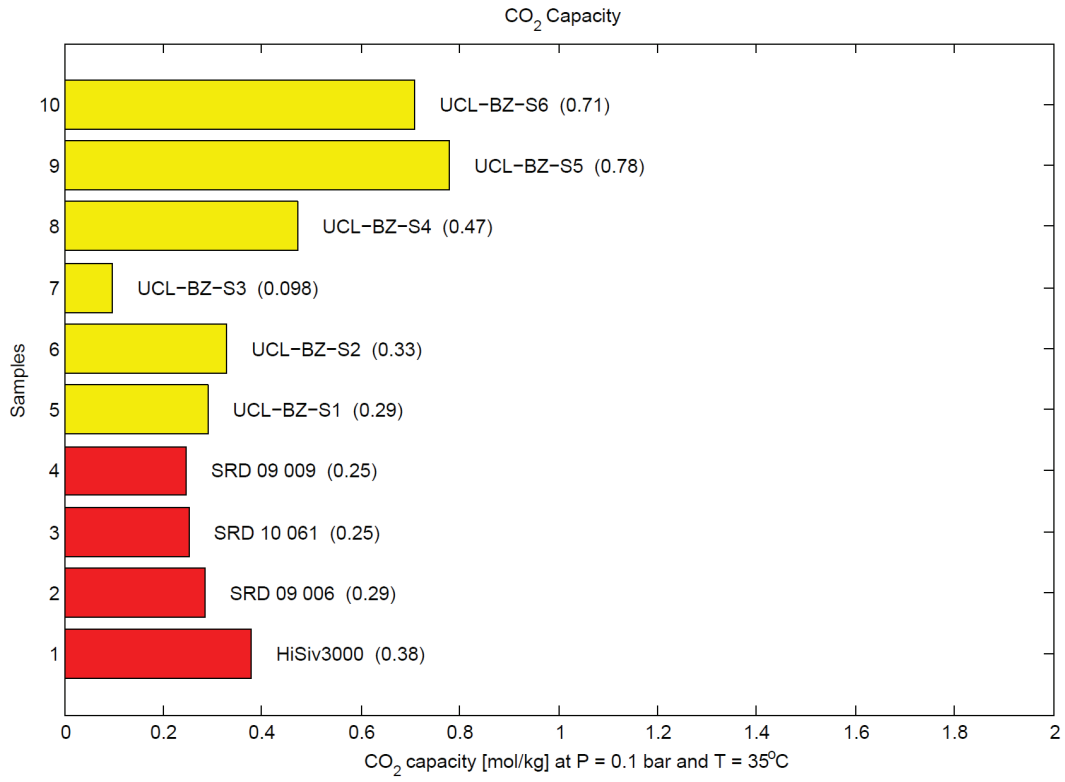

Figure 5.63: Ranking of the CO_2 capacity for carbon foams synthesised at University College London.

From the values of the capacity obtained it is clear that, as expected, the CO_2 uptake increases with the precursor concentration. In the case of UCL-BZ-S1 the treatment to increase the concentration of precursor in the solution seems to lower slightly the performance of the material, probably due to some loss of porosity.

The chemical activation with KOH has definitely a positive effect on the samples enhancing the capacity but the less activated sample seems to perform better than the one for which a higher content of KOH was used.

The same result was reported by Sevilla et al. [126] who investigated the effect of the activating conditions on carbonised polysaccharide samples. They also found that the sample (KOH/precursor = 4) more strongly activated, despite the higher surface area,

resulted in a lower uptake relative to the one mildly activated (KOH/precursor = 2). This was mainly due to the presence of narrow pores, which, having a high adsorption potential, enhance the affinity with CO_2 [126a]. Furthermore the values of the CO_2 uptake at 25 ºC and 0.1 bar reported by the authors are in reasonable agreement with those obtained in the present work.

Figure 5.64 shows the *Ft/M* plot for the samples tested: clearly from the plot it can be seen that UCL –BZ-S5 and UCL –BZ-S6 exhibit higher uptake relative to the non-activated samples.

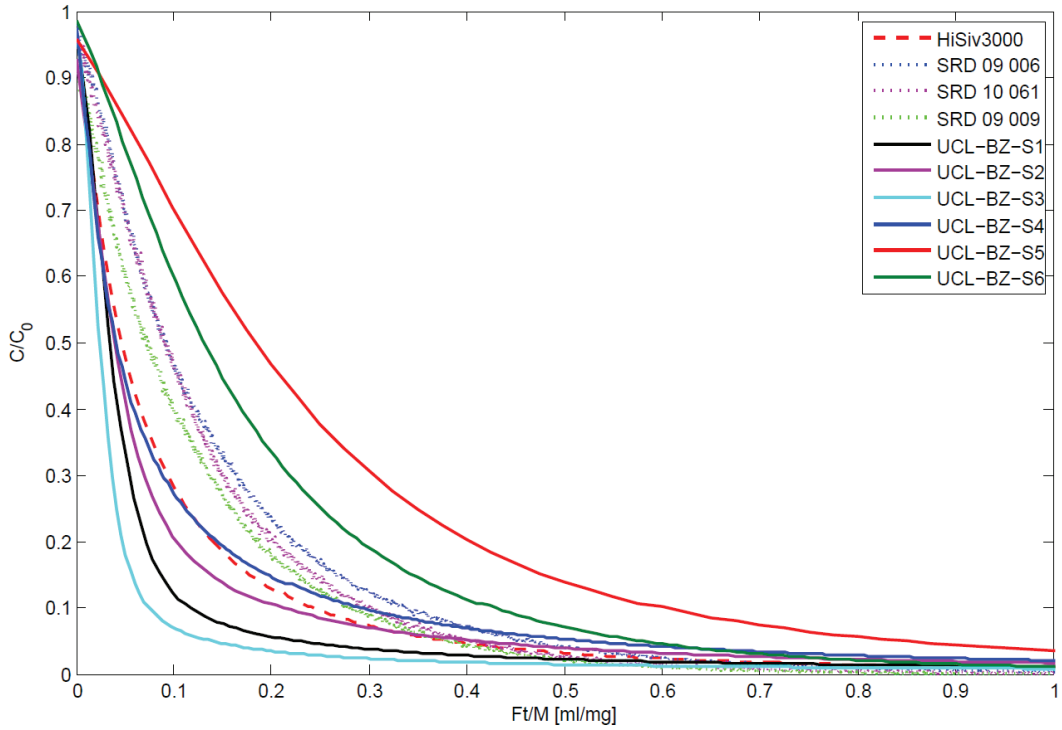

Figure 5.64: Ft/M plot for the carbon foam adsorbents, compared with the benchmark adsorbents.

5.3.3 Conclusions

Two classes of carbon based adsorbents were investigated using the ZLC method: different types of amine-functionalised carbon and carbon foams.

With regard to the amine-functionalised carbons, all the samples showed a considerably loss in the CO_2 capacity compared to the original material. The

functionalization process had the main effect of reducing the surface area of the samples and this definitely compromised the final adsorption performances of the materials.

The ZLC desorption curves of BPL carbon showed kinetic control in the desorption rate but the response curves were too close to the blank to be further analysed. Further tests will be carried out in the future with the low flow ZLC system and the volumetric Autosorb apparatus to try and establish the basis for a model of the uptake of CO_2 on amine functionalised adsorbents. Due to the limited CO_2 capacity of the samples tested, there was a decision taken to focus the kinetic studies on the Rho-type zeolites.

Carbon foams represent a novel class of carbon based adsorbents, synthesised at University College London, was tested using the ZLC technique. In order to optimise the preparation method, the samples were synthesised using different concentrations of the carbon precursor: as expected the CO_2 capacity increased with the precursor concentration. Two samples were also chemically activated using KOH to enhance the CO_2 uptake. The resulting adsorption performance was enhanced by the activation procedure and the results were in good agreement with results reported in literature. More samples were expected from University College London, which would have given more depth to this section, but due to a series of delays the samples were not submitted in time to be included in this thesis.

5.4 PIMs

In this section the results of the PIM samples are discussed. The materials were synthesised by the research groups of Prof. P. Budd at the University of Manchester and Prof. N. B. McKeown at Cardiff University, who are the inventors of this new class of polymers.

These polymers are meant to be used to make membranes for gas separations, for this reason high selectivity and permeability are the desired qualities for these materials. In this sense measurements of the CO_2 capacity give a very useful indication of the expected transport properties but the expected capacity for PIMs is low in comparison to HiSiv3000 and the Calgon activated carbons that were used as benchmark adsorbents.

Among all PIMs, PIM-1 seems to have the best compromise between high permeability and high selectivity [73, 127], but on the other hand the material has also poor stability. For this reason the work at the University of Manchester and Cardiff University is focused on the preparation of novel PIM1-based polymers with enhanced properties relative to the precursor.

Cardiff and Manchester are looking at different ways to increase the CO_2 solubility that is, for membranes, the equivalent of the CO_2 capacity for an adsorbent.

The work at the University of Manchester is mainly focused on the thermal rearrangement of PIM-polyimide (PIM-PI). The idea is to combine the good transport properties showed by the PIM-PI with the increase of microporous characteristics induced by the thermal rearrangement[76a, 127a, 128]. Different precipitation methods were used for the synthesis of PIM-1 and different types of PIM-PIs were prepared and then thermally rearranged.

The work at Cardiff University is based on increasing the affinity with CO_2 by incorporating amines directly into the framework of the polymer. Two main classes of polymers were developed: Tröger's Base PIMs (TB-PIMs), by introducing heterocycle amine groups, called Tröger's Base (TB); and triptycene polymers by nitration of triptycene.

For a better understanding of the results and in order to facilitate the correlation of the results between materials of the same series, the PIMs developed by the University of Manchester and Cardiff University will be analysed in separate sections.

5.4.1 PIMs – Manchester

In this section the results relative to the PIMs synthesised by the University of Manchester are presented. In Table 5.9 the amount used for the experiments and the BET surface areas measured at the University of Manchester are listed. All the samples were regenerated before the experiment at 125 ºC.

Table 5.9: Samples details, BET and TGA measurements were performed at the University of Manchester. (*) no TGA available; (**) tested in the Autosorb volumetric system.

Name	SAMPLE	BET [m^2/g]	Amount tested [mg]
EML004	PIM-PI-1	632.22	8.36
HS48−RT400	Thermally re-arranged PIM-PI-OH	104	10.1
HS61−TR400	Thermally re-arranged PIM-PI-OH	405.21	7.6
HS61	PIM-PI-OH	231.87	7.98
DNM82	amine-PIM	469.88	17.08
DNM98	PIM-PBI	124.87	7.89
HS77	PIM-PI-OH	-	7.94
HS77−TR450	PIM-PBO	-	17.08
LMA23	PIM-1	684.73	12.7*
LMA23−fibre	PIM-1 - fibre	729.05	1.5*
LMA27	PIM-1	719.65	125.6**
LMA27-spongy PIM	PIM-1	-	59.7**

All the PIM-1 samples listed in table 5.9 have the typical structure of PIM-1, shown in Figure 5.65 and a similar method of synthesis as described by Budd et al. [70, 72]. The main difference among the samples is the precipitation method.

The common way of precipitating PIM-1 is by dissolving in chloroform and mixing with methanol and then collecting the powder by filtration. This is the case for the LMA23 and LMA27 samples. For these two samples a "spongy" variant was also prepared, with the aim of increasing the void volume inside the material. A concentrated solution of PIM-1 was prepared in chloroform and then added with a syringe to the surface of water. This allowed the particles to precipitate as fibres and then be collected by a glass bobbin from the surface of the water. The product was finally dried in oven at 100 °C.

As a result the spongy version of PIM-1 shows higher BET surface area relative to the conventionally precipitated PIM-1, indicating that making polymer fibres opens up more pores in the PIM structure and this may improve the mass transfer and CO_2 uptake mechanism.

In the case of DNM82, PIM-1 is modified to amine-PIM-1 by substituting the nitrile groups with amine (Figure 5.65, right). The presence of amine groups is expected to increase the CO_2 uptake but a reduction of the free volume relative to the typical values of PIM-1 is observed.

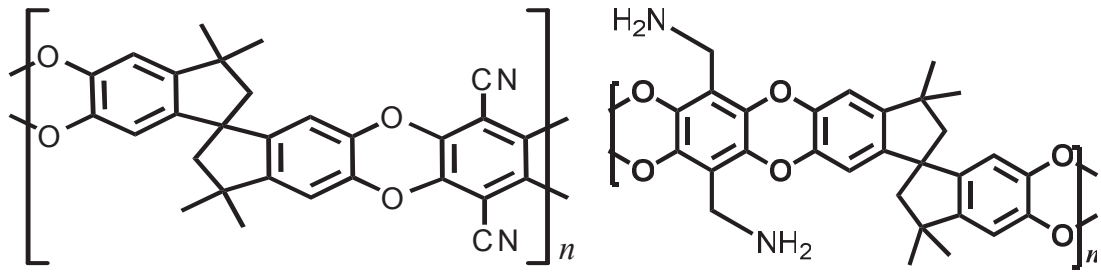

Figure 5.65: Left, structure of PIM-1. Right, structure of amine-PIM-1.

The polyimide sample, PIM-PI-1, was prepared according to the procedure used by Ghanem et al. [76a, 128c] . This variety of PIMs presents a dianhydride component very similar to PIM-1, but different diamine groups. The resulting polymers show molecular structures similar to PIM-1 with an increased rigidity due to the bonds in the backbones, Figure 5.66. Furthermore, the presence of polar groups in the structure contributes, together with the microporous structure of these materials, to increase the uptake and the solubility [76a, 128c].

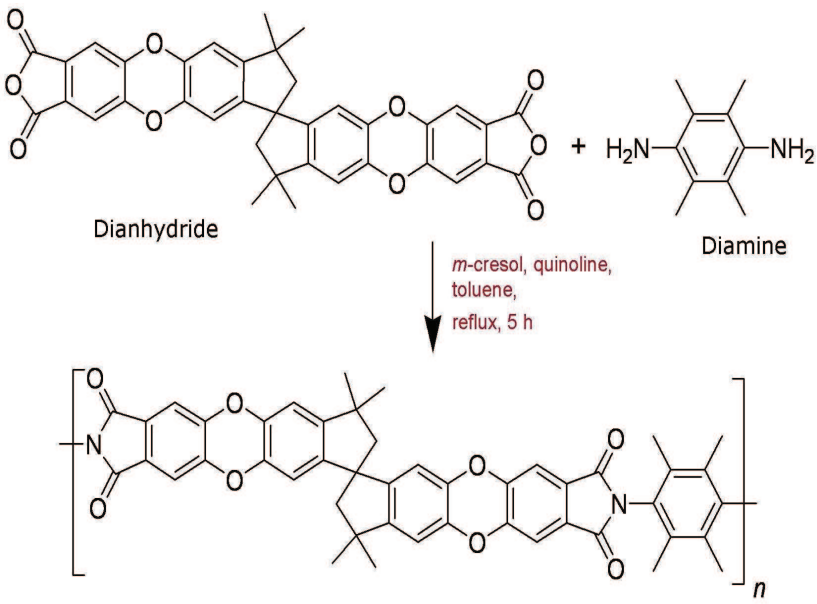

Figure 5.66: Synthesis scheme of PIM-PI-1.

PIM-PI-1 is also characterised by a relatively high molar mass: Figure 5.67 shows the gel permeation chromatography measurement performed on the EML004 PIM-PI-1 sample at the University of Manchester. As expected a bimodal mass distribution is observed: this is common also for PIM-1 and in agreement with previous literature data [76a, 128c].

.

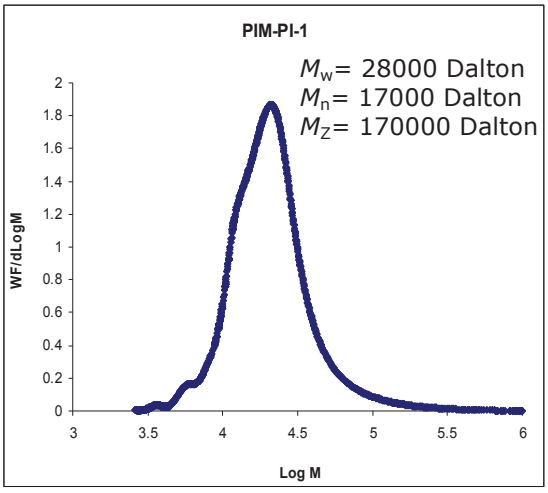

Figure 5.67: Molar mass distributions from gel permeation chromatography (University of Manchester).

PIM-PI-OHs are aromatic polyimides containing ortho-positioned hydroxyl groups. The presence of aromatic units, interconnected with heterocyclic rings gives to this class of polymers a characteristic flat linear structure with high chain rigidity and high torsional energy. The main disadvantage is that this structure allows for an efficient packing resulting in a very small free volume and furthermore they are not soluble in common solvents, which makes very difficult the use of the solvent casting method to prepare membranes [129]. In order to overcome this problem, polyimides can be thermally rearranged at high temperature, and as result polybenzoxazole is obtained (PBO). In the re-arrangement the free rotation around the imide bound is lost and the more rigid structure of PBO is unable to pack as efficiently as in the solid state [130]. The efficiency of cavity formation is then increased, resulting in a material with a higher free volume and a narrow size distribution of the cavities.

The samples HS61 and HS77 were prepared with two different methods, thermal and chemical, respectively. The samples were then both thermally re-arranged at 400 and 450 °C under N_2, (Figure 5.68). A considerable increase of the surface area was observed for the HS61 sample, proof of the higher free volume of the thermally re-arranged form.

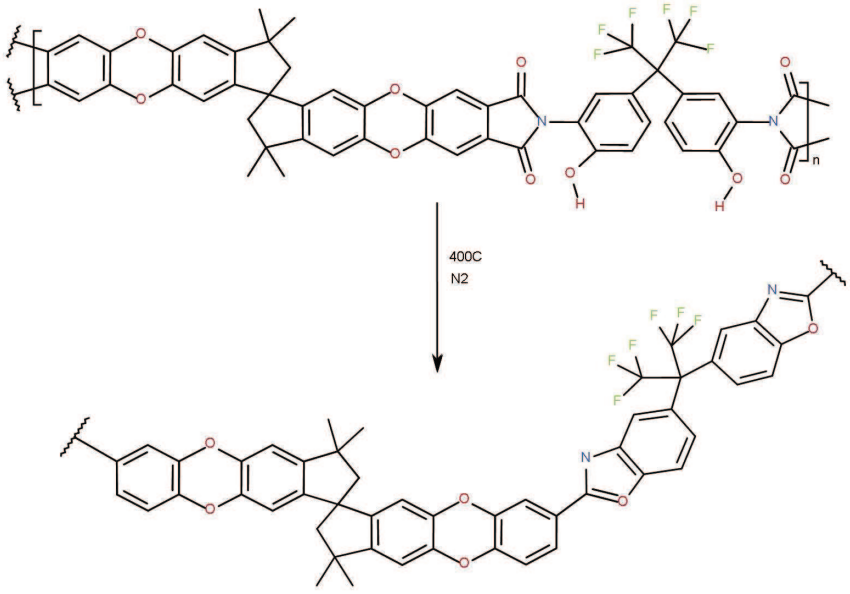

Figure 5.68: Scheme of the thermal re-arrangement of the HS 61 sample.

The DNM98 is a polybenzimidazole (PBI) polymer, Figure 5.69. This class of materials is characterised by high thermal and chemical stability and good mechanical properties, essential qualities for polymers to be used to make membranes for gas separation. This polymer shows an increase of the separation performance at higher temperatures, that, combined with a high resistance to the CO_2 plasticization, makes this class of materials suitable for high temperature membrane separations [131].

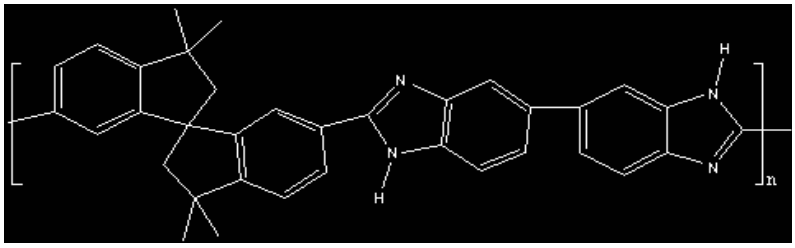

Figure 5.69: Structure of Polybenzimidazole.

In Figure 5.70 a chart with all the PIMs tested is shown, in red the benchmark materials are included for reference. As expected the capacity for these samples is relatively low and no sample reached the values of the CO_2 uptakes of the benchmark materials. The sample with the higher uptake seems to be the PIM-1 LMA23-spongy, but it has to be noted that, due the considerably low density of this sample, and its characteristic spongy structure, no more than 1.5 mg of material could be housed inside the ZLC. Due to the extremely low amount used the accuracy of the measurement is definitely affected by the fact that the desorption curve of the sample is too close to the blank. Unfortunately no more material was available for further tests on the volumetric system in which more material can be loaded, thanks to the higher volume of the sample cell.

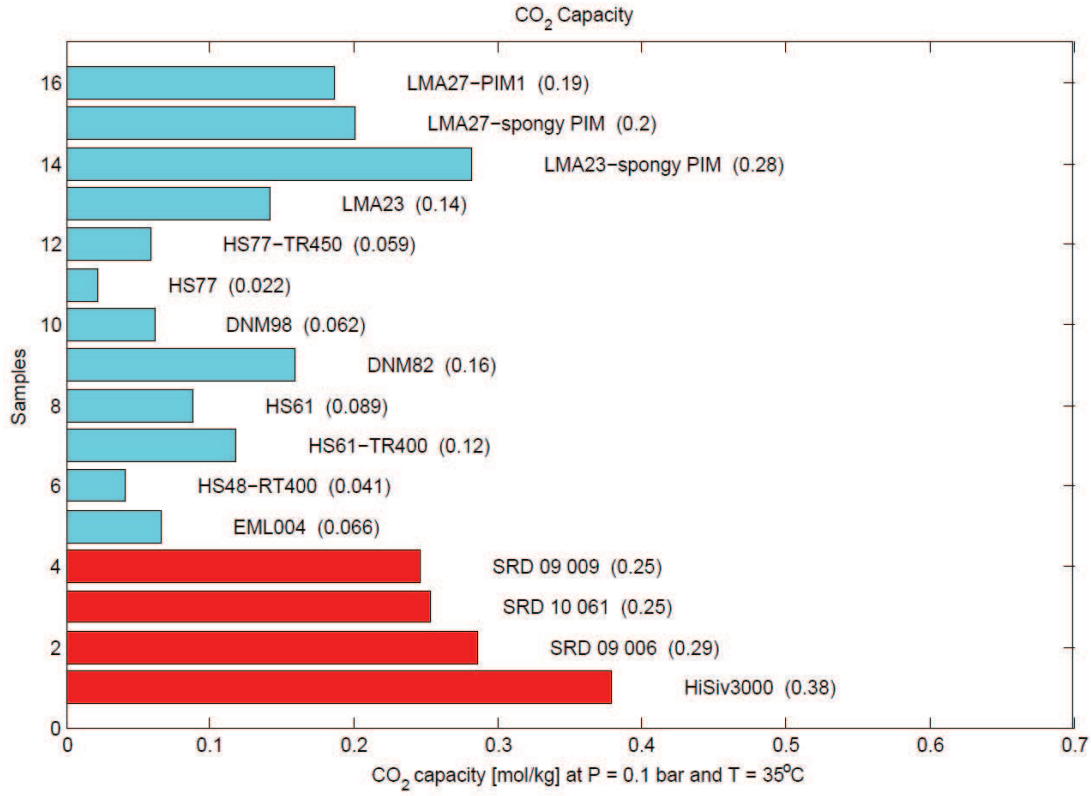

Figure 5.70: CO_2 capacity of PIM samples synthesised at the University of Manchester.

All the samples, due to their low capacity, showed ZLC curves relatively close to the blank, for this reason when the available amount of sample was enough to fill the cell of the Autosorb volumetric system, this one was preferred to the ZLC system.

This was the case of LMA27 and LMA27-spongy PIM-1: the adsorption isotherms obtained for these two samples are shown in Figure 5.71. A linear equilibrium relationship is observed for both the samples in the range of pressure investigated. The more open structure resulting from the different precipitation method allows for a slightly higher uptake in the spongy PIM-1 relative to the powder version.

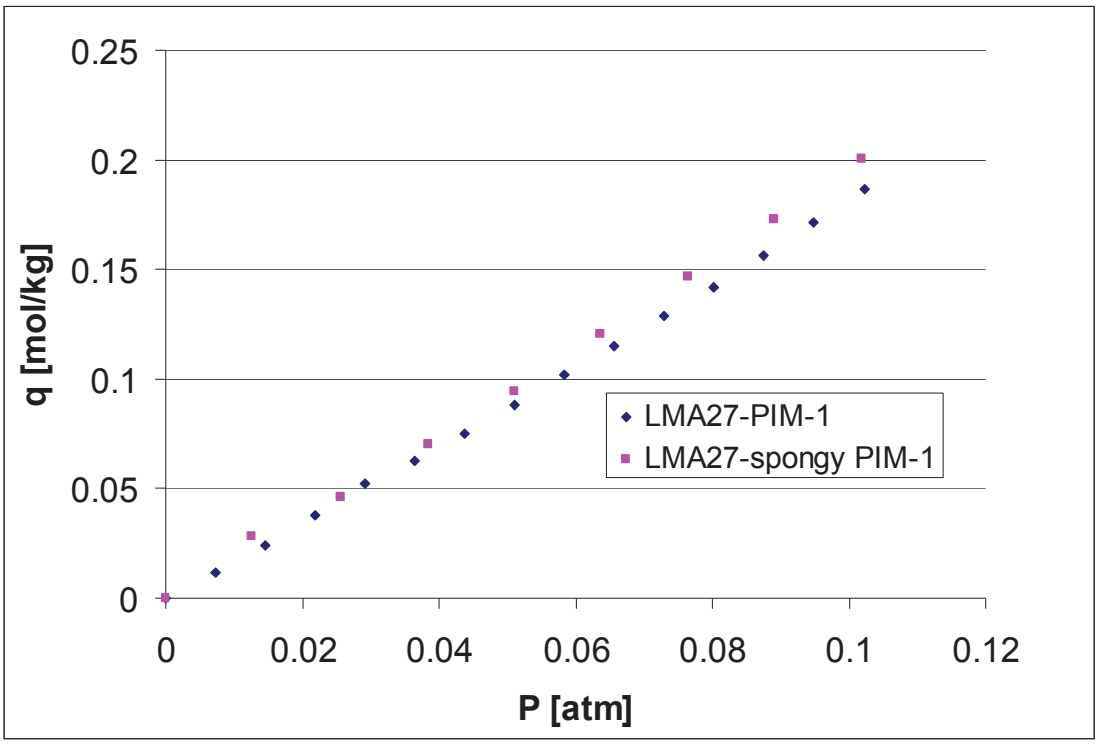

Figure 5.71: CO_2 isotherms at 35 °C measured with Quantachrome Autosorb volumetric system.

The thermal re-arrangement of the PIM-PI-OH samples increased the free volume available for the CO_2 molecules and this is reflected by the higher uptake observed in the thermally re-arranged samples relative to the pristine ones.

The introduction of amine groups in the structure of PIM-1 reduced the surface area, but the increased strength of the interaction with the CO_2 molecules seems to compensate for the reduced free volume. The resulting CO_2 capacity of DNM82 does not differ much from the one of LMA23, but it is higher than the capacity of the thermally re-arranged HS61 which has a similar value of the BET surface area. Figure 5.72 shows the ZLC desorption curves for DNM82. Even though the curves are quite close to the blank in the lower part of the long time asymptote, a kinetic effect is noted due probably to the strong interaction between the CO_2 molecules and the amine groups. Unfortunately, due to the low capacity of the sample, the kinetics of desorption could not be isolated from the response of the system, and no further investigations were performed.

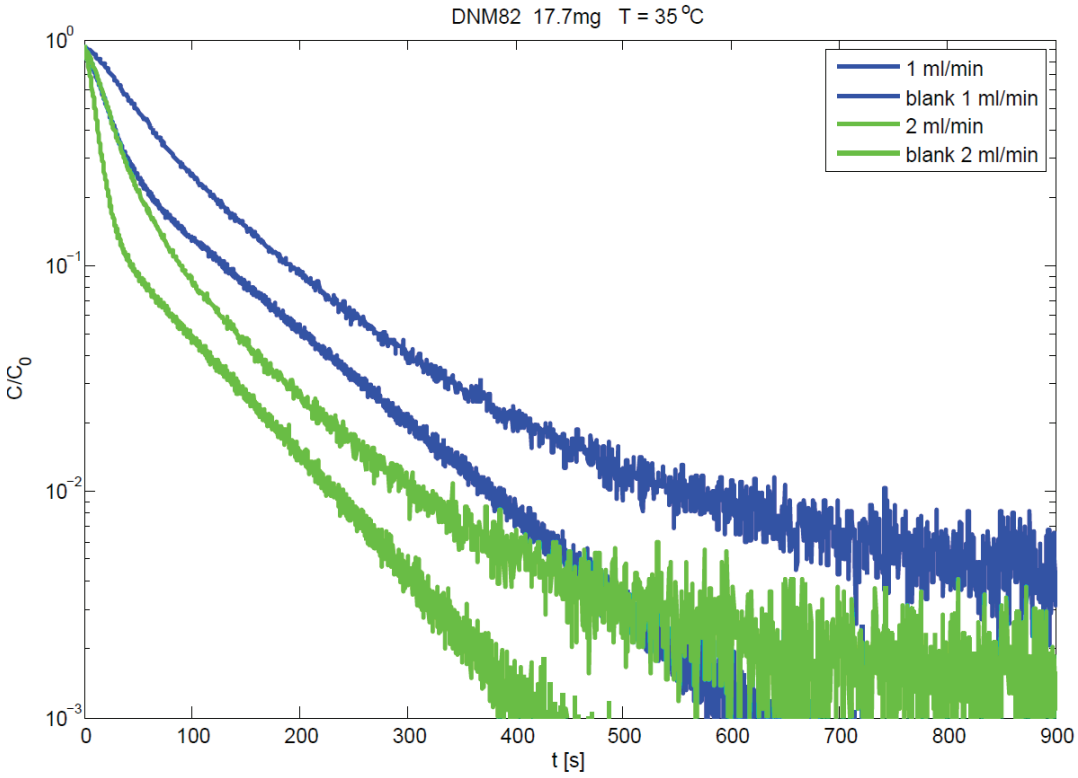

Figure 5.72: ZLC desorption curves for DNM82.

The poor performances of the PBI polymer at low temperatures were confirmed by the ZLC experiments. Due to the structure of the sample limited free space is available to the CO_2 adsorption, as shown by the BET measurement, resulting in a low value of the CO_2 uptake.

5.4.2 Conclusions

Different types of PIMs, synthesised at the University of Manchester, have been tested using the ZLC and the volumetric systems. All the samples showed a relatively low CO_2 uptake and none of them reached the CO_2 capacity of the benchmarks. For the different classes of PIMs the trend of the CO_2 capacity generally reflected the trend of the free volume available for the CO_2 adsorption. Some of the samples were subjected to specific treatments at the synthesis stage to open their structure creating more space for the adsorption CO_2. As a result the treated samples showed a higher uptake relative to the pristine samples.

Volumetric measurements on some the PIM-1 samples were used to obtain the CO_2 isotherms up to 0.1 bar and, as expected, a linear equilibrium was observed.

Due to the low uptakes, all the samples showed ZLC desorption curves too close to the blank response, but the ranking of the CO_2 capacity is in any case an useful indication of the expected trend of the solubilities in the case of using the materials to make mebranes. The low uptakes prevented further investigations with regard to the equilibrium and the kinetic properties of the materials, which are going to be carried out on a membrane permeation apparatus that has been built recently.

5.4.3 TB PIMS

As mentioned previously, the work at Cardiff University was mainly focused on the synthesis of Tröger's base PIMs and triptycene polymers. Tröger's base is a chiral molecule characterised by the presence of two nearly perpendicular aromatic rings fused to a central bicyclic. The resulting structure is a V-shaped molecular scaffold with total length of 1 nm. Incorporating this building block inside the structure of PIMs has the effect of increasing the rigidity of the chains, creating their characteristic "intrinsic" microporosity by reducing the efficiency of packing. On the other hand the presence of amine groups on the TB ring improves the affinity with the CO_2 molecules.

Triptycene is a molecule characterised by a rigid fused-ring skeleton, with a three fold symmetry which creates a high internal free volume. By nitration the molecule can be reduced to form a triptycene polymer which is characterised by high microporosity. Furthermore a decrease in surface area with increasing molecular weight is observed for the tryptycene polymer, which means that the longer chains reduce the accessibility of the resulting material.

Despite the promising characteristics of triptycene polymers the difficulty of synthesis and the relative high cost of this building block make this material not very suitable for large scale production; for this reason part of the samples were developed trying alternative synthesis solutions to triptycene. TB bisanilines, naphthalene polymers and anthracene polymers are some of the materials resulting from the use of building blocks cheaper than triptycene. On the other hand, different synthesis procedures were tried to overcome the difficulties deriving from the nitration of triptycene: the introduction of bromines, resulting in the synthesis of dibromotriptycene, was one of the attempts to simplify the preparation of triptycene. The obtained polymer had very low solubility which caused short polymeric chains and, as a result, a very low surface area.

The effect of quaternisation of the synthesised polymers was also investigated. The process consists in a series of reaction to convert the amine groups present in the structure creating ammonium compounds with four radicals. Generally a loss of

BET surface area is observed in the quaternised version of the materials, indicating that the pores have a poor accessibility for N_2 molecules.

In table 5.10 all the samples tested are listed, with the relative classification of the polymer type, BET surface area (measured at Cardiff University) and amount used in the experiments. All the tests were performed in the ZLC system, but as mentioned previously, due to the typical low uptakes of this class of materials, when enough amount was available, the Autosorb volumetric system was preferred. When thermo-gravimetric plots were provided with the samples, the amount used in the experiment was corrected for the weight loss due to the evaporation of water.

Table 5.10: Details of all the PIM samples. (*) No TGA available; (**) Tested in the Autosorb volumetric system.

Name	SAMPLE	BET [m^2/g]	Amount tested [mg]
CAT-A-TB	TB-spiro-bis-indane PIM ladder	628	7*
MC051	TB-Triptycene network	950	7.62
BD-154R	Triptycene-PIM-ladder	1064	7.76
PcFeBiPy450	Phthalocyanine	935	10.5*
MC060	TB-Triptycene ladder	850	8.56
EV37PPT3B	Indan TB-PIM	535	6*
MC108	Soluble TB –PIM ladder	400	6.3*
MC141	Insoluble TB –naphthalene PIM ladder	697	9.5*
MC143	Quaternised MC141	22	7.9*
MC158	Quaternary TB-crown ether PIM ladder	2	8.1*
MC164	Quaternary TB-PIM	0	14.7
MC165	Quaternary TB-PIM	3	16.3
FLU-ANILINE-TB	Flu-dianiline-TB PIM	80	10.8*
FLU-ANILINE-TB-Q	Quaternised Flu-dianiline-TB PIM	35	11.2*
MC209	Triptycene ladder	733	5.7*

1,3 DI-AMINO	TB-PIM	504	13.1*
2,5-dimethyl TB-poly	Dimethylbenzene- Triptycene	671	10.9*
SPIROFLUORENE	Spirobisfluorene ladder	566	7.3*
Ethano-Antracene	TB-PIM	870	12.6*
MC221	TB-bis-aniline	30	57.5**
MC224	TB-bis-aniline	73	83.8**
MC227	TB-bis-aniline	522	91.4**
MC231	Triptycene ladder	-	66.9**
MC245	Information not available	-	5.3**

A general synthesis procedure was followed for all the samples. First diamine is dissolved in trifluoroacetic acid stirring at 0 °C. Once diamine is dissolved, dimethoxymethane is slowly added. The reaction mixture is then stirred for 72 hours under nitrogen atmosphere and then quenched by adding water and aqueous ammonia (35%). The solution is then stirred vigorously for three hours and, finally, the polymer is collected by filtration. Once collected, the polymer is washed with water and acetone and dried under vacuum. The resulting polymer is then dissolved in chloroform and re-precipitated using hexane for three times and after that refluxed in acetone and methanol for 16 hours. Finally the product is dried at 120 °C for eight hours under vacuum.

Since the microporosity of PIMs is strictly dependent on the building blocks used, knowing the molecular structure is particularly useful in the discussion of the CO_2 adsorption properties: the different structures of all the samples tested are shown in Figure 5.80 to Figure 5.80 at the end of this section.

In Figure 5.73 the ranking of the CO_2 capacity for all the samples is reported. As for the other PIMs presented in the previous section the results are compared with HiSiv3000 and Calgon activated carbons as benchmarks.

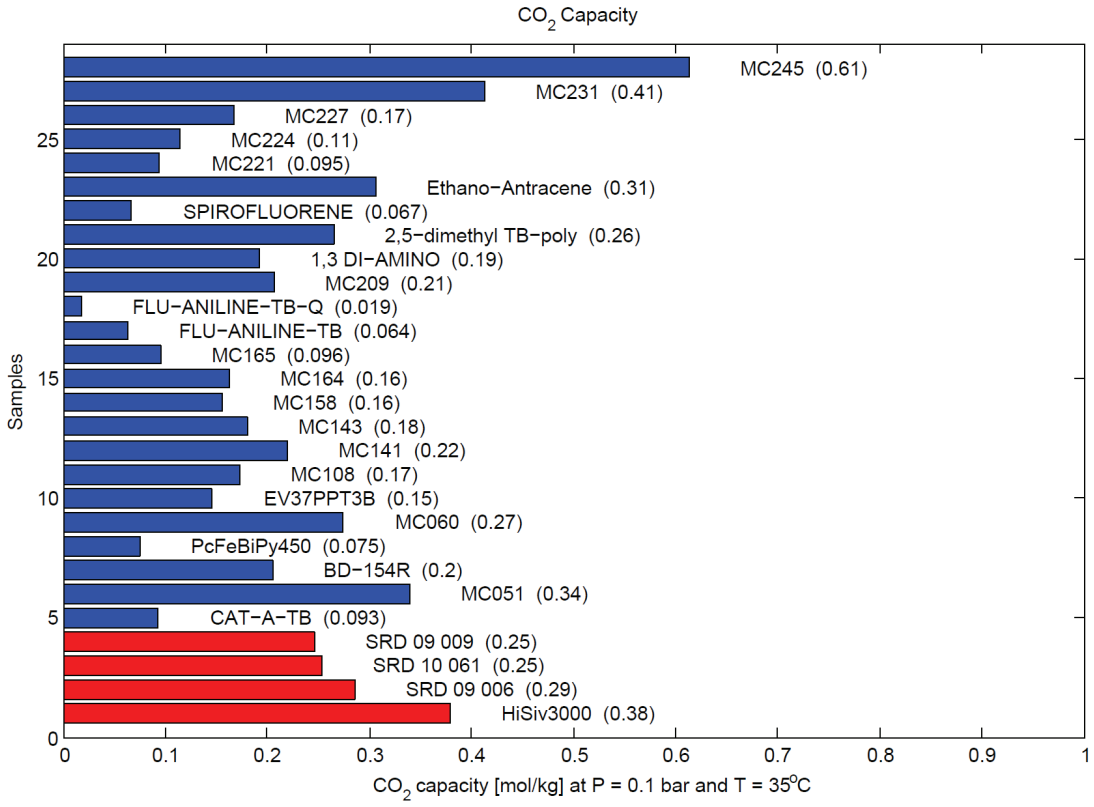

Figure 5.73: Ranking of the CO_2 capacity of the PIM samples. In the red the commercial adsorbents used as benchmark.

From Figure 5.73 it can be seen that, on average, the values of the CO_2 capacity obtained are higher than the ones observed for the PIMs synthesised at the University of Manchester. This proves that introducing amine groups into the structure of PIMs has generally a positive effect on the resulting CO_2 capacity of the materials due to the increased affinity with CO_2.

The sample that shows the highest capacity is the dibromotriptycene MC245.

The monomer showed poor solubility in chloroform, as a consequence of the low molecular weight of the polymer. Furthermore, the presence of bulky bromine atoms definitely hinders the access of N_2 molecules and, as a result, a very low value of the surface area is observed. All these are generally non-desirable features for a CO_2 adsorbent and for this reason a low capacity was expected for this sample. However the relative high value of the CO_2 capacity could be related to the presence of the bromine atoms, which somehow have a positive effect on the

affinity of this polymer with CO_2, even though the nitrogen content of the structure is a lot lower than other normal triptycenes.

It has also to be noted that despite the volume of the sample tested was enough to fill the sample cell of the volumetric system the total weigh of the sample was very low. This might introduce some uncertainty in the measurements of the isotherm, especially relative to the points at lower pressure, as can be seen from Figure 5.74. The experiment was repeated twice and the isotherm could be reproduced: the issue with the first point of the isotherm was then assumed to be more related to the accuracy of the instruments, due to the low weight of the sample and low partial pressure of CO_2 points.

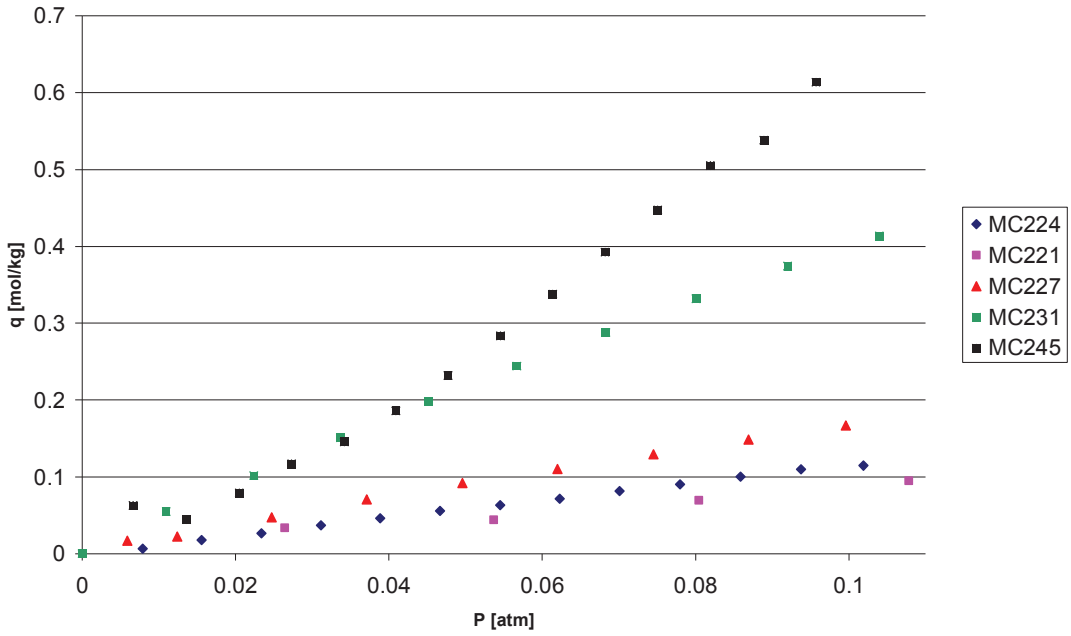

Figure 5.74 : CO_2 isotherms at T = 35 °C obtained from the Autosorb volumetric system.

The samples MC209, MC060 and MC231 are all triptycene polymers with the same structure. The samples present high surface areas and reasonable nitrogen content per unit cell, from which the generally good performance of the trypticene polymers arises. The difference in results between the three batches is mainly due to the molecular weight; it seems that as the molecular weight increases the pores become slightly less accessible (resulting in a lower surface area), but, on the other hand, the number of sites available for CO_2 adsorption increases.

The TB-PIMs show generally a good uptake and this confirms that the presence of the TB unit in the structure definitely improves carbon dioxide affinity of the polymers.

The MC051 and the ethano-antracene are characterised by a very high surface area (i.e. very accessible pores) and a reasonably high nitrogen content which obviously contribute to the very good performance of these samples relative to the other TB-PIMs.

A slightly lower capacity is observed for the dimenthylbenzene trpitycene polymer (2,5-dimethyl TB polymer). The sample has the same structure of MC108 but higher uptake. Both the samples present a structure with accessible pores and very high nitrogen content. As before, the difference in the results has to be associated to the difference in the polymer chains length: the shorter chains of the MC108 sample resulted in a lower capacity.

Looking at the effect of quaternisation of the PIMs is clear that the quaternised forms of the polymers show a considerable loss of CO_2 performances compared to the original polymers. In the case of the Flu-Aniline-TB the starting properties of the sample were pretty poor, due to the presence of the bulky fluorene group which greatly reduces the accessibility of the pores, as proved by the low value of the surface area. The quaternised form of this polymer registered the lowest CO_2 uptake among all the PIMs. This can be explained mainly by the reduced surface area induced by the quaternisation process.

The MC165 and MC164 have very similar structures. They both suffer from having no surface area due to the presence of the counter ion which fills up the available free volume. In the case of the MC164 the counter ion is smaller than the iodine ion present in MC165: this might help the diffusion of the CO_2 molecules allowing them to get closer to the quarternary nitrogen. This explains the higher uptake of MC164 relative to the similar MC165. However it has to be noted that both the polymers show an uptake higher than some other samples with higher surface area which proves the positive action of the presence of the quaternary nitrogen.

The MC141 sample showed a decent CO_2 capacity due to the high nitrogen content, high surface area and readily accessible pores. Its quaternised form, MC143, shows

a slight loss of performance but less than MC165. This is due to the fact that in this case this polymer was only 80-90% quarternised. The presence of less hindered space due to the lower content of iodine counter ions definitely aids the adsorption of CO_2.

The samples MC227, MC224 and MC221 are characterized by a similar molecular structure and relatively low nitrogen content, which prevent the samples to reach good uptakes. The trend of the CO_2 capacities basically reflects the trend of the surface area, in the order MC227 > MC224 > MC221.

With regard to the role of the surface area, the BD-154R sample is characterised by an extremely high surface area but, despite the expectations, this polymer suffers from poor carbon dioxide capacity. The main reason for this could be ascribed to the lack of basic nitrogen atoms, which should be helping affinity, and also to the lower accessibility of the pores of this structure relative to other PIMs with high surface area. In fact at the temperature at which the N_2 uptake experiment is carried out the chains of the polymer cannot move because of the low temperature: the structure is static. At higher temperature the mobility of the chains is increased, the structure is not more static and the movement of the chains can make the access of the CO_2 to the free volume of the material more difficult. The importance of this effect is different for the different polymers, but length and rigidity of the chains play clearly a critical role.

Poor accessibility of the pores is also the main reason for the lack of performance for TB Spirofluorene, which shows a reasonable surface area but one of the lowest observed uptake.

On the other hand, in the case of MC158, despite the lack of surface area and nitrogen content, the presence of large pores and high oxygen content per unit cell definitely contributes to the decent CO_2 capacity observed.

The phthalocyanine sample (PcFeBiPy450) is characterised by high nitrogen and oxygen content and a very high surface area. All these features suggest a good affinity with CO_2 which is not reflected by the results. This might be due to the high degree of flexibility of the polymer chains which somehow hinders the access for the CO_2 molecules.

Finally, the performance of EV37PPT3B and 1,3-diamino reflect what is expected from the respective values of the surface areas measured. The CAT-A-TB, despite the reasonable surface area, suffers from the low nitrogen content which reduces the affinity with CO_2.

In Figure 5.74 the CO_2 isotherms for some of the samples measured in the volumetric system are presented. The experiments were performed at 35 ºC up to a pressure of 0.1 bar. As expected, all the samples show a fairly linear isotherm in the range of interest. As mentioned previously the first point of the isotherm for the MC245 sample was attributed to some issue of the instrument due to the low amount of sample used.

Figure 5.75 and Figure 5.76 show the ZLC desorption curves for two of the best PIM samples. As observed for the PIM samples from the University of Manchester, the response curve is too close to the blank response of the system, due to the relatively low value of the CO_2 uptake. The impossibility of isolating the response of the system from the desorption curve of the sample prevents any further investigation with regard to the kinetic properties of the samples.

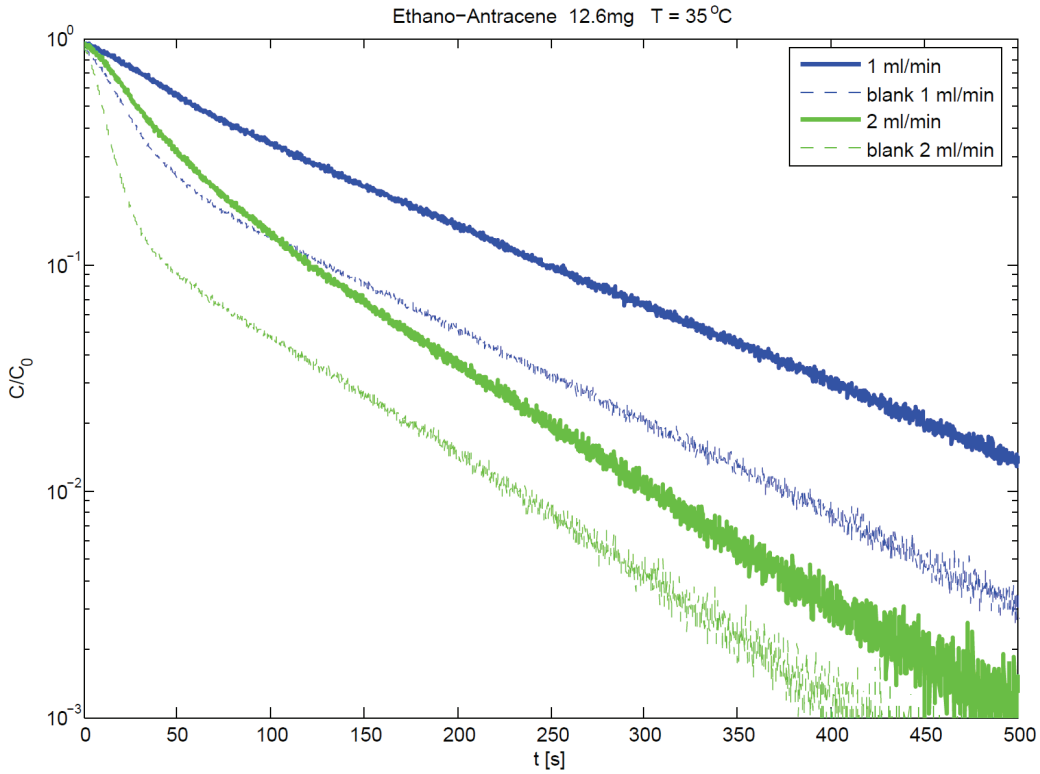

Figure 5.75: ZLC desorption curves for Ethano-Antracene, T = 35 °C and P = 0.1 bar.

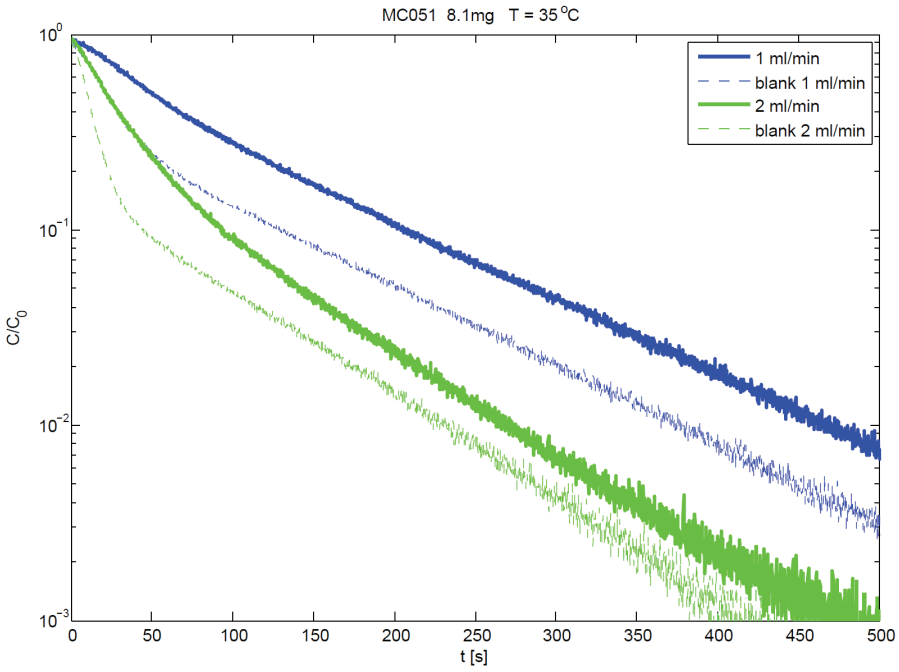

Figure 5.76: ZLC desorption curves for MC051, T = 35 °C and P = 0.1 bar.

5.4.4 Conclusions

Different types of Tröger's base PIM and triptycene polymers were tested using the ZLC and the volumetric system. Higher values of the CO_2 capacity were obtained for these samples relative to the PIMs synthesised at the University of Manchester. This confirmed that the introduction of amine groups in the structure of PIMs definitely increases the affinity with the CO_2 molecules. Three key factors were identified for the resulting CO_2 uptake: surface area, nitrogen content and accessibility of the pores. Ideally, high surface area and high nitrogen content are desirable, but a key role is also played by other characteristics of the polymers, such as chain length and rigidity, which can influence the accessibility of CO_2 to the free volume. Quaternisation of the polymers generally reduced the performances of adsorption, because of the presence of the counter ion which hinders the access to the quaternised nitrogen: this is also confirmed by the lower value of the surface areas observed. Due to the low capacities of the samples, the ZLC response curves

resulted to be too close to the blank to be further investigated with regard to the equilibrium and kinetic properties.

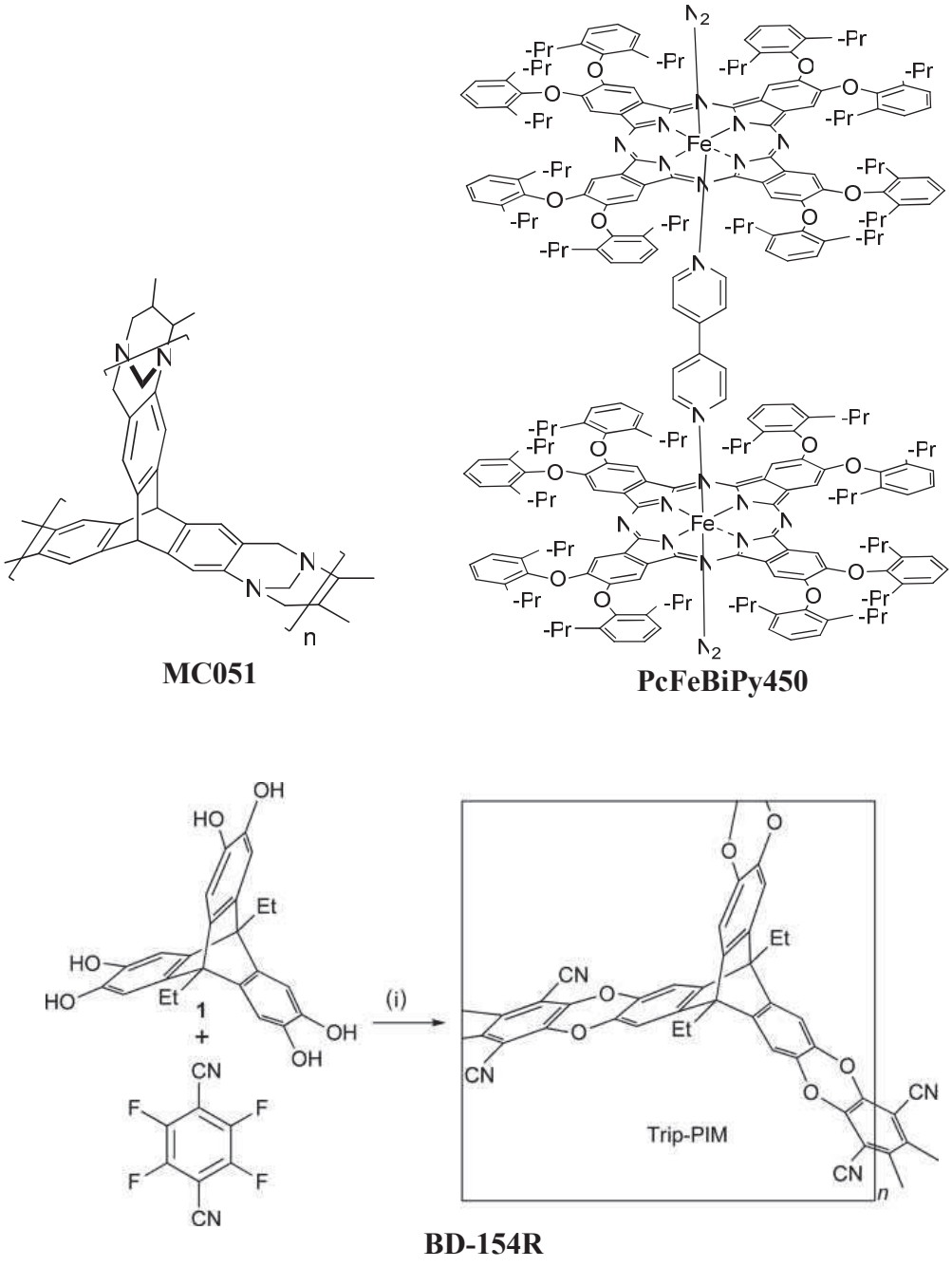

Figure 5.77: Molecular structures of the different PIMs, part 1.

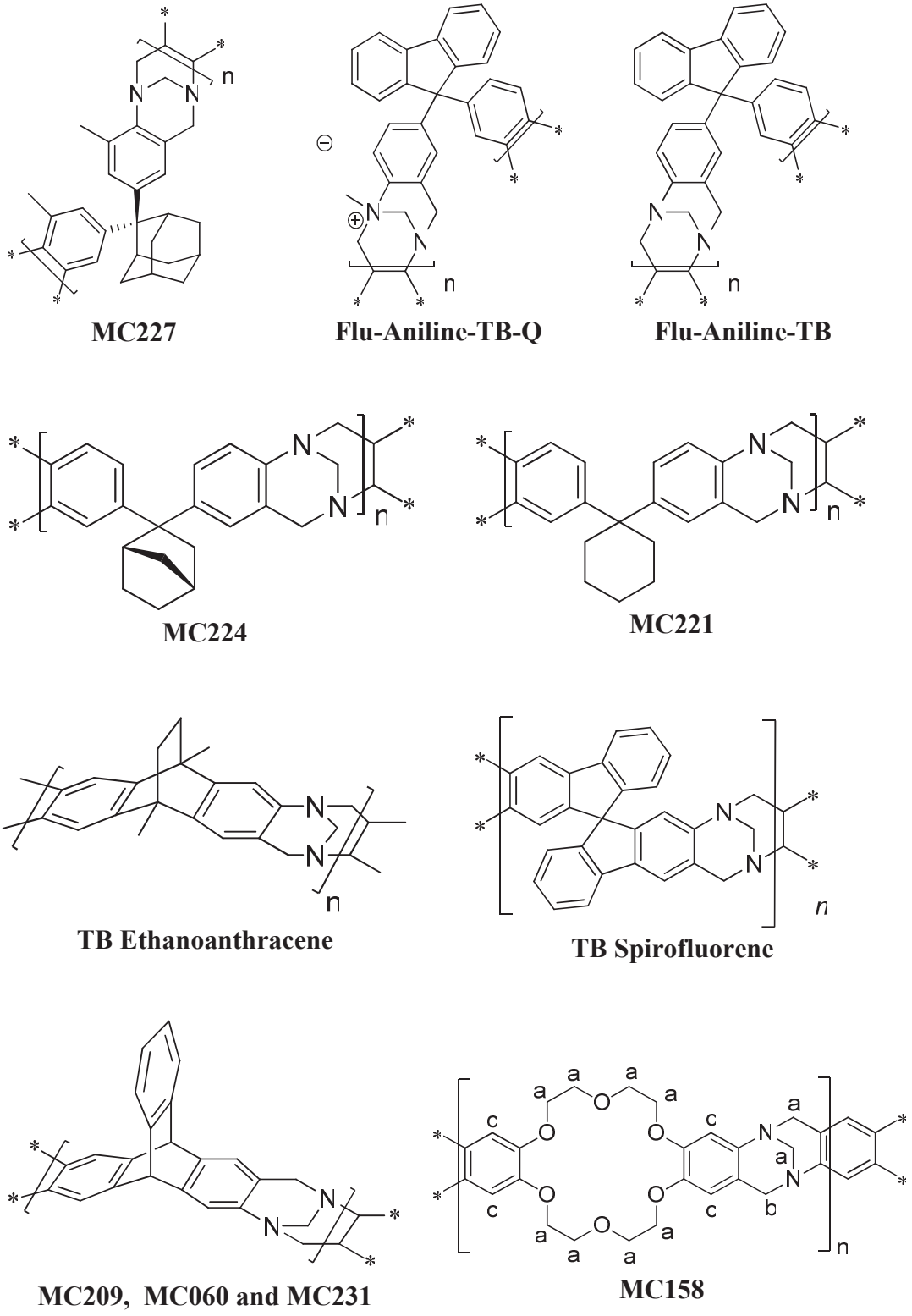

Figure 5.78: Molecular structures of the different PIMs, part 2.

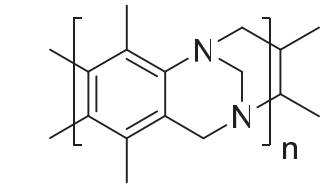

2,5-dimethyl TB polymer and MC108

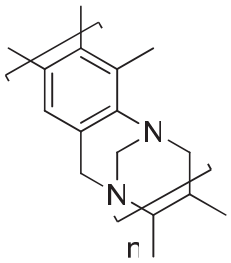

1,3 Diamino

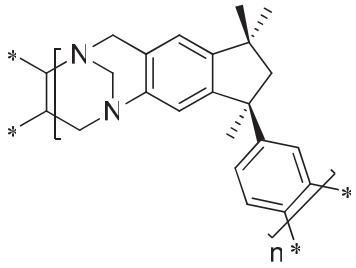

EV37PPT3B

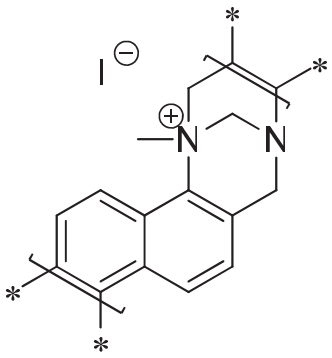

MC165

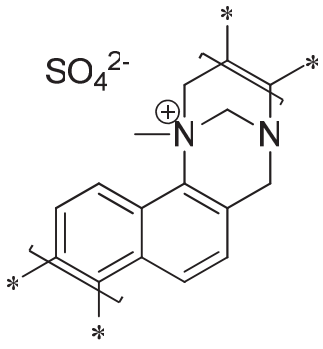

MC164

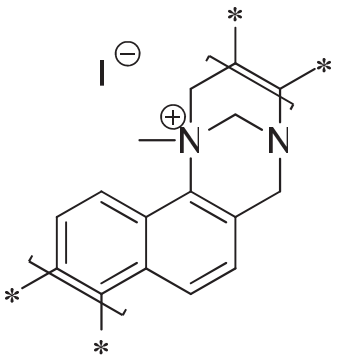

MC143

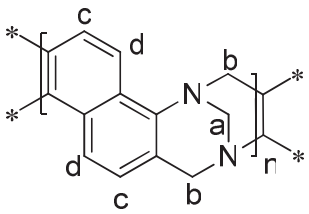

MC141

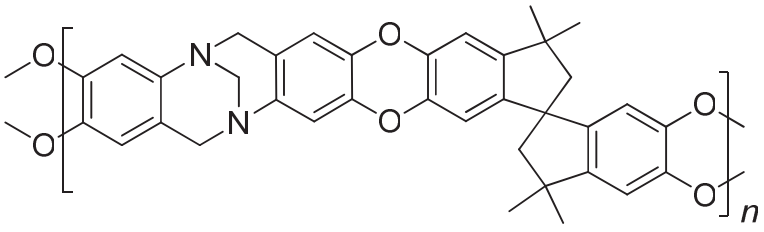

CAT-A-TB

Figure 5.79: Molecular structures of the different PIMs, part 3.

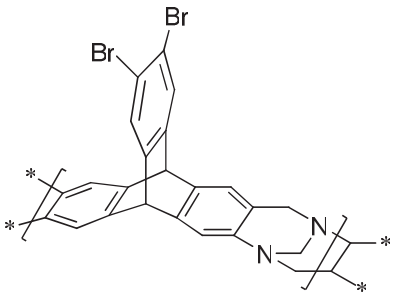

MC245

Figure 5.80: Molecular structures of the different PIMs, part 4.

6. DIFFUSION MEASUREMENTS IN ION-EXCHANGED RHO ZEOLITES USING THE ZLC METHOD

As reported in the chapter about to the ranking of the adsorbents, the ZLC experiments on some of the Rho zeolites showed evidence of a slow diffusion process which controlled the rate of desorption of CO_2 from the samples. The presence of a kinetically controlled adsorption process was not immediately identified and an apparent low capacity measured. The first sample of the series to be tested was Na,Cs-Rho (MML313). The initial experiments were carried out in the traditional ZLC system (at 30 and 40 ml/min) and the sample was saturated for 1 hr, following the procedure similar to other adsorbents. It was then observed that the time needed to reach the full desorption was longer than the one observed for the analogue ion-exchanged Chabazite samples, with similar structure. It was decided to re-test the sample in the semi-automated ZLC system in which it is possible to follow the signal more accurately and run the system at lower flowrates. The sample was saturated for 2 hr at low flowrate and the resulting capacity was almost double. Although the signal monitored by the mass spectrometer seemed already to have reached complete saturation the sample was re-tested increasing the saturation time first to 3 hr then to 5 hr and finally to 7 hr until the resulting CO_2 capacity did not vary with the saturation time. It has to be noted that the monitored variable is the concentration in the fluid phase, and this sample revealed to be a clear case in which even though the system appears to be equilibrated in the fluid phase the mass transfer resistance prevented equilibrium to be reached in the adsorbed phase [85].

The same procedure was followed for all the other samples tested in the present study with particular attention to all the Rho zeolites, which were then further investigated with regard to the kinetics of diffusion of CO_2. This section presents the results of the diffusion measurements on Na,Cs-, Na,H-(10, 8.5 and 7 Na/unit cell), K- and Li-Rho. The results obtained will be discussed in separate sections for each type of Rho zeolite.

6.1 Na,Cs- Rho

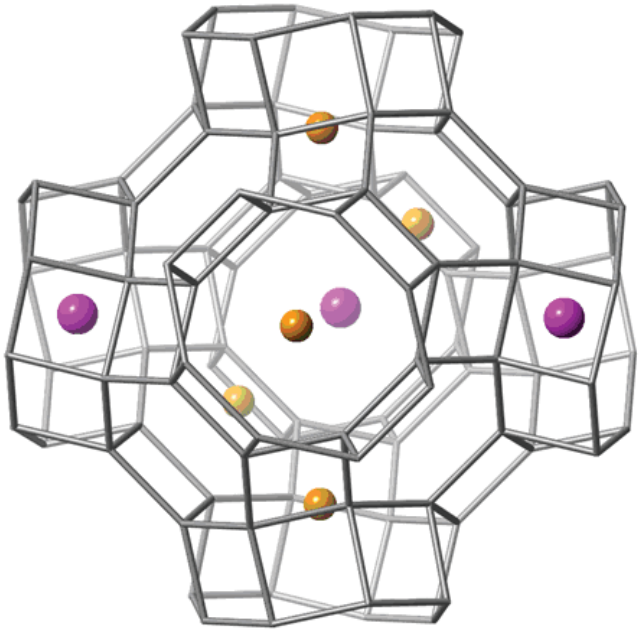

Figure 6.1: Possible cation distributions in one α-cage and associated D8R windows of dehydrated univalent cation forms of zeolite Na,Cs-Rho, determined from Rietveld refinement of laboratory X-ray powder diffraction data [107]. Larger spheres = Cs; smaller spheres = Na.

Figure 6.1 shows the cations distributions inside the framework of Na,Cs Rho as determined by the measurements carried out from the University of St. Andrews[107]. Clearly half of the D8R windows which allow the access to the α-cage are occupied by the large Cs cations while the other half are occupied by Na^+. It was already pointed out that the fact that a considerable CO_2 uptake is observed indicates that somehow the Na or Cs (or both) cations can move from their position to let the CO_2 enter inside the cage. This mechanism has been recognised as the origin of the slow adsorption/desorption rate characteristic of this sample.

The ZLC experiments on the Na,Cs-Rho samples resulted to be a very interesting example on how difficult it can be to obtain reliable diffusion measurements for particular systems. Figure 6.2 shows the ZLC experimental curves at two different flowrates. The curves are analysed at different desorption times (from 200 to 2000 s

from the start of the desorption) and the experimental data are fitted using the theoretical model for the ZLC response curves, eq. 3.5. The plots clearly show that by changing the final time of the analysis different values of L and D/R^2 can be used to produce a good fit of the experimental data. Table 6.1 shows the set of parameters used for the fitting at different desorption times (t_{fin}).

In order to obtain an unambiguous value of the diffusivity a series of partial loading experiments at different flowrates were carried out on the sample. Figure 6.3 shows the experimental curves of the fully and partially saturated experiments at 2 ml/min with the relative curves predicted using eq. 3.5 and 3.15. As comparison in the same plot the predicted curve for the partial loading using the time constant obtained from the fitting of Figure 6.2b is displayed. It can be easily seen that the only value of the diffusional time constant which allows to predict the partial loading response is the one relative to the last set of data from table 6.1. This indicates that the process is governed by a single diffusional time constant, excluding the presence of a particle size distribution inside the column (i.e. same D but different R^2).

Table 6.1: Values of γ, L and D/R^2 used to predict the experimental ZLC curves at different desorption times (t_{fin}).

t_{fin} [s]	L for 2 ml/min	D/R^2 [s^{-1}]	γ
200	10	$5x10^{-4}$	0.045
400	16	$2.5\ x10^{-4}$	0.045
1000	31	$1\ x10^{-4}$	0.045
1500	37	$8\ x10^{-5}$	0.045
2000	47	$6\ x10^{-5}$	0.045
4000	76	$3.5\ x10^{-5}$	0.045

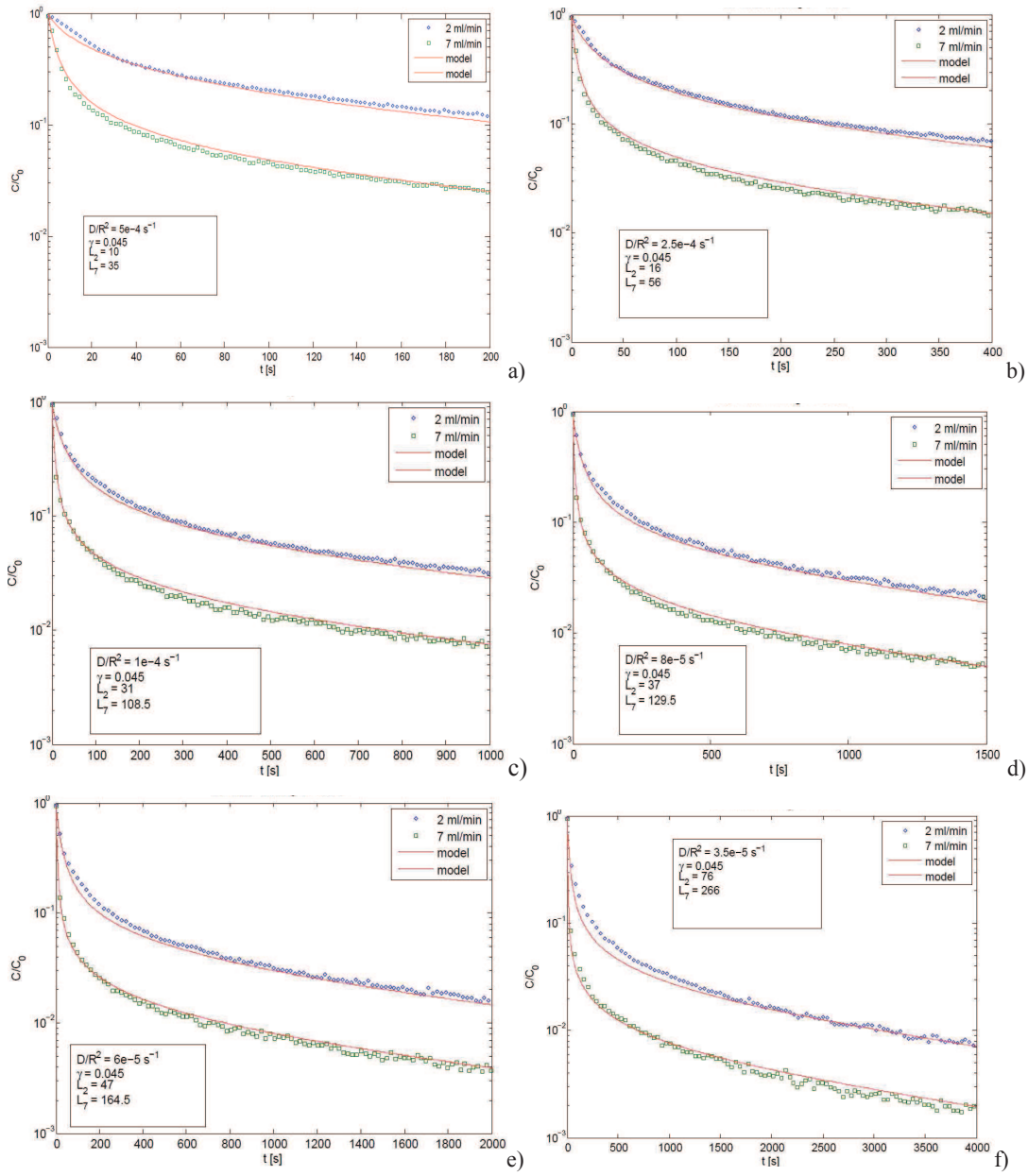

Figure 6.2: ZLC desorption curves at 35 °C for Na.Cs-Rho analysed at different desorption times. In red the predicted curves using eq. 3.5.

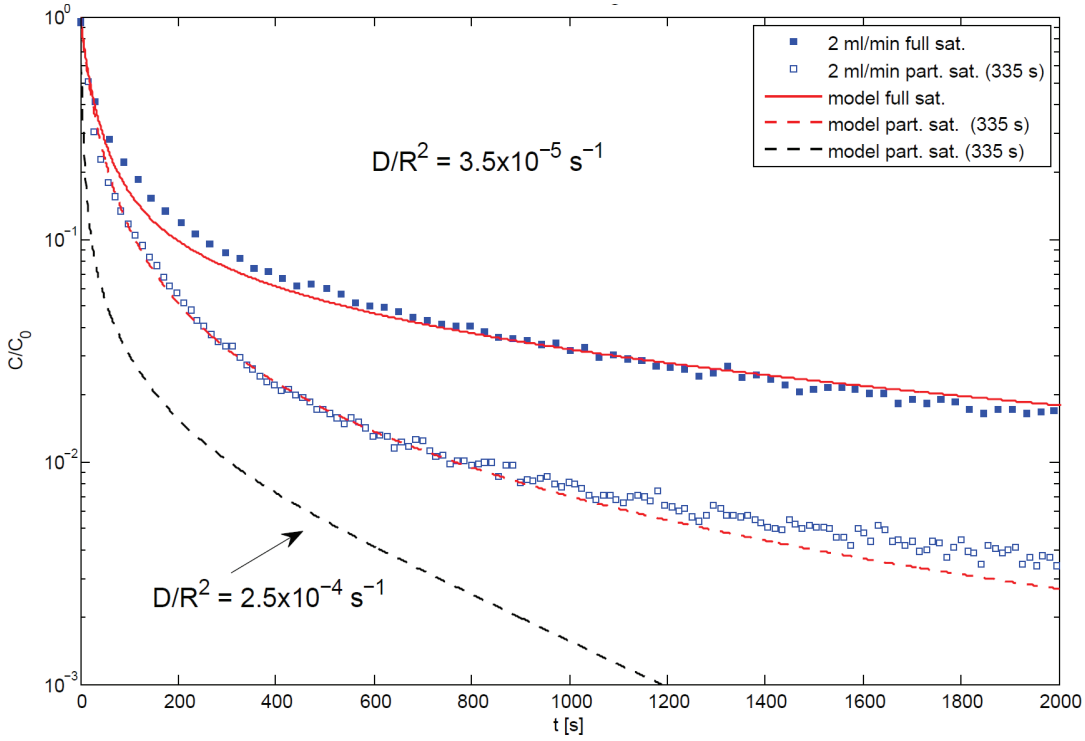

Figure 6.3: Experimental ZLC desorption curves for the fully and partially saturated Na,Cs-Rho sample; in red the predicted curves using eq. 3.5 and eq. 3.15.

The L and D/R^2 parameters, extracted from the fitting of the fully saturated experiment, allow to predict with a very good agreement the partial saturated experiment, by using the value of τ, the loading time known from the experiment. In the case of the fully equilibrated experiment the theoretical model slightly underestimates the desorption rate at high CO_2 concentration. This can be associated to the fact that, at the initial conditions of the desorption experiment, the system is operating beyond the Henry's law region, as confirmed by the CO_2 isotherm measured at the University of St. Andrews [107]. It is worth to point out that the deviation from linearity does not affect the slope of the long time asymptote, i.e. the estimation of the diffusional time constant, which falls in the Henry's law region [83]. Relative to a normal ZLC response curve the non-linearity increases the time needed to reach the long time asymptote resulting in a response curve with the same slope but a lower intercept. It has also to be noted that the non-linearity of the isotherm does not affect the partial loading experiment. Due to the limited exposure

time to the sorbate and the diffusional resistance, the average concentration inside the solid is maintained low enough to be within the linear region.

Figure 6.4 shows the concentration profile of the adsorbed phase for the fully and partially saturated experiment calculated by integrating the ZLC curves according to equation below:

$$\frac{q}{q_0} = 1 - \frac{\int_0^t \frac{c}{c_0} dt}{\int_0^{\infty t} \frac{c}{c_0} dt}$$

The fact that the curve of the partial loading experiment does not overlap with the one of the fully saturated experiment confirms the presence of an internal diffusion process.

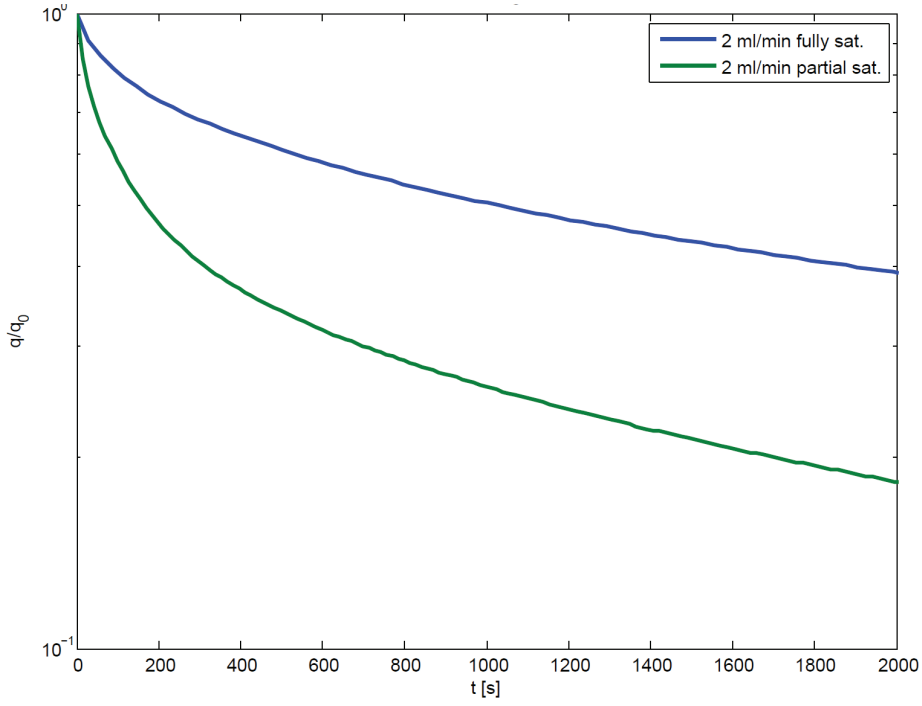

Figure 6.4: Concentration profile of the adsorbed phase for the fully and partial saturated experiment at 35 °C for Na,Cs-Rho.

In order to obtain the activation energy for the diffusion process, partial loading experiments were performed also at different temperatures: 35, 50, 70, and 90 ˚C. From the Arrhenius equation:

$$D = D_0 \exp\left(-\frac{E_a}{RT}\right)$$

the value obtained for the activation energy is 34 kJ/mol.

Table 5.2 shows the diffusional time contestants extracted from the experiments at different temperatures. The values of diffusivity reported are calculated assuming a crystal radius of 50 nm, according to the measurements performed at the University of St. Andrews [107]. The ZLC curves at the different temperatures are reported in Appendix B.

Table 6.2: Diffusional time constants and diffusivities at different temperatures for Na,Cs-Rho tested using the ZLC partial loading experiment. The diffusivity was calculated based on a particle radius of 50 nm [107].

SAMPLE	$D/R^2 \times 10^{-5}$	$D \times 10^{-19}$	T
	$[s^{-1}]$	$[m^2/s]$	[°C]
Na,Cs-Rho	3.50	0.875	35
	5.66	1.42	50
	8.70	2.18	70
	27.5	6.88	90

6.2 Na,H- Rho

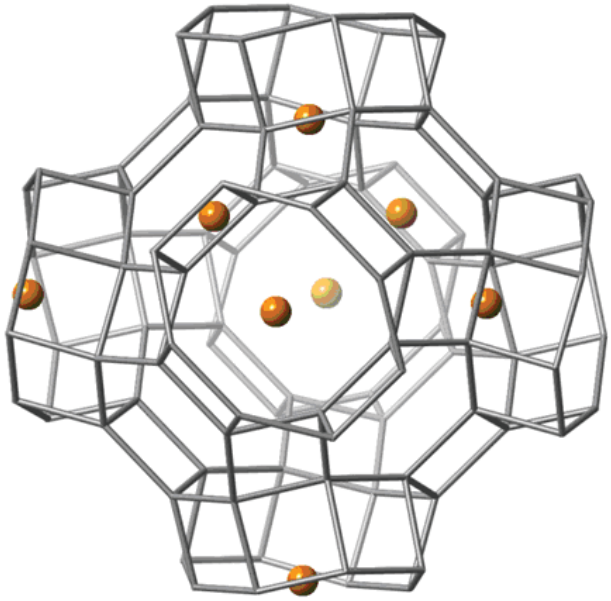

Figure 6.5: Possible cation distributions in one α-cage and associated D8R windows of dehydrated univalent cation forms of zeolite Na-Rho, determined from Rietveld refinement of laboratory X-ray powder diffraction data [107].

Figure 6.5 shows the distribution of the Na cations inside the α-cage of the fully exchanged Na-Rho, similarly to Na,Cs-Rho the cations are located in the D8R sites blocking the entrance to the cage, but in presence of CO_2 Na^+ is probably able to move allowing the diffusion of CO_2.

Figure 6.6 shows the experimental curves for the fully and partially saturated case and the relative predicted curves. As in the case of the Na,Cs-Rho sample the L and D/R^2 parameters from the fully equilibrated experiment allowed the prediction of the partially loaded ZLC response curve with a good agreement with the experimental data. Although there is a good fit of the partially saturated experiment, a considerable gap between the predicted curve and the experimental data is observed at high CO_2 concentrations for the fully equilibrated experiment. By looking at the initial part of the full saturated curve it can be seen that the experimental response is considerably faster at high CO_2 concentration if compared to the predicted curve: the model underestimates the desorption rate at high CO_2 concentrations.

Differently from the case of the Na,Cs-Rho sample this discrepancy cannot be addressed exclusively to the non-linearity of the isotherm, since the shape of the isotherm does not differ considerably from the one of Na,Cs-Rho [107]. Moreover by looking at the initial part of the experimental curve, the exclusive contribution of the non-linearity on the ZLC response should produce a curve with a shape similar to the one of the sample partially loaded: the approach to the long-time asymptote would be slower if compared with a ZLC experiment starting from the Henry's region. The trend observed indicates that a second contribution influences the response of the system. Measurements performed at the University of St. Andrews proved that structural changes occur in Na-Rho with variable CO_2 loading: the size of the 8MR windows increases from 2.26 Å in the dehydrated form to 2.75 Å at partial pressure of CO_2 of 0.1 bar, resulting in a faster diffusion of CO_2 at higher coverages [107]. The fact that this effect is visible in the ZLC experiments might indicate that the time constant of the kinetics of the structural changes is comparable to that of the diffusion of CO_2 through the sample. Should the structural change be a much slower process, a faster diffusivity would have been observed corresponding to the original structure. If the structural change was much faster, then the external layer of the crystals would rearrange rapidly to the final configuration and the measured curve would have been very similar to a single diffusion process.

To confirm this hypothesis, a low concentration ZLC experiment was carried out, Figure 6.7. In this experiment the sample was fully equilibrated with a feed mixture with just 1% of CO_2: the aim is to operate the system at a sorbate concentration low enough to exclude the contribution of the non-linearity. Moreover in these conditions the low concentration of CO_2 should induce only minor changes in the structure of the framework.

In Figure 6.7the diffusional time constant obtained from the fully saturated experiment at 10% of CO_2 was used to fit the experimental data. Clearly, the model allows to predict the experimental data in all the range of concentrations, indicating that under these conditions the desorption process is governed by a single diffusivity/structure.

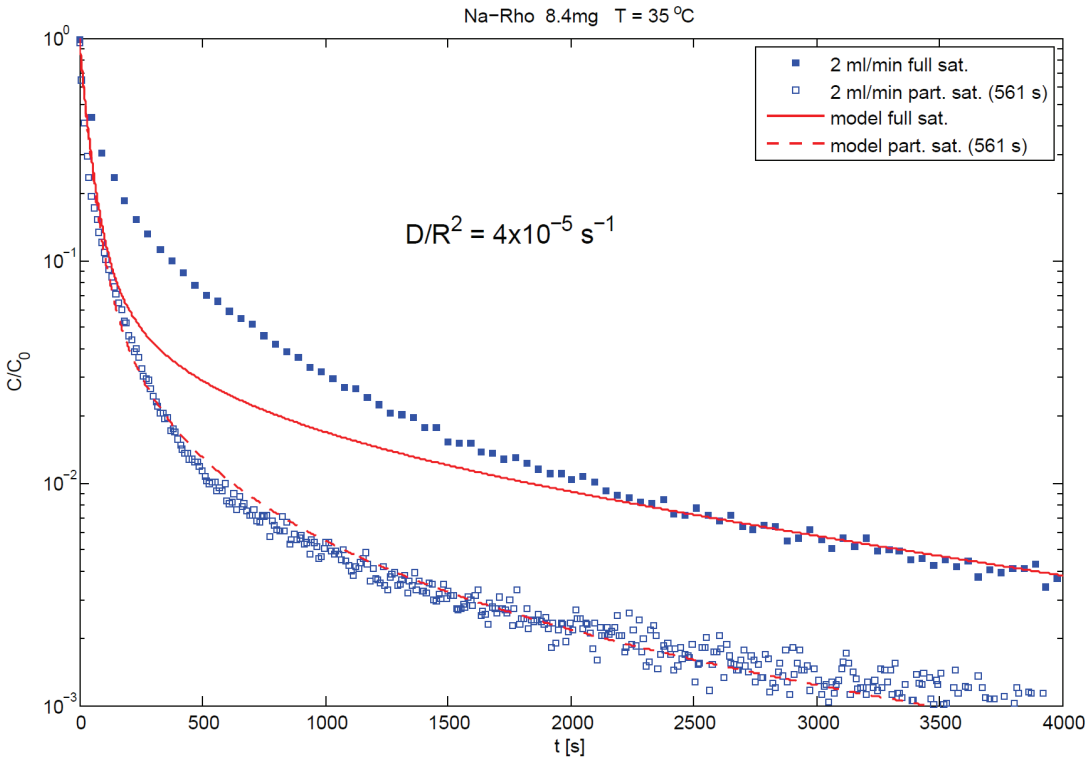

Figure 6.6: Experimental ZLC desorption curves for the fully and partially saturated Na-Rho sample; in red the predicted curves using eq. 3.5 and eq. 3.15.

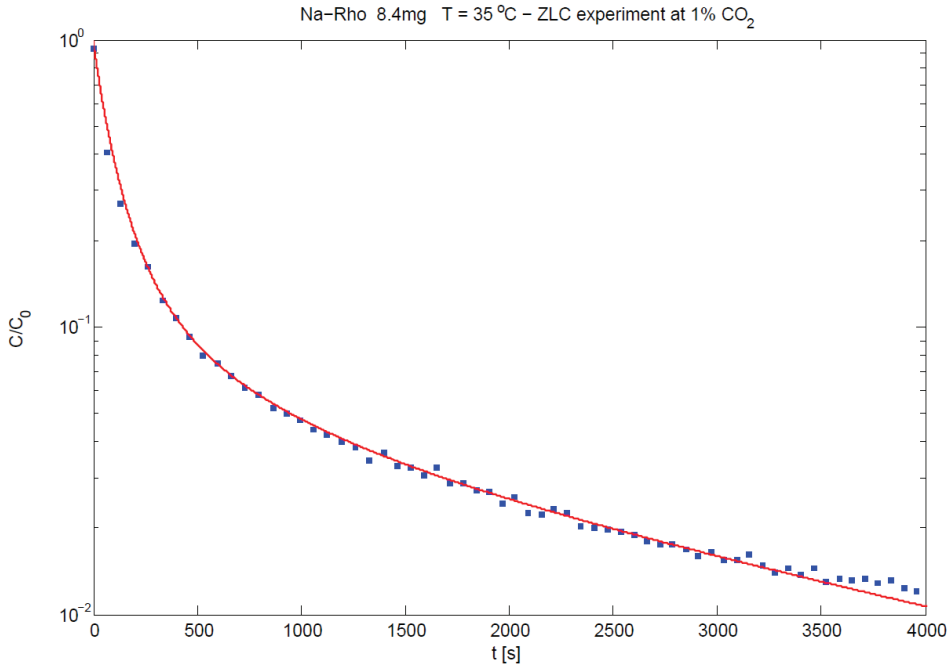

Figure 6.7: Low loading ZLC experiment on Na-Rho at 1% of CO_2 and 1ml/min; in red the predicted curve using eq. 3.5.

The good prediction of the partial loading experiment in Figure 6.6 indicates that, due to the diffusional resistance, the average concentration inside the solid is so low that no significant modifications occur to the structure: the operating conditions should not differ much from the ones of the experiment at 1% of CO_2. For this reason it becomes interesting to compare the profile of the adsorbed phase concentration between the three cases of interest: full saturation at 10% and 1% of CO_2, and partial saturation.

As explained in section 3 about the theory of the ZLC the theoretical model can be solved with respect to the adsorbed phase concentration obtaining eq. 3.19.

Figure 6.8 shows the predicted adsorbed phase profiles inside the crystal for the partially and fully saturated cases at different desorption times: the curves were obtained using the values of L, D/R^2 and γ, extracted from the fit of the experimental ZLC curves.

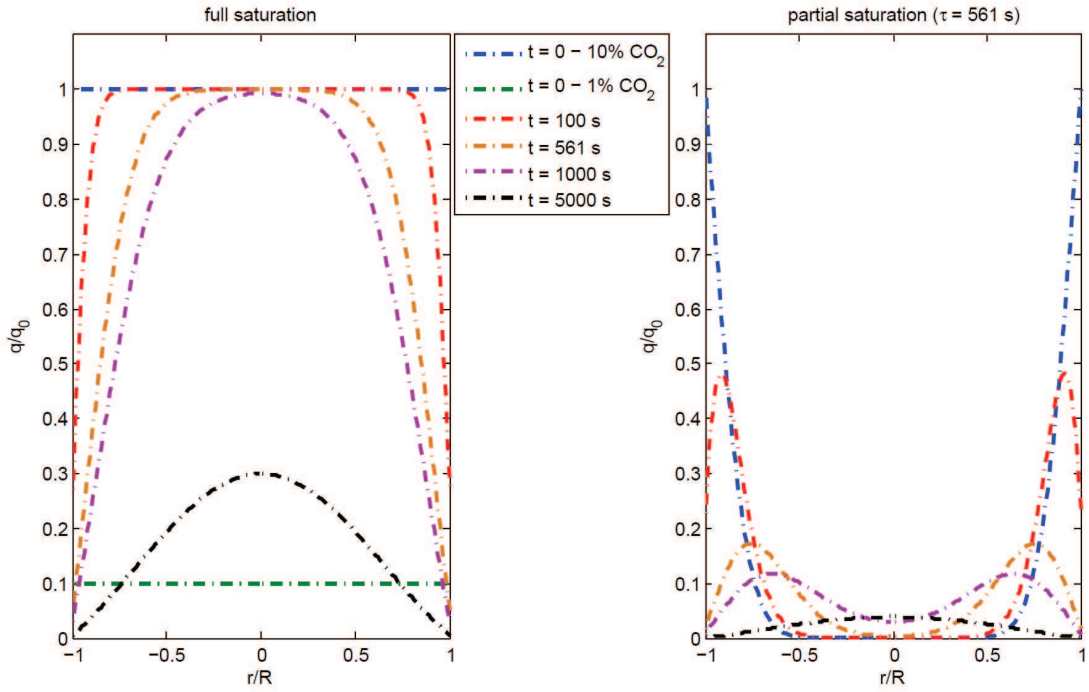

Figure 6.8: Adsorbed phase profile inside a crystal of Na-Rho for the full (left) and partial (right) saturation cases at different desorption times.

From the plots is possible to see how at time zero the average concentration inside the particle for the partially loaded sample is not very far from the adsorbed amount relative to the sample saturated with a CO_2 concentration of 1%. These conditions

are also the ones of the sample fully saturated in the long-time region (5000 s). All this confirms that for the partially loaded sample the concentration inside the solid is low enough that linear equilibrium and constant diffusivity can be considered valid assumptions.

For this sample partial loading experiments at different temperatures were also performed in order to calculate the activation energies for the diffusion and a value of 12 kJ/mol was obtained. Table 6.3 shows the diffusional time constants and diffusivities obtained at different temperatures for the fully exchanged Na-Rho and for the Na,H-Rho samples at 8.5 and 7 Na /unit cell. The corresponding ZLC curves are reported in Appendix B.

Table 6.3: Diffusional time constants and diffusivities at different temperatures for Na,H-Rho tested using the ZLC partial loading experiment.

SAMPLE	$D/R^2 \times 10^{-5}$	$D \times 10^{-19}$	T
	$[s^{-1}]$	$[m^2/s]$	[°C]
Na,H-Rho (10 Na units/cell)	4.0	1.0	35
	5.50	1.38	50
	6.50	1.63	70
Na,H-Rho (8.5 Na units/cell)	5.80	1.45	35
Na,H-Rho (7 Na units/cell)	5.50	1.38	35

6.3 K- Rho

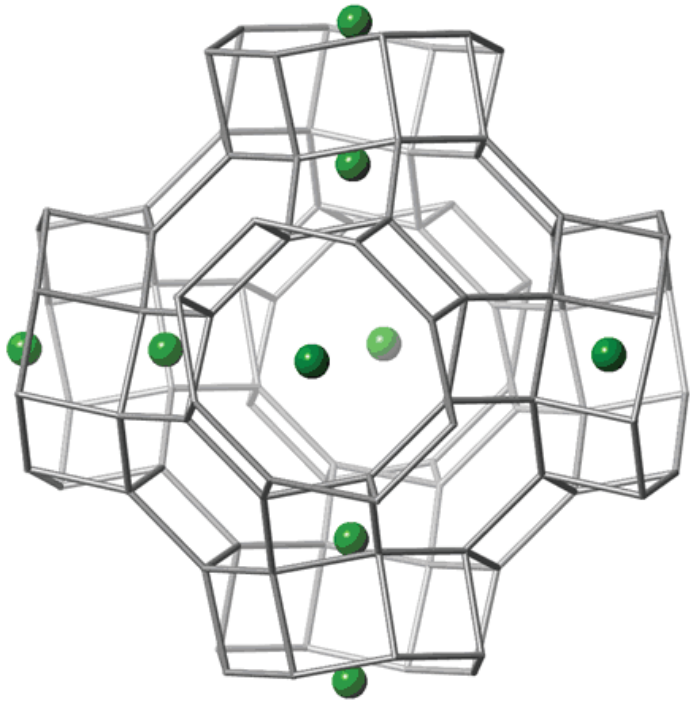

Figure 6.9: Possible cation distributions in one α-cage and associated D8R windows of dehydrated univalent cation forms of zeolite K-Rho, determined from Rietveld refinement of laboratory X-ray powder diffraction data [107].

In K-Rho K^+ cations are found to occupy window sites of both S8R and D8R types so that there will be at least one and in some case two K^+ cations per window, Figure 6.9.

Due to the lower capacity of this sample it was found more convenient to run the partial loading experiment at 1% of CO_2: in this way the region of interest for the analysis is not too close to the baseline.

Figure 6.10 shows the experimental and the predicted curves for the case of interest. Also in this case the predicted curves match the experimental data; the resulting value of diffusional time constant is 4.50×10^{-5} s^{-1}.

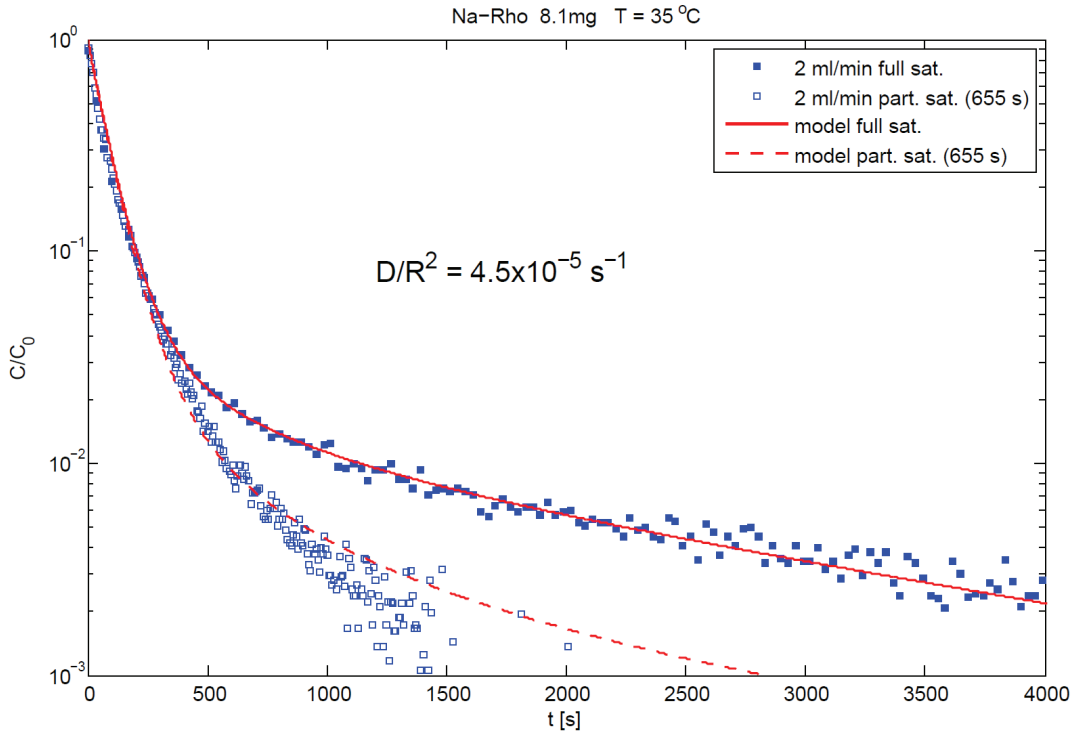

Figure 6.10: Experimental ZLC desorption curves for the fully and partially saturated K-Rho sample at 1% of CO_2; in red the predicted curves using eq. 3.5 and eq. 3.15.

6.4 Li-Rho

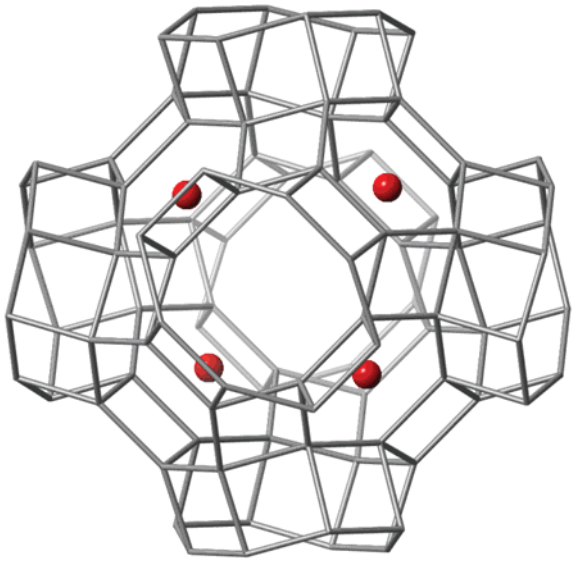

Figure 6.11: Possible cation distributions in one α-cage and associated D8R windows of dehydrated univalent cation forms of zeolite Li-Rho, determined from Rietveld refinement of laboratory X-ray powder diffraction data [107].

The last sample of the Rho series synthesised at the University of St. Andrews was the Li-Rho, which due to the smaller size of the Li cation was expected to be the sample of the series with the highest uptake. Moreover, as shown in Figure 6.11, based on the position of the cation in the cage, no hindering action was expected for this sample.

Figure 6.12 shows the different attempts to perform the fully and partially saturated experiment on the Li-Rho sample. It can be seen that all the curves obtained at different loading times lie above the full saturation one indicating that, due to the high hydrophilicity of the sample, it is likely that a small amount of water present in the system affected significantly the capacity at different loading times. Repeat experiments were carried out after some attempts to reduce any water source from the system: the drying columns were regenerated, the lines from the drying columns to the dosing oven were heated up, the cylinders of the dosing oven were heated up and flushed at high temperature, the entire the system was flushed overnight. At the end from the signal acquired from the mass spectrometer there was no evidence of water inside the system. On the other hand the ZLC experiment showed that the

capacity of the sample still decreased with longer loading times indicating that, even if not clearly detectable, a very small amount of water was still affecting the measurements.

Due to the need to continue the ranking experiments for the other samples provided by the IGSCC partners no further investigations were made on the Li-Rho sample. What emerged to be very interesting is the possibility of using the sample as "water detector": the partial loading technique using Li-Rho may provide an inexpensive method to detect the presence of very small quantity of water, hardly detectable by other instruments.

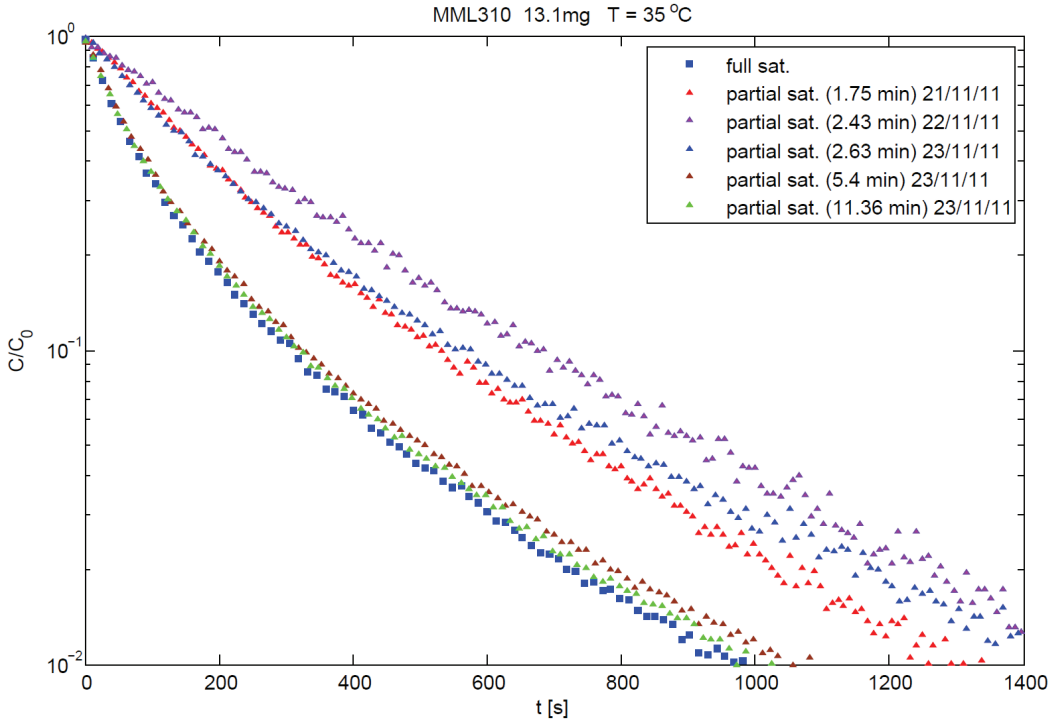

Figure 6.12: Experimental ZLC desorption curves for the fully and partially saturated Li-Rho sample at different loading times.

6.5 Conclusions

The ZLC technique was used to measure systems characterised by very slow kinetics. Very low values of diffusivity were obtained using the ZLC method by Cavalcante and Ruthven [132] for branched and cyclic C_6 paraffins in silicalite. In this study the use of the ZLC technique has been extended to measure the kinetics of

systems with even lower diffusional time constant. This was possible thanks to the new ZLC apparatus which allows measurements at very low flowrates.

From the ZLC experiments clear evidence of structural changes induced by the adsorption of CO_2 was obtained. The technique provided an *in situ*, and relatively cheap, way to detect the presence of such uncommon properties of the adsorbents. This might represent a new unexplored area toward which future developments of the technique can be explored.

Further investigations should be done on the Li-Rho sample. The high hydrophilicity of the sample did not allow to obtain at the moment the true value of the CO_2 capacity and modifications to the actual system might be needed in order to overcome the problems due to the presence of very small amounts of water.

7. USE OF A VOLUMETRIC SYSTEM FOR DIFFUSION MEASUREMENTS

In this section the use of a commercial volumetric system for measurements of diffusion will be described. The system used is a Quantachrome Autosorb-iQ™, a state-of-the-art volumetric system which allows measurements of BET surface areas, micropore volumes and adsorption isotherms of gases and vapours on solid adsorbents, which are automatically interpreted by the software tools provided with the instrument.

Among all the features enabled there is also the possibility to follow the dynamic response of the system during adsorption. The experiment consists in injecting a known volume of adsorbate in the sample cell and the pressure decay is recorded until equilibrium is reached. A sequence of injections can be programmed obtaining in this way equilibrium points at different pressures of sorbate, i.e. the isotherm up to the highest pressure value reached. The built-in software analyses the equilibrium data and gives as an output the relative isotherm, but does not interpret the dynamic response from which the information on the kinetics of the system can be extracted.

The system because of its configuration which consists of two volumes connected through a valve is more properly defined as a piezometric system. A solution for the determination of diffusion from piezometric experiments was proposed by Bülow and Micke [133] in 1994. Successively, between 1997 and 1999, two independent studies of the system were presented by Schumacher et al. [134] and Brandani [135]. The authors developed a model of the system and both the works similarly proved that the method presents severe limitations if used to measure the adsorption kinetics of fast systems or strongly adsorbed species.

In the present work an effort was made to adapt the existing model for a piezometric system, developed by Brandani in 1998 [135], to the Autosorb-iQ™ volumetric system.

Figure 7.1 shows the system and the relative simplified scheme.

The system consists of:

- a dosing cell, in which the known volume of gas is collected before the start of the experiment;

- an uptake cell which contains the sample. The cell is immersed in a bath at $T = T_u$.
- a valve which connects the two volumes;
- an O-ring to ensure the sealing at the point in which the uptake cell is connected to the system;
- three pressure transducers with different ranges of operation to monitor the pressure inside the system.

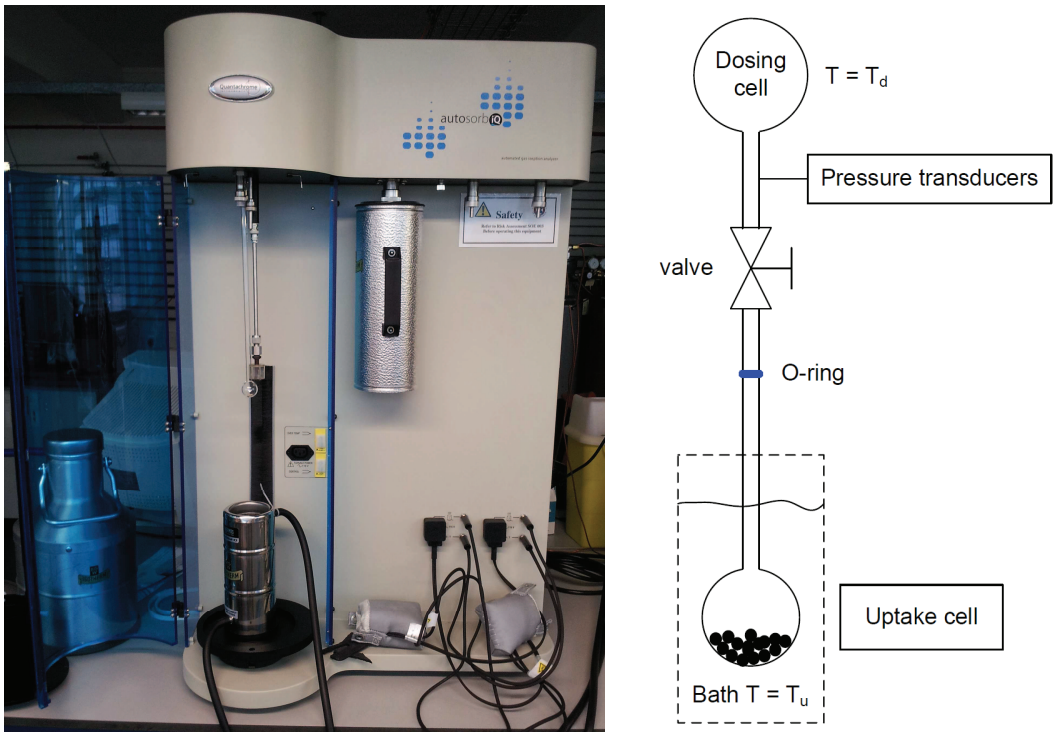

Figure 7.1: On the left side, Quantachrome Autosorb volumetric system; on the right side, schematic view of the volumetric system.

Before the start of the experiment the sample is placed inside the uptake cell and thermally regenerated overnight under vacuum. The regeneration station (right side of the instrument) is different from the measurement station (left side of the instrument) this means that when the regeneration is completed the sample cell is removed from the regeneration station, weighted to check the weight loss during the regeneration and placed in the uptake station. To secure the cell to the uptake station, a fitting system consisting in an adapter sleeve and one O-ring is provided.

For the correct interpretation of the data acquired by the system, the simplified model of Brandani [135] needed to be slightly modified in order to take account of two factors

which make the system more complex: the difference in temperature between the dosing and the uptake cell and a very small permation in correspondence of the O-ring. While the uptake cell is immersed in the bath at constant temperature, the dosing cell is at room temperature. With regard to the permeation, it was observed that for long measurements at low pressure in some experiments a small amount of air gets into the system causing a very slight pressure increase. Moreover the permeation rate may vary from one experiment to other one depending on the operator, O-ring used and strength used to secure the cell to the instrument, but the permeation rate is so low that typically it becomes apparent only after close inspection of the full experimental curve.

7.1 Mathematical Model

Similarly to the original model the flow through the valve is described assuming a small pressure difference between the two sides of the valve, which allows to assume a linear model (nomenclature at the and of the chapter):

$$\frac{dn_d}{dt} = -\overline{X}\left(P_d - P_u\right) \tag{7.1}$$

In which $\overline{X}$ is the constant of opening of the valve. The subscripts "*u*" and "*d*" refer to the uptake and dosing cell; *P* and *n* are the pressure and moles of CO_2, respectively. The mass balance in the dosing cell can be written as:

$$\frac{dn_d}{dt} = \frac{V_d}{\Re T_d}\frac{dP_d}{dt} \tag{7.2}$$

While for the uptake cell:

$$\frac{dn_u}{dt} = -\frac{V_d}{\Re T_d}\frac{dP_d}{dt} - \lambda\left(P_u - P_{atm}\right) \tag{7.3}$$

$$\frac{dn_u}{dt} = M_s \frac{d\overline{q}}{dt} + \frac{\varepsilon V_u}{\Re T_u} \frac{dP_u}{dt} \tag{7.4}$$

where λ is an empirical parameter that is used to model the permeation in correspondence of the O-ring; V is the volume of the cell (uptake and dosing), M_s is the sample mass and q is the adsorbed phase concentration.
Combining the equations above, equations 7.5 and 7.6 are obtained:

$$M_s \frac{d\overline{q}}{dt} + \frac{\varepsilon V_u}{\Re T_u} \frac{dP_u}{dt} + \frac{V_d}{\Re T_d} \frac{dP_d}{dt} + \lambda\left(P_u - P_{atm}\right) = 0 \tag{7.5}$$

$$\frac{dP_d}{dt} = \frac{\Re T_d}{V_d} \overline{X}\left(P_u - P_d\right) \tag{7.6}$$

The main assumptions for the system are:

- Fickian diffusion inside spherical particles:

$$\frac{\partial q}{\partial t} = D\left(\frac{\partial^2 q}{\partial r^2} + \frac{2}{r}\frac{\partial q}{\partial r}\right) \tag{7.7}$$

$$\frac{d\overline{q}}{dt} = \frac{3D}{R}\left(\frac{\partial q}{\partial r}\right)_{r=R} \tag{7.8}$$

- linear equilibrium relationship at the surface and symmetry condition:

$$q(R,t) - q_0 = H\left(P_u(t) - P_u^0\right) \tag{7.9}$$

$$\left(\frac{\partial q}{\partial r}\right)_{r=0} = 0 \tag{7.10}$$

The system of equations can be rewritten by introducing the following dimensionless groups:

$$\tau = \frac{tD}{R^2}; \qquad Q = \frac{q - q_0}{q_\infty - q_0}; \qquad N = Q\xi;$$

$$\rho_d = \frac{P_d - P_u^0}{P_\infty - P_u^0}; \qquad \rho_u = \frac{P_u - P_u^0}{P_\infty - P_u^0}; \qquad \rho_{atm} = \frac{P_{atm} - P_u^0}{P_\infty - P_u^0};$$

$$\gamma = \frac{1}{3}\frac{\varepsilon V_u}{\Re T_u H M_s}; \qquad \delta = \frac{1}{3}\frac{V_d}{\Re T_d H M_s}; \qquad \omega = \frac{\Re T_d}{V_d}\overline{X}\frac{R^2}{D};$$

$$\xi = \frac{r}{R}; \qquad \Gamma = \frac{\lambda}{3HM_s}\frac{R^2}{D};$$

The resulting mass balance equations in dimensionless terms are given by:

$$\frac{d\rho_d}{d\tau} = \omega(\rho_u - \rho_d) \tag{7.11}$$

$$\gamma\frac{d\rho_u}{d\tau} + \delta\frac{d\rho_d}{d\tau} + \left(\frac{\partial N}{\partial \xi} - N\right)_{\xi=1} + \Gamma(\rho_u - \rho_{atm}) = 0 \tag{7.12}$$

$$\frac{\partial N}{\partial \tau} = \frac{\partial^2 N}{\partial \xi^2} \tag{7.13}$$

Initial and boundary conditions for the system are set as follows:

$$\begin{aligned} &\rho_d(0) = 0; \\ &\rho_u(0) = 0; \\ &N(\xi, 0) = 0; \\ &N(0, \tau) = 0; \\ &N(1, \tau) = \rho_u(\tau); \end{aligned} \tag{7.14}$$

The system can now be solved analytically by the use of the Laplace transforms. The corresponding system of equations in the Laplace domain is as follows:

$$s\widetilde{\rho}_d - \rho_d^0 = \omega(\widetilde{\rho}_u - \widetilde{\rho}_d); \tag{7.15}$$

$$\widetilde{\rho}_u = \frac{(s + \omega)\widetilde{\rho}_d - \rho_d^0}{\omega} \tag{7.16}$$

$$s\widetilde{N} = \frac{\partial^2 \widetilde{N}}{\partial \xi^2} \tag{7.17}$$

By solving the system of equations with respect to the dimensionless pressure ρ_d, the expression of the dimensionless pressure of the dosing cell can be obtained:

$$\frac{\widetilde{\rho}_d}{\rho_d^0} = \frac{s\left(\gamma s + \sqrt{s}\coth\sqrt{s} - 1 + \Gamma + \delta\omega\right) + \Gamma\omega\dfrac{\rho_{atm}}{\rho_d^0}}{s\left[\left(\gamma s + \sqrt{s}\coth\sqrt{s} - 1 + \Gamma\right)(s+\omega) + \delta\omega s\right]} \tag{7.18}$$

The solution in the time domain is the inverse Laplace transform of eq. 7.18:

$$\frac{\rho_d}{\rho_d^0} = \frac{\rho_{atm}}{\rho_d^0} + \sum_{n=1}^{\infty} \frac{2\delta\omega^2\beta_n^2 - 2\Gamma\omega\left(\omega - \beta_n^2\right)\dfrac{\rho_{atm}}{\rho_d^0}}{2\delta\omega\beta_n^2\left(2\omega - \beta_n^2\right) + \left(\omega - \beta_n^2\right)^2\left(z_i^2 + \beta_n^2 + 4\gamma\beta_n^2 - 2\Gamma + 2 - 3z_i\right)} \exp\left(-\beta_n^2\tau\right) \tag{7.19}$$

In which β_n represents the non-zero roots of:

$$\beta_n \cot\beta_n = 1 + \gamma\beta_n^2 - \Gamma + \frac{\delta\omega\beta_n^2}{\left(\omega - \beta_n^2\right)} = z_i \tag{7.20}$$

The derivation of the solution can be found in Appendix C.

Eq. 7.19 can be reduced to the one of the simplified model in the limit case of no permeation through the O-ring ($\Gamma = 0$) and $T_d = T_u$, eq. 7.21. In this case the limit at $t = \infty$ will be given by the ratio between the volumes of the dosing and the uptake cell, and the amount adsorbed.

$$\frac{\rho_d}{\rho_d^0} = \frac{3\delta}{1 + 3\delta + 3\gamma} + \sum_{n=1}^{\infty} \frac{2\delta\omega^2\beta_n^2}{2\delta\omega^2\beta_n^2 + \left(\omega - \beta_n^2\right)^2\left(z_i^2 + \beta_n^2 + 2\gamma\beta_n^2 - z_i\right)} \exp\left(-\beta_n^2\tau\right) \tag{7.21}$$

The expression for the limit case of an equilibrium controlled process can be directly derived from eq. 7.19 by assuming infinite diffusivity, and the resulting expression is given by:

$$\frac{\rho_d}{\rho_d^0}=\frac{\rho_{atm}}{\rho_d^0}+\frac{\exp\left(\frac{-B}{2A}\tau\right)}{2\Delta}\left[2\left(6\delta\omega+6\Gamma-2B\right)\sinh\left(\frac{\Delta\tau}{2A}\right)+4AC\left(\frac{\rho_{atm}}{\rho_d^0}-1\right)\left(\frac{\exp\left(\frac{\Delta\tau}{2A}\right)}{(\Delta-B)}-\frac{\exp\left(-\frac{\Delta\tau}{2A}\right)}{(\Delta+B)}\right)\right] \tag{7.22}$$

In which:

$$\begin{aligned}A&=(1+3\gamma)\\B&=(\omega+3\gamma\omega+3\delta\omega+3\Gamma)\\C&=3\Gamma\omega\\\Delta&=\sqrt{B^2-4AC}\end{aligned} \tag{7.23}$$

7.2 Results

As a first test of the system CO_2 adsorption experiments were carried out on 13X pellets of 1 mm in diameter at 0 ºC. The experiment consisted of three consecutive injections of 8 ml (STP) of CO_2. At time zero the valve is opened allowing the contact between the sample and the CO_2 and the pressure is monitored. Once a stable point is reached, the system is at equilibrium and a new volume of CO_2 can be injected. Figure 7.2 shows the transient uptake curves at the different concentration steps for CO_2 on 13X pellets at 0 °C

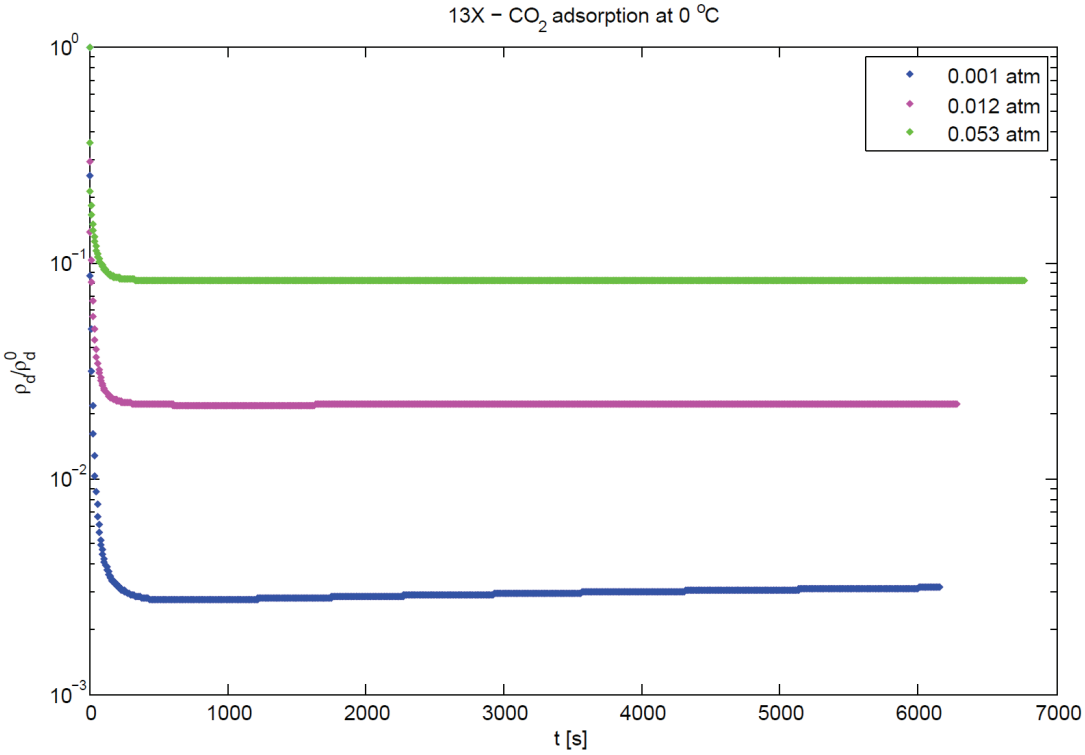

Figure 7.2: CO_2 adsorption at 0 ºC on zeolite 13X (beads of 2 mm of diameter from UOP) using Quantachrome Autosorb-iQ™ volumetric system.

From the curve relative to the experiment at lower pressure the increase of the pressure due to the infiltration of air in the uptake cell can be noted. Obviously the final point, detected by the instrument as "equilibrium", is not a real equilibrium value but just the point for which the oscillation of the pressure is below the set value of the tolerance. From the curves it is also possible to note that for each experiment the leak rate visibly decreases, this might be caused by the combination of a lower

driving force and possible changes in the properties of the o-ring due to the long exposure to CO_2.

Table 7.1: Fitting parameters used in eq. 719

Parameters	0.001 atm	0.012 atm	0.053 atm
Ms [g]	0.263		
V_d [ml]	17.508		
V_g [ml]	22.438		
V_u [ml]	22.756		
λ [mol/Pa*s]	0.12×10^{-12}	0.02×10^{-12}	0.01×10^{-12}
T_d [K]	295.8		
T_u [K]	273.15		
X [mol/Pa*s]	0.8e-9		
γ	0.0466		
δ	0.0336		
ω	375	160.5	125
Γ	4.8×10^{-5}	3.1×10^{-5}	5.2×10^{-5}
D/R^2 [s^{-1}]	3×10^{-4}	7×10^{-4}	9×10^{-4}

The experimental data were fitted using eq. 7.19 and the values displayed in table 7.1. In Figure 7.2 the experimental and predicted curves are shown.

As a comparison, Figure 7.3 shows the ZLC curves experiments carried out on the same 13X pellets and reported by Hu in his PhD thesis [51]. The experiment was performed using two different carrier gases and the fact that the ZLC curves do not overlap for the two different experiments is a clear proof a macropore diffusion process. D/R^2 from the ZLC experiments is of the order of 10^{-3} s^{-1}, which is a much faster process than that observed in the volumetric system. The actual mass transfer constant should be much higher in the volumetric system, since no inert gas is present and the mechanism of mass transfer at the operating conditions is Knudsen diffusion. The observed time constant is clearly an indication of a heat limited process. The data will be used in the adsorption course to show to students how very

low *apparent* diffusivities can be obtained if dynamic response data is analysed without taking into account heat effects.

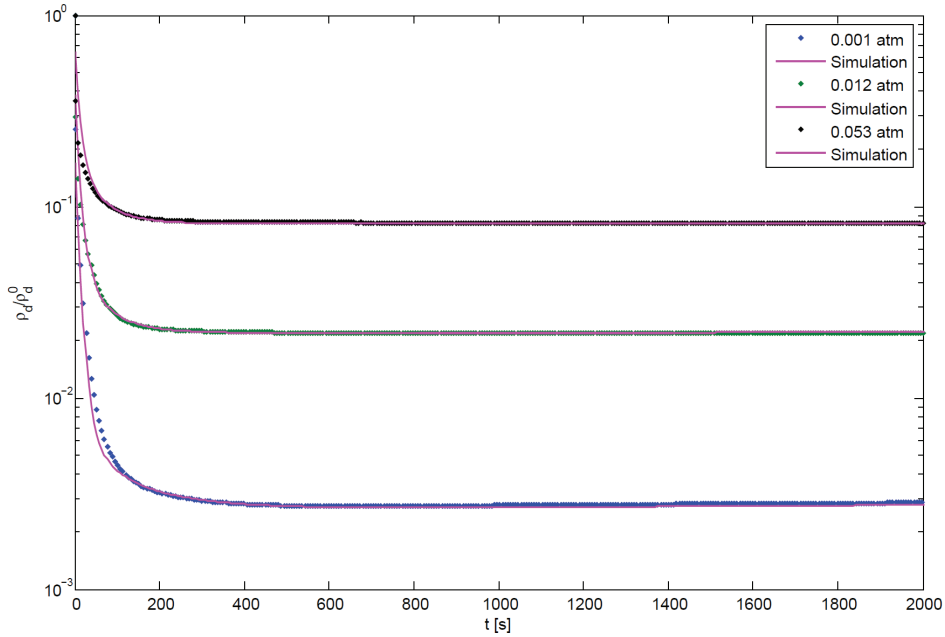

Figure 7.3: Fitting of the experimental transient curves for CO_2 adsorption on 13X at 0 ℃ using eq. 7.19. The parameters used are listed i n table 7.1.

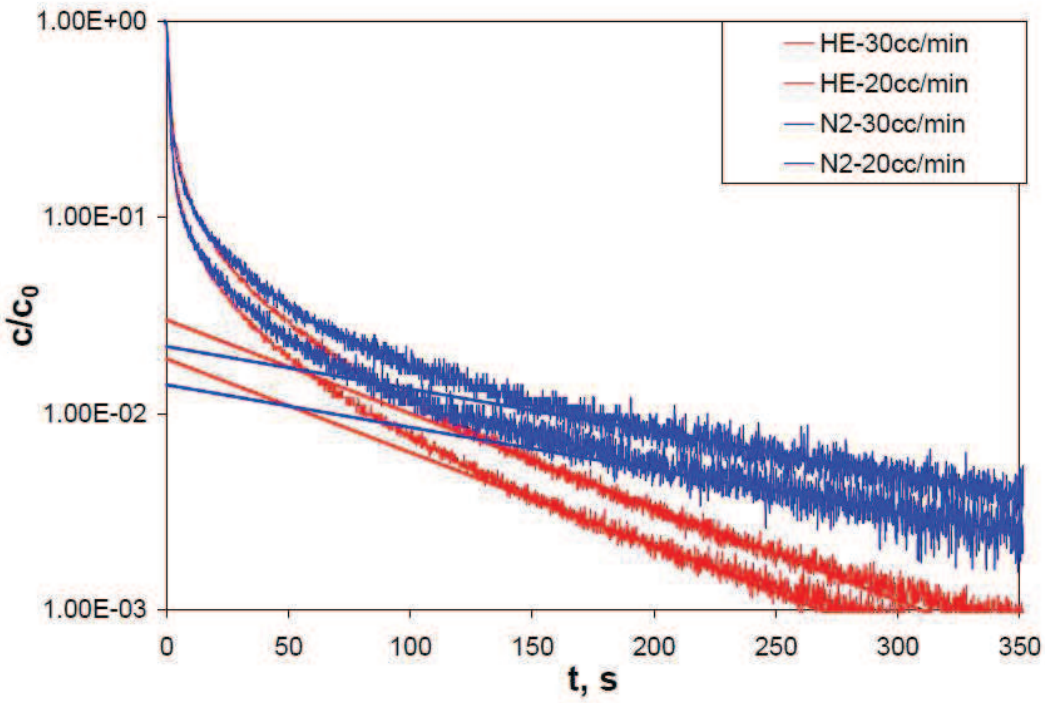

Figure 7.4: Comparison of experimental ZLC response curves of 13X pellet (R = 1.19 mm) at 0.1bar of CO_2 in two different purge gas (N_2 and He), 38 ℃, 20 and 30 ml/min from Hu, PhD thesis [51].

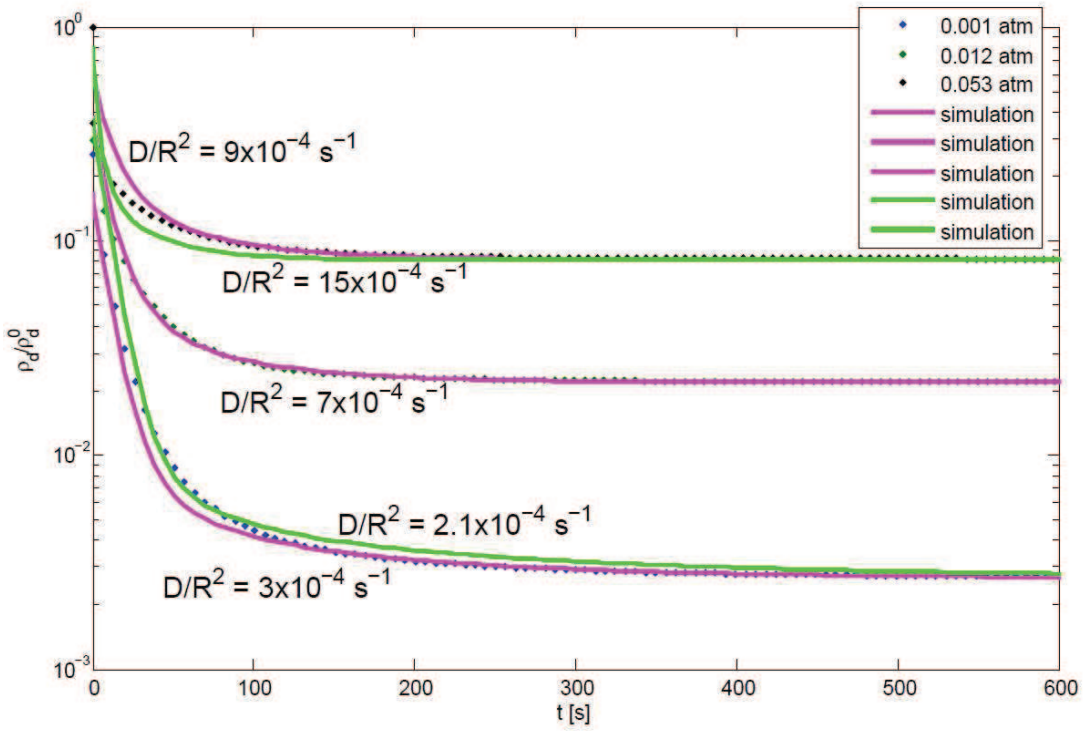

Figure 7.5: Fitting of the experimental curves using eq. 7.19: in purple the predicted curves using the parameters listed in table 6.1; in green the predicted curves using different diffusional time constants.

Figure 7.5 shows the curves of Figure 7.3 expanded in the short time range. It can be seen that the fit is acceptable but not very close, for this reason for two of the three experimental curves an additional predicted curve was provided in order to identify the range of values of the *apparent* diffusional time constant.

The volumetric system was also used to carry out additional measurements of diffusivity on the Rho zeolites in order to compare the results to those obtained from the ZLC experiments. Figure 7.6 shows the experimental data and the predicted curve for Na,Cs-Rho at 35 °C. In this case the adsorption process is extremely slow and as a result of the experience gained on the 13X sample the tube was connected carefully to avoid leaks. This may have also been a result of the long exposure of the O-ring material to CO_2. The results on the Rho sample showed no appreciable leak rates and it was then possible to fit the curves neglecting the leak term.

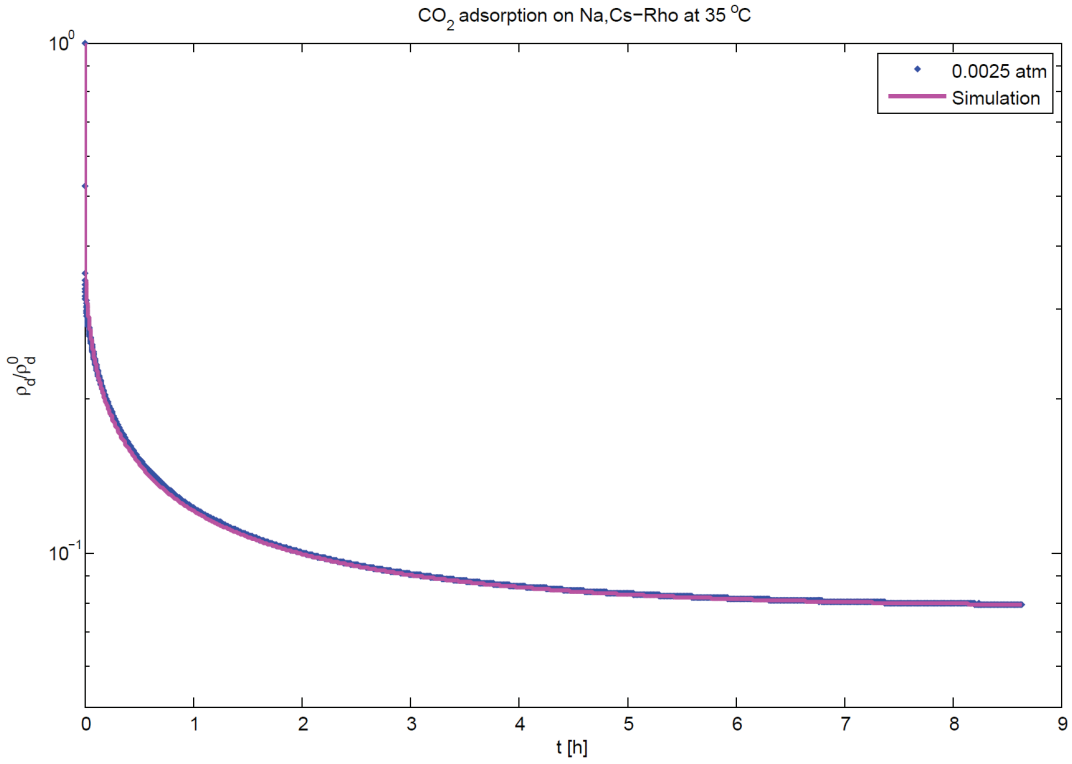

Figure 7.6: CO_2 adsorption on Na,Cs-Rho (0.878 g) at 35 ˚C: experimental data and predicted curve.

The value of D/R^2 obtained is 7.5 x10^{-6} s^{-1} which is about 1/3 of the value found from the kinetic experiments carried out on the ZLC system. This is a good agreement, considering that the conditions of the experiments are different and the diffusivities are very low. Clearly in this case the mass transfer process is sufficiently slow to achieve isothermal operation.

The lower diffusivities might be due to minor modifications of the structure, similarly with what observed for the Na-Rho sample. In the case of the ZLC experiment the sample is first saturated with CO_2, therefore the size of the windows is increased by the presence of the molecules of CO_2 allowing a relatively fast diffusion. In the case of the volumetric experiment, the sample is completely dehydrated and the smaller size of the windows is likely to result in a reduced diffusion coefficient of CO_2.

Moreover the sample might have not been perfectly dry because of the need to disconnect the cell from the regeneration station and re-connect to the uptake station.

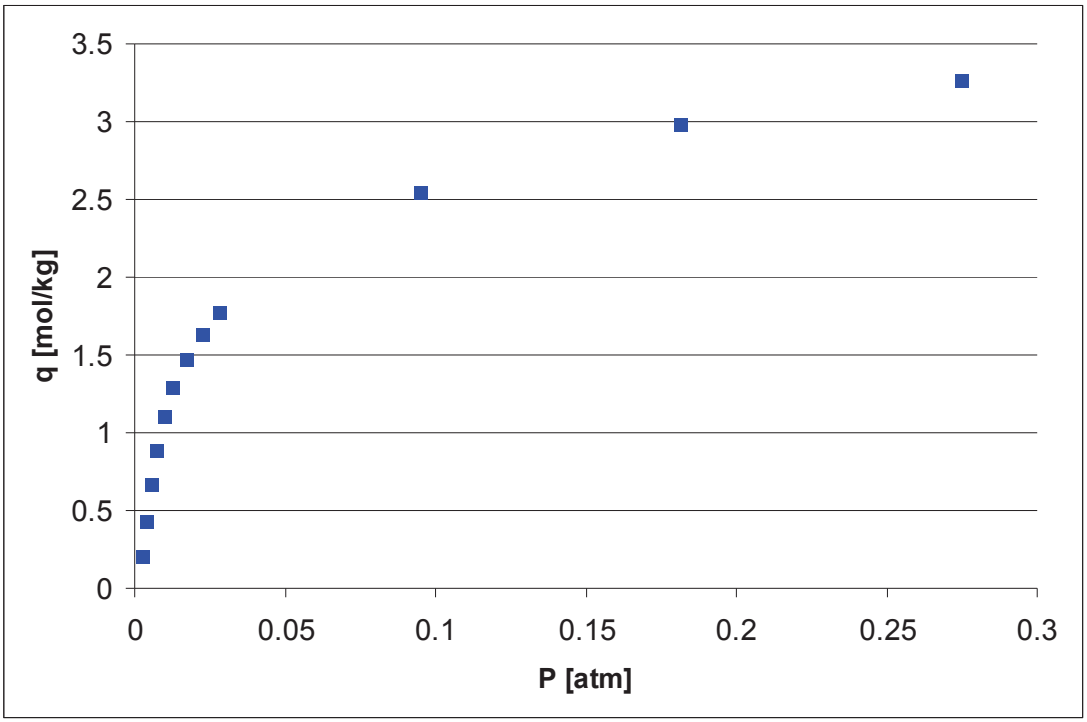

Figure 7.7: CO_2 isotherm obtained by the measurement on the Autosorb system

As mentioned previously the last point of the dynamic response is an equilibrium point, so if the experiment is set with successive injections of CO_2 the software extracts automatically the isotherm. Figure 7.7 shows the CO_2 isotherm for the Na,Cs-Rho sample. The isotherm was fitted with a Dual Site Langmuir model and the thermodynamic correction factor was calculated as dln(P)/dln(q). The value of the Darken correction factor was 1.15, which confirms that the experiments were carried out within the Henry law region.

The value of the parameter ω for the Rho zeolites case was greater than $3x10^5$ this means that the diffusion time constant relative to the opening of the valve is so high the system can be considered as a classic volumetric system of total volume V_d+V_u. Eq 7.21 can be derived for this limiting case and the resulting equation is given by:

$$\frac{P_d - P_\infty}{P_d^0 - P_\infty} = 1 - \frac{M_t - M_0}{M_\infty - M_0} = \sum_{n=1}^{\infty} \frac{2\delta\beta_n^2}{3(\gamma+\delta)\beta_n^2 + \beta_n^2 + \left((\gamma+\delta)\beta_n^2\right)^2} \exp\left(-\beta_n^2 \tau\right) \qquad (7.24)$$

In which M_0 is the amount adsorbed at time 0 and M_∞ is the total amount adsorbed at equilibrium; β_n represents the non-zero roots of:

$$\beta_n \cot \beta_n = 1 + (\gamma + \delta)\beta_n^2 \qquad (7.25)$$

The plot of Figure 7.6 can be then displayed in terms of amount adsorbed, as shown in Figure 7.8. Eq. 7.24 was used to fit the data, but the predicted curve perfectly overlapped with the one derived from eq. 7.21.

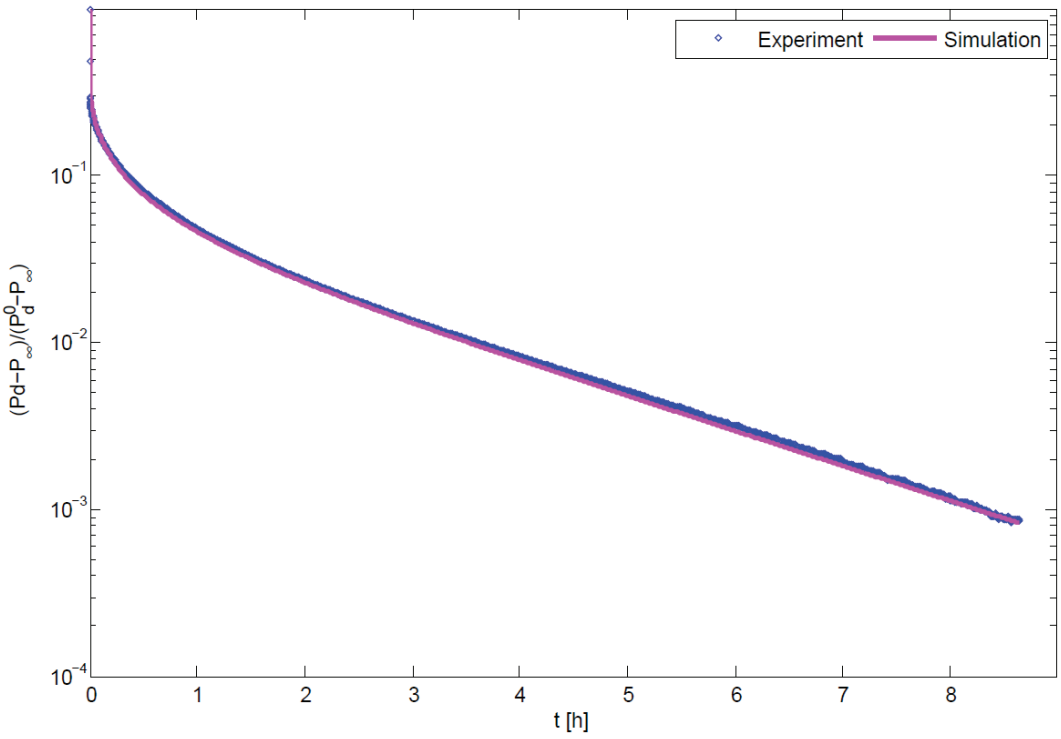

Figure 7.8: CO_2 adsorption on Na,Cs-Rho (0.878 g) at 35 °C: experimental data and predicted curve in terms of amount adsorbed.

7.3 Conclusions

The simplified model for a piezometric system was adapted to the operative conditions of a real volumetric system. The introduction of the temperature

difference between the two cells and the leak in the uptake cell allowed a more precise analysis of the experimental data.

This allowed for the first time, the use of the dynamic response of the Quantachrome Autosorb to extract the diffusivity from system characterised by a slow kinetics. Tests were performed on zeolite 13X and Na,Cs-Rho samples.

The value of the *apparent* diffusional time constant obtained from the experiment in 13X resulted to be significantly lower if compared to ZLC response curves reported by Hu [51] using the same commercial pellets, this indicated the presence of a heat limited process.

The value obtained for the kinetics of CO_2 in Na,Cs-Rho was found to be 1/3 of the one obtained from the ZLC experiments, probably due to a minor difference in the windows size of the cages, as reported for the analogue Na-Rho [107], or to a not-perfectly dry sample.

Further tests on the Rho samples should be done by successive injections to investigate if it is possible to identify any structural modification using the Autosorb system.

Nomenclature

c	Gas phase concentration, mol/ m^3
C	Dimensionless gas phase concentration,
D	Diffusivity, m^2/s
H	Equilibrium constant, mol/(kg × Pa)
n	Moles, mol
N	$Q\xi$
P	Pressure, Pa
q	Adsorbed phase concentration, mol/ kg
$\overline{q}$	Average adsorbed phase concentration, mol/ kg
Q	Dimensionless adsorbed phase concentration
r	Radial coordinate, m
R	Radius of crystals, m

$\Re$	Ideal gas constant, J/K
s	Laplace domain variable
t	Time, s
T	Temperature, K
V	Volume, m^3
M_s	Mass of the sample, kg

Greek Letters

β_i	Eigenvalues of the system
γ	Ratio of the accumulation in the uptake cell and in the solid,
δ	Ratio of the accumulation in the dosing cell and in the solid,
ε	Void fraction in uptake cell
ξ	Dimensionless radial coordinate
ρ	Reduced pressure
τ	Dimensionless time
$\overline{X}$	Linearised valve constant, mol/(Pa*s)
ϕ	Ratio between the temperatures of uptake and dosing cells
λ	Leak rate, mol/(Pa*s)
ω	Ratio of the diffusional and the valve time constants

The subscripts "*d*" and "*u*" refer to dosing and uptake cell, "*s*" refers to sample.

8. CONCLUSIONS

For the first time, a wide range of materials belonging to the most promising classes were systematically tested and compared at the same conditions and using the same technique. With this regard the Zero Length Column (ZLC) revealed to be an essential tool for the rapid ranking of prototype adsorbents, allowing the characterisation of the equilibrium and kinetic properties of more than 120 different samples. The experimental conditions were chosen in order to be representative of a typical real flue gas stream from a power plant: 0.1 bar of CO_2 and 35 °C.

The novel adsorbent materials were synthesised as part of the "Innovative Gas Separations for Carbon Capture" (IGSCC) project, a UK-wide research consortium which involves the University of St. Andrews (StA), Cardiff University (CU), Imperial College London (ICL), the University of Manchester (UoM), and University College London (UCL). As a result of the different expertise contributed by the members of the consortium, several classes of materials were investigated: several types of Zeolites and MOFs (StA); Carbons (UoM, CU, and UCL); and Oxides with surface functional groups (UCL).

With regard to the ranking of the CO_2 capacity the samples with the highest capacity were Mg-CPO-27 samples with surface modifications, which exhibited CO_2 uptakes from 5 to 6.55 mol/kg at 0.1bar and 35 ˚C. In addition most of these samples showed a fairly linear CO_2 isotherm. The main disadvantage emerged from the present study is the stability of the Mg-CPO-27 adsorbents: the rapid deactivation rate in presence of water seriously impairs the utilisation of the adsorbents in a real carbon capture PSA unit.

Despite a significantly lower capacity than Mg-CPO-27, the water stability test showed that Ni-CPO-27 preserved more than 90% of the original capacity over a long period of time and repeated exposure cycles. The good stability exhibited, combined with the relatively low regeneration temperature and the linear isotherm,

makes Ni-CPO-27 a promising material which should be considered further for post-combustion capture using rapid VSA cycles.

Zeolites showed also very good performances with regard to the CO_2 capacity, with the highest value of 4 mol/kg for Li- and K- Chabazites, but the CO_2 isotherms resulted to be less linear than the ones exhibited by the MOF samples. Further tests should be carried out on these samples and on the other ion-exchanged zeolites to investigate how their stability to water and impurities compares to the MOFs.

The carbon based material showed relatively low capacity. The modification on the BPL carbon did not result in higher uptake and no more samples were synthesised. With regard to the carbon foams, the synthesis procedure is not mature yet but good improvements were observed in the modified samples.

For the first time a study of the adsorption capacity of different types of PIMs was carried out. All the samples showed a relatively low CO_2 uptake and none of them reached the CO_2 capacity of the benchmarks. For the different classes of PIMs the trend of the CO_2 capacity generally reflected the trend of the free volume available and the functionalisation with amine groups proved to increase the CO_2 uptake. Due to the low uptakes, all the samples showed ZLC desorption curves too close to the blank response. This prevented further investigations with regard to the equilibrium and the kinetic properties of the materials. It would be very interesting to investigate in more details the kinetics of CO_2 adsorption in this class of materials using the volumetric system and the membrane permeation apparatus that has been built recently.

No mesoporous silicas could be included in the comparison, but it would have been very interesting to include in the ranking some amine-based silicas which represent at the moment some of the most promising candidates for CO_2 capture, mainly due to their outstanding performances in presence of water.

Table 8.1 summaries all the samples tested in the present study with the relative CO_2 capacity at 35 °C and 0.1 bar.

In this study the use of the ZLC technique has been extended to measure the kinetics of systems with diffusional time constant lower than other reported works on the ZLC. The diffusion measurements on the Rho zeolites showed evidence of structural modifications of the materials dependent on the CO_2 concentration. The ZLC

technique provided an *in situ*, and relatively cheap, way to detect the presence of such uncommon properties of the adsorbents. This might represent a new unexplored area toward which future developments of the technique can be explored. For example the ZLC system could be modified allowing for differential desorption steps. This would imply the use of mixtures at different concentrations connected to the inlet of the ZLC with separate lines. Further modifications to the actual system might be needed in order to overcome the problems in testing highly hydrophilic samples like Li-Rho zeolite.

Finally, for the first time the Quantachrome Autosorb volumetric system was used to extract the diffusivity from system characterised by a slow kinetics. This was possible by adapting an existing model for a piezometric system to the operative conditions of a real volumetric system. Further tests at increasing concentration of CO_2 should be done on the Rho samples to investigate the possibility of identifying structural modifications using the Autosorb system.

Table 8.1: List of the CO_2 capacity for all the adsorbents tested at 35 ℃ an d 0.1 bar.

Name	Sample	CO_2 capacity[mol/kg]
MML37	ITQ-13	0.26
MML77	K-Chabazite (less crystalline)	1.85
MML146	K,H-Chabazite (0 K/Unit cell)	0.493
MML142	K,H-Chabazite (1.5 K/Unit cell)	1.37
MML140	K,H-Chabazite (3 K/Unit cell)	1.8
MML148	K,H-Chabazite (3.5 K/Unit cell)	2
MML284	K-Chabazite (4 K/unit cell)	1.91
MML162	K,H-Chabazite (4.5 K/Unit cell)	1.61
MML241	K,H-Chabazite (6 K/Unit cell)	2.2
MML138	K-Chabazite (9 K/Unit cell)	4.08
MML247	K-Chabazite (9 K/Unit cell)	2.67
MML270	Na,H -Chabazite (8.8 Na/unit cell)	3.5

MML276	Na,H -Chabazite (6.5 Na/unit cell)	3.26
MML267	Na,H -Chabazite (6 Na/unit cell)	2.39
MML268	Na,H -Chabazite (5 Na/unit cell)	2.18
MML251	Na,H -Chabazite (3 Na/unit cell)	1.19
MML308	Na,H-Chabazite (2.5 Na/unit cell)	1.22
MML256	Na,H -Chabazite (2 Na/unit cell)	0.483
MML309	Na,H-Chabazite (1 Na/unit cell)	0.331
MML266	Na,H -Chabazite (0 Na/unit cell)	0.082
MML313	Na,Cs-Rho	2.13
MML283	Li-Chabazite	4.14
MML239	K-ZK-5	2.14
MML274	H-ZK-5	0.63
MML269	Na-Rho (10 Na/unit cell)	3.22
MML275	Na,H-Rho (8.5 Na/unit cell)	2.01
MML280	Na,H-Rho (7 Na/unit cell)	1.72
MML299	Na,H-Rho (6 Na/unit cell)	2.01
MML286	Na,H-Rho (4.5 Na/unit cell)	1.57
MML287	Na,H-Rho (3.5 Na/unit cell)	1.39
MML288	Na,H-Rho (2.5 Na/unit cell)	1.29
MML200	Steamed Rho@ 470 ˚C-fast flow	0.85
MML180	Steamed Rho @ 470 ˚C	0.88
MML182	Steamed Rho @ 500 ˚C	0.7
MML183	Steamed Rho @ 550 ˚C	0.61
MML404	Ca,H-Rho (5 Ca/unit cell)	0.167
MML417	Ca,H -Rho (4 Ca/unit cell)	1.28
MML416	Ca,H -Rho (3 Ca/unit cell)	1.01
MML415	Ca,H -Rho (2 Ca/unit cell)	0.78
MML297	Ca,H-Chabazite (4.5 Ca/unit cell)	3.1
MML322	Ca,H-Chabazite (3.5 Ca/unit cell)	2.25
MML324	Ca,H-Chabazite (3 Ca/unit cell)	1.36
MML353	Ca,H-Chabazite (2.5 Ca/unit cell)	1.32
MML361	Ca,H-Chabazite (2 Ca/unit cell)	1.11

MML363	Ca,H-Chabazite (1.5 Ca/unit cell)	0.766
MML365	Ca,H-Chabazite (1 Ca/unit cell)	0.89
MML362	Ca,H-Chabazite (0 Ca/unit cell)	0.11
MML462	K-Rho	0.88
JK43A	ScBDC pure Sc_2	0.065
JK44B	ScBDC 100% Amine functionalized	0.181
JK45A	ScBDC 50% Amine functionalized	0.108
JMEX301	STA-12(Ni)	0.197
JMEX342	Sc-ABTC (calcined at 200 ˚C)	0.117
JMEX 433	MIL-100(Sc)	0.281
JK33A	Ni-CPO-27	1.68
JK34D	Mg-CPO-27	5.01
JK34A not activ.	Mg-CPO-27 (as prep. / not activated)	0.918
JK34A	Mg-CPO-27 (activated in water)	4.66
JK34M	Mg-CPO-27 (modified)	4.01
JK-34N	Mg-CPO-27 (heated in vacuo at 250 ˚C for ~16h)	2.38
JK53R	Mg-CPO-27 (modified)	4.44
JK53Y	Mg-CPO-27 (modified)	5.01
JK53Z	Mg-CPO-27 (modified)	4.42
JK53G	Mg-CPO-27 (modified)	2.97
JK61J	Mg-CPO-27 (modified)	4.1
JK61K	Mg-CPO-27 (modified)	3.06
JK61B	Mg-CPO-27 (modified)	6.55
JK61V	Mg-CPO-27 (modified)	5.34
ACM1	Mg-CPO-27	0.176
ACM2	Mg-CPO-27	0.566
ACM3	Mg-CPO-27	0.394
ACM4	Mg-CPO-27	1.29
MTW622	STA-12(Mg)	0.144
MTW559d	STA-16(Co)	0.111
LM303	STA-12(Co)	0.093

BPL Carbon	BPL Carbon	0.35
MOD163D	BPL-Piperazine	0.091
MOD198	BPL-Crown ether	0.082
MOD183B	BPL- Benzeneacetamide, N-[2-(dimethylamino)ethyl]-	0.064
MOD183A	Information not available	0.12
MOD229	Information not available	0.12
UCL-BZ-S1	Templated Carbon	0.29
UCL-BZ-S2	Templated Carbon	0.33
UCL-BZ-S3	Templated Carbon	0.098
UCL-BZ-S4	Templated Carbon	0.47
UCL-BZ-S5	Templated Carbon activated (KOH/precursor = 2)	0.78
UCL-BZ-S6	Templated Carbon activated (KOH/precursor = 3)	0.71
EML004	PIM-PI-1	0.066
HS48−RT400	Thermally re-arranged PIM-PI-OH	0.041
HS61−TR400	Thermally re-arranged PIM-PI-OH	0.12
HS61	PIM-PI-OH	0.089
DNM82	amine-PIM	0.16
DNM98	PIM-PBI	0.062
HS77	PIM-PI-OH	0.022
HS77−TR450	PIM-PBO	0.059
LMA23	PIM-1	0.14
LMA23−fibre	PIM-1 - fibre	0.28
LMA27	PIM-1	0.19
LMA27-spongy PIM	PIM-1	0.2
CAT-A-TB	TB-spiro-bis-indane PIM ladder	0.093
MC051	TB-Triptycene network	0.34
BD-154R	Triptycene-PIM-ladder	0.2
PcFeBiPy450	Phthalocyanine	0.075
MC060	TB-Triptycene ladder	0.27

EV37PPT3B	Indan TB-PIM	0.15
MC108	Soluble TB –PIM ladder	0.17
MC141	Insoluble TB –naphthalene PIM ladder	0.22
MC143	Quaternised MC141	0.18
MC158	Quaternary TB-crown ether PIM ladder	0.16
MC164	Quaternary TB-PIM	0.16
MC165	Quaternary TB-PIM	0.096
FLU-ANILINE-TB	Flu-dianiline-TB PIM	0.064
FLU-ANILINE-TB-Q	Quaternised Flu-dianiline-TB PIM	0.19
MC209	Triptycene ladder	0.21
1,3 DI-AMINO	TB-PIM	0.19
2,5-dimethyl TB-poly	Dimethylbenzene- Triptycene	0.26
SPIROFLUORENE	Spirobisfluorene ladder	0.067
Ethano-Antracene	TB-PIM	0.31
MC221	TB-bis-aniline	0.095
MC224	TB-bis-aniline	0.11
MC227	TB-bis-aniline	0.17
MC231	Triptycene ladder	0.41
MC245	Information not available	0.61

REFERENCES

1. *Climate Change 2007: Synthesis Report*; 2007.
2. Mauna Loa Observatory: Scripps Institution of Oceanography. http://co2now.org/Current-CO2/CO2-Now/scripps-co2-data-mauna-loa-observatory.html.
3. (a) *IPCC Special Report on Carbon Dioxide Capture and Storage*; 2005; (b) Olivier, J. G. J.; Janssens-Maenhout, G.; Peters, J. A. H. W., Trends in Global CO_2 Emissions 2012 Report. **2012**.
4. (a) *IEA. Energy Technology Transitions for Industry: Strategies for the Next Industrial Revolution.* ; International Energy Agency: Paris, France, 2009; (b) Luis, P.; Van Gerven, T.; Van der Bruggen, B., Recent Developments in Membrane-Based Technologies for CO_2 Capture. *Progress in Energy and Combustion Science* **2012,** *in press*, 1 - 30; (c) Kuramochi, T.; Ramírez, A.; Turkenburg, W.; Faaij, A., Comparative Assessment of CO_2 Capture Technologies for Carbon-Intensive Industrial Processes. *Progress in Energy and Combustion Science* **2012,** *38*, 87 - 112.
5. Coal-fired power plants capacity to grow by 35 per cent in next 10 years. *Power Engineer - Focus On Coal* **2012**.
6. (a) *The Costs of CO_2 Capture: Post-demonstration CCS in the EU*; Brussels, Belgium, 2011; (b) Herzog, H.; Drake, E.; Adams, E. *CO_2 Capture, Reuse, and Storage Technologies for Mitigating Global Climate Change*; Energy Laboratory, Massachusetts Institute of Technology: Cambridge, MA, 1997; (c) Ebner, A. D.; Ritter, J. A., State-of-the-art Adsorption and Membrane Separation Processes for Carbon Dioxide Production from Carbon Dioxide Emitting Industries. *Separation Science and Technology* **2009,** *44*, 1273 - 1421.
7. Kikkinides, E. S.; Yang, R. T.; Cho, S. H., Concentration and Recovery of CO_2 from Flue Gas by Pressure Swing Adsorption. *Ind. Eng. Chem. Res.* **1993,** *32*, 2714 - 2720.
8. (a) Gomes, V. G.; Yee, K. W. K., Pressure Swing Adsorption for Carbon Dioxide Sequestration from Exhaust Gases. *Sep. Purif. Technol.* **2002,** *28*, 161 - 171; (b) Chou, C. T.; Chen, C. Y., Carbon Dioxide Recovery by Vacuum Swing Adsorption. *Sep. Purif. Technol.* **2004,** *39*, 51 - 64; (c) Xiao, P.; Zhang, J.; Webley, P.; Li, G.; Singh, R.; Todd, R., Capture of CO_2 from Flue Gas Streams with Zeolite 13X by Vacuum-Pressure Swing Adsorption. *Adsorption* **2008,** *14*, 575 - 582; (d) Ishibashi, M.; Ota, H.; Akutsu, N.; Umeda, S.; Tajika, M.; Izumi, J.; Yasutake, A.; Kabata, T.; Kageyama, Y., Technology for Removing Carbon Dioxide from Power Plant Flue Gas by the Physical Adsorption Method. *Energy Convers. Manage.* **1996,** *37*, 929 - 933.
9. (a) Samanta, A.; Zhao, A.; Shimizu, G. K. H.; Sarkar, P.; Gupta, R., Post-Combustion CO_2 Capture Using Solid Sorbents: A Review. *ind. Eng. Chem. Res.* **2012,** *51*, 1438 - 1463; (b) Hedin, N.; Chen, L.; Laaksonen, A., Sorbents for CO_2 Capture from Flue Gas - Aspects from Materials and Theoretical

Chemistry. *Nanoscale* **2010,** *2*, 1819 - 1841; (c) Jones, C. W.; Choi, S.; Drese, J. H., Adsorbent Materials for Carbon Dioxide Capture from Large Anthropogenic Point Sources. *ChemSusChem* **2009,** *2*, 796 - 854.
10. Brandani, S., Analysis of the Piezometric Method for the Study of Diffusion in Microporous Solids: Isothermal Case. *Adsorption* **1998,** *4*, 17 -24.
11. (a) Chue, K. T.; Kim, J. N.; Yoo, Y. J.; Cho, S. H., Comparison of Activated Carbon and Zeolite 13X for CO_2 Recovery from Flue Gas by Pressure Swing Adsorption. *Ind. Eng. Chem. Res.* **1995,** *34*, 591 - 598; (b) Harlick, P. J. E.; Tezel, F. H., An Experimental Adsorbent Screening Study for CO_2 Removal from N_2. *Microporous and Mesoporous Materials* **2004,** *76*, 71 – 79.
12. Ruthven, D. M., *Principles of Adsorption and Adsorption Processes*. Wiley: New York, 1984.
13. Siriwardane, R. V.; Shen, M. S.; Fisher, E. P., Adsorption of CO_2, N_2, and O_2 on Natural Zeolites. *Energy & Fuels* **2003** *17*, 571 - 576.
14. Siriwardane, R. V.; Shen, M. S.; Fisher, E. P., Adsorption of CO_2 on Zeolites at Moderate Temperatures. *Energy & Fuels* **2005,** *19*, 1153 - 1159.
15. Cavenati, S.; Grande, C. A.; Rodrigues, A. E., Adsorption Equilibrium of Methane, Carbon Dioxide, and Nitrogen on Zeolite 13X at High Pressures. *J. Chem. Eng. Data ,* **2004,** *49*, 1095 - 1101.
16. Dasgupta, S.; Biswas, N.; Aarti; Gode, N. G.; Divekar, S.; Nanoti, A.; Goswami, A. N., CO_2 Recovery from Mixtures with Nitrogen in a Vacuum Swing Adsorber Using Metal Organic Framework Adsorbent: A Comparative Study. *International Journal of Greenhouse Gas Control* **2012,** *7*, 225 - 229.
17. (a) Yi, H.; Deng, H.; Tang, X.; Yu, Q.; Zhou, X.; Liu, H., Adsorption Equilibrium and Kinetics for SO_2, NO, CO_2 on Zeolites FAU and LTA. *Journal of Hazardous Materials* **2012,** *203 - 204*, 111 - 117; (b) Deng, H.; Yi, H.; Tang, X.; Yu, Q.; Ning, P.; Yang, L., Adsorption Equilibrium for Sulfur Dioxide, Nitric Oxide, Carbon Dioxide, Nitrogen on 13X and 5A Zeolites. *Chemical Engineering Journal* **2012,** *188*, 77 - 85.
18. Brandani, F.; Ruthven, D. M.; Coe, C. G., Measurement of Adsorption Equilibrium by the Zero Length Column (ZLC) Technique Part 1: Single-Component Systems. *Ind. Eng. Chem. Res.* **2003,** *42*, 1451 - 1461.
19. Ruthven, D. M.; Brandani, F., The Effect of Water on the Adsorption of CO_2 and C_3H_8 on Type X Zeolites. *Ind. Eng. Chem. Res.* **2004,** *43*, 8339 - 8344.
20. Li, G.; Xiao, P.; Webley, P.; Zhang, J.; Singh, R.; Marshall, M., Capture of CO_2 from High Humidity Flue Gas by Vacuum Swing Adsorption with Zeolite 13X. *Adsorption* **2008,** *14*, 415 - 422.
21. (a) Yucel, H.; Ruthven, D. M., Diffusion of CO_2 in 4A and 5A Zeolite Crystals. *Journal of Colloid and Interface Science* **1980,** *74* (1), 186 – 195; (b) Karger, J.; Ruthven, D. M., *Diffusion in Zeolites and Other Microporous Solids*. Wiley: New York, 1992.
22. Haq, N.; Ruthven, D. M., Chromatographic Study of Sorption and Diffusion in 4A Zeolite. *Journal of Colloid and Interface Science* **1986,** *112* (1).
23. Khodakov, A. Y.; Rees, L. V. C., Effect of Propane on the Kinetics of Carbon Dioxide Adsorption in NaA Zeolites. *Gas. Sep. Purif.* **1995,** *9* (4), 253 - 257.
24. Onyestiak, G.; Shen, D.; Rees, L. V. C., Frequency-Response Studies of CO_2 Diffusion in Commercial 5A Powders and Pellets. *Microporous Materials* **1996,** *5*, 279 - 288.

25. Ruthven, D. M., Diffusion of Xe and CO_2 in 5A Zeolite Crystals. *Zeolites* **1993,** *13*, 594.
26. Ahn, H.; Moon, J. H.; Hyun, S. H. L., C. H., Diffusion Mechanism of Carbon Dioxide in Zeolite 4A and CaX Pellets. *Adsorption* **2004,** *10*, 111 - 128.
27. Kamiuto, K.; Goubaru, A.; Ermalina, Diffusion Coefficients of Carbon Dioxide within Type 13X Zeolite Particles. *Chem. Eng. Comm.* **2006,** *193*, 628 - 638.
28. Li, P.; Tezel, F. H., Equilibrium and Kinetic Analysis of CO_2–N_2 Adsorption Separation by Concentration Pulse Chromatography. *Journal of Colloid and Interface Science* **2007,** *313*, 12 - 17.
29. Ridha, F. N.; Webley, P. A., Investigation of the Possibility of Low Pressure Encapsulation of Carbon Dioxide in Potassium Chabazite (KCHA) and Sodium Chabazite (NaCHA) Zeolites. *Journal of Colloid and Interface Science* **2009,** *337*, 332 - 337.
30. Pirngruber, G. D.; Raybaud, P.; Belmabkhout, Y.; Cejka, J.; Zukal, A., The Role of the Extra-Framework Cations in the Adsorption of CO_2 on Faujasite Y. *Phys. Chem. Chem. Phys.* **2010,** *12*, 13534 - 13546.
31. Walton, K. S.; Abney, M. B.; LeVan, M. D., CO_2 Adsorption in Y and X Zeolites Modified by Alkali Metal Cation Exchange. *Microporous and Mesoporous Materials* **2006,** *91*, 78 - 84.
32. Lee, K. M.; Lim, Y. H.; Jo, Y. M., Evaluation of Moisture Effect on Low-Level CO_2 Adsorption by Ion-Exchanged Zeolite. *Environmental Technology* **2012,** *33* (1), 77 - 84.
33. Yang, S. T.; Kim, J.; Ahn, W. S., CO_2 Adsorption Over Ion-Exchanged Zeolite Beta with Alkali and Alkaline Earth Metal Ions. *Microporous and Mesoporous Materials* **2010,** *135*, 90 - 94.
34. (a) Johnson, G. M.; Reisner, B. A.; Tripathi, A.; Corbin, D. R.; Toby, B. H.; Parise, J. B., Flexibility and Cation Distribution upon Lithium Exchange of Aluminosilicate and Aluminogermanate Materials with the RHO Topology. *Chem. Mater.* **1999,** *11*, 2780 - 2787; (b) Parise, J. B.; Abrams, L.; Gier, T. E.; Corbin, D. R., Flexibility of the Framework of Zeolite Rho. Structural Variation from 11 to 573 K. A Study Using Neutron Powder Diffraction Data. *J. Phys. Chem.* **1984,** *88*, 2303 - 2307; (c) Corbin, D. R.; Abrams, L.; Jones, G. A., *Flexibility of the Zeolite Rho Framework. In situ X-Ray and Neutron Powder Structural Characterization of Divalent Cation-Exchanged Zeolite Rho*. 1989; (d) Smith, M. L.; Corbin, D. R.; Abrams, L.; Dybowski, C., Flexibility of Zeolite Rho: Xe-129 NMR Studies of Entrapped Xenon in Cd-Rho. *J. Phys. Chem.* **1993,** *97*; (e) Parise, J. B.; Gier, T. E.; Corbin, D. R.; Cox, D. E., Structural Changes Occurring upon Dehydration of Zeolite Rho. A Study Using Neutron Powder Diffraction and Distance-Least-Squares Structural Modeling. *J. Phys. Chem.* **1984,** *88*, 1635 - 1640; (f) McCusker, L. B., Zeolite Crystallography. Structure Determination in the Absence of Conventional Single-Crystal Data. *Acta Cryst.* **1991,** *A47*, 297 - 313.
35. Baerlocher, C.; McCusker, L. B.; Olson, D. H., *Atlas of Zeolite framework types*. 6th ed.; 2007.
36. Lee, Y.; Reisner, B. A.; Hanson, J. C.; Jones, G. A.; Parise, J. B.; Corbin, D. R.; Toby, B. H.; Freitag, A.; Larese, J. Z., New Insight into Cation Relocations within the Pores of Zeolite Rho: In Situ Synchrotron X-Ray and

Neutron Powder Diffraction Studies of Pb- and Cd-Exchanged Rho. *J. Phys. Chem.* **2001,** *105*, 7188-7199.
37. Corbin, D. R.; Abrams, L.; Jones, G. A.; Eddy, M. M.; Stucky, G. D.; Cox, D. E., Flexibility of the Zeolite Rho Framework. Neutron Powder Structural Characterization of Ca-Exchanged Zeolite Rho. *J. Chem. Soc., Chem. Commun.* **1989**.
38. Palomino, M.; Corma, A.; Jorda´, J. L.; Rey, F.; Valencia, S., Zeolite Rho: a Highly Selective Adsorbent for CO_2/CH_4 Separation Induced by a Structural Phase Modification. *Chem. Commun.* **2012,** *48*, 215 - 217.
39. Dietzel, P. D. C.; Panella, B.; Hirscher, M.; Blom, R.; Fjellvåg, H., Hydrogen Adsorption in a Nickel Based Coordination Polymer with Open Metal Sites in the Cylindrical Cavities of the Desolvated Framework. *Chem. Commun.* **2006**, 959 - 961.
40. Millward, A. R.; Yaghi, O. M., Metal-Organic Frameworks with Exceptionally High Capacity for Storage of Carbon Dioxide at Room Temperature. *Journal of the American Chemical Society* **2005,** *127*, 17998 - 17999.
41. McDonald, T. M.; D'Alessandro, D. M.; Krishna, R.; Long, J. R., Enhanced Carbon Dioxide Capture upon Incorporation of N,N'-dimethylethylenediamine in the Metal–Organic Framework CuBTTri. *Chem. Sci.* **2011,** *2*, 2022 - 2028.
42. Dietzel, P. D. C.; Besikiotis, V.; Blom, R., Application of Metal Organic Frameworks with Coordinatively Unsaturated Metal Sites in Storage and Separation of Methane and Carbon Dioxide. *J. Mater. Chem.* **2009,** *19*, 7362 - 7370.
43. LeVan, M. D.; Liu, J.; Wang, Y.; Benin, A. I.; Jakubczak, P.; Willis, R. R., CO_2/H_2O Adsorption Equilibrium and Rates on Metal-Organic Frameworks: HKUST-1 and Ni/DOBDC. *Langmuir* **2010,** *26(17)*, 14301 14307.
44. Caskey, S. R.; Wong-Foy, A. G.; Matzger, A. J., Dramatic Tuning of Carbon Dioxide Uptake via Metal Substitution in a Coordination Polymer with Cylindrical Pores. *Journal of the American Chemical Society* **2008,** *130*, 10870 - 10871.
45. Valenzano, L.; Civalleri, B.; Chavan, S.; Palomino, G. T.; Area´n, C. O.; Bordiga, S., Computational and Experimental Studies on the Adsorption of CO, N_2, and CO_2 on Mg-MOF-74. *J. Phys. Chem.* **2010,** *114*, 11185 - 11191.
46. Valenzano, L.; Vitillo, J. G.; Chavana, S.; Civalleri, B.; Bonino, F.; Bordiga, S.; Lamberti, C., Structure–Activity Relationships of Simple Molecules Adsorbed on CPO-27-Ni Metal–Organic Framework: In Situ Experiments vs. Theory. *Catalysis Today* **2012,** *182*, 67 - 79.
47. Liu, J.; Tian, J.; Thallapally, P. K.; McGrail, B. P., Selective CO_2 Capture from Flue Gas Using Metal−Organic Frameworks—A Fixed Bed Study. *J. Phys. Chem.* **2012,** *116*, 9575 − 9581.
48. Krishna, R.; van Baten, J. M., A Comparison of the CO_2 Capture Characteristics of Zeolites and Metal-Organic Frameworks. *Separation and Purification Technology* **2012,** *87*, 120 - 126.
49. Herm, Z. R.; Krishna, R.; Long, J. R., CO_2/CH_4, CH_4/H_2 and $CO_2/CH_4/H_2$ Separations at High Pressures Using Mg_2(dobdc). *Microporous and Mesoporous Materials* **2012,** *151*, 481 - 487.

50. Choi, S.; Watanabe, T.; Bae, T. H.; Sholl, D. S.; Jones, C. W., Modification of the Mg/DOBDC MOF with Amines to Enhance CO_2 Adsorption from Ultradilute Gases. *J. Phys. Chem. Lett.* **2012,** *3*, 1136 − 1141.
51. Hu, X. Development of a Semi-Automated ZLC System for Rapid Screening of Adsorbents for Carbon Capture. University of Edinburgh, Edinburgh, 2012.
52. Poston, J. A.; Siriwardane, R. V.; Shen, M.; Fisher, E. P., Adsorption of CO_2 on Molecular Sieves and Activated Carbon. *Energy & Fuels* **2001,** *15*, 279 - 284.
53. Rodrigues, A. E.; Yong, Z.; Mata, V. G., Adsorption of Carbon Dioxide on Chemically Modified High Surface Area Carbon-Based Adsorbents at High Temperature. *Adsorption* **2001,** *7*, 41 - 50.
54. Himeno, S.; Komatsu, T.; Fujita, S., High-Pressure Adsorption Equilibria of Methane and Carbon Dioxide on Several Activated Carbons. *J. Chem. Eng. Data* **2005,** *50*, 369 - 376.
55. Shen, C.; Grande, C. A.; Li, P.; Yua, J.; Rodrigues, A. E., Adsorption Equilibria and Kinetics of CO_2 and N_2 on Activated Carbon Beads. *Chemical Engineering Journal* **2010,** *160*, 398 - 407.
56. Nitta, T.; Shigetomi, T.; Kurooka, M.; Katayama, T., An Adsorption Isotherm of Multi-Site Occupancy Model for Homogeneous Surface. *J. Chem. Eng. Jpn.* **1984,** *17*, 39 - 45.
57. Xu, R.; Chen, J.; Gao, Z.; Yan, W., *From Zeolites to Porous MOF Materials - The 40th Anniversary of International Zeolite Conference* Elsevier: Amsterdam, 2007.
58. Shen, C.; Yu, J.; Li, P.; Grande, C. A.; Rodrigues, A. E., Capture of CO_2 from Flue Gas by Vacuum Pressure Swing Adsorption Using Activated Carbon Beads. *Adsorption* **2011,** *17*, 179 - 188.
59. Shen, C.; Liu, Z.; Li, P.; Yu, J., Two-Stage VPSA Process for CO_2 Capture from Flue Gas Using Activated Carbon Beads. *Ind. Eng. Chem. Res.* **2012,** *51*, 5011 − 5021.
60. Carruthers, J. D.; Petruska, M. A.; Sturm, E. A.; Wilson, S. M., Molecular Sieve Carbons for CO_2 Capture. *Microporous and Mesoporous Materials* **2012,** *154*, 62 - 67.
61. Maroto-Valer, M. M.; Lu, Z.; Zhang, Y.; Tang, Z., Sorbents for CO_2 Capture from High Carbon Fly Ashes. *Waste Management* **2008,** *28*, 2320 - 2328.
62. Chew, T. L.; Ahmad, A. L.; Bhatia, S., Ordered Mesoporous Silica (OMS) as an Adsorbent and Membrane for Separation of Carbon Dioxide (CO_2). *Advances in Colloid and Interface Science* **2010,** *153*, 43 - 57.
63. Zeleˇnák, V.; Badaniˇcová, M.; Halamová, D.; ˇCejka, J.; Zukal, A.; Murafa, N.; Goerigk, G., Amine-Modified Ordered Mesoporous Silica: Effect of Pore Size on Carbon Dioxide Capture. *Chemical Engineering Journal* **2008,** *144* 336 - 342.
64. Belmabkhout, Y.; Serna-Guerrero, R.; Sayari, A., Adsorption of CO_2 from Dry Gases on MCM-41Silica at Ambient Temperature and High Pressure. 1: Pure CO_2 Adsorption. *Chemical Engineering Science* **2009,** *64*, 3721 - 3728.
65. Belmabkhout, Y.; Sayari, A., Adsorption of CO_2 from Dry Gases on MCM-41 Silica at Ambient Temperature and High Pressure. 2: Adsorption of

CO_2/N_2, CO_2/CH_4 and CO_2/H_2 Binary Mixtures. *Chemical Engineering Science* **2009,** *64*, 3729 - 3735.

66. (a) Serna-Guerrero, R.; Belmabkhout, Y.; Sayari, A., Further investigations of CO2 capture using triamine-grafted pore-expanded mesoporous silica. *Chemical Engineering Journal* **2010,** *158* 513 – 519; (b) Belmabkhout, Y.; Serna-Guerrero, R.; Sayari, A., Adsorption of CO2-Containing Gas Mixtures over Amine-Bearing Pore-Expanded MCM-41 Silica: Application for Gas Purification. *Ind. Eng. Chem. Res.* **2010,** *49*, 359 - 365; (c) Belmabkhout, Y.; Sayari, A., Effect of pore expansion and amine functionalization of mesoporous silica on CO_2 adsorption over a wide range of conditions. *Adsorption* **2009,** *15*, 318 – 328.
67. Xu, X. C.; Song, C. S.; Andresen, J. M.; Miller, B. G.; Scaroni, A. W., Preparation and Characterization of Novel CO_2 "Molecular Basket" Adsorbents Based on Polymer-Modified Mesoporous Molecular Sieve MCM-41. *Microporous and Mesoporous Materials* **2003,** *62* (1 - 2), 29 - 45
68. Xu, X. C.; Song, C. S.; Andresen, J. M.; Miller, B. G.; Scaroni, A. W., Adsorption Separation of CO_2 from Simulated Flue Gas Mixtures by Novel CO_2 "Molecular Basket" Adsorbents. *Int. J. Environ. Technol. Manage.* **2004,** *4*, 32 - 52.
69. Zhao, H.; Yan, W.; Bian, Z.; Hu, J.; Liu, H., Investigation of Mg Modified Mesoporous Silicas and their CO_2 Adsorption Capacities. *Solid State Sciences* **2012,** *14*, 250 - 257.
70. Budd, P. M.; Ghanem, B. S.; Makhseed, S.; McKeown, N. B.; Msayib, K. J.; Tattershall, C. E., Polymers of Intrinsic Microporosity (PIMs): Robust, Solution-Processable, Organic Nanoporous Materials. *Chem. Commun.* **2004**, 230 - 231.
71. McKeown, N. B.; Budd, P. M., Polymers of Intrinsic Microporosity (PIMs): Organic Materials for Membrane Separations, Heterogeneous Catalysis and Hydrogen Storage. *Chem. Soc. Rev.* **2006,** *35*, 675 - 683.
72. Budd, P. M.; Elabas, E. S.; Ghanem, B. S.; Makhseed, S.; McKeown, N. B.; Msayib, K. J.; Tattershall, C. E.; Wang, D., Solution-Processed, Organophilic Membrane Derived from a Polymer of Intrinsic Microporosity. *Adv. Mater.* **2004,** *16* (5), 456 - 459.
73. Budd, P. M.; Msayib, K. J.; Tattershall, C. E.; Ghanem, B. S.; Reynolds, K. J.; McKeown, N. B.; Fritsch, D., Gas Separation Membranes from Polymers of Intrinsic Microporosity. *Journal of Membrane Science* **2005,** *251*, 263 - 269.
74. Robeson, L. M., Correlation of separation factor versus permeability for polymeric membranes. , , . *Journal of Membrane Science* **1991,** *62*, 165 - 185.
75. Robeson, L. M., The Upper Bound Revisited. *Journal of Membrane Science* **2008,** *320*, 390 - 400.
76. (a) Ghanem, B. S.; McKeown, N. B.; Budd, P. M.; Selbie, J. D.; Fritsch, D., High-Performance Membranes from Polyimides with Intrinsic Microporosity. *Adv. Mater.* **2008,** *20*, 2766 - 2771; (b) Ghanem, B. S.; McKeown, N. B.; Budd, P. M.; Al-Harbi, N. M.; Fritsch, D.; Heinrich, K.; Starannikova, L.; Tokarev, A.; Yampolskii, Y., Synthesis, Characterization, and Gas

Permeation Properties of a Novel Group of Polymers with Intrinsic Microporosity: PIM-Polyimides. *Macromolecules* **2009,** *42*, 7881 - 7888.
77. Mason, C. R.; Maynard-Atem, L.; Al-Harbi, N. M.; Budd, P. M.; Bernardo, P.; Bazzarelli, F.; Clarizia, G.; Jansen, J. C., Polymer of Intrinsic Microporosity Incorporating Thioamide Functionality: Preparation and Gas Transport Properties. *Macromolecules* **2011,** *44*, 6471 - 6479.
78. Yong, W. F.; Li, F. Y.; Xiaoa, Y. C.; Li, P.; Pramoda, K. P.; Tong, Y. W.; Chung, T. S., Molecular Engineering of PIM-1/Matrimid Blend Membranes for Gas Separation. *Journal of Membrane Science* **2012,** *407- 408* 47 - 57.
79. (a) Li, F. Y.; Xiao, Y.; Chung, T. S.; Kawi, S., High-Performance Thermally Self-Cross-Linked Polymer of Intrinsic Microporosity (PIM-1) Membranes for Energy Development. *Macromolecules* **2012,** *45*, 1427 − 1437; (b) Du, N.; Dal- Cin, M. M.; Pinnau, I.; Nicalek, A.; Robertson, G. P.; Guiver, M. D., Azide-based Cross-Linking of Polymers of Intrinsic Microporosity (PIMs) for Condensable Gas Separation. *Macromol. Rapid Commun.* **2011,** *32*, 631 - 636.
80. Eic, M.; Ruthven, D. M., A New Experimental Technique for Measurement of Intracrystalline Diffusivity. *Zeolites* **1988,** *8*, 40 - 45.
81. Kärger, J.; Ruthven, D. M., *Diffusion in Zeolites and other Microporous Solids*. Wiley: New York, 1992.
82. Ruthven, D. M.; Brandani, F., ZLC Response for Systems with Surface Resistance Control. *Adsorption* **2005,** *11*, 31 - 34.
83. (a) Brandani, S., Effects of Nonlinear Equilibrium on Zero Length Column Experiments. *Chemical Engineering Science* **1998,** *53* (15), 2791 - 2798; (b) Brandani, S.; Jama, M. A.; Ruthven, D. M., ZLC Measurements Under Non-Linear Conditions. *Chemical Engineering Science* **2000,** *55*, 1205 - 1212.
84. Crank, J., *The Mathematics of Diffusion* Oxford University Press: London, 1956.
85. Brandani, S.; Ruthven, D. M., Analysis of ZLC Desorption Curves for Gaseous Systems. *Adsorption* **1996,** *2*, 133 - 143.
86. Brandani, S.; Ruthven, D. M., Analysis of ZLC Desorption Curves for Liquid Systems. *Chemical Engineering Science* **1995,** *50*, 2055 - 2059.
87. Ruthven, D. M.; Brandani, S.; Eic, M., Measurement of Diffusion in Microporous Solids by Macroscopic Methods. In *Molecular Sieves - Science and Technology*, Karge, H. G.; Weitkamp, J., Eds. Springer-Verlag: Berlin, 2008; Vol. 7, pp 45 - 84.
88. Brandani, F.; Rouse, A.; Brandani, S.; Ruthven, D. M., Adsorption Kinetics and Dynamics behavior of a Carbon Monolith. *Adsorption* **2004,** *10*, 99 - 109.
89. Brandani, F.; Ruthven, D. M., Measurement of Adsorption Equilibria by the Zero Length Column (ZLC) Technique Part 2: Binary Systems. *Ind. Eng. Chem. Res.* **2003,** *42*, 1462 1469.
90. Wang, H.; Brandani, S.; Lin, G.; Hu, X., Flowrate Correction for the Determination of Isotherms and Darken Thermodynamic Factors from Zero Length Column (ZLC) Experiments. *Adsorption* **2011,** *17*, 687 - 694.
91. Brandani, S.; Ruthven, D. M., Moments Analysis of the Zero Length Column Method. **1996**.

92. Gunadi, A.; Brandani, S., Diffusion of Linear Paraffins in NaCaA Studied by the ZLC Method. *Microporous and Mesoporous Materials* **2006,** *90*, 278 - 283.
93. Brandani, S.; Hufton, J.; Ruthven, D. M., Self-Diffusion of Propane and Propylene in 5A and 13X Zeolite Crystals Studied by the Tracer ZLC Method. *Zeolites* **1995,** *15*, 624 - 631.
94. Ruthven, D. M.; Farooq, S.; Knaebel, K. S., *Pressure Swing Adsorption*. VCH: New York, 1994.
95. (a) Smith, L. J.; Eckert, H.; Cheetham, A., Potassium Cation Effects on Site Preferences in the Mixed Cation Zeolite Li,Na-Chabazite. *Chem. Mater.* **2001,** *13*, 385 - 391; (b) Smith, L. J.; Eckert, H.; Cheetham, A., Site Preferences in the Mixed Cation Zeolite, Li,Na-Chabazite: A Combined Solid-State NMR and Neutron Diffraction Study. *J. Am. Chem. Soc.* **2000,** *122*, 1700 - 1708.
96. Ridha, F. N.; Webley, P. A., Anomalous Henry's law behavior of nitrogen and carbon dioxide adsorption on alkali-exchanged chabazite zeolites. *Separation and Purification Technology* **2009,** *67*, 336 - 343.
97. (a) Saxton, G. C.; Kruth, A.; Castro, M.; Wright, P. A.; Howe, R. F., Xenon adsorption in synthetic chabazite zeolites. *Microporous and Mesoporous Materials* **2010,** *129* 68 - 73; (b) Civalleri, B.; Ferrari, A. M.; Llunell, M.; Orlando, R.; Merawa, M.; Ugliengo, P., Cation Selectivity in Alkali-Exchanged Chabazite: An ab Initio Periodic Study. *Chem. Mater.* **2003,** *15*, 3996 - 4004.
98. Yakubovich, O. V.; Massa, W.; Gavrilenko, P. G.; Pekov, V., Crystal Structure of Chabazite K. *Crystallography Reports* **2005,** *50* (4), 544 - 553.
99. Ridha, F. N.; Yang, Y.; Webley, P. A., Adsorption characteristics of a fully exchanged potassium chabazite zeolite prepared from decomposition of zeolite Y. *Microporous and Mesoporous Materials* **2009,** *117*, 497 - 507.
100. (a) Shim, S. H.; Navrotsky, A.; Gaffney, T. R.; MacDougall, J. E., Chabazite: Energetics of hydration, enthalpy of formation, and effect of cations on stability. *American Mineralogist* **1999,** *84*, 1870 - 1882; (b) Jeanvoine, Y.; Ángyán, J. G.; Kresse, G.; Hafner, J., Brønsted Acid Sites in HSAPO-34 and Chabazite: An Ab Initio Structural Study. *J. Phys. Chem. B* **1998,** *102*, 5573 - 5580.
101. Ridha, F. N.; Webley, P. A., Entropic effects and isosteric heats of nitrogen and carbon dioxide adsorption on chabazite zeolites. *Microporous and Mesoporous Materials* **2010,** *132*, 22 - 30.
102. Watson, G. C.; Jensen, N. K.; Rufford, T. E.; Ida Chan, K.; May, E. F., Volumetric Adsorption Measurements of N_2, CO_2, CH_4, and a $CO_2 + CH_4$ Mixture on a Natural Chabazite from (5 to 3000) kPa. *J. Chem. Eng. Data* **2012,** *57*, 93 - 101.
103. Khvoshchev, S. S.; Zverev, A. V., Heats of sorption of carbon dioxide and ammonia on ion-exchange forms of synthetic chabazite. *ZEOLITES* **1991,** *11*.
104. Zhang, J.; Singh, R.; Webley, P. A., Alkali and alkaline-earth cation exchanged chabazite zeolites for adsorption based CO_2 capture *Microporous and Mesoporous Materials* **2008,** *111*, 478 - 487.

105. Parise, J. B.; Liu, X.; Corbin, D. R., Flexibility of the Zeolite RHO Framework; Relocation of Cadmium accompanying Transformation of the Unit Cell at High Temperatures. *J. Chem. Soc., Chem. Commun.* **1991**.
106. Chatelain, T.; Patarin, J.; Fousson, E.; Soulard, M.; Guth, J. L.; Schulz, P., Synthesis and characterization of high-silica zeolite RHO prepared in the presence of 18-crown-6 ether as organic template. *Microporous Materials* **1995,** *4* 231 - 238.
107. Lozinska, M. M.; Mangano, E.; Mowat, J. P. S.; Shepherd, A. M.; Howe, R. F.; Thompson, S. P.; Parker, J.; Brandani, S.; Wright, P. A., Understanding carbon dioxide adsorption on univalent cation forms of the flexible zeolite Rho at conditions relevant to carbon capture from flue gases. *Journal of the American Chemical Society* **2012,** *accepted*.
108. Araki, S.; Kiyohara, Y.; Tanaka, S.; Miyake, Y., Carbon Dioxide Adsorption Properties in Ion-exchanged Zeolites Rho. *Chem. Lett.* **2012,** *41*, 125 - 126.
109. Araki, S.; Kiyohara, Y.; Tanaka, S.; Miyake, Y., Carbon Dioxide Adsorption Properties in Ion-exchanged Zeolites Rho. *Chem. Lett.* **2012,** *41*, 125 - 126.
110. Langmi, H. W.; Book, D.; Walton, A.; Johnson, S. R.; Al-Mamouri, M. M.; Speight, J. D.; Edwards, P. P.; Harris, I. R.; Anderson, P. A., Hydrogen storage in ion-exchanged zeolites. *Journal of Alloys and Compounds* **2005,** *404-406*, 637 - 642.
111. (a) Shannon, R. D.; Staley, R. H.; Vega, A. J.; Fischer, R. X.; Baur, W. H.; Auroux, A., Nature of the Framework Hydroxyl Groups in Steamed H-RHO and H-Erionite Zeolites. *J. Phys. Chem.* **1989,** *93*, 2019 - 2027; (b) Callanan, L. H.; O'Connor, C. T.; van Steen, E., The effect of the adsorption properties of steamed zeolite rho on its methanol amination activity. *Microporous and Mesoporous Materials* **2000,** *35-36*, 163 - 172.
112. (a) Lievens, J. L.; Verduijn, J. P.; Mortier, W. J., Cation site energies in dehydrated KFI-type zeolites: d-NaKFI, d-NaHKFI, and d-KKFI. *ZEOLITES* **1992,** *12*, 690 - 697; (b) van Well, W. J. M.; Janchen, J.; de Haan, J. W.; van Santen, R. A., Adsorption of Linear Alkanes in the α-Cages and γ-Cages of H-ZK-5 and K-ZK-5. *J. Phys. Chem. B* **1999,** *103*, 1841 - 1853.
113. Corma, A.; Puche, M.; Rey, F.; Sankar, G.; Teat, S. J., A Zeolite Structure (ITQ-13) with Three Sets of Medium-Pore Crossing Channels Formed by 9- and 10-Rings. *Angew. Chem. Int. Ed.* **2003,** *42* (10), 1156 - 1159.
114. Pires, J.; Brotas de Carvalho, M.; Ribeiro, F. R.; Derouane, E. G., Carbon dioxide in Y and ZSM-20 zeolites: adsorption and infrared studies. *Journal of Molecular Catalysis* **1993,** *85*, 295 - 303.
115. (a) Dietzel, P. D. C.; Johnsen, R. E.; Fjellvåg, H.; Bordiga, S.; Groppo, E.; Chavanc, S.; Blom, R., Adsorption properties and structure of CO_2 adsorbed on open coordination sites of metal organic framework Ni_2(dhtp) from gas adsorption, IR spectroscopy and X-ray diffraction. *Chem. Commun.* **2008**, 5125 - 5127; (b) Dietzel, P. D. C.; Blom, R.; Fjellvåg, H., Base-Induced Formation of Two Magnesium Metal-Organic Framework Compounds with a Bifunctional Tetratopic Ligand. *Eur. J. Inorg. Chem.* **2008,** *3624 - 3632*.
116. Miller, S. R.; Wright, P. A.; Serre, C.; Loiseau, T.; Marrot, J.; Ferey, G., A microporous scandium terephthalate, $Sc_2(O_2CC_6H_4CO_2)_3$, with high thermal stability. *Chem. Commun.* **2005**, 3850 - 3852.

117. Miller, S. R.; Wright, P. A.; Devic, T.; Serre, C.; Ferey, G.; Llewellyn, P. L.; Denoyel, R.; Gaberova, L.; Filinchuk, Y., Single Crystal X-ray Diffraction Studies of Carbon Dioxide and Fuel-Related Gases Adsorbed on the Small Pore Scandium Terephthalate Metal Organic Framework, $Sc_2(O_2CC_6H_4CO_2)_3$. *Langmuir* **2009,** *25*, 3618 - 3626.
118. Mowat, J. P. S.; Miller, S. R.; Slawin, A. M. Z.; Seymour, V. R.; Ashbrook, S. E.; Wright, P. A., Synthesis, characterisation and adsorption properties of microporous scandium carboxylates with rigid and flexible frameworks. *Microporous and Mesoporous Materials* **2011,** *142*, 322 - 333.
119. Miller, S. R.; Pearce, G. M.; Wright, P. A.; Bonino, F.; Chavan, S.; Bordiga, S.; Margiolaki, I.; Guillou, N.; Ferey, G.; Bourrelly, S.; Llewellyn, P. L., Structural Transformations and Adsorption of Fuel-Related Gases of a Structurally Responsive Nickel Phosphonate Metal-Organic Framework, Ni-STA-12. *J. AM. CHEM. SOC.* **2008,** *130*, 15967 - 15981.
120. Wharmby, M. T.; Pearce, G. M.; Mowat, J. P. S.; Griffin, J. M.; Ashbrook, S. E.; Wright, P. A.; Schilling, L. H.; Lieb, A.; Stock, N.; Chavan, S.; Bordiga, S.; Garcia, E.; Pirngruber, G. D.; Vreeke, M.; Gora, L., Synthesis and crystal chemistry of the STA-12 family of metal N,N'-piperazinebis(methylenephosphonate)s and applications of STA-12(Ni) in the separation of gases. *Microporous and Mesoporous Materials* **2012,** *157*, 3 - 17.
121. Wharmby, M. T.; Mowat, J. P. S.; Thompson, S. T.; Wright, P. A., Extending the Pore Size of Crystalline Metal Phosphonates toward the Mesoporous Regime by Isoreticular Synthesis. *J. Am. Chem. Soc.* **2011,** *133*, 1266 - 1269.
122. Dietzel, P. D. C.; Georgiev, P. A.; Eckert, J.; Blom, R.; Strassle, T.; Unruh, T., Interaction of hydrogen with accessible metal sites in the metal–organic frameworks M_2(dhtp) (CPO-27-M; M = Ni, Co, Mg). *Chem. Commun.* **2010,** *46*, 4962 - 4964.
123. Yang, D. A.; Cho, H. Y.; Kim, J.; Yang, S. T.; Ahn, W. S., CO_2 capture and conversion using Mg-MOF-74 prepared by a sonochemical method. *Energy Environ. Sci.* **2012,** *5*, 6465 - 6473.
124. Liu, J.; Wang, Y.; Benin, A. I.; Jakubczak, P.; Willis, R. R.; LeVan, M. D., CO_2/H_2O Adsorption Equilibrium and Rates on Metal-Organic Frameworks: HKUST-1 and Ni/DOBDC. *Langmuir* **2010,** *26* (17), 14301 - 14307.
125. (a) MacDonald, J. A. F.; Evans, M. J. B., Adsorption and enthalpy of phenol on BPL carbon. *Carbon* **2002,** *40*, 703 - 707; (b) He, Y.; Yun, J. H.; Seaton, N. A., Adsorption Equilibrium of Binary Methane/Ethane Mixtures in BPL Activated Carbon: Isotherms and Calorimetric Heats of Adsorption. *Langmuir* **2004,** *20*, 6668 - 6678.
126. (a) Sevilla, M.; Fuertes, A. B., Sustainable porous carbons with a superior performance for CO_2 capture. *Energy Environ. Sci.* **2011,** *4*, 1765 - 1771; (b) Sevilla, M.; Valle-Vigón, P.; Fuertes, A. B., N-Doped Polypyrrole-Based Porous Carbons for CO_2 Capture. *Adv. Funct. Mater.* **2011,** *21*, 2781 - 2787.
127. (a) Budd, P. M.; McKeown, N. B., Highly permeable polymers for gas separation membranes. *Polym. Chem.* **2010,** *1*, 63 - 68; (b) Budd, P. M.; McKeown, N. B.; Ghanem, B. S.; Msayib, K. J.; Fritsch, D.; Starannikova, L.; Belov, N.; Sanfirova, O.; Yampolskii, Y.; Shantarovich, V., Gas permeation parameters and other physicochemical properties of a polymer of

intrinsic microporosity: Polybenzodioxane PIM-1. *Journal of Membrane Science* **2008,** *325*, 851 - 860.

128. (a) Tullos, G. L.; Mathias, L. J., Unexpected thermal conversion of hydroxy-containing polyimides to polybenzoxazoles. *Polymer* **1999,** *40* 3463 - 3468; (b) Park, H. B.; Han, S. H.; Jung, C. H.; Lee, C. H.; Hill, A. J., Thermally rearranged (TR) polymer membranes for CO_2 separation. *JOURNAL OF MEMBRANE SCIENCE* **2010,** *359* (1 - 2), 11 - 24; (c) Ghanem, B. S.; McKeown, N. B.; Budd, P. M.; Al-Harbi, N. M.; Fritsch, D.; Heinrich, K.; Starannikova, L.; Tokarev, A.; Yampolskii, Y., Synthesis, Characterization, and Gas Permeation Properties of a Novel Group of Polymers with Intrinsic Microporosity: PIM-Polyimides. *Macromolecules 2009* **2009,** *42*, 7881 - 7888.
129. (a) Park, H. B.; Jung, C. H.; Lee, Y. M.; Hill, A. J.; Pas, S. J.; Mudie, S. T.; Van Wagner, E.; Freeman, B. D.; Cookson, D. J., Polymers with Cavities Tuned for Fast Selective Transport of Small Molecules and Ions. *Science* **2007,** *318*, 254 - 258; (b) Park, H. B.; Han, S. H.; Jung, C. H.; Lee, Y. M.; Hill, A. J., Thermally rearranged (TR) polymer membranes for CO_2 separation. *Journal of Membrane Science* **2009**.
130. Tullos, G. L.; Mathias, L. J., Unexpected thermal conversion of hydroxy-containing polyimides to polybenzoxazoles. *Polymer* **1999,** *40*, 3463 - 3468.
131. (a) Pesiri, D. R.; Jorgensen, B.; Dye, R. C., Thermal optimization of polybenzimidazole meniscus membranes for the separation of hydrogen, methane, and carbon dioxide. *JOURNAL OF MEMBRANE SCIENCE* **2003,** *218* (1 - 2), 11 - 18; (b) Kumbharkar, S. C.; Liu, Y.; Li, K., High performance polybenzimidazole based asymmetric hollow fibre membranes for H_2/CO_2 separation. *Journal of Membrane Science* **2011,** *375*, 231 - 240.
132. Cavalcante, C. L.; Ruthven, D. M., Adsorption of Branched and Cyclic Paraffins in Silicalite. 2. Kinetics. *Ind. Eng. Chem. Res.* **1995,** *34*, 185 - 191.
133. Bulow, M., lntracrystalline Diffusion of Benzene in Microporous Gallosilicate with MFI Structure. *J. Chem. Soc. Faraday Trans.* **1994,** *90* (17), 2585 - 2590.
134. (a) Chon, H.; Ihm, S.-K.; Uh, Y. S., *On the sorption of ethylbenzene in ZSM-5* Amsterdam, 1997; Vol. 105, p 1747 - 1754; (b) Schumacher, R.; Ehrhardt, K.; Karge, H. G., Determination of Diffusion Coefficients from Sorption Kinetic Measurements Considering the Influence of Nonideal Gas Expansion. *Langmuir* **1999,** *15*, 3965 - 3971.
135. Brandani, S., Analysis of the Piezometric Method for the Study of Diffusion in Microporous Solids: Isothermal Case. *Adsorption* **1998,** *4*, 17 - 24.

APPENDIX A – RANKING OF CO_2 CAPACITY

Na,H Chabazites

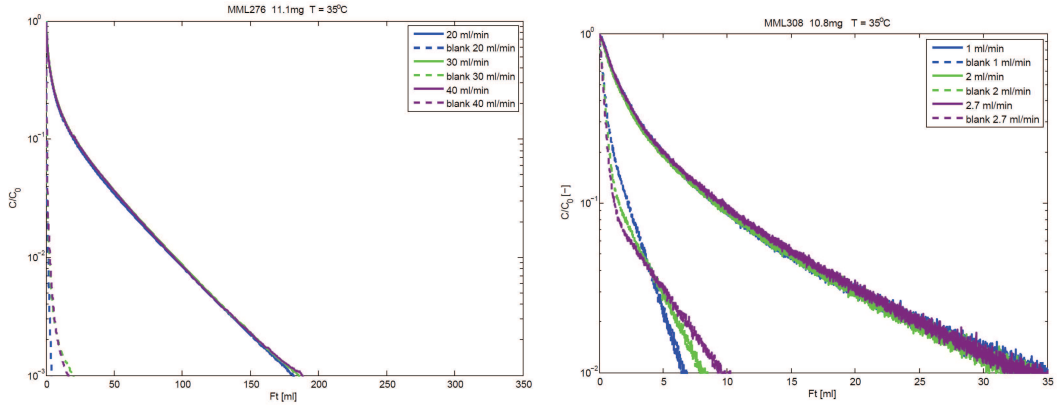

Figure-A. 1: ZLC Ft plot for MML276 (left) and MML308 (right)

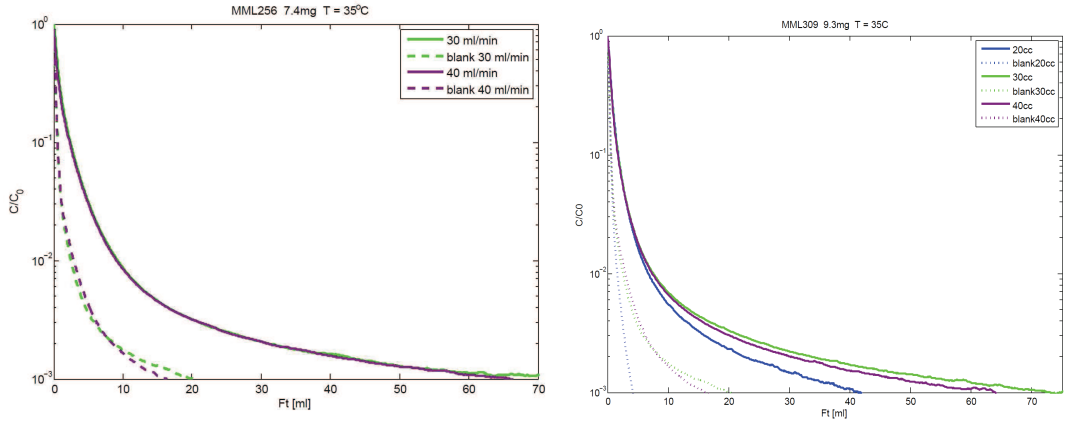

Figure-A. 2: ZLC Ft plot for MML256 (left) and MML309 (right).

Ca,H Chabazites

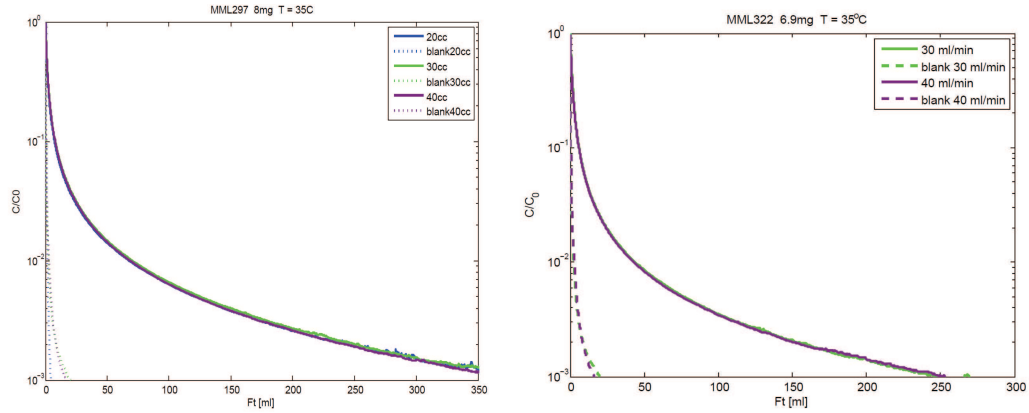

Figure-A. 3: ZLC Ft plot for MML297 (left) and MML322 (right).

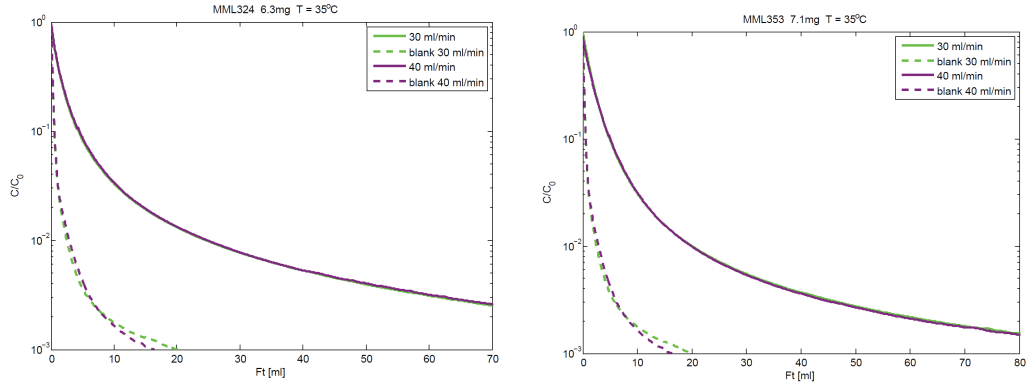

Figure-A. 4: ZLC Ft plot for MML324 (left) and MML353 (right).

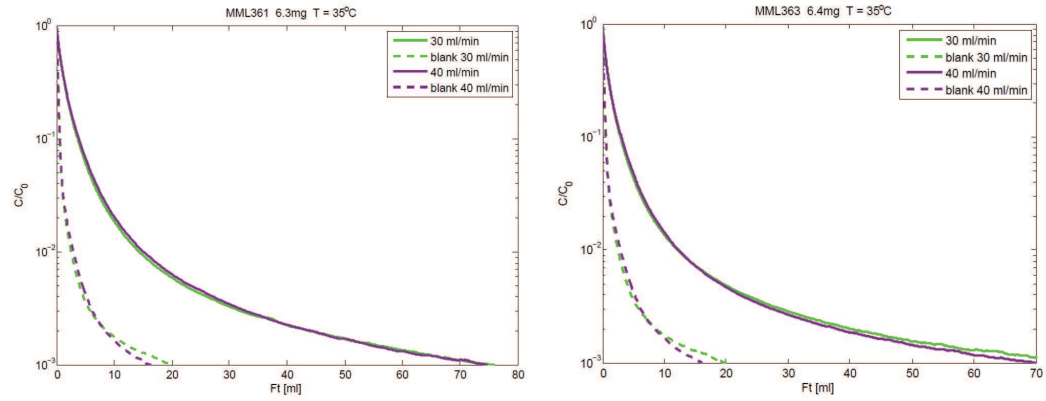

Figure-A. 5: ZLC Ft plot for MML361 (left) and MML363 (right).

Na,H Rho

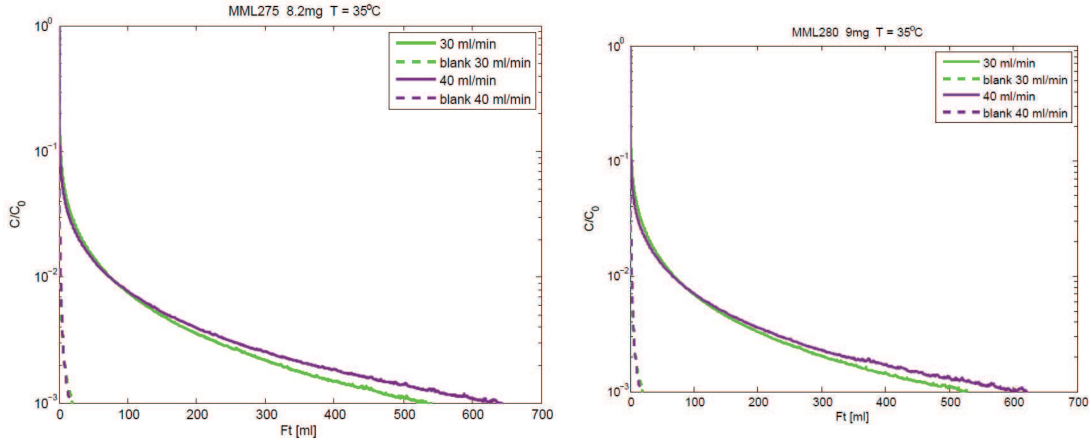

Figure-A. 6: ZLC Ft plot for MML275 (left) and MML380 (right).

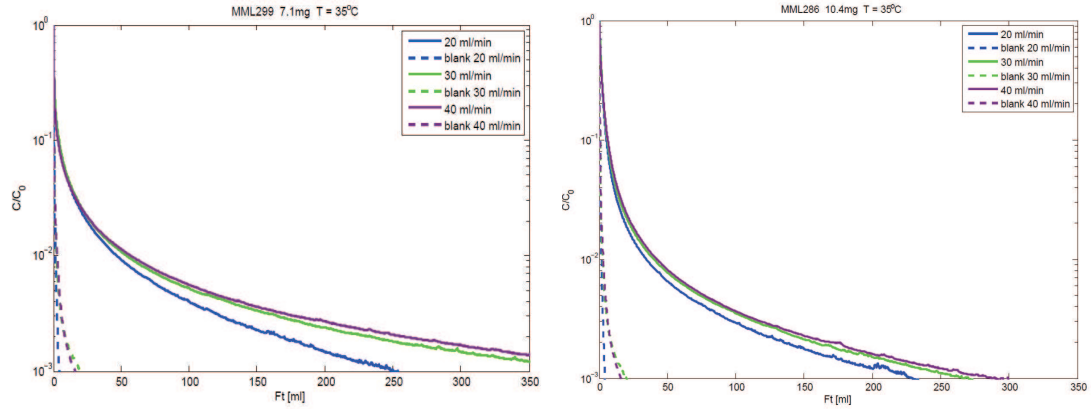

Figure-A. 7: ZLC Ft plot for MML299 (left) and MML286 (right).

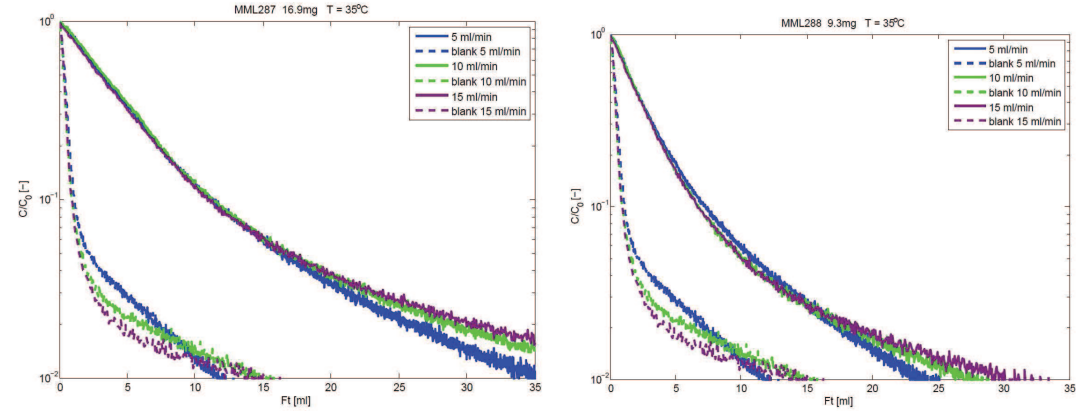

Figure-A. 8: ZLC Ft plot for MML287 (left) and MML288 (right).

Mg-CPO-27

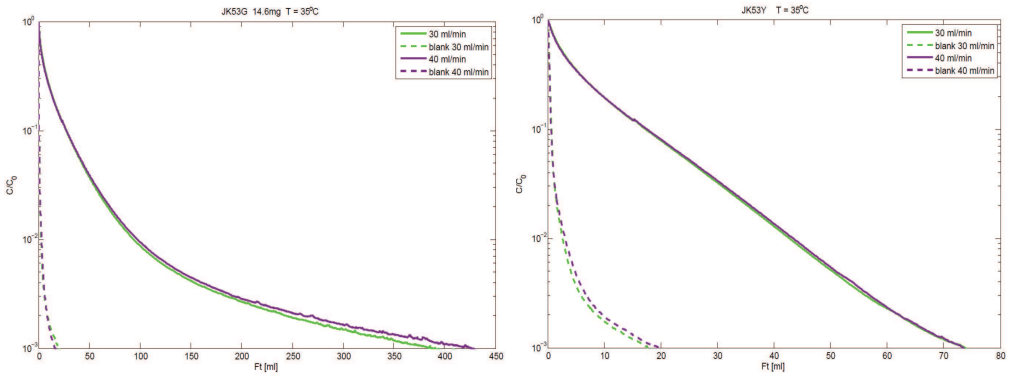

Figure-A. 9: ZLC Ft plot for JK-53G (left) and JK-53Y (right).

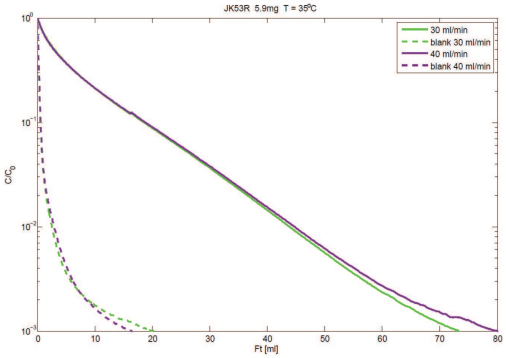

Figure-A. 10: ZLC Ft plot for JK-53R.

APPENDIX B – DIFFUSION OF CO_2 IN ION EXCHANGED RHO ZEOLITES

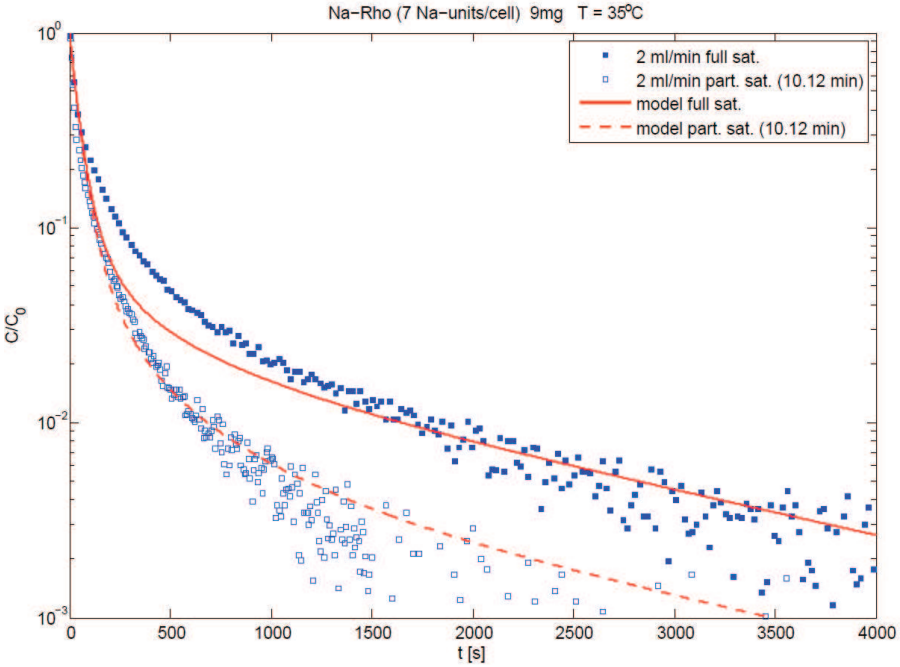

Figure-B 1: Experimental ZLC desorption curves for the fully and partially saturated Na,H-Rho (7 Na units/cell); in red the predicted curves using eq. 3.5 and eq. 3.15.

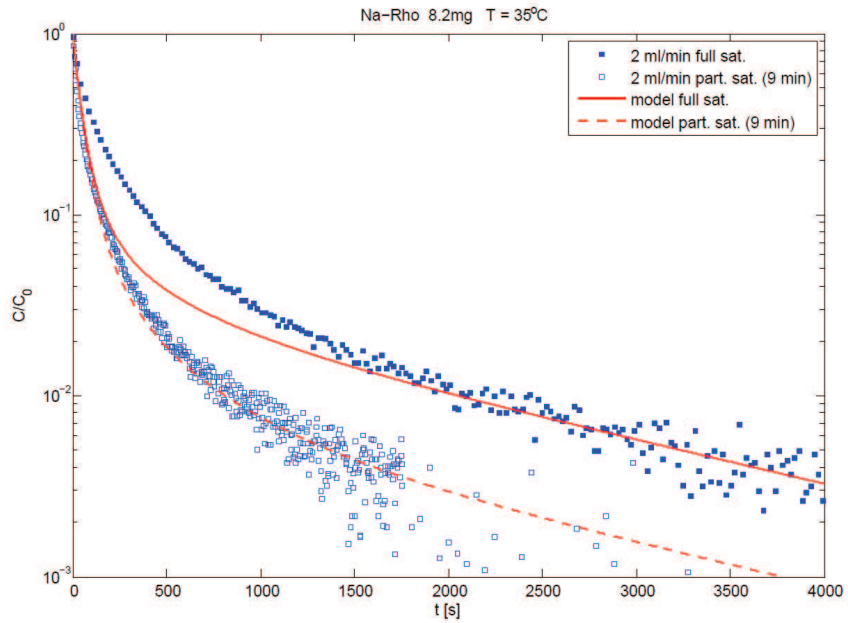

Figure-B 2: Experimental ZLC desorption curves for the fully and partially saturated Na,H-Rho (8.5 Na units/cell); in red the predicted curves using eq. 3.5 and eq. 3.15.

APPENDIX C – ANALYTICAL SOLUTION FOR PIEZOMETRIC MODEL

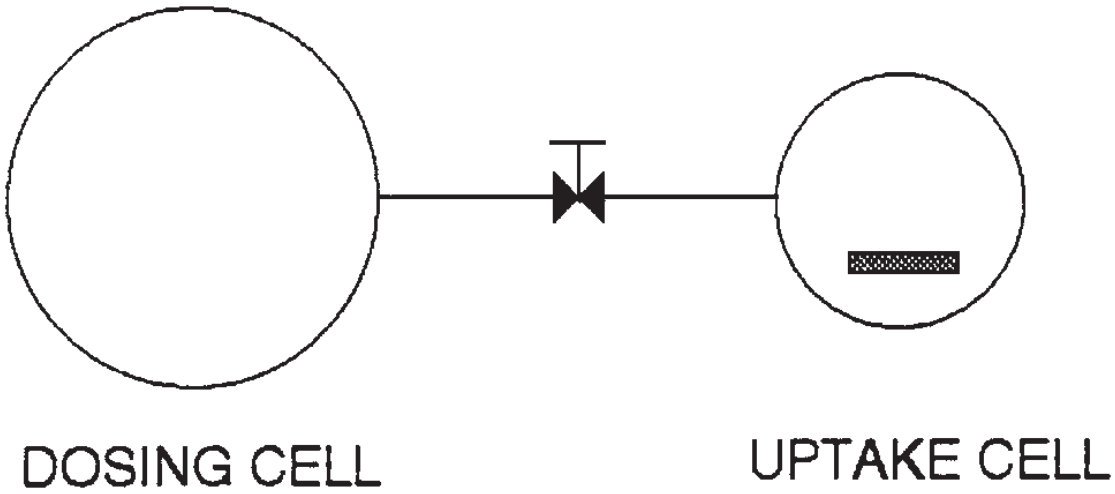

(*) The subscripts d and u refers to dosing and uptake cell

Nomenclature

c	Gas phase concentration, mol/ m^3
C	Dimensionless gas phase concentration,
D	Diffusivity, m^2/s
H	Equilibrium constant, mol/(kg*Pa)
n	Moles, mol
N	$Q\xi$
P	Pressure, Pa
q	Adsorbed phase concentration, mol/ kg
$\bar{q}$	Average adsorbed phase concentration, mol/ kg
Q	Dimensionless adsorbed phase concentration
r	Radial coordinate, m
R	Radius of crystals, m
$\Re$	Ideal gas constant, J/K
s	Laplace domain variable

t	Time, s
T	Temperature, K
V	Volume, m^3
M_s	Mass of the sample, kg

Greek Letters

β_i	Eigenvalues of the system
γ	Ratio of the accumulation in the uptake cell and in the solid,
δ	Ratio of the accumulation in the dosing cell and in the solid,
ε	Void fraction in uptake cell
ξ	Dimensionless radial coordinate
ρ	Reduced pressure
τ	Dimensionless time
$\overline{X}$	Linearised valve constant, mol/(Pa*s)
ϕ	Ratio between the temperatures of uptake and dosing cells
λ	Leak rate, mol/(Pa*s)
ω	Ratio of the diffusional and the valve time constants

Mass balance equations

Mass balance through the valve:

$$\frac{dn_d}{dt} = -\overline{X}\left(P_d - P_u\right) \qquad 0.1$$

Mass balance in the dosing cell

$$\frac{dn_d}{dt} = \frac{V_d}{\Re T_d}\frac{dP_d}{dt} \qquad 0.2$$

Mass balance in the uptake cell

$$\frac{dn_u}{dt} = -\frac{V_d}{\Re T_d}\frac{dP_d}{dt} - \lambda\left(P_u - P_{atm}\right) \qquad 0.3$$

$$\frac{dn_u}{dt} = M_s\frac{d\overline{q}}{dt} + \varepsilon V_u\frac{dc}{dt} \qquad 0.4$$

Combining eq. 0.3 and 0.4

$$M_s\frac{d\overline{q}}{dt} + \varepsilon V_u\frac{dc}{dt} = -\frac{V_d}{\Re T_d}\frac{dP_d}{dt} - \lambda\left(P_u - P_{atm}\right) \qquad 0.5$$

Combining eq. 0.1 and 0.2

$$\overline{X}\left(P_d - P_u\right) = -\frac{V_d}{\Re T_d}\frac{dP_d}{dt} \qquad 0.6$$

Assuming Fickian diffusion inside the particle

$$\frac{\partial q}{\partial t} = D\left(\frac{\partial^2 q}{\partial r^2} + \frac{2}{r}\frac{\partial q}{\partial r}\right) \qquad 0.7$$

$$\frac{d\overline{q}}{dt} = \frac{3D}{R}\left(\frac{\partial q}{\partial r}\right)_{r=R} \qquad 0.8$$

And linear equilibrium isotherm

$$q(R,t) - q_0 = H\left(P_u(t) - P_u^0\right) \qquad 0.9$$

Equilibrium at the surface is assumed as well as the following symmetry condition

$$\left(\frac{\partial q}{\partial r}\right)_{r=0}=0 \qquad 0.10$$

Dimensionless groups

$$\tau=\frac{tD}{R^2};\qquad Q=\frac{q-q_0}{q_\infty-q_0};\qquad C=\frac{c-c_0}{c_\infty-c_0};$$

$$\rho_d=\frac{P_d-P_u^0}{P_\infty-P_u^0};\qquad \rho_u=\frac{P_u-P_u^0}{P_\infty-P_u^0};\qquad \rho_{atm}=\frac{P_{atm}-P_u^0}{P_\infty-P_u^0};$$

$$\gamma=\frac{1}{3}\frac{\varepsilon V_u}{\Re T_u HM_s};\qquad \delta=\frac{1}{3}\frac{V_d}{\Re T_d HM_s};\qquad \omega=\frac{\Re T_d}{V_d}\overline{X}\frac{R^2}{D};$$

$$\xi=\frac{r}{R};\qquad N=Q\xi;\qquad \Gamma=\frac{\lambda}{3HM_s}\frac{R^2}{D};\qquad \phi=\frac{T_u}{T_d}$$

Combining mass balance equations and dimensionless variables:

$$\frac{dP_d}{dt}=\frac{\Re T_d}{V_d}\overline{X}\left(P_u-P_d\right) \qquad 0.11$$

$$M_s\frac{d\overline{q}}{dt}+\varepsilon V_u\frac{dc}{dt}+\frac{V_d}{\Re T_d}\frac{dP_d}{dt}+\lambda\left(P_u-P_{atm}\right)=0 \qquad 0.12$$

$$\frac{d\overline{q}}{dt}=\frac{3D}{R}\left(\frac{\partial q}{\partial r}\right)_{r=R}=\frac{3D}{R^2}\left(q_\infty-q_0\right)\left(\frac{\partial Q}{\partial\xi}\right)_{\xi=1} \qquad 0.13$$

$$\left(\frac{\partial Q}{\partial\xi}\right)_{\xi=1}=\left(\frac{\partial\left(\frac{N}{\xi}\right)}{\partial\xi}\right)_{\xi=1}=\left(\frac{1}{\xi}\frac{\partial N}{\partial\xi}+N\frac{\partial\left(\frac{1}{\xi}\right)}{\partial\xi}\right)_{\xi=1}=\left(\frac{\partial N}{\partial\xi}-N\right) \qquad 0.14$$

$$\frac{d\rho_d}{d\tau}=\omega\left(\rho_u-\rho_d\right); \qquad 0.15$$

$$\gamma\frac{d\rho_u}{d\tau}+\delta\frac{d\rho_d}{d\tau}+\left(\frac{\partial N}{\partial\xi}-N\right)_{\xi=1}+\Gamma\left(\rho_u-\rho_{atm}\right)=0 \qquad 0.16$$

$$\frac{\partial N}{\partial\tau}=\frac{\partial^2 N}{\partial\xi^2} \qquad 0.17$$

Initial and boundary conditions

$$\rho_d(0)=0;$$
$$\rho_u(0)=0;$$
$$N(\xi,0)=0;$$
$$N(0,\tau)=0;$$
$$N(1,\tau)=\rho_u(\tau);$$

0.18

Laplace transforms

$$s\tilde{\rho}_d-\rho_d^0=\omega(\tilde{\rho}_u-\tilde{\rho}_d);$$

0.19

$$\tilde{\rho}_u=\frac{(s+\omega)\tilde{\rho}_d-\rho_d^0}{\omega}$$

0.20

$$s\tilde{N}=\frac{\partial^2\tilde{N}}{\partial\xi^2}$$

0.21

$$\left.\frac{\partial\tilde{N}}{\partial\xi}\right|_{\xi=1}=\tilde{\rho}_u\sqrt{s}\coth\sqrt{s}$$

0.22

$$\tilde{N}\big|_{\xi=1}=\tilde{\rho}_u$$

0.23

$$\gamma s\tilde{\rho}_u+\delta\left(s\tilde{\rho}_d-\rho_d^0\right)+\tilde{\rho}_u\sqrt{s}\coth\sqrt{s}-\tilde{\rho}_u+\Gamma\left(\tilde{\rho}_u-\frac{\rho_{atm}}{s}\right)=0$$

0.24

Rearranging

$$\left(\gamma s+\sqrt{s}\coth\sqrt{s}-1+\Gamma\right)\tilde{\rho}_u+\delta s\tilde{\rho}_d-\delta\phi\rho_d^0-\Gamma\frac{\rho_{atm}}{s}=0$$

0.25

Substituting 0.18 in 0.23:

$$\left[\left(\gamma s+\sqrt{s}\coth\sqrt{s}-1+\Gamma\right)(s+\omega)+\delta\omega s\right]\tilde{\rho}_d-\rho_d^0\left(\gamma s+\sqrt{s}\coth\sqrt{s}-1+\Gamma+\delta\omega\right)-\Gamma\omega\frac{\rho_{atm}}{s}=0$$

Rearranging

$$\frac{\tilde{\rho}_d}{\rho_d^0}=\frac{s\left(\gamma s+\sqrt{s}\coth\sqrt{s}-1+\Gamma+\delta\omega\right)+\Gamma\omega\dfrac{\rho_{atm}}{\rho_d^0}}{s\left[\left(\gamma s+\sqrt{s}\coth\sqrt{s}-1+\Gamma\right)(s+\omega)+\delta\omega s\right]}$$

0.26

Inverse Laplace

Solving for l(s)=0:

$s_1 = 0;$

$$\sqrt{s_n}\coth\sqrt{s_n} = 1 - \gamma s_n - \Gamma - \frac{\delta\omega s_n}{(s_n+\omega)} = z_i; \qquad 0.27$$

$$\frac{dl(s)}{ds} = 2\delta\omega s + 3\gamma s^2 + 2\gamma\omega s + 2\Gamma s + \frac{1}{2}(5s+3\omega)\sqrt{s}\coth\sqrt{s} - \frac{(s+\omega)}{2}\left(s\coth^2\sqrt{s} - s\right) - 2s + \Gamma\omega - \omega$$

Solution = $\sum\rho(s_n) = \frac{j(s_n)}{l(s_n)}\exp(s_n\tau)$

$$\rho(s) = \frac{s\left(\gamma s + \sqrt{s}\coth\sqrt{s} - 1 + \Gamma + \delta\omega\right) + \Gamma\omega\frac{\rho_{atm}}{\rho_d^0}}{2\delta\omega s + 3\gamma s^2 + 2\gamma\omega s + 2\Gamma s + \frac{1}{2}(5s+3\omega)\sqrt{s}\coth\sqrt{s} - \frac{(s+\omega)}{2}\left(s\coth^2\sqrt{s} - s\right) - 2s + \Gamma\omega - \omega}$$

For s= s_1=0:

$$\rho(0) = \frac{0\left(\gamma 0 + 1 - 1 + \Gamma + \delta\omega\right) + \Gamma\omega\frac{\rho_{atm}}{\rho_d^0}}{2\delta\omega 0 + 3\gamma 0 + 2\gamma\omega 0 + 2\Gamma 0 + \frac{1}{2}(0+3\omega) - \frac{(0+\omega)}{2}(1-0) - 0 + \Gamma\omega - \omega}$$

$$\rho(0) = \frac{\rho_{atm}}{\rho_d^0}$$

For s= s_n:

$$\sqrt{s_n}\coth\sqrt{s_n} = 1 - \gamma s_n - \Gamma - \frac{\delta\omega s_n}{(s_n+\omega)} = z_i$$

$$\rho(s_n) = \frac{s_n\left(\gamma s_n + \sqrt{s_n}\coth\sqrt{s_n} - 1 + \Gamma + \delta\omega\right) + \Gamma\omega\frac{\rho_{atm}}{\rho_d^0}}{2\delta\omega s_n + 3\gamma s_n^2 + 2\gamma\omega s_n + 2\Gamma s_n + \frac{1}{2}(5s_n+3\omega)\sqrt{s_n}\coth\sqrt{s_n} - \frac{(s_n+\omega)}{2}\left(s_n\coth^2\sqrt{s_n} - s_n\right) - 2s_n + \Gamma\omega - \omega}$$

$$\rho(s_n) = \frac{2\left(s_n\left(\gamma s_n + 1 - \gamma s_n - \Gamma - \frac{\delta\omega s_n}{(s_n+\omega)} - 1 + \Gamma + \delta\phi\omega\right) + \Gamma\omega\frac{\rho_{atm}}{\rho_d^0}\right)}{4\delta\omega s_n + 6\gamma s_n^2 + 4\gamma\omega s_n + 4\Gamma s_n + (5s_n+3\omega)z_i - (s_n+\omega)\left(z_i^2 - s_n\right) - 4s_n + 2\Gamma\omega - 2\omega}$$

$$\rho(s_n)=\frac{2s_n\left(\frac{\delta\omega^2}{(s_n+\omega)}\right)+2\Gamma\omega\frac{\rho_{atm}}{\rho_d^0}}{4\delta\omega s_n+6\gamma s_n^{\,2}+4\gamma\omega s_n+4\Gamma s_n+(5s_n+3\omega)z_i-(s_n+\omega)(z_i^2-s_n)-4s_n+2\Gamma\omega-2\omega}$$

$$\rho(s_n)=\frac{2s_n\left(\frac{\delta\omega^2}{(s_n+\omega)}\right)+2\Gamma\omega\frac{\rho_{atm}}{\rho_d^0}}{4\delta\omega s_n+2\gamma s_n^{\,2}+2\Gamma s_n+2s_nz_i-2s_n-(s_n+\omega)(z_i^2-s_n-4\gamma s_n-2\Gamma+2-3z_i)}$$

$$\rho(s_n)=\frac{\frac{1}{(s_n+\omega)}\left(2s_n\delta\omega^2+2\Gamma\omega(s_n+\omega)\frac{\rho_{atm}}{\rho_d^0}\right)}{\frac{1}{(s_n+\omega)}\left(2s_n(\delta\omega(s_n+2\omega))-(s_n+\omega)^2(z_i^2-s_n-4\gamma s_n-2\Gamma+2-3z_i)\right)}$$

$$\rho(s_n)=\frac{2s_n\delta\omega^2+2\Gamma\omega(s_n+\omega)\frac{\rho_{atm}}{\rho_d^0}}{2\delta\omega s_n(s_n+2\omega)-(s_n+\omega)^2(z_i^2-s_n-4\gamma s_n-2\Gamma+2-3z_i)}$$

For $s_n=-\beta_n^2$

$$\rho(\beta_n^2)=\frac{-2\delta\omega^2\beta_n^2+2\Gamma\omega(-\beta_n^2+\omega)\frac{\rho_{atm}}{\rho_d^0}}{-2\delta\omega\beta_n^2(-\beta_n^2+2\omega)-(-\beta_n^2+\omega)^2(z_i^2+\beta_n^2+4\gamma\beta_n^2-2\Gamma+2-3z_i)}$$

$$\rho(\beta_n^2)=\frac{2\delta\omega^2\beta_n^2-2\Gamma\omega(\omega-\beta_n^2)\frac{\rho_{atm}}{\rho_d^0}}{2\delta\omega\beta_n^2(2\omega-\beta_n^2)+(\omega-\beta_n^2)^2(z_i^2+\beta_n^2+4\gamma\beta_n^2-2\Gamma+2-3z_i)}\exp(-\beta_n^2\tau)$$

Final equation:

$$\frac{\rho_d}{\rho_d^0} = \frac{\rho_{atm}}{\rho_d^0} + \sum_{n=1}^{\infty} \frac{2\delta\omega^2\beta_n^2 - 2\Gamma\omega\left(\omega - \beta_n^2\right)\frac{\rho_{atm}}{\rho_d^0}}{2\delta\omega\beta_n^2\left(2\omega - \beta_n^2\right) + \left(\omega - \beta_n^2\right)^2\left(z_i^2 + \beta_n^2 + 4\gamma\beta_n^2 - 2\Gamma + 2 - 3z_i\right)} \exp\left(-\beta_n^2\tau\right)$$

APPENDIX D – Understanding carbon dioxide adsorption on univalent cation forms of the flexible zeolite Rho at conditions relevant to carbon capture from flue gases

Magdalena M. Lozinska,[1] Enzo Mangano,[2] John P. S. Mowat,[1] Ashley M. Shepherd,[3] Russell F. Howe,[3] Stephen P. Thompson,[4] Julia E. Parker,[4] Stefano Brandani[2] and Paul A. Wright[1,*]

[1] *EaStCHEM School of Chemistry, University of St Andrews, Purdie Building, North Haugh, St Andrews, Fife, KY16 9ST, Scotland,* paw2@st-andrews.ac.uk

[2] *Institute of Materials and Processes, University of Edinburgh, King's Buildings, Mayfield Rd, Edinburgh, EH9 3JL, Scotland*

[3] *School of Chemistry, University of Aberdeen, Meston Building, King's College, Aberdeen AB24 3UE, Scotland*

[4] *Diamond Light Source Ltd, Harwell Science and Innovation Campus, Didcot, Oxfordshire, OX11 0DE, UK*

JACS
JOURNAL OF THE AMERICAN CHEMICAL SOCIETY

Article

pubs.acs.org/JACS

Understanding Carbon Dioxide Adsorption on Univalent Cation Forms of the Flexible Zeolite Rho at Conditions Relevant to Carbon Capture from Flue Gases

Magdalena M. Lozinska,[†] Enzo Mangano,[‡] John P. S. Mowat,[†] Ashley M. Shepherd,[§] Russell F. Howe,[§] Stephen P. Thompson,[∥] Julia E. Parker,[∥] Stefano Brandani,[‡] and Paul A. Wright*[,†]

[†]EaStCHEM School of Chemistry, University of St. Andrews, Purdie Building, North Haugh, St Andrews, Fife KY16 9ST, Scotland
[‡]Institute for Materials and Processes, University of Edinburgh, King's Buildings, Mayfield Rd, Edinburgh EH9 3JL, Scotland
[§]Department of Chemistry, University of Aberdeen, Meston Building, King's College, Aberdeen AB24 3UE, Scotland
[∥]Diamond Light Source Ltd., Harwell Science and Innovation Campus, Didcot, Oxfordshire OX11 0DE, U.K.

Supporting Information

ABSTRACT: A series of univalent cation forms of zeolite Rho ($M_{9.8}Al_{9.8}Si_{38.2}O_{96}$, M = H, Li, Na, K, NH_4, Cs) and ultrastabilized zeolite Rho (US-Rho) have been prepared. Their CO_2 adsorption behavior has been measured at 298 K and up to 1 bar and related to the structures of the dehydrated forms determined by Rietveld refinement and, for H-Rho and US-Rho, by solid state NMR. Additionally, CO_2 adsorption properties of the H-form of the silicoalumino-phosphate with the RHO topology and univalent cation forms of the zeolite ZK-5 were measured for comparison. The highest uptakes at 0.1 bar, 298 K for both Rho and ZK-5 were obtained on the Li-forms (Li-Rho, 3.4 mmol g^{-1}; Li-ZK-5, 4.7 mmol g^{-1}). H- and US-Rho had relatively low uptakes under these conditions: extra-framework Al species do not interact strongly with CO_2. Forms of zeolite Rho in which cations occupy window sites between α-cages show hysteresis in their CO_2 isotherms, the magnitude of which (Na^+,NH_4^+ < K^+ < Cs^+) correlates with the tendency for cations to occupy double eight-membered ring sites rather than single eight-membered ring sites. Hysteresis is not observed for zeolites where cations do not occupy the intercage windows. *In situ* synchrotron X-ray diffraction of the CO_2 adsorption on Na-Rho at 298 K identifies the adsorption sites. The framework structure of Na-Rho "breathes" as CO_2 is adsorbed and desorbed and its desorption kinetics from Na-Rho at 308 K have been quantified by the Zero Length Column chromatographic technique. Na-Rho shows much higher CO_2/C_2H_6 selectivity than Na-ZK-5, as determined by single component adsorption, indicating that whereas CO_2 can diffuse readily through windows containing Na^+ cations, ethane cannot.

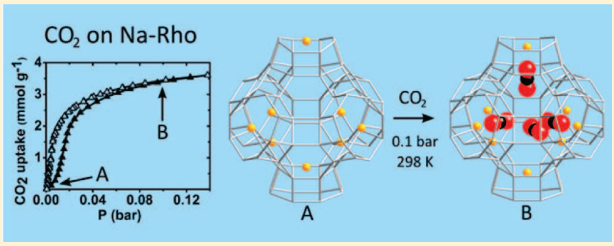

1. INTRODUCTION

Cationic zeolites with relatively high extra-framework cation contents are effective CO_2 adsorbents that can adsorb significant amounts of this greenhouse gas even at the low partial pressures of CO_2 (*ca.* 0.1 bar) and ambient temperatures relevant to carbon capture from flue gases.[1−7] Zeolites A, X, and Y, for example, which have relatively low Si/Al ratios and high extra framework cation contents adsorb CO_2 strongly at ambient temperature.[1−3] In each of these zeolites, however, much of the open space is inaccessible to CO_2 because the sodalite cages that are part of these structures cannot admit CO_2 (because it cannot pass through their six-membered ring (6MR) openings). Another approach is to use zeolites that have a larger fraction of their pore volume accessible but still have relatively small cages that facilitate strong interactions with adsorbed molecules, even at the highest levels of pore filling. The zeolites chabazite[4−7] and Rho[8] are attractive in this regard. In chabazitic zeotypes, for example, pore volumes of 0.33 cm^3 g^{-1} are available if no pore space is taken up by extra-framework cations, whereas in Rho, where all pore space is available, this value (see later) is 0.36 cm^3 g^{-1}.

Ridha et al. report the adsorption of CO_2 on Li-, Na-, and K-chabazite,[4−6] indicating that uptakes of between 4 and 5 mmol g^{-1} were obtained at 303 K and 0.1 bar, with the highest values obtained for Li-chabazite due to the high electrostatic interactions on the small Li^+ cation. The presence of the larger K^+ cation in the pores imparts the advantage of increasing the selectivity over N_2, which is both larger and interacts more weakly than CO_2 and so is less readily taken up. Hudson et al. report CO_2 adsorption on Cu-SSZ-13 (a high Si/Al chabazite) to be selective, although with lower uptake, and attribute the selectivity to the favorable interaction with the framework rather than with the extra-framework Cu^{2+} cations.[7] Very

Received: July 19, 2012
Published: September 26, 2012

   dx.doi.org/10.1021/ja3070864 | J. Am. Chem. Soc. 2012, 134, 17628−17642

recently, work on zeolite Na,Cs-Rho by Palomino et al.[9] showed very high CO_2/CH_4 selectivity at <1 bar and also non-type I adsorption behavior for CO_2 above *ca.* 1 bar that results from the structural flexibility of the Rho structure. *In situ* X-ray diffraction showed that at pressures of around 1 bar the framework structure undergoes the transformation from *I*-43*m* to *Im*-3*m* that is well characterized for Rho, in which both the pore volume and the window size increases (Figure 1).[10] Also,

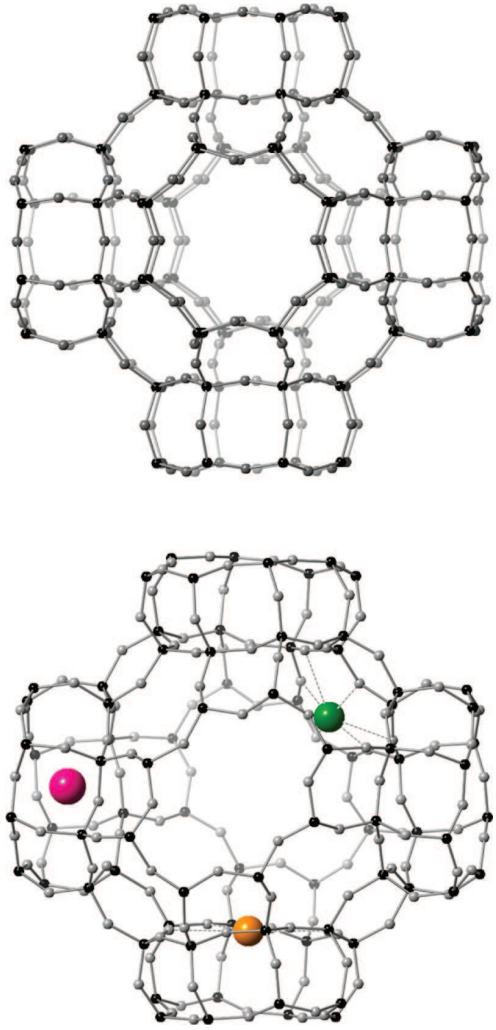

Figure 1. (Top) Framework structure of zeolite Rho in *Im*-3*m* symmetry, showing an α-cage surrounded by six double eight-membered ring (D8R) units that act as windows. (Bottom) Structure of zeolite Rho in *I*-43*m* symmetry, showing position of extra-framework cations in sites of type I, D8R, red sphere; type II, single eight-membered ring, S8R, orange sphere; and type III, single six-membered ring, S6R, green sphere.

recent publication of CO_2 isotherms on a range of different cation forms of zeolite Rho show strongly compositional adsorption effects and also strong hysteresis and non-type I behavior.[11] Only a very general explanation was suggested for this complex behavior, which is expected to result in part from the extra-framework cation distribution and strong cation-dependent structural flexibility of the Rho structure.[12−15]

We report here measurements of CO_2 adsorption on zeolite Rho samples fully exchanged with a range of univalent cations (Li^+, Na^+, K^+, Cs^+, NH_4^+, H^+) prepared by exhaustive cation exchange. The presence of univalent cations (other than protons) is observed to prevent the uptake of N_2 at 77 K but allow CO_2 uptake at 298 K, and CO_2 adsorption isotherms reveal a range of behavior, including strong deviation from Type I adsorption and hysteresis. Additional insight is available from measurements of reversible CO_2 uptake made using the Zero Length Column (ZLC) method[16−19] on fully and partially cation-exchanged samples. These data on zeolite Rho are compared with similar measurements performed on a zeolite ZK-5[20,21] of framework composition similar to that of the Rho studied here: ZK-5 is a structure that does not show flexibility upon dehydration and acts as a good example of a rigid, small pore structure with permanent porosity to N_2 and CO_2. In a first step, the adsorption behavior of all Rho and ZK-5 materials has been discussed by reference to the crystal structures of the dehydrated forms.

The CO_2 adsorption on zeolite Rho is found to be a complex function of cation type and loading. According to these measurements, and also because sodium is inexpensive, Na-Rho possesses the most potential as an adsorbent for the selective uptake of CO_2 at reasonable rates and with accessible uptake capacity at low partial pressures and ambient temperatures. Consequently, the mechanism of CO_2 adsorption and desorption on Na-Rho under conditions relevant to carbon capture from flue gases was studied in greater depth by a combination of *in situ* powder synchrotron XRD and IR spectroscopy. These reveal the response of the framework structure to CO_2 uptake and desorption and locate and quantify the adsorption sites for CO_2. The strongest CO_2 adsorption sites involve coordination of the molecules with extra-framework Na^+ cation sites, in a way similar to that proposed previously from modeling studies for adsorption of zeolites Na-Y,[2] Na-ferrierite,[22] and Na-A.[23] In addition to providing sites for strong adsorption via electrostatic interactions, the Na^+ cations occupy sites in single eight-membered ring (S8R) sites in windows between the α-cages and must move away from these window sites to enable adsorption to occur. The CO_2 diffusivity on Na-Rho at "zero coverage" has been measured directly using the versatile ZLC method.[16−19]

2. EXPERIMENTAL SECTION

Zeolite Na,Cs-Rho was prepared in the presence of 18-crown-6 according to published procedures.[24,25] The silicoaluminophosphate (SAPO) form of Rho[26] and the zeolite K-ZK-5[21] were also synthesized according to published methods. EDX analysis on these and all other samples was performed in a JEOL JSM 5600 SEM, with an Oxford INCA Energy 200 EDX analyzer. In addition, the morphology of zeolite Rho crystals was measured by field emission scanning electron microscopy (FEG-SEM) on a Jeol JSM-6700F electron microscope. Solid-state ^{27}Al and ^{29}Si MASNMR were performed on selected samples using a Varian VNMRS spectrometer operating at 79.44 MHz for ^{29}Si and 104.20 MHz for ^{27}Al. Deconvolution of the ^{29}Si MASNMR of the as-prepared Na,Cs-Rho, in which all aluminum occupies tetrahedral sites, was used to determine the framework Si/Al ratio of zeolite Rho and used to calibrate the Si/Al ratios determined via EDX.

The as-prepared Na,Cs-crown ether form of zeolite Rho was calcined at 823 K in oxygen for 12 h to remove all organic molecules. The resulting Na,Cs-Rho was fully exchanged to the ammonium form with 3 M ammonium chloride solution at 333 K, eight times for 5 h, until no cesium or sodium could be observed by EDX analysis. By contrast, most reported structural work on cationic forms of Rho[14] (often performed on larger multigram batches for neutron diffraction studies[14]) possessed significant levels of Cs^+ cations, which influence

dx.doi.org/10.1021/ja3070864 | J. Am. Chem. Soc. 2012, 134, 17628−17642

the structural behavior upon dehydration and CO_2 adsorption. Subsequently the ammonium form was converted to sodium, potassium, and cesium forms by additional repeated extended cation exchange treatments at 353 K using 10 wt % metal nitrate solutions, according to published procedures.[15,27] Finally, the lithium form of zeolite Rho was prepared by lithium exchange of the sodium form until no sodium could be observed by EDX. The lithium content was confirmed by subsequent repeated ion exchange with ammonium and measurement by atomic absorption of the lithium content of the resulting solutions. Any residual trace ammonium was converted to H^+ prior to all subsequent adsorption, structural, and spectroscopic measurements by heating at 623 K prior to analysis.

It was also possible to prepare mixed Li/NH_4 and Na/NH_4 zeolite Rho solids (general formula $(M^+)_{x-y}(NH_4^+)_yAl_xSi_{1-x}O_2$ via careful removal of cations by subsequent controlled ion exchange at 333 K for 30 min. Weighed portions (0.2 g) of Na-Rho and Li-Rho zeolites were stirred with 10 mL of ammonium chloride solution, with concentrations in the range of 0.01−3 M NH_4Cl. The amount of sodium remaining in the Na,NH_4-zeolites was determined by EDX. To determine the lithium content of the Li,NH_4-zeolites, the amount of Li^+ ions lost to the solution during ion exchange was measured by atomic absorption spectroscopy.

Thermogravimetry of all pure univalent cation forms of Rho was performed using a Netzsch TG 209 instrument with a heating rate of 5 K min^{-1} up to 973 K in flowing air, in order to determine the temperature at which water (or ammonia in the case of NH_4-Rho) was evolved (see Supporting Information). The protonic form of zeolite Rho and mixed cation/H^+-forms were prepared via deammoniation of the parent NH_4- or mixed NH_4/M-forms by heating under shallow bed conditions in dry flowing nitrogen at 823 K for 12 h, conditions known from literature data[10,28] and also our own TGA analysis to result in complete NH_3 removal. In addition, a sample of NH_4-Rho was "steamed" by heating under a high partial pressure of H_2O, to prepare "ultrastabilized" Rho, US-Rho.[14,29,30] In these experiments, a bed of pelletized NH_4-Rho was steamed in water vapor using water flow rates of 2.0 mL h^{-1} in flowing nitrogen at 743, 773 ,and 823 K for 8 h. To follow the effects of the deammoniation and steaming, ^{29}Si and ^{27}Al MASNMR were performed as described above, and for the sample steamed at 743 K, a two-dimensional ^{27}Al MQMAS spectra was obtained using a pulse sequence consisting of two pulses (of duration 2.8 and 1.0 μs at an RF field equivalent to 105 kHz) and a z-filter (at an RF field equivalent to 15 kHz). A total of 4000 repetitions were acquired for each of 32 increments in t_1. The recycle delay was 0.2 s, and the spinning rate was 12 kHz. Spectral referencing is with respect to external 1 M aqueous $AlCl_3$. The spectrum is plotted after shearing, and the indirectly detected, "isotropic", axis is scaled by a factor of 12/31. The protonic form of SAPO Rho was prepared by calcination in O_2 at 823 K for 12 h, conditions known to remove the organic template.

For comparison, sodium and lithium forms of ZK-5 were obtained by repeated cation exchange of the as-prepared potassium form at 353 K (8 exchanges for 4 h, using 1 M chloride solutions). In this case small amounts of potassium were observed to remain by EDX, giving unit cell compositions of $Na_{16.6}K_2Al_{18.6}Si_{77.4}O_{192}$ and $Li_{17.8}K_{0.8}Al_{18.6}Si_{77.4}O_{192}$. TGA analysis was performed as for the zeolite Rho samples.

The crystallinity of all as-prepared, cation-exchanged and calcined samples was confirmed by laboratory PXRD using a Stoe STAD I/P diffractometer using Cu Kα_1 X-radiation (1.54056 Å).

N_2 adsorption isotherms were measured volumetrically at 77 K using a Micromeritics Tristar II 3020. CO_2 adsorption isotherms were measured volumetrically starting at lower pressures using a Micromeritics 2020 porosimeter. This was typically performed from 0 to 1 bar at 298 K, although for Na-Rho isotherms up to 0.14 bar were also collected sequentially on the same sample at 273, 298, and 308 K. Prior to N_2 and CO_2 adsorption/desorption isotherms being measured, the samples were degassed under high vacuum at temperatures chosen from examination of the TGA plots that would result in the removal of all physically bound water. The temperature of 623 K was used for all samples except NH_4-Rho, which is known to undergo partial deammoniation at this temperature. For NH_4-Rho, 500 K was chosen as a compromise temperature to remove most of the physisorbed water while resulting in minor amounts of deammoniation. Indeed, prolonged evacuation at 500 K removed H_2O from all except the Li-forms of the zeolites. During measurement of the CO_2 adsorption isotherms each measurement on the adsorption and desorption branches was allowed up to 2.5 h to reach equilibrium, if this time was required. Ethane adsorption isotherms were measured volumetrically at 293 K using a custom-built glass line.

IR spectra of samples with and without adsorbed CO_2 were measured at room temperature on self-supporting wafers (~30 mg, 2 cm^2) placed in a pyrex cell with KBr windows using a Nicolet Magna instrument (DTGS detector, 4 cm^{-1} resolution). The infrared cell was connected to a vacuum line for evacuation and dehydration. The wafers were heated at 673 K for 4 h to ensure full dehydration, and CO_2 (BOC, SFC grade, >99.9995%) was admitted to give a range of equilibrium pressures.

For all Na,H-Rho samples the reversible capacity for CO_2 adsorption at 0.1 bar CO_2 and at 308 K was estimated by the ZLC method.[16−19] The technique is based in following the desorption curve of a sample previously saturated with a mixture of 10% CO_2 (sorbate) in He (carrier). When equilibrium between the gas phase and the adsorbed phase is reached, the flow is switched to pure He (purge) and the outlet gas phase concentration from the column is monitored. An online quadrupole mass spectrometer (Ametek Benchtop) is connected to the ZLC to monitor the outlet gas concentration. The apparatus is provided with drying columns to ensure predried gases entering the system; high and low flow rate mass flow controllers (0−50 mL/min and 0−3 mL/min, respectively) allowed experiments to be conducted under kinetic and equilibrium control. A very small amount of material (*ca.* 10 mg) is required to fill a ZLC. Before each experiment the samples were dehydrated overnight at 623 K under flow of pure He. The calculations of the CO_2 capacities are based on the dry weight of the sample. To ensure that full saturation was reached, preliminary ZLC experiments were run increasing the exposure time to the sorbate: the sample was fully equilibrated when the CO_2 capacity obtained did not change with the exposure time. Na,Cs-Rho registered the higher saturation time, 5 h; all the Na-Rho samples were saturated for 3 h.

Diffusion measurements at 308 K were performed via analysis of desorption curves obtained by ZLC on Na,Cs-Rho and Na-Rho following equilibration in 10% CO_2 (full saturation) or partial saturation in flowing 10% CO_2 for a shorter time (5.6 min for Na,Cs-Rho, 9.3 min for Na-Rho). In order to confirm the nature of the diffusion process over Na-Rho, experiments were also performed for Na-Rho at 308 K following saturation in 1% CO_2. Further details about the technique and the interpretation of the results are given in section 3.3.6 and in the Supporting Information.

In order to measure the structure of dehydrated zeolites, the powders were loaded into 0.7 mm quartz glass capillaries and dehydrated at 623 K at 10^{-5} mbar on a glass line for 12 h. The powder diffraction patterns of samples were measured in Debye−Scherrer geometry on a Stoe STAD i/p diffractometer with monochromated Cu Kα_1 X-rays (λ = 1.54056 Å). The structures were determined by Rietveld refinement against the XRD data, using the GSAS suite of programs.[31] For zeolite Rho, starting framework models were adapted from literature examples with the unit cell modified to that derived from the diffraction pattern. Starting cation positions were estimated from literature models and the framework atomic positions were refined with geometric constraints on Al,Si−O and O−O distances to maintain regular tetrahedral coordination. Final extra-framework cation positions and occupancies were determined by refinement of starting positions and by using difference Fourier methods to look for additional positions. ZK-5 was similarly refined from a starting model.[20] The ZK-5 prepared here contains a small amounts of chabazite (a polytype of ZK-5), so that the diffraction data was analyzed via a two-phase refinement, using a structural model for chabazite as a starting point.[32] Around 10% of the material was found to be chabazite.

For the fully exchanged sodium form of zeolite Rho, written Na-Rho, the structural response to CO_2 adsorption was measured by *in*

Table 1. Comparison of N_2 Uptake at p/p_o = 0.1 bar, 77 K and CO_2 Uptake at 0.1 and 0.8 bar at 298 K for a series of Rho and ZK-5 Structures of Different Compositions

sample name	unit cell formula of dehydrated sample	N_2 uptake at 0.1 bar, 77 K (mmol g^{-1})	adsorption CO_2 uptake at 0.1 bar, 298 K (mmol g^{-1})	adsorption CO_2 uptake at 0.8 bar 298 K (mmol g^{-1})
Na_xCs-Rho	$Na_{6.8}Cs_{3.0}$ $Al_{9.8}Si_{38.2}O_{96}$	0.27	2.25	3.55
NH_4-Rho	$(NH_4)_{9.8}Al_{9.8}Si_{38.2}O_{96}$	0.20	1.15	4.11
H-Rho	$(AlO_xH_y)_{0.6}H_{9.3\text{-}\delta}Al_{9.3}Si_{38.7}O_{96}$	10.5	1.63	3.97
H-SAPO(RHO)	$H_5Al_{24}Si_5P_{19}O_{96}$	10.4	0.98	3.29
US-Rho (743 K)	$(AlO_xH_y)_{5.4}Al_{4.6}Si_{43.4}O_{96}$	9.36	0.92	2.70
Cs-Rho	$Cs_{9.8}Al_{9.8}Si_{38.2}O_{96}$	0.12	0.07	0.53
Na-Rho	$Na_{9.8}Al_{9.8}Si_{38.2}O_{96}$	0.16	3.07	4.23
K-Rho	$K_{9.\ 8}Al_{9.8}Si_{38.2}O_{96}$	0.13	1.50	4.50
Li-Rho	$Li_{9.8}Al_{9.8}Si_{38.2}O_{96}$	0.30	3.36	4.96
Na-ZK-5	$Na_{16.6}K_2Al_{18.6}Si_{77.4}O_{192}$	5.81	4.05	4.81
Li-ZK-5	$Li_{17.8}K_{0.8}Al_{18.6}Si_{77.4}O_{192}$	7.08	4.67	6.09

situ synchrotron X-ray diffraction performed at beamline I-11 at the Diamond Light Source.[33] This was achieved using a custom-built gas handling line.[34] Sample was loaded into a 0.7 mm quartz glass capillary to a depth of around 1 cm, and a quartz wool plug was packed above this to prevent loss of powder upon evacuation and dehydration. The capillary was attached to a gas dosing line attached to a goniometer head, which was permitted to rock by 20° in the beam to improve powder averaging during diffraction. The sample was dehydrated under evacuation (10^{-3} mbar) using an Oxford Cryosystems Cryostream (700 plus) blowing hot air at 500 K for 2 h, under which conditions the sample was observed to have transformed to the dehydrated *I*-43*m* phase. Series of diffraction patterns, each of 2 min and over the 2θ range of 2−140°, were collected at 298 K before and after dehydration and also after dosing with 0.1 and 0.2 bar CO_2, each time after 15 min equilibration. Subsequently, diffraction patterns were measured during evacuation of the sample at 298 K, as carbon dioxide was removed. For the dehydrated zeolite and that on which CO_2 was adsorbed at 0.1 and 0.2 bar, five patterns were summed and the data binned to 0.005(2θ). For other patterns, the data in individual patterns was binned to 0.005(2θ). Full Rietveld refinement was then performed for Na-Rho after dehydration, in equilibrium with 0.1 and 0.2 bar CO_2, and after prolonged evacuation, in each case to determine the framework zeolite structure and the location and site occupancy of sodium cations and any CO_2 molecules. CO_2 adsorption sites were located by difference Fourier mapping. The starting framework model used was that refined against the synchrotron XRD data collected immediately prior to the CO_2 loading. The occupancy and location of the cations and the identified CO_2 positions were then refined against the data with constraints applied to maintain a linear CO_2 geometry and chemically reasonable bond lengths.

3. RESULTS AND DISCUSSION

3.1. Overview of Preparation, Structure, and Adsorption Properties. Rho and ZK-5 zeolites were prepared by hydrothermal synthesis according to the literature.[21,24] For zeolite Rho, the synthesis gave 2 μm particles built up from smaller crystallites around 0.1 μm in size. Zeolite ZK-5 formed as 1.4 μm cubes. Series of Rho and ZK-5 zeolites were prepared by extensive cation exchange and calcination as described in the Experimental Section. Their unit cell compositions were estimated from a combination of EDX and MASNMR analysis. The Si/Al ratio measured in the as-prepared zeolite Rho was measured by EDX as 4.0 and by deconvolution of the ^{29}Si spectrum as 3.9. The latter value was taken as the more accurate, and compositions calculated accordingly for both Rho and ZK-5 materials. Full details of the composition of cation-exchanged zeolites are given in Table 1. These assume full charge balance by univalent cations, and EDX measurements are within experimental error of this.

The H-form was prepared by deammoniation of NH_4-Rho under shallow bed heating. The bulk Si/Al ratio was not affected, but the framework Si/Al was shown by ^{29}Si MASNMR to have increased slightly (to 4.15) and ^{27}Al MASNMR indicated the presence of a small amount of octahedrally coordinated and therefore presumably extra-framework aluminum species corresponding to a loss of *ca.* 0.5 Al^{3+} per unit cell from the framework. The charge balance for the framework Al^{3+} is attributed to protons. Indeed, previous neutron diffraction studies of deammoniated Rho have located bridging hydroxyl groups in the structure.[30]

We were also interested in the effect on CO_2 adsorption of framework dealumination of the Rho structure during steaming, in which hydrothermal treatment of the NH_4-Rho results in migration of tetrahedrally coordinated framework Al to extra-framework positions and recrystallization of the framework with a higher Si/Al ratio. For all steamed samples (at 743, 773, and 823 K) the framework Si/Al ratio was the same (within the limits of accuracy) at 9.4. This indicates a framework Al content of 4.6 per unit cell, and therefore a loss of *ca.* 5.4 Al per unit cell during deammoniation. The coordination geometry of the extra framework Al was investigated by a combination of ^{27}Al MASNMR and MQ MASNMR (Figure 2). Aluminum removed from the framework is observed to move to extra-framework sites that can be 4-, 5-, or 6-fold coordinated, behavior very similar to that reported for Al^{3+} cations in dealuminated zeolite Y.[35] It was not possible to exchange any of this extra-framework aluminum. The only effect of higher steaming temperatures was to reduce the pore volume, so that the results presented in Table 1 are for the sample steamed at 743 K.

For each of the Rho materials, PXRD of the dehydrated samples were measured at 298 K, and the structures were refined by Rietveld analysis as described in the Experimental Section. Crystallographic details are given in Table 2, including the minimum O···O distance across the elliptical (or circular) windows delimited by 8MRs and calculated from the distance between the O atom centers, minus twice the ionic radius of O^{2-}, 1.35 Å. It should be noted that Cook and Conner[36] suggest that the effective pore size of zeolites is consistently 0.7 Å more than that usually quoted on the basis of this hard sphere model, especially when comparing these values with Lennard-Jones radii (2.98 Å for the smaller dimension of CO_2

dx.doi.org/10.1021/ja3070864 | J. Am. Chem. Soc. 2012, 134, 17628−17642

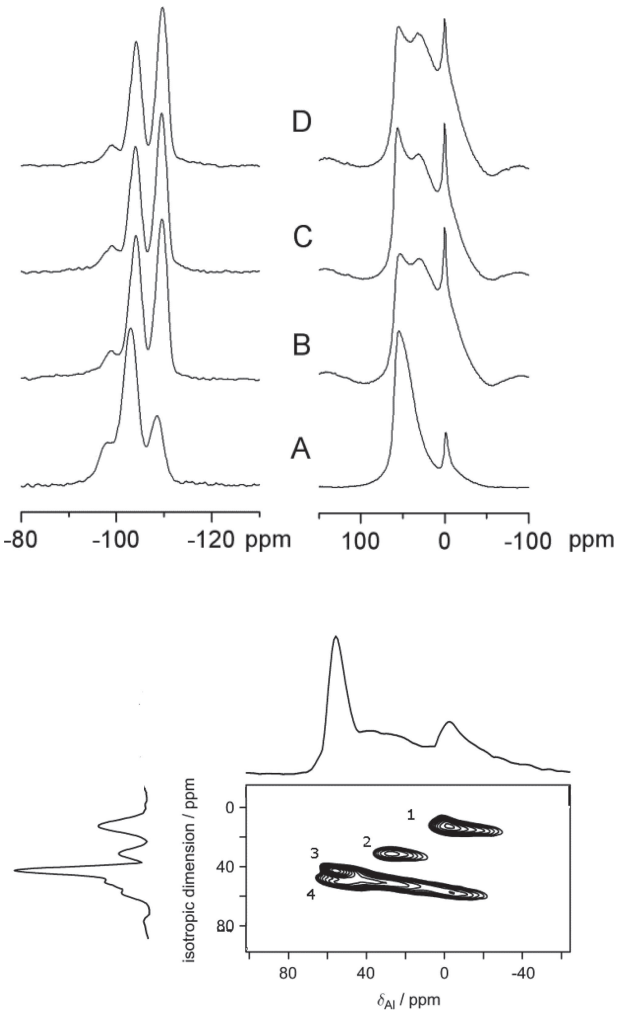

Figure 2. (Top) (left) ^{29}Si and (right) ^{27}Al MASNMR of NH_4-Rho (A) heated at 773 K in dry N_2 flow and steamed at (B) 743 K, (C) 773 K, and (D) 823 K. (Bottom) 3Q ^{27}Al MASNMR of sample steamed at 743 K: 1, octahedral Al in extra-framework positions; 2, five-coordinate Al in extra-framework positions; 3, tetrahedral framework Al; 4, Al in a distorted tetrahedral extra-framework environment.

via a 2-center Lennard-Jones model[37]). This difference between crystallographic values using ionic radii and empirical observations is attributed to thermal motion, chemical interaction, and the difference in the type of atomistic model. The occupancy of the cation sites, defined as types I, II, and III as described below, are also given in Table 2, with full details of the atomic coordinates supplied in the Supporting Information.

For all Rho zeolites in the hydrated form the structure adopts the centrosymmetric structure. Upon dehydration H-Rho remains centrosymmetric (*Im*-3*m*), whereas for all cation-exchanged Rho materials dehydration resulted in transformation to the noncentrosymmetric *I*-43*m* form. Univalent cation positions were located within the center of the double eight ring window site, D8R (coordinates (1/2,0,0) denoted site I here), at a site close to the plane of the 8MR (S8R site, coordinates (x,0,0), $x \approx 0.4$, denoted site II), or at sites close to 6MRs in the α-cage (S6R, coordinates (x,x,x), $x \approx 0.2 - 0.3$, denoted site III). These sites are consistent with those reported in the literature and are illustrated in Figure 3 for Na,Cs-Rho, Na-Rho, Cs-Rho, NH_4-Rho, Li-Rho, and K-Rho, showing for each a possible arrangement of cations in a single cage. The cation occupancies given in Table 2 are those from unconstrained refinement. Differences from the expected 9.8 cations per unit cell are thought to derive from inherent uncertainties in refinement against laboratory XRD data.

Although cation rearrangement is possible upon CO_2 uptake, as observed by Palomino et al. in Na,Cs-Rho,[9] these framework structures and cation positions are a good starting point for understanding the adsorptive properties of Rho as the solid is first put in contact with CO_2. The structures are described below for H-forms of Rho and related solids; Na,Cs-, Na-, and Cs-forms; and the other cation forms (NH_4, Li, K). In addition, the cation location in a partially exchanged Na,H-Rho is also given in Table 2.

The structure of cation-exchanged zeolites Na- and Li-ZK-5 were also determined by Rietveld refinement, taking into account the residual K^+ in these materials and also the presence of chabazite impurity. Two extra-framework cation site locations were located for Na^+ cations. The first type is in strongly nonplanar 8MRs of the PAU cages between α-cages (Type 1 in Table 3), whereas the second is in 6MRs of the α-cages (Type 2 in Table 3). For Na-ZK-5 the Na−O distances in the 8MR sites are 2.67(1) Å and for the 6MR are 2.35(1) Å. In Li-ZK-5 the 6MR sites are fully occupied by Li^+ cations, and there is some scattering (assigned as K^+) in the 8MR sites. The Li−O distances in the 6MR sites are 2.09(1) Å, as expected, and the K−O distance is 2.89(1) Å. The locations are

Table 2. Space Group, Minimum O−O Distance of 8MR Windows, and Cation Site Occupancies in Dehydrated Zeolite Rho (Site I, D8R; Site II, S8R; Site III, S6R)[a]

				site I		site II		site III	
sample	unit cell parameter (Å)	space group	O···O (Å)	frac occup	atoms/unit cell	frac occup	atoms/unit cell	frac occup	atoms/unit cell
Na,Cs-Rho	14.5307(4)	*I*-43*m*	2.69	0.4258(25)	2.55(2)	0.252(11)	3.02(13)	0.317(18)	2.54(14)
NH_4-Rho	14.7018(2)	*I*-43*m*	2.85	0.323(6)	1.93(4)	0.677(6)	8.12(7)		
H-Rho	15.0352(2)	*Im*-3*m*	3.88						
Na-Rho	14.3771(2)	*I*-43*m*	2.26			0.539(7)	6.47(8)	0.372(11)	2.98(9)
Na-Rho (50%)	14.3447(2)	*I*-43*m*	2.21	0.269(6)	1.61(4)	0.241(3)	2.89(4)		
Li-Rho	14.2448(2)	*I*-43*m*	1.90					1.00	8.00
Li-Rho (50%Li)	14.4239(5)	*I*-43*m*	2.24					0.65(3)	5.20(24)
K-Rho	14.5951(2)	*I*-43*m*	2.72	0.343(4)	2.06(2)	0.571(3)	6.85(4)		
Cs-Rho	14.5947(3)	*I*-43*m*	2.85	1.00	6.00			0.424(3)	3.39(2)

[a] As determined by Rietveld refinement from laboratory powder X-ray diffraction collected at 293 K.

dx.doi.org/10.1021/ja3070864 | J. Am. Chem. Soc. 2012, 134, 17628−17642

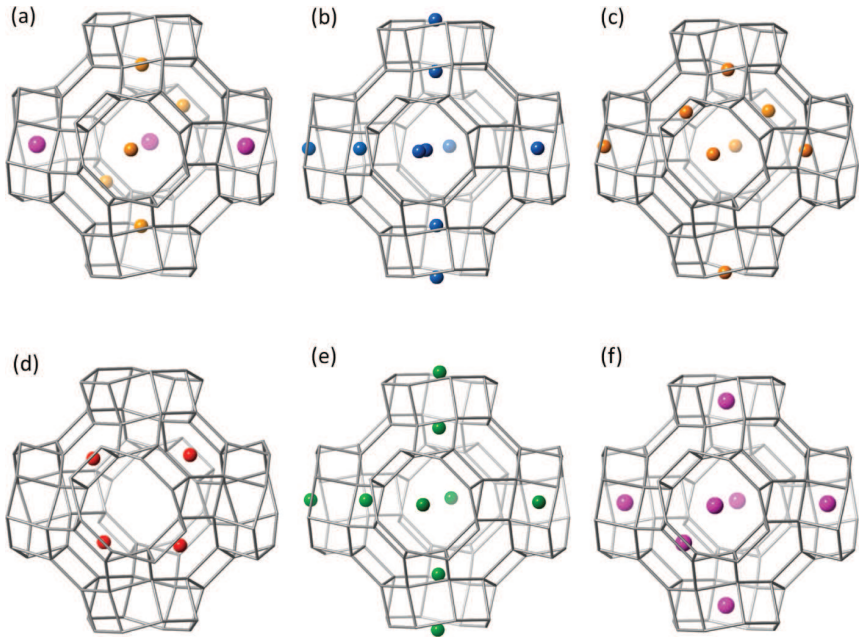

Figure 3. Possible cation distributions in one α-cage and associated D8R windows of dehydrated univalent cation forms of zeolite Rho, determined from Rietveld refinement of laboratory X-ray powder diffraction data. (a) Na,Cs-Rho (larger spheres, Cs; smaller spheres, Na), (b) NH_4-Rho (N only represented), (c) Na-Rho, (d) Li-Rho, (e) K-Rho, (f) Cs-Rho.

Table 3. Refined Unit Cell Parameters, Window Size, Cation Locations, and Occupancies in Na-ZK-5 and Li-ZK-5 of Table 1[a]

				8MR site occupancy		6MR site occupancy	
sample	unit cell parameter (Å)	space group	O···O (Å)	frac occup	cations/unit cell	frac occup	cations/unit cell
Na-ZK-5	18.6142(2)	*Im*-3*m*	4.00	0.166(1) K	1.99(2) K	0.536(4) Na	8.57(6) Na
				0.636(5) Na	7.63(5) Na		
Li-ZK-5	18.5985(3)	*Im*-3*m*	3.90	0.089(5) K	1.08(1) K	1 Li	16 Li

[a]Obtained by Rietveld analysis of laboratory X-ray data collected at 293 K.

illustrated for Na-ZK-5 in Figure 4, which shows that the 8MR windows between cages do not have cations in them and have O···O distances (taking ionic radii into account) of 4.0 Å.

3.2. CO_2 Adsorption Performance of Different Univalent Cationic Forms of Zeolite Rho Related to Their Dehydrated Structures. *3.2.1. CO_2 Adsorption on the H-Form of Zeolite Rho and Related Materials.* Although none of the materials was cation-free, the closest estimate of the intracrystalline pore volume of an "empty" framework can be made by considering adsorption on the protonic form. H-Rho possesses a pore volume of 0.36 $cm^3\ g^{-1}$ (10.5 $mmol(N_2)\ g^{-1}$), and H-Rho has previously been shown to possess Brønsted acid sites.[38] H-zeolites are known in general to show weaker electrostatic effects than cationic forms, due to the polarizing effect of the protons in the bridging hydroxyl groups. As a result, the uptake of CO_2 at 298 K and 0.1 bar on H-Rho is relatively low (1 mmol g^{-1}) due to the weak interactions (Figure 5). This uptake increases to 3.5 mmol g^{-1} by 0.9 bar and is fully reversible. The structure of dehydrated H-Rho was confirmed to have *Im*-3*m* symmetry, a = 15.0352(2) Å, where the circular 8-rings have an opening large enough to admit both N_2 and CO_2. Notably, the isotherm is very different from that reported by Araki et al. for the so-called H-Rho of their work.[11] The difference arises because at their lower ion exchange temperature not all of the Cs^+ is exchanged by ammonium and the non-Type I isotherm shape probably results from a structural change occurring as P_{CO_2} increases, controlled by the presence of the residual Cs^+ cations in D8R sites.

The calcined, dehydrated H-SAPO(RHO) structure has been reported previously in the *I*23 space group, to permit ordering of Al and P (and Si, which substitutes for P).[39] The window size of the dehydrated solid is large enough to permit uptake of N_2 and CO_2. Direct comparison of the CO_2 isotherm of H-SAPO(RHO), consistent with those reported elsewhere,[40] with H-Rho, indicates that H-SAPO(RHO) is a weaker adsorbent (Figure 5). The overall anionic charge on the framework in the SAPO form is lower than that of the aluminosilicate, so that there will be less electrostatic interaction.

The N_2 uptake of steamed (ultrastabilized) zeolite Rho at 0.1 bar at 77 K (9.6 mmol g^{-1}) was close to that of the H-Rho, but CO_2 adsorption at 0.1 bar and 298 K is lower, indicating that there is a weaker interaction. That there is no strong interaction with the extra framework aluminum species indicates that the trivalent Al^{3+} cations must be shielded by associated hydroxide and/or oxide species, either within the cages, or in their own nonporous alumina phase. The observed weaker interaction is attributed to the lower framework charge in the dealuminated framework.

3.2.2. CO_2 Adsorption Related to Structure for Na,Cs-, Na-, and Cs-Rho. Na,Cs-Rho showed no N_2 adsorption at 77 K, but appreciable CO_2 uptake at 298 K (Table 1 and Figure 6), with significant hysteresis observed under the conditions of the

dx.doi.org/10.1021/ja3070864 | J. Am. Chem. Soc. 2012, 134, 17628–17642

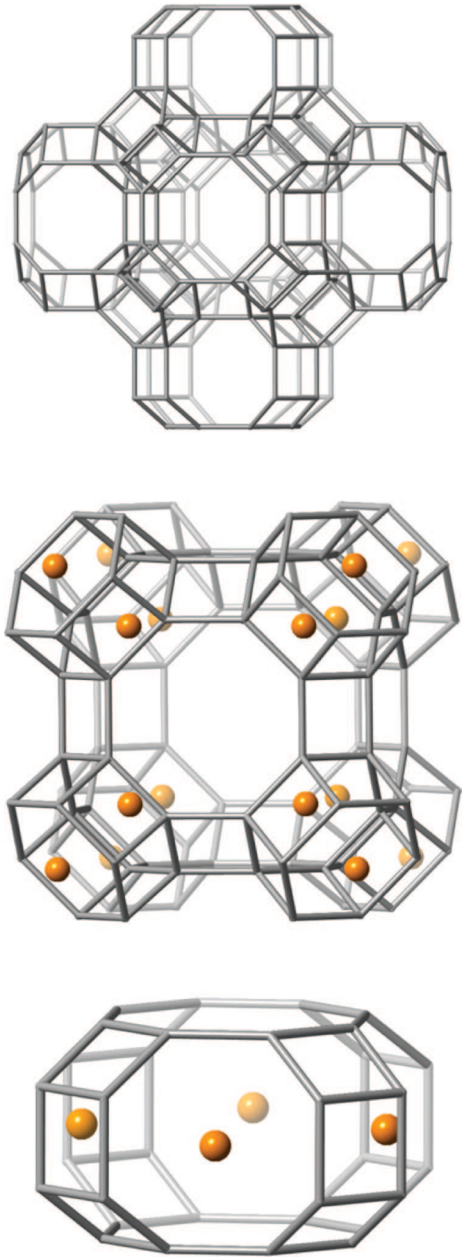

Figure 4. (Top) Framework structure of ZK-5 with O atoms omitted for clarity and T−T linkages represented by gray sticks, showing α-cage surrounded by six *pau* cages (which lead to six other α-cages). (Middle) Type 1 cations in 6MR sites in α-cage. (Bottom) Type 2 cations in puckered 8MR sites in *pau* cage.

measurement of the adsorption isotherm (max 2.5 h equilibration time). In this structure, when dehydrated, around one-half of the D8R sites are occupied by Cs^+ while Na^+ cations occupy sites of type II near the 8MRs in other windows of the large α-cages (Figure 2). That CO_2 is adsorbed must indicate that either the Cs^+ or the Na^+ cations (or both) must be able to move to permit diffusion. The *in situ* XRD structural studies of Palomino et al.[9] indicate that above 1 bar at 298 K the structure changes symmetry to *Im*-3*m* and that at 5 bar Cs^+ is displaced from its position in site I to occupy a position at site II. The adsorption data here confirms that some cations must move

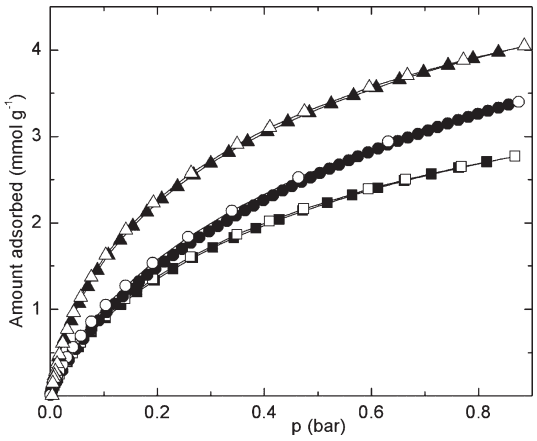

Figure 5. CO_2 isotherms at 298 K for H-Rho (triangles), US-Rho (squares), and the H-form of SAPO(RHO) (circles). Adsorption, closed symbols; desorption, open symbols.

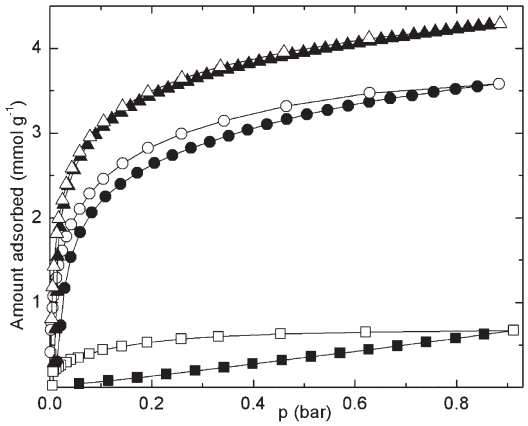

Figure 6. CO_2 isotherms at 298 K for Na,Cs-Rho (circles), Na-Rho (triangles), and Cs-Rho (squares). Adsorption, closed symbols; desorption, open symbols.

sufficiently far away from their S8R site to permit the CO_2 molecules to enter the cage.

To determine the relative mobility of Cs^+ and Na^+ in these window sites, the pure Na^+ and Cs^+ cation forms were prepared, and the structures of the dehydrated cationic forms were measured by Rietveld refinement of laboratory X-ray data (Table 2). In each case, the dehydrated form distorts to the noncentrosymmetric *I*-43*m* structure, with different unit cell parameters and 8MR openings. In Cs-Rho the cations fully occupy the D8R sites and also occupy S6R (type III) sites within the α-cages. In Na-Rho the cations occupy S8R sites as well as some S6R (type III) sites, so that each window has a cation at site II, assuming that two Na^+ cations will favor being distributed over two D8R windows rather than occupying two sites in one and none in another. This is supported by the observation of Na^+ cations in S6R sites as soon as there are enough cations per unit cell to exceed one per window (observed in Na-Rho, Na,Cs-Rho). In neither Cs- nor Na-Rho was N_2 adsorbed at 77 K, due to the blocking action of the cations, further supporting evidence for Na^+ cations in all D8R windows. Adsorption isotherms at 298 K up to 1 bar show the Cs^+ form adsorbs only low amounts of CO_2, whereas the Na-form adsorbs CO_2 strongly, even at low partial pressures (3.2

dx.doi.org/10.1021/ja3070864 | *J. Am. Chem. Soc.* 2012, 134, 17628−17642

mmol g^{-1} at 0.1 bar) (Figure 6) even though the window size in Na-Rho (neglecting cations) is smaller than that in Cs-Rho. Na-Rho adsorption and desorption isotherms show relatively little hysteresis at most of the pressures under these conditions of measurement, although more careful examination (see section 3.3.2) showed significant hysteresis at low pressures. Comparing these results, we conclude that at $P < 1$ bar the Cs^+ cations in D8R sites block the windows and also that diffusion of CO_2 into and through Na,Cs-Rho must occur largely through the 8MR windows occupied by Na^+ cations. The uptake on the Na-form is considerably higher than on the H-form at comparable pressures, as a result of the increased electrostatic interaction.

3.2.3. CO_2 Adsorption Related to Structure for NH_4-, Li-, and K-Rho. Additional univalent cation forms of zeolite Rho were prepared to determine the effects of different univalent cations on CO_2 adsorption on zeolite Rho. These were, in order of increasing cationic radius, Li^+, K^+, and NH_4^+. For Li-Rho, the low atomic number of lithium makes determination of the lithium site occupancies difficult, but significant scattering was measured at the S6R sites, corresponding to between 5 and 6 Li^+ cations. This is unlikely to be an accurate value due to the low electron density of Li^+ but a previous structural analysis by neutron diffraction of a dehydrated mixed Li,Na,Cs-aluminosilicate zeolite indicated that the S6R site is the preferred position for the small Li^+ cation.[15] It is therefore probable that most of the Li^+ cations required for charge balance are located in this site and not in the window sites. In K-Rho, by contrast, K^+ cations are found to occupy window sites of both S8R and D8R types so that there will be at least one and in some case two K^+ cations per window (which would in the latter case occupy two S8R sites 4.0 Å apart). Available structural data on ammonium forms of Rho by neutron and X-ray diffraction indicate that at high ammonium contents (12 per unit cell) the cations occupy S8R sites upon dehydration, whereas partially deammoniated samples with 6 NH_4^+ per unit cell the cations occupy D8R sites.[29,41] For the sample measured here it is likely that NH_4^+ cations occupy both D8R and S6R sites in a similar way to K^+ in K-Rho.

None of these forms of zeolite Rho adsorbed N_2 at 77 K. For K- and NH_4-Rho, as for its Na- and Cs-forms, the very low uptake of N_2 at 77 K is due to cations blocking window sites and not being mobile at the low temperature. For Li-Rho the window size is the more important parameter because Li^+ cations do not occupy window sites, but even at room temperature the narrowest O···O window opening is only 1.9 Å. In Li-Rho the strong distortion away from *Im-3m* results as the 6MRs distort to afford the small Li^+ cations better coordination in type III sites (rather than due to distortion of the 8MRs to give better coordination to cations in sites I and/or II as is the case for the other cation forms).

To investigate further the effect of Li^+ ions on adsorption onto Li-Rho, N_2 adsorption was measured on samples with different Li^+ contents (Supporting Information). Adsorption decreased steadily above 2 Li^+ per unit cell, from a maximum of 10.4 mmol g^{-1}, to negligible amounts at full exchange. As Li^+ cations are located mainly at the S6R sites the decrease in uptake is due to the decrease of the window size that results from the framework distortion. At room temperature, for example, the O···O distance (taking ionic radii into account) is already reduced to 2.24 Å by the presence of 5 Li^+ per unit cell.

Li-, K-, and NH_4-Rho, like Na-Rho, all adsorb CO_2 at 298 K, as shown in Figure 7. CO_2 adsorption onto Li-Rho gave very high uptakes, even at low partial pressures. Also, the adsorption was Type I in character. Most of the Li^+ cations are in the S6R sites, leaving the window sites empty. The CO_2 is small enough to pass through the open windows of the dehydrated Li-Rho structure, even though the crystallographic distance is apparently too small (1.9 Å), suggesting that the framework is flexible locally at 298 K.

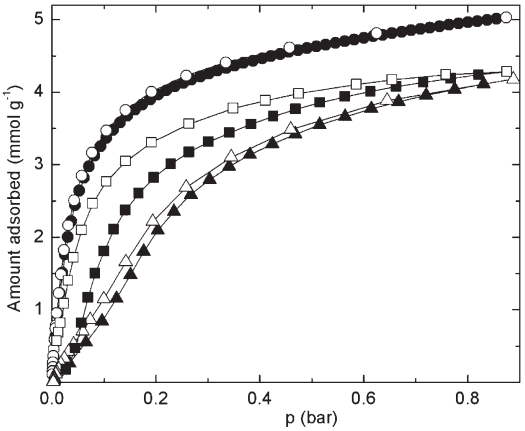

Figure 7. CO_2 isotherms at 298 K for Li-Rho (circles), K-Rho (squares), and NH_4-Rho (triangles). Adsorption, closed symbols; desorption, open symbols.

The adsorption and desorption branches of NH_4-Rho show relatively little hysteresis, but the uptake at 0.1 bar is not as high as that observed for the Na^+ form. This indicates that the ammonium ions must be able to move from their position within the D8R windows to allow diffusion through the windows. The lower uptake may partly be because the sample was not heated above 493 K under vacuum, to avoid deammoniation, and so might have some residual physically adsorbed water, but it is likely that the electrostatic interaction between the CO_2 and the NH_4^+ cations is weaker than that with the smaller Na^+ cations.

By comparison with Na-Rho and NH_4-Rho, adsorption and desorption isotherms on the K-form of zeolite Rho show much more marked non-type I behavior and hysteresis, even with equilibration times of 2 h. Nevertheless, high uptakes at partial pressures approaching 1 bar are achieved. Since all K^+ cations in K-Rho occupy sites either in the D8R position or in S8R sites on either face of the window, the K^+ cations must move to allow CO_2 uptake. The observed hysteresis results from the need for the movement of K^+ cations to allow passage of the CO_2 molecules: this must be energetically more difficult than movement of the Na^+ cations, possibly because it must move from D8R sites rather than S8R sites, and the former have coordination from more O atoms.

To further confirm that it is the displacement of the K^+ cation that inhibits the CO_2 adsorption, rather than a molecular sieving effect due to distortion of the 8MR away from circular, comparison of the minimum ring distance (Table 2) in the Na- and K-Rho indicates that this is smaller for the Na-Rho than for the K-Rho, but hysteresis is greater for the K-Rho. As previously discussed, for the Li-Rho the distance is smaller still, but no hysteresis is observed because Li^+ cations are not present in the window sites.

3.2.4. CO_2 Adsorption Related to Structure for Li- and Na-ZK-5. To examine the role of structure type on adsorption, CO_2 isotherms were also collected at 298 K on the Li- and Na-forms

dx.doi.org/10.1021/ja3070864 | J. Am. Chem. Soc. 2012, 134, 17628−17642

of ZK-5 of similar framework composition to the Rho material (Supporting Information). The ZK-5 materials have permanent porosity for N_2 (Table 1), and for CO_2 adsorption no hysteresis was observed and high uptakes were achieved at 0.1 bar (Li-ZK-5, 4.67 mmol g^{-1}; Na-ZK-5, 4.05 mmol g^{-1}), comparable to values reported for its polytype chabazite.[4,5] The framework structure of ZK-5 contains α-cages (as found in zeolite Rho) but linked via larger paulingite *pau* cages (Figure 4). In Na-ZK-5 the Na^+ cations occupy sites either within strongly nonplanar 8MR sites in these *pau* cages, which do not block access between α-cages, or in 6MR sites within the α-cages themselves, whereas in Li-ZK-5 most of the Li cations occupy 6MR sites. Direct comparison of the adsorption behavior of Na-ZK-5 with that of Na-Rho confirms that the hysteresis observed over Na-Rho is not due to the interaction of CO_2 with the cations, but rather due to their effect when occupying sites in the distorted 8MR windows connecting the α-cages. More detailed adsorption data on different cationic forms of ZK-5 (Si/Al = 4.7) published very recently confirm the levels of CO_2 uptake described here.[42]

3.3. Detailed Examination of CO_2 Adsorption on Sodium Rho. Of the different cation forms of Rho examined, the Na-form was chosen for more detailed investigation. Although the Li-form has higher CO_2 uptakes, the lower cost and lower affinity for water of the Na-form would be practical advantages. Furthermore, Na-Rho shows appreciable uptake at 0.1 bar, 298 K (at 3.2 mmol g^{-1} this is the same as that observed for Na-13X under the same conditions, Supporting Information) and the presence of Na^+ cations in window sites leads to hysteresis, which is unusual for zeolites. The related Na,Cs-Rho shows high selectivity for CO_2 compared to other larger, nonpolar molecules (CH_4), as illustrated by Palomino et al.,[9] so it was also of interest to investigate the uptake of Na-Rho for small hydrocarbons. Finally, adsorption of CO_2 was faster and uptake higher on Na-Rho than on K-Rho, and so more likely to be useful in processes requiring successive adsorption and desorption cycles. For these reasons, the mechanism of CO_2 adsorption on Na-Rho was studied in more detail. The additional studies included (i) examination of the adsorption properties of a series of Na,H-Rho samples with varying Na^+ content; (ii) measurement of high resolution, low P_{CO_2} adsorption/desorption isotherms on Na-Rho at different temperatures; (iii) *in situ* synchrotron X-ray diffraction during CO_2 adsorption and desorption on Na-Rho; (iv) *in situ* IR spectroscopy of CO_2 adsorption on Na-Rho and other cationic forms; (v) adsorption of ethane; and (vi) ZLC analysis to give details on the kinetics of CO_2 desorption on Na-Rho. Together, these experiments give an atomistic and quantitative description of the mechanism by which CO_2 is adsorbed and desorbed from zeolite Na-Rho.

3.3.1. N_2 and CO_2 Adsorption on Partially Exchanged Na,H-Rho. Examination of the N_2 capacity at 77 K and reversible CO_2 uptake at 300 K and 0.1 bar, measured by ZLC, of a series of Na,H-Rho materials of different cation contents (Figure 8) shows that by the inclusion of 4 Na^+ cations per unit cell the permanent porosity to N_2 at 77 K is reduced to zero. Furthermore, when reversible CO_2 adsorption measurements are made on Na,H-Rho with variable Na^+ content, there is only a small increase in the amount of reversibly bound CO_2 measured at 0.1 bar by ZLC as the number of Na^+ cations is increased up to 4, but at 6 cations per unit cell and above the uptake increases as the sodium content increases.

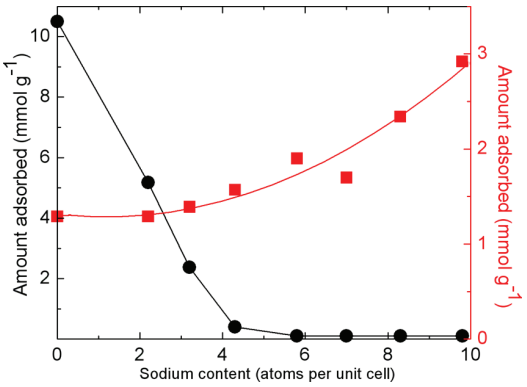

Figure 8. Uptake of N_2 at pore filling at 77 K (left) and reversible CO_2 adsorption measured by ZLC at 308 K (right) as a function of Na content in Na,H-Rho.

These observations are partially explained by reference to the structural analyses of a Na,H-Rho containing 4.9 Na^+ cations per unit cell and of fully exchanged Na-Rho (Table 2). At this level of Na^+ cations per unit cell, the sodium cations occupy almost all of the windows, distributed over sites I and II. It is likely that they are not mobile at 77 K so that there are no easy routes for N_2 through the pore space. They are mobile at 298 K in the presence of CO_2, permitting uptake, but there are few strong adsorption sites at this Na^+ level. At higher Na^+ contents the S6R sites become occupied, and the presence of additional cations in these S6R sites results in the creation of more energetic sites for CO_2 adsorption.

3.3.2. Variable Temperature CO_2 Adsorption/Desorption Isotherms. The Na-Rho CO_2 adsorption/desorption isotherms at 273, 298, and 308 K (measured up to 140 mbar) show strong deviation from Type I behavior at low pressure, and strong hysteresis in the desorption branch (Figure 9). The CO_2

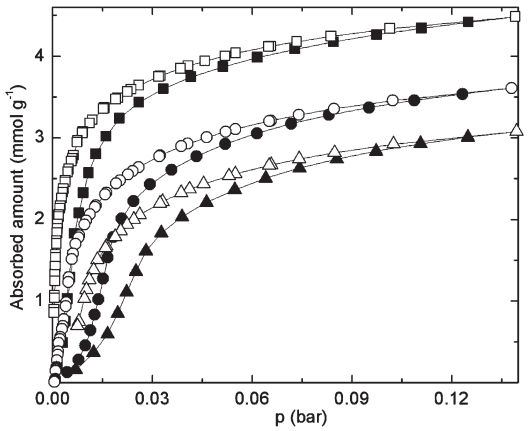

Figure 9. CO_2 isotherms up to 140 mbar for Na-Rho at 273 K (squares), 298 K (circles), and 308 K (triangles). Adsorption, closed symbols; desorption, open symbols.

adsorption behavior of Na-Rho lies intermediate between that of Li-Rho, which shows a type I isotherm with very little hysteresis (Figure 7), and that of K-Rho, which shows more strongly pronounced deviation (Figure 7). Hysteresis and non-type I isotherms suggest that there is a structural change and/or dynamic effects during the adsorption, as frequently observed during adsorption on flexible metal organic frameworks,

dx.doi.org/10.1021/ja3070864 | J. Am. Chem. Soc. 2012, 134, 17628–17642

including during CO_2 adsorption.[43] To investigate possible structural changes upon CO_2 adsorption onto Na-Rho, structural studies during the adsorption and desorption process were performed *in situ* by synchrotron PXRD.

3.3.3. In Situ XRD Studies of CO_2 Adsorption. X-ray diffraction patterns were collected on a sample of dehydrated Na-Rho before and after admitting CO_2 to the gas cell at equilibrium P_{CO_2} values of 0.1 and 0.2 bar. Subsequently, the pressure was reduced to 0.045 bar and a diffraction pattern taken at equilibrium, before the gas cell was evacuated and the diffraction pattern measured every 2 min (Supporting Information). Rietveld refinement gives the structures (Figure 10, Table 4, Supporting Information). Hydrated Na-Rho solid

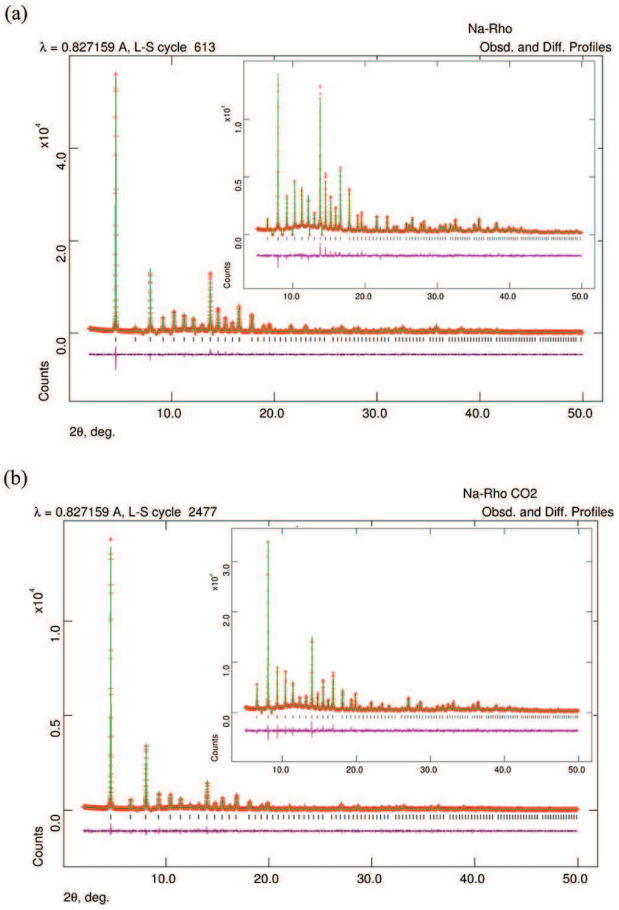

Figure 10. Rietveld plots of synchrotron PXRD profiles (λ = 0.827159 Å, T = 298 K) of (a) Na-Rho (dehydrated) and (b) Na-Rho with CO_2 adsorbed at an equilibrium pressure of 0.1 bar.

has *Im*-3*m* symmetry, a = 14.9573(1) Å, and in the dehydrated state has *I*-43*m* symmetry, with a = 14.4136(3) Å. As observed for the laboratory data, sodium cations occupy S8R sites (*ca.* one cation per window between cages) with *ca.* 2 Na^+ cations in S6R sites in each α-cage (around 1 per two sites). Upon adsorption of CO_2 at 0.1 bar, the unit cell increased to a = 14.6281(7) Å, but the symmetry remained *I*-43*m*. The expected uptake at 0.1 bar on the adsorption branch of the isotherm is 3.1 mmol g^{-1}, corresponding to 9.8 molecules of CO_2 per unit cell. Difference Fourier analysis together with constrained refinement locates two sites for CO_2 molecules in the Na-Rho structure at this point on the isotherm, total occupancy 10.1 molecules per unit cell, one of which resides partly in the D8R and the other fully in the α-cage. Careful examination of the refined positions of the CO_2 molecules, together with those of the Na^+ cations (all at partial occupancy) suggest a likely configuration for CO_2 at the two sites (Figure 11). In the first location (A) the CO_2 molecule adopts end-on coordination with one Na^+ cation in the S8R, with a Na^+—O distance of 2.88(2) Å, through the D8R cage windows to project into the α-cage, where its other O atom is 4 Å from Na^+ cations of type III. Possible disordered canting of the OCO molecules toward the type III cations, which would be difficult to confirm, could reduce that distance. The Na^+ cations in the D8R adjust their position as this adsorption occurs (see Supporting Information) so the crystallographic Na^+—Na^+ distance, at 1.73(1) Å, precludes occupancies above 50% and so supports a model where there is one Na^+ cation per D8R window. In the second location (B) the CO_2 molecule adopts end-on coordination with one α-cage Na^+ cation, with a Na— O distance of 2.58(1) Å, with the second O atom at its closest 4.5 Å from a second *a*-cage Na^+ cation. Adjacent OCO molecules could align as shown in Figure 11. Two possible arrangements of Na^+ cations and CO_2 molecules in Na-Rho at 298 K in contact with 0.1 bar CO_2 are shown in Figure 12, taking into account possible arrangements of Na^+ cations and CO_2 molecules derived from the refinements. At 0.2 bar CO_2 there is a slight expansion in the unit cell (to 14.6348 Å) as additional CO_2 molecules are adsorbed (total refined content 10.8 per unit cell).

Simulation of adsorption of CO_2 in zeolite Na-A at levels up to 3 molecules per α-cage suggests all CO_2 molecules interact with two (or three) Na^+ cations, and the CO_2 molecules interact most strongly with cations in 6MR and 8MR sites in this solid.[23] The structure reported here, together with the nonlinear increase in strongly bound CO_2 with increasing Na^+ content, suggests 2-cation—CO_2 interactions might also be important in zeolite Rho.

Upon reducing the equilibrium pressure to 0.045 bar, there is a small reduction in the unit cell parameter (to 14.6219 Å) and the refined site occupancies remain similar (the total refined CO_2 occupancy per unit cell drops to 9.8 molecules). This is expected from the shallow desorption branch observed in the low pressure isotherms shown in Figure 9. It is only when the sample is opened to vacuum that the unit cell begins to contract sharply, as the steep part of the desorption branch is descended (Supporting Information). Refinement indicates that already after a few minutes of evacuation the amount of ordered CO_2 in the pores has decreased, but the occupancy of the two sites has not decreased evenly. The CO_2 molecules in site B are held more weakly than those in site A, so that whereas the number in site A drops by 27% (from 6 to 4.4 molecules), that in site B drops by 58% (from 3.8 to 1.6). At any time there is a single phase present, so that changes in the framework must propagate rapidly throughout the crystallites. Only after prolonged evacuation does the unit cell parameter approach that of the empty structure, as a result of slow desorption.

3.3.4. In Situ IR Spectroscopy of CO_2 Adsorption. The *in situ* IR spectroscopy of CO_2 adsorbed on zeolite Na-Rho can be interpreted in the light of the adsorption isotherms and the structural information and also compared with the results on Li-Rho, Na,Cs-, and K-Rho. The infrared spectrum of CO_2 adsorbed on Na-Rho at low coverages showed a single strong band at 2358 cm^{-1} due to the ν_3 asymmetric stretching vibration of adsorbed CO_2. (Figure 13a). This is shifted to

dx.doi.org/10.1021/ja3070864 | J. Am. Chem. Soc. 2012, 134, 17628–17642

Table 4. Atomic Coordinates, Site Multiplicities, Occupancies, and Displacement Parameters for Na-Rho at 298 K, (i) Dehydrated, *I*-43*m*, a = 14.4134(1) Å and (ii) in Equilibrium with 0.1 bar CO_2 during Adsorption, *I*-43*m*, a = 14.62823(6) Å, Determined by Rietveld Analysis of Synchrotron PXRD

atom	x	y	z	multiplicity	frac occup	U_{iso}/Å^2
			(i) Na-Rho (Dehydrated)			
Si1	0.27429(15)	0.12260(18)	0.42518(17)	48	0.8	0.0132(5)
Al1	0.27429(15)	0.12260(18)	0.42518(17)	48	0.2	0.0132(5)
O1	0.0388(3)	0.2113(2)	0.3868(3)	48	1	0.0045(8)
O2	0.2194(3)	0.2194(3)	0.4039(5)	24	1	0.0045(8)
O3	0.1170(3)	0.1170(3)	0.6275(4)	24	1	0.0045(8)
Na(II)	0.3869(9)	0	0	12	0.5	0.0490(5)
Na(III)	0.3103(8)	0.3103(8)	0.3103(8)	8	0.389(8)	0.0490(5)
			(ii) Na-Rho (0.1 bar CO_2)			
Si1	0.26879(10)	0.11856(12)	0.41920(11)	48	0.8	0.0064(2)
Al1	0.26806(10)	0.11889(12)	0.41992(11)	48	0.2	0.0064(2)
O1	0.0302(2)	0.20921(18)	0.38306(24)	48	1	0.0085(5)
O2	0.2092(2)	0.2092(2)	0.3916(3)	24	1	0.0085(5)
O3	0.1276(2)	0.1276(2)	0.6274(3)	24	1	0.0085(5)
NaIII	0.3084(6)	0.3084(6)	0.3084(6)	8	0.4	0.053(3)
NaII	0.4408(5)	0	0	12	0.5	0.053(3)
OC1	0.3828(7)	0	0	12	0.5	0.053(3)
OC2	0.2306(7)	0	0	12	0.5	0.053(3)
CO1	0.3074(7)	0	0	12	0.5	0.053(3)
OC3	0.3683(7)	0.4863(15)	0.3683(7)	24	0.171(1)	0.053(3)
CO2	0.3489(7)	0.5597(15)	0.3711(18)	48	0.0855(5)	0.053(3)
OC4	0.3206(7)	0.6306(15)	0.3849(18)	48	0.0855(5)	0.053(3)

higher frequency relative to the gas phase molecule (2349 cm^{-1}). A similar shift has been reported for CO_2 adsorbed in Na-ZSM5 and attributed to interaction of CO_2 with the Na^+ cations.[44] A much smaller shift (to 2351 cm^{-1}) is reported for CO_2 adsorbed in NaY,[45] presumably reflecting a weaker interaction.

Direct evidence for a CO_2–Na^+ interaction comes from observation of the ν_1 symmetric stretching vibration of adsorbed CO_2 in Na-Rho as a weak band at 1378 cm^{-1} (Figure 13b). This vibration is infrared forbidden for the gas phase molecule (at 1388 cm^{-1}) but becomes weakly allowed when the symmetry is lowered due to interaction with zeolite cations. Garrone et al.[44] report this frequency to be 1382 cm^{-1} for CO_2 adsorbed in Na-ZSM-5.

As the CO_2 coverage is increased in Na-Rho, the ν_3 band broadens and becomes too intense to monitor. Several weak bands then become evident on either side of this feature, at 2293, 2405, 2450, and 2503 cm^{-1}. The 2293 cm^{-1} band is due to the ν_3 mode of 1% abundant $^{13}CO_2$ (2284.5 cm^{-1} in gas phase CO_2). The higher frequency bands have been discussed at length by Garrone et al.[44] and attributed by them to combinations of the ν_3 mode with low frequency lattice modes of the zeolite framework. Support for these assignments came from computational results and direct observation of far-infrared bands corresponding to the lattice modes. For CO_2 in Na-Rho, the lattice modes corresponding to the three combination bands observed must have frequencies of 47, 92, and 145 cm^{-1} respectively. These values are different from those reported by Garrone et al. for CO_2 adsorbed in Na-ZSM-5 (two combination bands observed corresponding to lattice mode frequencies of 45 cm^{-1} and 60 cm^{-1}). As discussed by them, however, the low frequency lattice modes vary with the zeolite framework structure and do not depend on the particular cation with which the CO_2 is interacting. The coupling of the ν_3 mode of adsorbed CO_2 with zeolite lattice modes was inferred by Garrone et al. to mean that the primary interaction between oxygen atoms of the adsorbed CO_2 and zeolite cations is accompanied by a secondary interaction between the carbon atoms and adjacent oxide ions of the zeolite lattice.

As the CO_2 coverage is increased in Na-Rho, an additional band appears on the ν_1 region at 1416 cm^{-1}. In light of the structural evidence for two different CO_2 adsorption sites in Na-Rho (see above), we assign this second band to the ν_1 mode of a second form of adsorbed CO_2, occupying sites at higher coverage. As the extinction coefficient for this mode of adsorbed CO_2 will depend strongly on the local symmetry at the adsorption site, it is not possible to quantify from the infrared data the relative amounts of the two species. The occurrence of two different ν_1 frequencies for CO_2 in Na-Rho might be expected to result in different ν_3 frequencies as well, but the intensity and breadth of the ν_3 band at higher coverages prevents confirmation of this.

In the case of Na,Cs-Rho, only the 1378 cm^{-1} band was observed, increasing in intensity with increasing surface coverage (Supporting Information, S12). The infrared measurements thus indicate a single adsorption site for CO_2 in Na,Cs-Rho. The ν_3 region of the spectrum of CO_2 adsorbed in NaCs-Rho is indistinguishable from that in Na-Rho at lower coverages, but any differences would only be evident at higher coverages where bands in this region cannot be resolved. For K-Rho also, a single band was observed in the ν_1 region (Supporting Information, S12), although this band only became evident at pressures higher than those seen with Na-Rho. In the ν_3 region a band at 2351 cm^{-1} was seen for CO_2 in K-Rho at low pressures, although this band was much weaker than those for Na-Rho, NaCs-Rho and Li-Rho at the same pressures. At higher pressures, CO_2 in K-Rho showed higher frequency shoulders and a lower frequency $^{13}CO_2$ component similar to those seen with the other zeolites.

dx.doi.org/10.1021/ja3070864 | J. Am. Chem. Soc. 2012, 134, 17628–17642

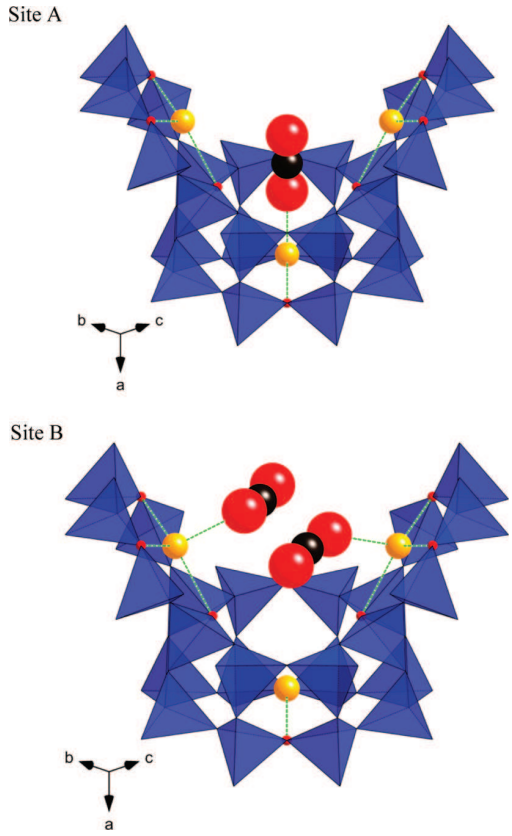

Figure 11. Adsorption sites for CO_2 in Na-Rho, as determined by Rietveld refinement of the synchrotron X-ray diffraction data at 298 K, with an equilibrium pressure of 0.1 bar. In adsorption site A the O═C═O molecules adopt end-on coordination with Na^+ cations (orange spheres) in the S8R site, whereas in site B they directly coordinate a S6R Na^+ cation.

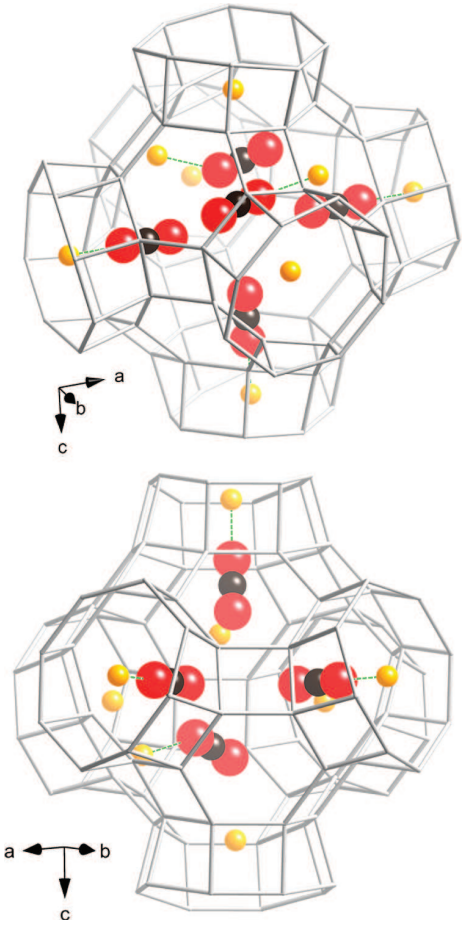

Figure 12. Two possible arrangements of Na^+ cations and CO_2 molecules within an α-cage of Na-Rho that is in equilibrium with 0.1 bar of CO_2 at 298 K. These are based on the refined structure and a consideration of possible arrangements of cations and CO_2 molecules, given the observed statistical occupancies.

In the case of Li-Rho, the ν_1 region shows two distinct bands at all CO_2 coverages (1374 and 1382 cm^{-1}, Supporting Information, S12). Although this might be taken as evidence for the existence of two different CO_2 adsorption sites, an additional band was also seen to appear in parallel at 1635 cm^{-1}, which was not seen with any of the other zeolites. Many authors report bands in this region due to adsorbed carbonate or bicarbonate when CO_2 is adsorbed in alkali metal zeolites, particularly in the presence of adsorbed water. For example, bands at 1670 and 1335 cm^{-1} observed when CO_2 is adsorbed in zeolite KX have been assigned to a bidentate carbonate species[46] (while Galhotra et al.[45] attribute bands at 1640, 1461, and 1381 cm^{-1} to carbonate and bicarbonate species in nanosized NaY zeolites). They further suggest that the presence of adsorbed water enhances the formation of bicarbonate species in BaY. We suggest from these comparisons that small amounts of carbonate and/or bicarbonate species are formed when CO_2 is adsorbed in Li-Rho. In the ν_3 region, CO_2 adsorption in Li-Rho gave initially a band at 2355 cm^{-1}, shifted from the frequency obtained with Na-Rho and Na,Cs-Rho. The higher frequency bands assigned to combination modes are present at approximately the same frequencies as in Na-Rho, Na,Cs-Rho, and K-Rho. Notably, however, the bands due to adsorbed CO_2 in Li-Rho are already well developed at a pressure of 0.25 mbar, more so than with the other zeolites,

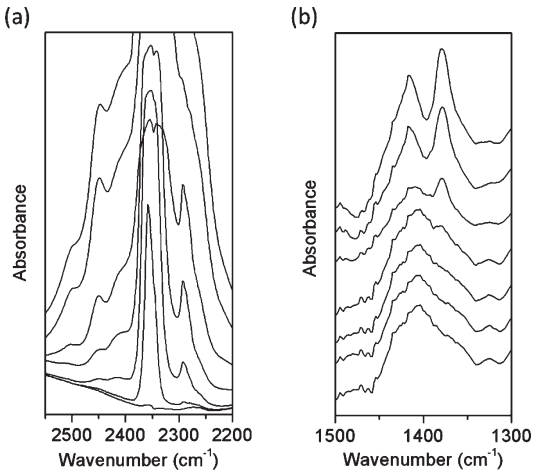

Figure 13. Infrared spectra of CO_2 adsorbed on dehydrated Na-Rho at different equilibrium pressures at room temperature. The increasing signals correspond to CO_2 pressures of 0, 0.25, 5, 10, 25, 50, and 150 mbar.

dx.doi.org/10.1021/ja3070864 | J. Am. Chem. Soc. 2012, 134, 17628–17642

consistent with the different shapes of the adsorption isotherms.

3.3.5. Comparison of Ethane Uptake on Na-Rho with That on Na-ZK-5. The adsorption behavior of ethane on Na-Rho at 298 K was compared with that over H-Rho and Na-ZK-5. Whereas ethane is readily taken up by Na-ZK-5 and H-Rho (at 0.7 bar, the uptakes are 1.8 and 1.65 mmol g^{-1}, respectively), it is effectively blocked from adsorption into Na-Rho (Supporting Information). Ethane is a larger molecule than CO_2 (3.90 Å), so this may be due to the restricted size of the 8MR opening in the presence of cations in the windows or due to the physical presence of the cations; in fact, the two are related. The resultant effect is likely to be high selectivity for Na-Rho for CO_2 over ethane in mixtures, similar to that observed previously for Na,Cs-Rho for CO_2/CH_4 mixtures.[9]

3.3.6. Zero Length Column Analysis of CO_2 Desorption from Na,Cs-Rho and Na-Rho. Dehydrated Na,Cs- and Na-Rho can adsorb CO_2 only if the Na^+ cations move, so that analysis of the desorption data measured by ZLC gives a measure of the rate of the diffusion that relies on this process (See Supporting Information for theoretical details). Figure 14a shows the desorption curves at 308 K for the fully and partially saturated ZLC experiment on the Na,Cs-Rho sample, fitted well by curves assuming a single value for the diffusivity of 0.875×10^{-19} m^2 s^{-1} (calculated using a value of the crystal radius of 50 nm, as measured from the SEM). This diffusivity is calculated from the long-time desorption data, which corresponds to desorption under the Henry's law regime.[47,48]

It was not possible to fit the desorption data for the Na-Rho fully saturated at 10% CO_2 in a similar way (see Supporting Information), but it was possible to fit the desorption curve from a sample of Na-Rho saturated with 1% CO_2 with a single diffusivity, calculated from the long-time desorption data as 1.0×10^{-19} m^2 s^{-1} (Figure 14b), and the same diffusivity value enabled the desorption from the partial saturation experiment to be fitted (Supporting Information). The discrepancy of modeled and observed desorption curve for the fully saturated 10% CO_2 experiment cannot be due mainly to isotherm nonlinearity of the isotherm, since the shape of the desorption isotherm does not differ strongly from that of Cs,Na-Rho. It could be associated with concentration dependence of the diffusivity resulting from the structural changes that occur in Na-Rho with variable CO_2 loading. The conditions for desorption at low coverage will approach those for desorption via diffusion through the empty Na-Rho (I-43m, α = 14.4137(1) Å, O−O distance = 2.26 Å). As CO_2 is adsorbed into the structure, the distortion of the 8MRs decreases, and it becomes easier for the CO_2 to diffuse at higher coverages.

3.3.7. Summary of the CO_2 Adsorption Mechanism for Na-Rho. For diffusion of CO_2 through the dehydrated Na-form of zeolite Rho, the cations must move away from the sites that they occupy in the windows. The mobility of Na^+ cations via a hopping motion in the presence of CO_2 has previously been predicted for faujasitic Na-X and Na-Y zeolites by molecular dynamics simulations.[49] That the site occupancies in Na-Rho measured by diffraction change little during adsorption and desorption indicates that the cations can rapidly move back to their original site once the CO_2 molecule has passed through the window.

At very low surface coverages on Na-Rho, the diffusivity is estimated from ZLC studies to be 1.0×10^{-19} m^2 s^{-1}. This is significantly lower than the micropore diffusivities for CO_2 on Ca-A (4A) and Ca-X determined by Ahn et al.[50] over the range

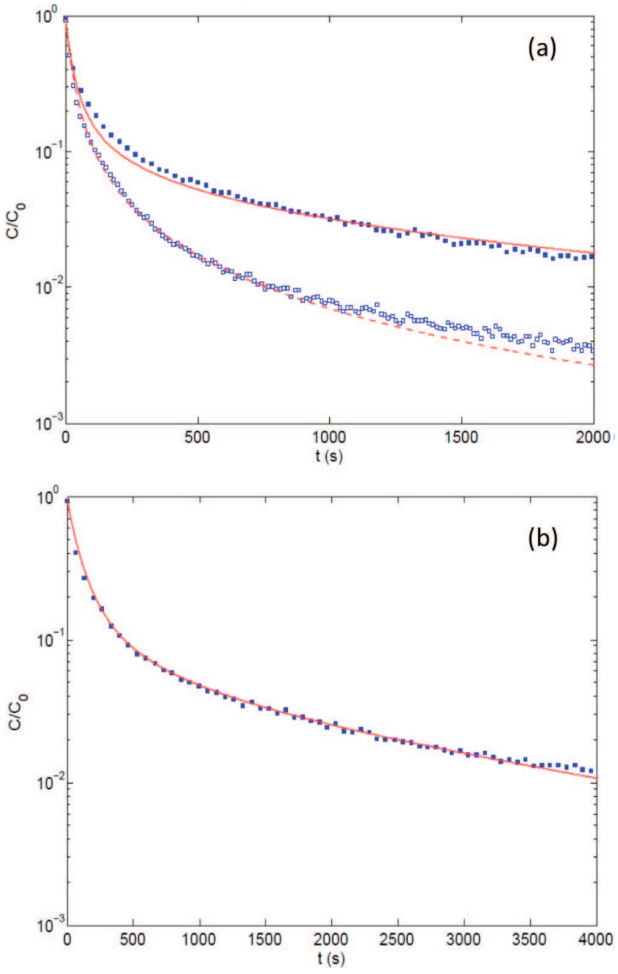

Figure 14. Experimental ZLC desorption curves at 308 K for (a) the fully and partially (5.6 min) saturated Na,Cs-Rho sample using 2 mL/min 10% CO_2 and (b) Na-Rho saturated using 1 mL/min 1% CO_2 and desorbing in a 1 mL/min flow of He. The data are given in blue as individual points (solid for fully saturated, open for partially saturated). The fitted curves (red) are calculated using a single value for the diffusivity as described in eqs 2 and 5 in the Supporting Information.

273−313 K by analysis of gravimetric data to be 10^{-16} and 10^{-14} m^2 s^{-1}, respectively. The diffusivity is increased at higher coverages by the influence of other adsorbed CO_2 molecules and by the increase in 8MR window size (2.75 Å by 0.1 bar, cf. 2.26 Å in the dehydrated form). A suggested mechanism for "trapdoor" CO_2 migration at low coverages is depicted schematically in Figure 15. The presence of additional CO_2 molecules will result in additional coordination of Site II Na^+ cations, reducing the energy for cation displacement, in a similar way to that proposed for the water-mediated migration of Cd^{2+} ions from window sites to S6R sites upon dehydration of Cd-Rho.[51]

4. CONCLUSIONS

Univalent cationic forms of zeolite Rho show remarkable CO_2 adsorption behavior that results from a combination of its flexible framework structure, the distribution of extra-framework cations over different sites, and the mobility of those cations that occupy window sites between α-cages.

dx.doi.org/10.1021/ja3070864 | J. Am. Chem. Soc. 2012, 134, 17628−17642

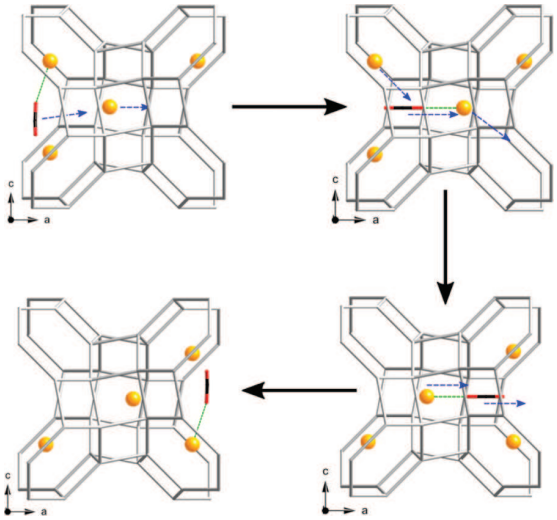

Figure 15. Postulated cooperative mechanism by which CO_2 molecules (represented by red and black sticks) could pass through a window site between α-cages in zeolite Na-Rho, where a Na^+ cation (yellow sphere) occupies one of the S8R sites in the window.

H-Rho has the highest pore volume of all Rho samples examined but does not show strong adsorption of CO_2 at conditions relevant to carbon capture from flue gases. Adsorption is of type I and shows no hysteresis. H-SAPO(RHO) CO_2 interacts more weakly still than the aluminosilicate, due to its lower framework charge. US-Rho, in which there are extra-framework Al species, also takes up less CO_2 at 0.1 bar and 298 K than H-Rho.

The highest values of CO_2 adsorption for zeolite Rho are observed on the lithium form. Li^+ cations are expected to occupy S6R sites in the α-cage and so leave window sites free of cations. As a result the CO_2 adsorption isotherms at 298 K do not show hysteresis. The strong interaction with Li-Rho is expected on electrostatic grounds and also because all the Li^+ cations in the S6R sites are accessible. The ability of Li-Rho to admit CO_2, even though the opening of the windows is only 1.90 Å, indicates that there is sufficient framework flexibility and interaction at 298 K to permit CO_2 diffusion.

In contrast to the Li-Rho behavior, the Na-, K-, NH_4-, and Cs-forms of Rho show hysteresis in their CO_2 adsorption isotherms ($Na,NH_4 < K < Cs$), with the adsorption at 298 K and 0−1 bar decreasing in the order Na > K, NH_4 > Cs. This effect is much more marked than that expected on the basis of increased cation volume occupying pore space, since Cs-Rho shows very little uptake. In all these cases cations occupy window sites in the dehydrated form, as "sentinels", either in D8R or S8R sites, so there must be cation displacement to allow CO_2 uptake to occur. In Na-Rho the cations occupy S8R sites in the windows, in K- and NH_4-Rho both D8R and S8R sites are occupied, and in Cs-Rho all the D8R sites are occupied. The movement of larger cations to S8R sites (as previously observed to occur for Cs^+ cations at pressures greater than 1 bar in Na,Cs-Rho) results in a decrease in the coordination of the cation by framework oxygen atoms and a distortion away from *I*-43*m* to *Im*-3*m* which involves an energetic cost.

No such hysteresis in CO_2 adsorption isotherms is observed for the Na-form of ZK-5, which does not have cations in positions that block windows between the α-cages. The uptakes on the Na- (and also the Li-) forms of ZK-5 are high at low CO_2 pressures, but the selectivity to CO_2 over other gases (e.g., light hydrocarbons) is much lower because there is no barrier to their adsorption. The unprecedented selectivity of Na,Cs-Rho to CO_2 over CH_4 reported by Palomino et al.[9] and the high ratio of single component adsorption uptakes of CO_2 to ethane over Na-Rho reported here results from the ability of sodium cations to move to allow the passage of CO_2 molecules into Rho while the larger size (4 Å) and lower interaction of hydrocarbons results in their exclusion.

The Na^+ cations in fully exchanged Na-Rho remain in S8R and S6R positions during adsorption and CO_2 molecules occupy two positions, in each of which the O═C═O molecule adopts end-on coordination with one Na^+ cation and may interact with another. The stronger of these adsorption sites involves one cation in a S8R site; the other involves interaction with a Na^+ cation in a S6R site. Upon desorption of CO_2 from Na-Rho at 298 K, there is a gradual decrease in the single unit cell *a* parameter within the *I*-43*m* space group, indicating a concerted structural change, and ZLC measurements of desorption indicate a "zero-coverage" diffusivity of 1.0×10^{-19} m^2 s^{-1} at 308 K. At these low loadings there is reduced window size, and fewer CO_2 molecules able to act to mediate the displacement of cations away from window sites where they block molecular transport. The transport is faster at higher loadings.

Fully exchanged Na-Rho is the most promising CO_2 adsorbent of those studied, when taking into account cost, uptake, selectivity, and kinetics. Adsorption occurs on S8R and S6R sites: that these two adsorption sites exist is a consequence of both framework and extra framework composition, so that manipulation of these can give rise to "adsorption site engineering". It should therefore be possible to modify chemical composition to optimize CO_2 uptake with this knowledge of the structural chemistry of Rho.

That Na-Rho (and the NH_4^+ and K^+ forms) demonstrate reversible uptake of CO_2 at all is due to the ability of the cations in window sites to undergo local displacement, leading to a proposed mechanism that involves a CO_2-mediated migration from a window site to a vacant α-cage site. The selectivity for CO_2 over small hydrocarbons observed over Na-Rho arises from the difficulty for small hydrocarbons (diameter 4 Å) to pass through windows that are both highly elliptical and also blocked with cations. Future studies will aim to deconvolute the roles of cation−adsorbate interactions and molecular sieving in determining this selectivity.

Na-Rho could be used as a selective CO_2 adsorbent in kinetic gas separation applications, either as a packed bed or in membrane form. The extended time to achieve full desorption of adsorbed CO_2 observed by measurement of adsorption isotherms and by ZLC suggest temperature swing adsorption may be more appropriate than pressure swing adsorption applications. Furthermore, it should be possible to optimize its uptake and diffusional properties by modification of framework and mixed cation composition. It is also likely that the trapdoor behavior and high selectivity of zeolite Rho will be observed in structurally related and similarly flexible zeolites, widening the types of observed adsorption behavior in zeolitic solids.

■ ASSOCIATED CONTENT

Ⓢ Supporting Information

Details of the syntheses, powder diffraction patterns, ion exchange conditions, TGA data, structural and refinement

dx.doi.org/10.1021/ja3070864 | *J. Am. Chem. Soc.* 2012, 134, 17628−17642

details as well as crystallographic information files, additional adsorption isotherm data, solid state NMR and full infrared spectra. This material is available free of charge via the Internet at http://pubs.acs.org.

AUTHOR INFORMATION

Corresponding Author

paw2@st-andrews.ac.uk

Notes

The authors declare no competing financial interest.

ACKNOWLEDGMENTS

We gratefully acknowledge the EPSRC (EP/G062129/1, Innovative Gas Separations for Carbon Capture: M.M.L., E.M., S.B., P.A.W.) for funding, Mrs. Sylvia Williamson for collection of the adsorption isotherms, Professor Chiu C. Tang for assistance at the I-11 beamline at the Diamond Light Source (DLS), and DLS for beamtime. Solid State NMR spectra were obtained at the EPSRC facility in Durham. Drs. Miguel Palomino and Susanna Valencia and Professors Fernando Rey and Avelino Corma are thanked for helpful discussions.

REFERENCES

(1) Barrer, R. M.; Gibbons, R. M *Trans. Faraday Soc.* **1965**, *61*, 948−961.

(2) Pirngruber, G. D.; Raybaud, P.; Belmabkhout, Y.; Cejka, J.; Zukal, A. *Phys. Chem. Chem. Phys.* **2010**, *12*, 13534−13546.

(3) Palomino, M.; Corma, A.; Rey, F.; Valencia, S. *Langmuir* **2010**, *26*, 1910−1917.

(4) Ridha, F. N.; Yang, Y. X.; Webley, P. A. *Microporous Mesoporous Mater.* **2009**, *117*, 497−507.

(5) Ridha, F. N.; Webley, P. A. *Sep. Purif. Technol.* **2009**, *67*, 336−343.

(6) Ridha, F. N.; Webley, P. A. *Microporous Mesoporous Mater.* **2010**, *132*, 22−30.

(7) Hudson, M. R.; Queen, W. L.; Mason, J. A.; Fickel, D. W.; Lobo, R. F.; Brown, C. M. *J. Am. Chem. Soc.* **2012**, *134*, 1970−1973.

(8) Robson, H. E.; Shoemaker, D. P.; Ogilvie, R. A.; Manor, P. C. In *Molecular Sieves*; Meier, W. M., Uytterhoeven, J. B., Eds.; American Chemical Society: Washington, DC, 1973; *Adv. Chem. Ser. No.* 121, p 106.

(9) Palomino, M.; Corma, A.; Jorda, J. L.; Rey, F.; Valencia, S. *Chem. Commun.* **2012**, *48*, 215−217.

(10) Parise, J. B.; Abrams, L.; Gier, T. E.; Corbin, D. R.; Jorgensen, J. D.; Prince, E. *J. Phys. Chem.* **1984**, *88*, 2303−2307.

(11) Araki, S.; Kiyohara, Y.; Tanaka, S.; Miyake, Y. *Chem. Lett.* **2012**, *41*, 125−126.

(12) Parise, J. B.; Abrams, L.; Gier, T. E.; Corbin, D. R.; Jorgensen, J. D.; Prince, E. *J. Phys. Chem.* **1984**, *88*, 203.

(13) Corbin, D. R.; Abrams, L.; Jones, G. A.; Eddy, M. M.; Harrison, W. T. A.; Stucky, G. D.; Cox, D. E. *J. Am. Chem. Soc.* **1990**, *112*, 4821−4830.

(14) Fischer, R. X.; Baur, W. H.; Shannon, R. D.; Staley, R. H.; Vega, A. J.; Abrams, L.; Prince, E. *J. Phys. Chem.* **1986**, *90*, 4414−4423.

(15) (a) Johnson, G. M.; Reisner, B. A.; Tripathi, A.; Corbin, D. R.; Toby, B. H.; Parise, J. B. *Chem. Mater.* **1999**, *11*, 2780−2787. (b) Corbin, D. R. U.S. Patent 7,169,212, 2007

(16) Eic, M.; Ruthven, D. M. *Zeolites* **1988**, *8*, 472−479.

(17) Ruthven, D. M.; Brandani, S.; Eic, M. *Mol. Sieves* **2008**, *7*, 45−84.

(18) Brandani, S.; Hufton, J.; Ruthven, D. M. *Zeolites* **1995**, *15*, 624−631.

(19) Brandani, S.; Ruthven, D. M. *Adsorption* **1996**, *2*, 133−143.

(20) Lievens, J. L.; Verduijn, J. P.; Mortier, W. J. *Zeolites* **1992**, *12*, 690−697.

(21) Verduijn, J. P. U.S. Patent 5,944,249, 1991.

(22) Pulido, A.; Nachtigall, P.; Zukal, A.; Dominguez, I.; Cejka, J. *J. Phys. Chem. C* **2009**, *113*, 2928−2935.

(23) Zukal, A.; Arean, C. O.; Delgado, M. R.; Nachtigall, P.; Pulido, A.; Mayerova, J.; Cejka, J. *Microporous Mesoporous Mater.* **2011**, *146*, 97−105.

(24) Chatelain, T.; Patarin, J.; Fousson, E.; Soulard, M.; Guth, J. L.; Schulz, P. *Microporous Mater.* **1995**, *4*, 231−238.

(25) Araki, S.; Kiyohara, Y.; Tanaka, S.; Miyake, Y. *J. Colloid Interface Sci.* **2012**, *376*, 28−33.

(26) Su, X.; Tian, P.; Li, J.; Zhang, Y.; Meng, S.; He, Y.; Fan, D.; Liu, Z. *Microporous Mesoporous Mater.* **2011**, *144*, 113−119.

(27) Langmi, H. W.; Book, D.; Walton, A.; Johnson, S. R.; Al-Mamouri, M. M.; Speight, J. D.; Edwards, P. P.; Harris, I. R.; Anderson, P. A. *J. Alloys Compd.* **2005**, *404*, 637−642.

(28) Udovic, T. J.; Cavanagh, R. R.; Rush, J. J.; Wax, M. J.; Stucky, G. D.; Jones, G. A.; Corbin, D. R. *J. Phys. Chem.* **1987**, *91*, 5968−5973.

(29) Fischer, R. X.; Baur, W. H.; Shannon, R. D.; Staley, R. H. *J. Phys. Chem.* **1987**, *91*, 2227−2230.

(30) Fischer, R. X.; Baur, W. H.; Shannon, R. D.; Staley, R. H.; Abrams, L.; Vega, A. J.; Jorgensen, J. D. *Acta Crystallogr.* **1988**, *B44*, 321−334.

(31) Larson, A. C.; Von Dreele, R. B. *General Structure Analysis System (GSAS)*; Los Alamos National Laboratory: Los Alamos, 1994.

(32) Cartlidge, S.; Meier, W. M. *Zeolites* **1984**, *4*, 218−225.

(33) Thompson, S. P.; Parker, J. E.; Potter, J.; Hill, T. P.; Birt, A.; Cobb, T. M.; Yuan, F.; Tang, C. C. *Rev. Sci. Instrum.* **2009**, *80*, 075107−9.

(34) Parker, J. E.; Potter, J.; Thompson, S. P.; Lennie, A. R.; Tang, C. C. *Mater. Sci. Forum* **2012**, *706*−*709*, 1707−1712.

(35) Yu, Z. W.; Zheng, A. M.; Wang, Q. A.; Chen, L.; Xu, J.; Amoureux, J. P.; Deng, F. *Angew. Chem., Int. Ed.* **2010**, *49*, 8657−8661.

(36) Cook, M.; Conner, W. C. in *Proceedings of the 12th International Zeological Conference*; Treacy, M. M. J., Marcus, B. K., Bisher, M. E., Higgins, J. B., Eds.; Materials Research Society, Warrendale, PA, 1999; p 409.

(37) Vrabec, J.; Stoll, J.; Hasse, H. *J. Phys. Chem. B.* **2001**, *105*, 12126−12133.

(38) Fischer, R. X.; Baur, W. H.; Shannon, R. D.; Parise, J. B.; Faber, J.; Prince, E. *Acta Crystallogr.* **1989**, *C45*, 983−989.

(39) Tian, P.; Su, X.; Wang, Y.; Xia, Q; Zhang, Q.; Fan, D.; Meng, S.; Liu, Z. *Chem. Mater.* **2011**, *23*, 1406−1413.

(40) Cheung, O.; Liu, Q. L.; Bacsik, Z.; Hedin, N. *Microporous Mesoporous Mater.* **2012**, *156*, 90−96.

(41) McCusker, L. B. *Zeolites* **1984**, *4*, 51−55.

(42) Liu, Q.; Pham, T.; Porosoff, M. D.; Lobo, R. F. *ChemSusChem* **2012**, DOI: 10.1002/cssc.201200339.

(43) (a) Bourrelly, S.; Llewellyn, P. L.; Serre, C.; Millange, F.; Loiseau, T.; Férey, G. *J. Am. Chem. Soc.* **2005**, *127*, 13519−13521. (b) Llewellyn, P. L.; Bourrelly, S.; Serre, C.; Filinchuk, Y.; Férey, G. *Angew. Chem., Int. Ed.* **2006**, *45*, 7751−7754. (c) Coudert, F. X.; Boutin, A.; Jeffroy, M.; Mellot-Draznieks, C.; Fuchs, A. H. *ChemPhysChem* **2011**, *12*, 247−258.

(44) Garrone, E.; Bonelli, B.; Lamberti, C.; Civalleri, B.; Rocchia, M.; Roy, P.; Otero-Arean, C. *J. Chem. Phys.* **2002**, *117*, 10274−10282.

(45) Galhotra, P.; Navea, J. G.; Larsen, S. C.; Grassian, V. H. *Energy Environ. Sci.* **2009**, *2*, 401−409.

(46) Siporin, S. E.; McClaine, B. C.; Davis, R. J. *Langmuir* **2003**, *19*, 4707−4713.

(47) Brandani, S. *Chem. Eng. Sci.* **1998**, *53*, 2791−2798.

(48) Brandani, S.; Jama, M. A.; Ruthven, D. M. *Chem. Eng. Sci.* **2000**, *55*, 1205−1212.

(49) Plant, D. F.; Maurin, G.; Jobic, H.; Llewellyn, P. L. *J. Phys. Chem. B* **2006**, *110*, 14372−14378.

(50) Ahn, H.; Moon, J.-H.; Hyun, S.-H.; Lee, C.-H. *Adsorption* **2004**, *10*, 111−128.

(51) Reisner, B. A.; Lee, Y.; Hanson, J. C.; Jones, G. A.; Parise, J. B.; Corbin, D. R.; Toby, B. H.; Freitag, A.; Larese, J. Z.; Kahlenberg, V. *Chem. Commun.* **2000**, 2221−2222.